Amplitude analysis for the measurement of the photon polarisation in B → Kππγ decays

Violaine BELLÉE

Au temps qui passe
et qui tout efface.

Abstract

This work proposes a method to measure the photon polarisation in $B^+ \to K^+\pi^-\pi^+\gamma$ decays and prepares the necessary elements for this measurement using the data sets collected by the LHCb experiment at CERN in 2011, 2012, 2016 and 2017.

In the Standard Model of particle physics, the photon emitted in $b \to s\gamma$ transitions is predicted to be mostly left-handed. Additional couplings that enhance the right-handed photon component could be introduced by some new physics models. A direct and precise experimental test of the photon handedness is still missing. Thanks to the interference between various hadronic resonances in the $K^+\pi^-\pi^+$ system, $B^+ \to K^+\pi^-\pi^+\gamma$ decays give access to a photon polarisation parameter λ_γ, which is predicted to be $+1$ in the Standard Model up to small corrections of the order of m_s^2/m_b^2. The value of this parameter has never been measured in these decays and could help constrain new physics effects.

This thesis presents a method to measure the photon polarisation parameter using a complex amplitude analysis in the five-dimensional phase-space of $B^+ \to K^+\pi^-\pi^+\gamma$ decays. The performed studies demonstrate that, in the ideal case of a background-free sample without distortions due to experimental effects, and ignoring the differences between non-factorisable hadronic parameters between the resonances in the $K^+\pi^-\pi^+$ system, this amplitude analysis allows the measurement of the photon polarisation with a statistical uncertainty of around 0.018 with a sample of $14\,000$ $B^+ \to K^+\pi^-\pi^+\gamma$ decays, corresponding to the signal statistics for LHCb in 2011 and 2012.

The second part of this work consists in the selection and mass fit of $B^+ \to K^+\pi^-\pi^+\gamma$ decay candidates using a total of 6.6 fb^{-1} of data collected by LHCb at centre-of-mass energies of 7, 8 and $13\,\text{TeV}$, in order to prepare for an amplitude analysis of these decays. After the selection and mass fit, a total of $47\,449 \pm 321$ signal candidates are found, and a background-subtraction method is applied in order to obtain signal-like data sets that will be used in the amplitude fit.

A roadmap for the amplitude analysis of $B^+ \to K^+\pi^-\pi^+\gamma$ decays using LHCb data is also presented, and the main sources of systematic uncertainties that are expected to affect the measurement of λ_γ are described, as well as suggested methods to evaluate them. Finally, the sensitivity of the measurement in the presence of background is evaluated and the resulting uncertainty on λ_γ is of the order of 0.028, indicating good prospects for the future amplitude analysis.

Résumé

Ce travail propose une méthode pour mesurer la polarisation du photon dans les désintégrations $B^+ \to K^+\pi^-\pi^+\gamma$ et met en place les éléments nécessaires à une telle mesure sur les données prises par le détecteur LHCb au CERN en 2011, 2012, 2016 et 2017.

Le Modèle Standard de la physique des particules prédit que les photon émis dans la transition $b \to s\gamma$ sont principalement gauchers. Cependant, certains modèles de nouvelle physique pourraient introduire de nouveaux couplages et augmenter la proportion de photons droitiers. À ce jour, il n'existe pas de test experimental direct et précis sur la chiralité de ces photons. Grâce aux interférences entre les différents modes de désintégration qui contribuent à l'état final $K^+\pi^-\pi^+$, les désintégrations $B^+ \to K^+\pi^-\pi^+\gamma$ permettent d'accéder à un paramètre de polarisation du photon noté λ_γ, dont la valeur est $+1$ (à quelques corrections de l'ordre de m_s^2/m_b^2 près) dans le cadre du Modèle Standard. La valeur de ce paramètre n'a jamais été mesurée et pourrait permettre de contraindre les modèles de nouvelle physique.

Dans cette thèse, une méthode permettant de mesurer la polarisation du photon grâce à une analyse d'amplitude utilisant les cinq dimensions de l'espace de phase des désintégrations $B^+ \to K^+\pi^-\pi^+\gamma$ est présentée. Les études effectuées avec cette méthode montrent que dans le cas idéal d'échantillons sans bruits de fond et sans distorsions inhérentes au détecteur, et en négligeant les différences entre les paramètres hadroniques non factorisables des résonances du système $K^+\pi^-\pi^+$, l'analyse d'amplitude permet de mesurer la polarisation du photon avec une incertitude statistique d'environ $0,018$ sur un échantillon de $14\,000$ désintégrations $B^+ \to K^+\pi^-\pi^+\gamma$ qui correspondent au signal observé à LHCb en 2011 et 2012.

La seconde partie de ce travail consiste à préparer l'analyse d'amplitude des désintégrations $B^+ \to K^+\pi^-\pi^+\gamma$ en développant la sélection et le fit de masse sur les candidats de signal dans les $6,6$ fb^{-1} de données enregistrées par LHCb à des énergies dans le centre de masse de 7, 8 et $13\,\text{TeV}$. À l'issue de cette étape, $47\,449 \pm 321$ candidats ont été identifiés, et une méthode de soustraction de bruit de fond est appliquée afin d'obtenir un set de données équivalent à un échantillon de signal pur en vue de l'analyse d'amplitude.

Un plan du déroulement de cette future analyse de données est présenté, et les principales sources d'incertitude systématique affectant la mesure de λ_γ sont décrites, ainsi que les méthodes proposées pour évaluer ces incertitudes. Enfin, la sensibilité de la mesure qui pourrait être obtenue en présence de bruits de fond est évaluée, et il en résulte une incertitude sur la valeur de λ_γ de l'ordre de $0,028$, ce qui ouvre de belles perspectives

pour l'analyse d'amplitude à venir.

Mots clés : LHC, LHCb, physique des particules, physique des saveurs, analyse d'amplitude, désintégrations radiatives, polarisation du photon.

Acknowledgements

I am glad we could support each other and I knew I could always count on you.

Mes colocataires du "33", Marine, Julien, Céline, David, Léonore, Anaëlle, Anne-Charlotte, Timo, Erik, Joséphine et Robin méritent aussi de chaleureux remerciements pour les bons repas partagés et les Mardi Pardi.

Merci à Augustin pour les ramen et les voyages en train depuis Genève.

Merci à mes amis du lycée, et en particulier à Hélène, Marine, Maxime et Mélina, pour avoir su garder le contact.

Merci aux fous du 2A et de l'École Centrale : Sophie, Alexandre, Antoine et Solange.

Merci à Mohammad, Ghafoor et Sediqa, dont le courage restera toujours une source d'inspiration.

J'éprouve une reconnaissance toute particulière à l'égard de Frédéric Bruneau, extraordinaire prof de classe préparatoire à l'humour décapant qui a cru en moi dans une période difficile, qui m'a poussée au delà de ce que je pensais réalisable et qui m'a transmis le virus de la physique des particules.

Merci aux nombreux membres de mes familles, celles de sang et celles de cœur (les unes n'excluant pas les autres), qui se sont inquiétés pour moi, qui m'ont fait rire, qui m'ont soutenue et ont été aux petits soins. Citer tous vos noms aurait probablement rempli un chapitre entier de cette thèse, aussi vais-je devoir les garder pour moi, mais cela n'atténue en rien ma gratitude à votre égard.

Merci à mon père, amoureux de montagnes, de physique et de métaphysique, pour ne s'être jamais lassé de ma curiosité insatiable.

Merci à ma mère, femme de science et sportive invétérée, pour m'avoir appris l'obstination et l'indépendance.

Merci à ma sœur adorée pour être restée si proche de moi, même en étant au loin.

Il n'y a pas de mot assez doux et assez intense pour exprimer à Ian l'ampleur de la plénitude que j'éprouve quand je pense aux quelques huit années que nous avons passées ensemble. Alors, tout simplement, merci à toi. Pour être toi.

Lausanne, Février 2020   Violaine

Contents

Introduction

Our current understanding of the fundamental constituents of matter and of their interactions is described in the Standard Model of particle physics (SM), a mathematical framework that has been developed throughout the second half of the twentieth century. While the theoretical construction of the SM was achieved in the late 1970's, the experimental proof of the existence of all its pieces took forty more years. In 2012, the discovery of its last unobserved particle, the Higgs boson [1, 2], confirmed the surprising success of the SM as a predictive theory. Not only has this last component been found to behave exactly as predicted – its quantum numbers and couplings are found to be mostly consistent with the SM [3, 4] – but no additional fundamental component of matter has been observed since then.

In spite of this success, intriguing observations, mainly astrophysical, are not explained by the SM in its current form. In particular, it cannot account for the overwhelming predominance of matter over antimatter, and some gravitational anomalies seem to point in the direction of the existence of a new kind of matter, called *dark matter*, for which the SM does not provide any candidate.

As of today, the SM is still subject to rigorous testing in particle colliders in order to pin down its possible flaws and understand which sectors of particle physics may need a new theoretical description. If new physics is present, it is already severely constrained by all the measurements that have been performed up to now. Therefore, it is expected to manifest itself in processes that are either rare or forbidden in the SM. A class of such processes consists of the $b \to s\gamma$ transitions, where a beauty (b) quark decays to a strange (s) quark and a photon (γ). These flavour-changing neutral currents are rare in the SM, with branching ratios of the order of 10^{-5} or below, and provide many observables sensitive to new physics effects. In particular, the polarisation of the emitted photon, which is predicted to be mostly left-handed in the SM, could be significantly affected. Thanks to their four-body final state that enables the construction of observables directly proportional to the photon polarisation parameter, $B^+ \to K^+\pi^-\pi^+\gamma$ decays are an ideal playground to study the polarisation of the photon in $b \to s\gamma$ transitions. Despite being rare, these decays are recorded in significant numbers by the LHCb experiment at CERN, where about 10^{12} B^+ mesons have been produced in pp collisions delivered by the Large

Hadron Collider (LHC) in 2011–2012 (Run 1) and 2015–2018 (Run 2).

This thesis focuses on the phenomenology and data analysis of $B^+ \to K^+\pi^-\pi^+\gamma$ decays. The two main achievements of the present work are the development of a method to measure the photon polarisation using an amplitude analysis of these decays, and the preparation for such a measurement using data sets collected by the LHCb experiment in 2011, 2012, 2016 and 2017.

In Chapter 1, the Standard Model of particle physics is presented, followed by a description of the the theoretical framework used in the description of radiative B meson decays. The method proposed to measure the photon polarisation in $B \to K\pi\pi\gamma$ decays is explained in Chapter 2. The LHC and the LHCb experiment at CERN, which allow the production and detection of B meson decays, are described in Chapter 3. The selection of $B \to K\pi\pi\gamma$ decays in the data collected at LHCb in Run 1 and Run 2 is presented in Chapter 4, while the prospects for a measurement of the photon polarisation parameter using LHCb data are presented in Chapter 5. Finally, conclusions are drawn in Chapter 6.

1 Photon polarisation in the Standard Model and beyond

If bees can orient themselves and indicate the position of the most delightful flowers to other bees even in cloudy days, it is because they can detect a property of sunlight when it crosses the atmosphere: its polarisation [5,6]. The principle of the so-called 3D movies, which only emulate an impression of depth, is also based on the polarisation of light. It consists in recording two movies with lenses placed side by side (to reproduce the difference of point of view between our eyes) and in projecting them simultaneously on the same screen using two beamers with different light polarisation. The 3D glasses act as filters that select one polarisation for the left eye and another one for the right eye, allowing each of them to see the image corresponding to its own point of view, which can then be interpreted as a single 3D image by our brain.

The polarisation of light is a property of the electromagnetic field carried by light waves. By convention, it refers to the movements of the electric field in the plane perpendicular to the direction of propagation of light. In circular polarisations, the field rotates at constant rate in this plane, either clockwise with respect to an observer placed in front of the direction of motion, which is referred to as a *left-handed* circular polarisation, or anticlockwise, which is called a *right-handed* circular polarisation, as shown in Fig. 1.1.

In particle physics, the electromagnetic fields are carried by particles of light, the photons. At this level, the rotation of the field is represented by a vector called spin. A right-handed photon has its spin along its direction of motion while for a left-handed photon the spin and direction of motion are opposite. The *helicity h* of the photon refers to the value of the projection of the spin vector $\vec{s}$ onto the direction of motion, $h = \vec{s} \cdot \vec{p}/|\vec{p}|$, where $\vec{p}$ is the momentum of the particle. In the case of a photon, the helicity can take only two values, $+\hbar$ and $-\hbar$, which in natural units (where the speed of light c and the reduced Planck constant $\hbar$ are set to 1) translate to $+1$ for the right-handed photon and -1 for the left-handed.

In the current efforts to search for new physics phenomena beyond our current description of particle physics, two main strategies are explored. *Direct searches* consist in looking
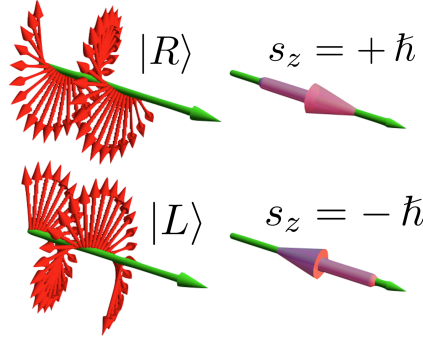
Figure 1.1 – Sketch of an electromagnetic wave with right-handed circular polarisation (top left) and left-handed circular polarisation (bottom left), where the rotating electric field is shown in red and the direction of motion in green [7]. The equivalent polarisation states for the photon are shown on the right, with the spin in pink.

for signatures of the decays or interactions of new particles, while in *indirect searches* the goal is to measure very precisely the values of some observables that are well predicted by the Standard Model of particle physics, and to look for deviations that could be explained by new physics phenomena. The observable chosen in this thesis is the polarisation of the photons emitted in $B^+ \to K^+\pi^-\pi^+\gamma$ decays, which are expected to be mostly right-handed in the Standard Model.

In this chapter, an overview of the Standard Model will be given first, as well as a summary of its limitations that justify the searches for new physics phenomena. Section 1.2 will show why and how radiative B decays are used as probes for new physics, while Section 1.3 will introduce the $B^+ \to K^+\pi^-\pi^+\gamma$ decays and the photon polarisation parameter λ_γ.

1.1 The Standard Model of particle physics

1.1.1 Fields and interactions of the Standard Model

Overview   The Standard Model (SM) is a unified theory that describes the basic particles of matter (the fermions) and three of their possible interactions:

- the electromagnetic force (responsible for electric current),

- the weak force (involved in the production of energy in the Sun),

- the strong force (that holds the nuclei together).

These interactions are modeled as exchanges of force carriers with spin 1: the *gluons* for the strong force, the *photon* for the electromagnetic force and the Z^0, W^+ and W^- *bosons* for the weak force. The SM also includes the mechanism that gives rise to the masses of

fermions and Z^0, W^+ and W^- bosons, which is referred to as the *Higgs mechanism* and involves interactions with a spin 0 neutral particle: the *Higgs boson*.

Contrary to the aforementioned bosons (force carriers and Higgs boson) that are characterized by integer spins, the fermions have a spin of $1/2$. They are grouped in three families, or *generations*, each of them being a heavier version of the previous one. Most of the matter on Earth consists of particles from the first family while the two other generations are basic components of the so-called *exotic matter*. Each family is made out of an up-type and a down-type quark with respective electric charges of $+2/3$ and $-1/3$, of a charged lepton (such as the electron in the lightest family) and of a neutrino, a neutral lepton with an extremely small mass. The fermions and bosons of the SM are shown in Fig. 1.2. Each particle has an anti-particle counterpart, which has the same mass and spin but opposite quantum numbers, except for the neutral bosons which are their own antiparticles.
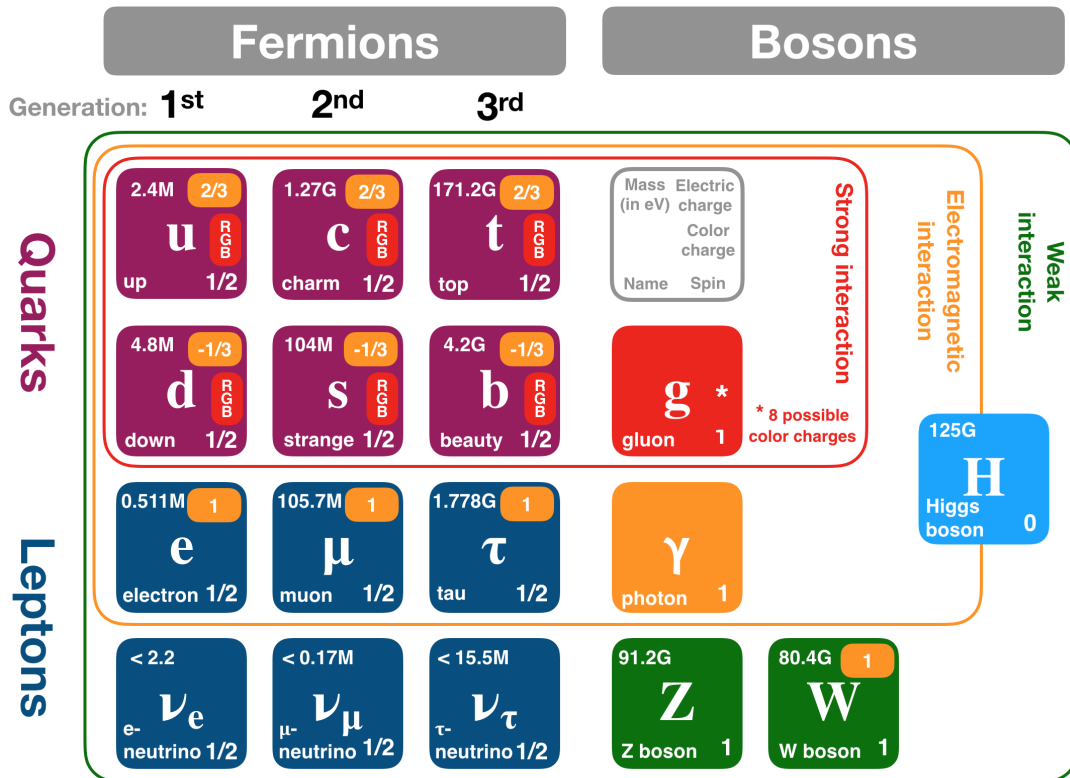
Figure 1.2 – Summary of the Standard Model particles. Absence of information about colour charge or electric charge implies that the particle is not affected by the strong or electromagnetic interaction. All 12 fermions and the W boson also have an antimatter counterpart which has the same spin and mass, and opposite values of all quantum numbers.

Quarks The quarks are particles of matter affected by all three interactions: strong, electromagnetic and weak. There are six flavours of quarks: the positively charged are

the *up*, *charm* and *top* quarks, while the negatively charged are the *down*, *strange* and *bottom* quarks. The masses of the different flavours cover five orders of magnitudes between the mass of the down quark, $m_d = 4.8\,\mathrm{MeV}/c^2$, and that of the top quark, $m_t = 173.5\,\mathrm{GeV}/c^2$. In addition to their electric charge, quarks carry a colour charge (red, green or blue) which defines their interaction under the strong force. With the exception of the top quark, which decays immediately after being produced, quarks are always found in groups of strongly bound states with zero net colour charge: the hadrons. This phenomenon is know as *colour confinement*. The most common hadrons are the *baryons*, three-quark systems in which each of the quarks carries a different colour, and the *mesons*, quark-antiquark systems where the quark and anti-quark have opposite colour charges (for example, blue-antiblue). Some well known baryons are the components of the nuclei: the protons (two up-quarks and one down quark) and the neutrons (two down-quarks and one up-quark). At particle physics colliders, some very common mesons are the charged pions π^+ and π^- which are respectively up-antidown and down-antiup quark systems, and the charged kaons K^+ and K^- (respectively up-antistrange and strange-antiup systems). These are characterized by long lifetimes: 2.6×10^{-8} s for the charged pions, and 1.2×10^{-8} s for the charged kaons. Mesons with a b or a c quark such as the B^+ meson (up-antibottom system) are also relatively long-lived, with lifetimes of the order of 10^{-12} s which allow them to fly at measurable distances in the detectors before decaying. This feature enables precise selection and studies, as described in Chapter 3.

Leptons The leptons can be divided into two categories: the charged leptons are sensitive to the electromagnetic and weak interactions, while the neutral ones, the neutrinos, interact only through weak interactions, which makes them very difficult to detect. There are three flavours associated to each of the families: the electron ($m_e = 511\,\mathrm{keV}/c^2$) and electronic neutrino for the first family, the muon ($m_\mu = 106\,\mathrm{MeV}/c^2$) and muonic neutrino for the second family, and the tau ($m_\tau = 1777\,\mathrm{MeV}/c^2$) and tauonic neutrino for the third family.

The neutrinos were originally described without mass in the SM, but the observation of neutrino oscillations [8, 9] indicated that at least two of the neutrino flavours must have a non-zero mass, though possibly very small. Two types of descriptions could accomodate neutral massive neutrinos: these particles could be *Dirac fermions* or *Majorana particles*. The first case would imply the conservation of a lepton charge carried by the neutrinos during their interactions, and would result in the neutrinos and antineutrinos being two distinct entities characterized with different quantum numbers. If the neutrinos were Majorana particles, no lepton flavour number would be conserved in the interactions and the neutrinos and antineutrinos would be exactly the same particle. At the moment, no experimental data determines which scenario describes the massive neutrinos. However, current observations indicate that neutrinos of all flavours are produced in a left-handed state (and the antineutrinos are produced right-handedly), so they are described in the SM by chiral left-handed fields.

A gauge invariant theory As it deals with phenomena characterized by small scales and relatively high energies, the SM is a mathematical construction based on both quantum field theory and special relativity. In this theory, the particles are described as quantum excitations of fields that are entitled with local degrees of freedom (which describe the internal properties of the particles) and whose dynamics are obtained by minimizing the action $\mathcal{S} = \int \mathcal{L} d^4 x$, where x is a four-vector indicating the space-time position, and $\mathcal{L}$ is the Lagrangian of the system.

The SM is a *gauge-invariant* theory, which means that the Lagrangian is required to be invariant under a Lie Group of local transformations $\mathcal{G}$ called *gauge transformations*. The transformations are called local because they are dependent on the space-time coordinate x. A gauge-invariant field theory is entirely defined by its gauge group, and the generators of the Lie Group are interpreted as the mediators of the interactions between the fields. In the particular case of the SM, the Lagrangian of the system is required to be invariant under $SU(3)_c \times SU(2)_L \times U(1)_Y$. $SU(3)_c$ describes the strong interaction which is mediated by 8 massless bosons, the gluons, while $SU(2)_L \times U(1)_Y$ encodes the electroweak (EW) interaction mediated by the massive W^+, W^- and Z bosons and the massless γ boson. The supplementary requirement of Lorentz invariance implies that all these mediators have spin 1; they are referred to as *gauge bosons*. All the particles in the SM are classified according to their quantum numbers which encode their behaviour under the gauge symmetries. When requiring the Lagrangian to be invariant under $SU(2)_L \times U(1)_Y$, the generators of the electroweak interaction arise without mass. This symmetry needs to be *spontaneously broken* by the non-zero vacuum expectation of a scalar field, the Higgs field, in order to add mass terms for the gauge bosons in the Lagrangian. In turn, new mass terms for the fermions are obtained through interactions between the Higgs field and the fermionic fields, called Yukawa couplings, which result in mixing between the different quark flavours (see Sec. 1.1.2).

The strong interaction and $SU(3)_c$ The gauge field theory that formalizes the strong interaction linked to $SU(3)_c$ is referred to as Quantum Chromodynamics (QCD). It includes the description of the six quarks and the eight kinds of gluons that all carry a colour charge. The peculiarity of the strong force is that its associated coupling constant α_s is very large at small energy scales and decreases asymptotically at high energy scales. This phenomenon is called *asymptotic freedom* and has been proven analytically within QCD [10,11]. When trying to make predictions for processes governed by QCD, the fact that α_s is small enough in some regimes allows for simplifications in the computations which can be done perturbatively. However, below a scale $\Lambda_{\mathrm{QCD}} \sim 250\,\mathrm{MeV}$, the interactions between quarks and gluons are very strong (*colour confinement*), and the dynamics of the system cannot be described in the context of a perturbative theory. Some results at low energy scales can be obtained theoretically using lattice computations for example, but most of the time predictions for processes below Λ_{QCD} are obtained using phenomenological models.

The electroweak interaction and $SU(2)_L \times U(1)_Y$ The electroweak interactions are described by the spontaneously broken $SU(2)_L \times U(1)_Y$ symmetry. The $SU(2)$ invariance is linked to the conservation of the weak isospin number T_3, a quantum number that describes the behaviour under weak interactions. The most striking aspect of this symmetry is that it acts differently on the fermionic fields depending on their *chirality*: the generators of $SU(2)$ (the W^+, W^0 and W^- bosons) couple only to the fermionic fields of negative chirality (called *left-handed* fermions) which have $T_3 = \pm 1/2$, while the fermionic fields of positive chirality (and antifermionic fields of negative chirality) are $SU(2)$ singlets (they do not interact through weak interactions) with $T_3 = 0$. The $U(1)_Y$ invariance relates to the conservation of the weak hypercharge number Y_W and its generator is the B boson. Under spontaneous symmetry breaking, the number that is actually conserved in electroweak interactions is the total electric charge (in elementary charge units) which is given by the sum of the weak hypercharge and the weak isospin number $Q = T_3 + \frac{1}{2}Y_W$. The interactions with the Higgs field cause the B and W^0 bosons to mix, giving rise to the photon and the Z^0 boson.

Discrete symmetries of the Standard Model of particle physics On top of the continuous symmetries presented before, the various interactions are characterized by their behaviour under the three following discrete transformations:

- Time reversal (T) changes the sign of the time coordinate.

- Parity (P) simultaneously changes the sign of the three spatial coordinates. Under this transformation, fermionic fields change chirality.

- Charge conjugation (C) transforms all particles into their antiparticles.

In the SM, the strong and electromagnetic interactions are invariant under each of these transformations (they are said to conserve C, P and T symmetries). However, the weak interaction violates P maximally (it couples only to left-handed fermions and not to right-handed fermions). For some time, this interaction was thought to conserve CP, but small amounts of CP violation were actually observed in weakly interacting kaon systems [12], B systems [13,14], and more recently in D meson systems [15].

The conservation of CPT however is considered to be a fundamental law of physics and is implied in all quantum field theories with a Hermitian Hamiltonian (CPT theorem). One of its most important consequences is that particles and antiparticles must have the same masses and lifetimes.

1.1.2 Flavour structure and CKM matrix

After the introduction of the spontaneous symmetry breaking terms in the SM Lagrangian, the term describing the weak interactions between the quarks and the W bosons reads

$$\mathcal{L} = \frac{g}{\sqrt{2}} \left[(\bar{u},\bar{c},\bar{t})_L \, \gamma^\mu W_\mu^+ V_{\mathrm{CKM}} \begin{pmatrix} d \\ s \\ b \end{pmatrix}_L + (\bar{d},\bar{s},\bar{b})_L \, \gamma^\mu W_\mu^- V_{\mathrm{CKM}}^\dagger \begin{pmatrix} u \\ c \\ t \end{pmatrix}_L \right] . \quad (1.1)$$

Here, g is a coupling constant, γ^μ are Dirac matrices and V_{CKM} is the Cabibbo-Kobayashi-Maskawa (CKM) matrix which by convention transforms the mass eigenstates of the left-handed down-type quarks (d', s', b') into the flavour eigenstates (d, s, b) of the electroweak interaction:

$$\begin{pmatrix} d \\ s \\ b \end{pmatrix}_L = V_{\mathrm{CKM}} \begin{pmatrix} d' \\ s' \\ b' \end{pmatrix}_L = \begin{pmatrix} V_{ud} & V_{us} & V_{ub} \\ V_{cd} & V_{cs} & V_{cb} \\ V_{td} & V_{ts} & V_{tb} \end{pmatrix} \begin{pmatrix} d' \\ s' \\ b' \end{pmatrix}_L . \quad (1.2)$$

The CKM matrix elements V_{ij} connect up-type and down-type quark flavours of the three families. The transition probability from a quark of flavour i to a quark of flavour j is given by $|V_{ij}|^2$ indicating that flavour-changing transitions can happen through the exchange of a charged $W^\pm$ boson.

Making use of the CKM matrix unitarity and of the freedom of choice of the relative phases in the six quark fields, the number of free parameters of this complex 3×3 matrix is reduced from 18 to 4. A standard exact parametrization of the CKM matrix, called the Chau-Keung parametrization [16], consists in expressing all the elements as a function of three real mixing angles θ_{12}, θ_{13}, θ_{23} and an imaginary phase δ,

$$V_{\mathrm{CKM}} = \begin{pmatrix} c_{12}c_{13} & s_{12}c_{13} & s_{13}e^{-i\delta} \\ -s_{12}c_{23} - c_{12}s_{23}s_{13}e^{i\delta} & c_{12}c_{23} - s_{12}s_{23}s_{13}e^{i\delta} & s_{23}c_{13} \\ s_{12}s_{23} - c_{12}c_{23}s_{13}e^{i\delta} & -c_{12}s_{23} - s_{12}c_{23}s_{13}e^{i\delta} & c_{23}c_{13} \end{pmatrix} , \quad (1.3)$$

where $c_{ij} = \cos\theta_{ij}$ and $s_{ij} = \sin\theta_{ij}$.

However, in order to highlight the hierarchy of the various elements of the CKM matrix, the approximate Wolfenstein parametrization [17] is more commonly used. It consists in expanding the CKM matrix in terms of orders of the parameter λ defined by $\lambda = s_{12}$.
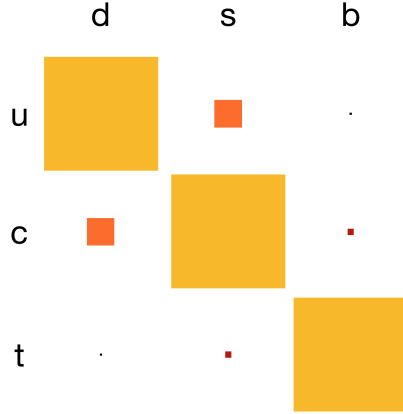
Figure 1.3 – Sketch of the relative importance of the various elements of the CKM matrix, where the area of each square is proportionnal to the square of the corresponding matrix element [18].

The Wolfenstein parametrization of the CKM matrix at order 3 reads

$$V_{\mathrm{CKM}} = \begin{pmatrix} 1 - \frac{\lambda^2}{2} & \lambda & A\lambda^3(\rho - i\eta) \\ -\lambda & 1 - \frac{\lambda^2}{2} & A\lambda^2 \\ A\lambda^3(1 - \rho - i\eta) & -A\lambda^2 & 1 \end{pmatrix} + \mathcal{O}(\lambda^4) \,, \tag{1.4}$$

where A, ρ and η are defined by $s_{12} = \lambda$, $s_{23} = A\lambda^2$ and $s_{13}e^{i\delta} = A\lambda^3(\rho + i\eta)$.

The measured values of the parameters are $\lambda \simeq 0.23$, $A \simeq 0.82$, $\rho \simeq 0.13$ and $\eta \simeq 0.26$. The expressions of the matrix elements highlight the existence of a hierarchy between the probabilities of the various transitions, as illustrated on Fig. 1.3. The most probable transitions are between quarks of the same family, followed by transitions between the first and second family, between the second and the third family, and finally between the first and third family.

The unitarity of V_{CKM} $(V_{\mathrm{CKM}}V_{\mathrm{CKM}}^{\dagger} = 1)$ translates into six relations between the matrix elements, amongst which the most relevant is

$$V_{ud}V_{ub}^* + V_{cd}V_{cb}^* + V_{td}V_{tb}^* = 0 \,. \tag{1.5}$$

Introducing $\bar{\rho}$ and $\bar{\eta}$ such that

$$\bar{\rho} + i\bar{\eta} = -\frac{V_{ud}V_{ub}^*}{V_{cd}V_{cb}^*} \,, \tag{1.6}$$

Eq. 1.5, divided by $V_{cd}V_{cb}^*$, is that of a triangle in the complex plane (called *unitary triangle*) represented in Fig. 1.4. Experiments can measure the angles defined by the
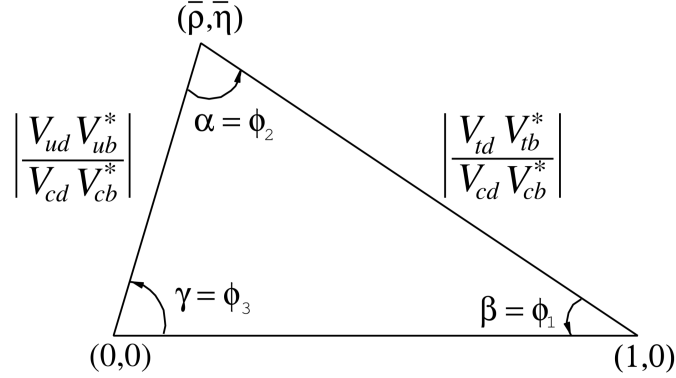
Figure 1.4 – The CKM unitary triangle [19].

relations

$$\alpha = \phi_2 = -\frac{V_{td}V_{tb}^*}{V_{ud}V_{ub}^*}, \tag{1.7}$$

$$\beta = \phi_1 = -\frac{V_{cd}V_{cb}^*}{V_{td}V_{tb}^*}, \tag{1.8}$$

$$\gamma = \phi_3 = -\frac{V_{ud}V_{ub}^*}{V_{cd}V_{cb}^*}. \tag{1.9}$$

The precise measurement of the sides and of the angles of this triangle is a validity test of the Standard Model, which predicts the shape to be closed. Figure 1.5 shows the most recent constraints on the unitarity triangle from experimental data and lattice QCD, which form a consistent set within the SM.

1.1.3 Flavour puzzle and limitations of the Standard Model

In the flavour sector, the SM is endowed with 13 parameters that are not constrained by theory (the 6 quark masses, the 3 charged lepton masses and the 4 parameters of the CKM matrix). This large number of free parameters limits the predictive power of the SM, and it is all the more intriguing as the relations between the CKM coefficients do not appear as random. There seems to be a hierarchy between the various elements of the CKM matrix, and also between the masses of the particles of the three generations, which is not at all described by the SM. This might be a hint for a more fundamental theory of which the SM would be an effective theory, *i.e.* an approximate theory valid only in a certain range of energies and couplings.

The flavour sector is not the only one with unexplained phenomena. For example, the Standard Model with its three generations does not provide an explanation for the observed quantisation of electric charges [21]. Also, from the point of view of the theory, CP violation is allowed in strong interactions, whereas there has never been
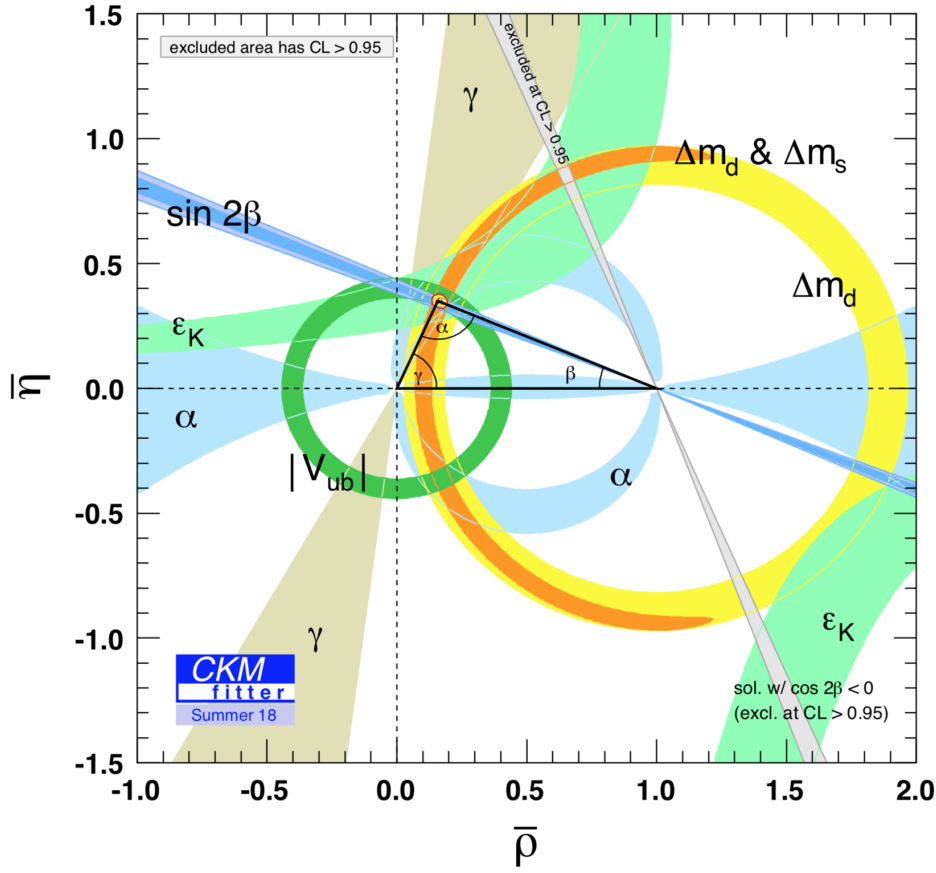
Figure 1.5 – Combined constraints on the unitary triangle from experimental data, as of 2018 [20].

any evidence of a violation of this symmetry in experimental data [22]. Additionally, several cosmological observations are not explained by the SM. The first one is the matter-antimatter asymmetry [23]. Although early universe scenarios predict that matter and antimatter should have been produced in equal amounts, observations show that today's universe is mainly filled with matter while antimatter is very rare. One of the necessary conditions for a model to explain this asymmetry is to allow for a rather large amount of *CP* violation. In the SM, this type of violation happens only in the weak sector, and it has been measured to be insufficient to explain the disappearance of antimatter. The second set of observations which is not explained in the SM is referred to as Dark Matter. Several phenomena, including high rotational velocity of stars around the galaxies but also spectral studies of the cosmic microwave background and gravitational lensing studies of the Bullet Cluster seem to indicate that some astrophysical objects are submitted to an additional gravitational field compatible with matter, but invisible. None of the particles of the Standard Model is a good candidate to explain Dark Matter, either because they are not massive enough or because they interact too much with the other known particles.

For these reasons, hints of new phenomena beyond the Standard Model are actively looked for in order to feed the development of new theories of particle physics. Recently, results of lepton-flavour universality tests performed by the Belle, BaBar and LHCb collaborations have raised a new interest in indirect searches for new physics in the flavour sector. The goal of these tests is to check the validity of the Standard Model which predicts *lepton universality*: the three types of leptons (electronic, muonic and tauonic) should couple exactly in the same way through electroweak interaction because the photon, W and Z bosons do not "see" any difference between the three generations. The studies conducted by the three experiments consist in measuring ratios of decay rates involving leptons from different families. They have focused on two main kinds of transitions:

- $b \to sl^+l^-$ transitions are studied using the b-hadron decays $H_b \to H_s l^+l^-$ (for example $B^+ \to K^+l^+l^-$ or $B^+ \to K^{*+}l^+l^-$). In this case, the observables are defined as ratios of differential decay rates,

$$
R_{H_s} = \frac{\int_{q^2_{\min}}^{q^2_{\max}} \dfrac{d\Gamma(H_b \to H_s \mu^+ \mu^-)}{dq^2} dq^2}{\int_{q^2_{\min}}^{q^2_{\max}} \dfrac{d\Gamma(H_b \to H_s e^+ e^-)}{dq^2} dq^2} ,
\tag{1.10}
$$

where q^2 is the dilepton invariant mass squared while $q^2_{\min}$ and $q^2_{\max}$ define the interval chosen for the study.

- $b \to cl^-\bar{\nu}_l$ transitions are studied in $H_b \to H_c l^-\bar{\nu}_l$ decays (for example $\bar{B}^0 \to D^{*+}l^-\bar{\nu}_l$), where the observables are the ratios of branching fractions:

$$
R_{H_c} = \frac{\mathcal{B}(H_b \to H_c \tau^- \bar{\nu}_\tau)}{\mathcal{B}(H_b \to H_c l'^- \bar{\nu}_{l'})} .
\tag{1.11}
$$

The lepton l' is a muon or an electron in Belle and BaBar measurements, and a muon in LHCb measurements.

The results of these measurements are summarized in Fig. 1.6, which shows that the combined values of R_D and R_{D^*} exceed the SM predictions by 2.3 σ and 3 σ respectively, while the LHCb measurements of R_K and R_{K^*} are in agreement with the predictions at the level of 2.6 σ and 2.1–2.5 σ respectively.

Though insufficient yet to determine whether lepton flavour universality is violated, these tests are very powerful probes for NP because the SM predictions are relatively clean (most of the theoretical uncertainties cancel in the ratios) and deviations from the predicted value would be a clear sign of New Physics (NP). However, in order to better constrain NP effects, the results of these tests are combined with many other observables in the flavour sector, and another type of decays also provides excellent probes for these
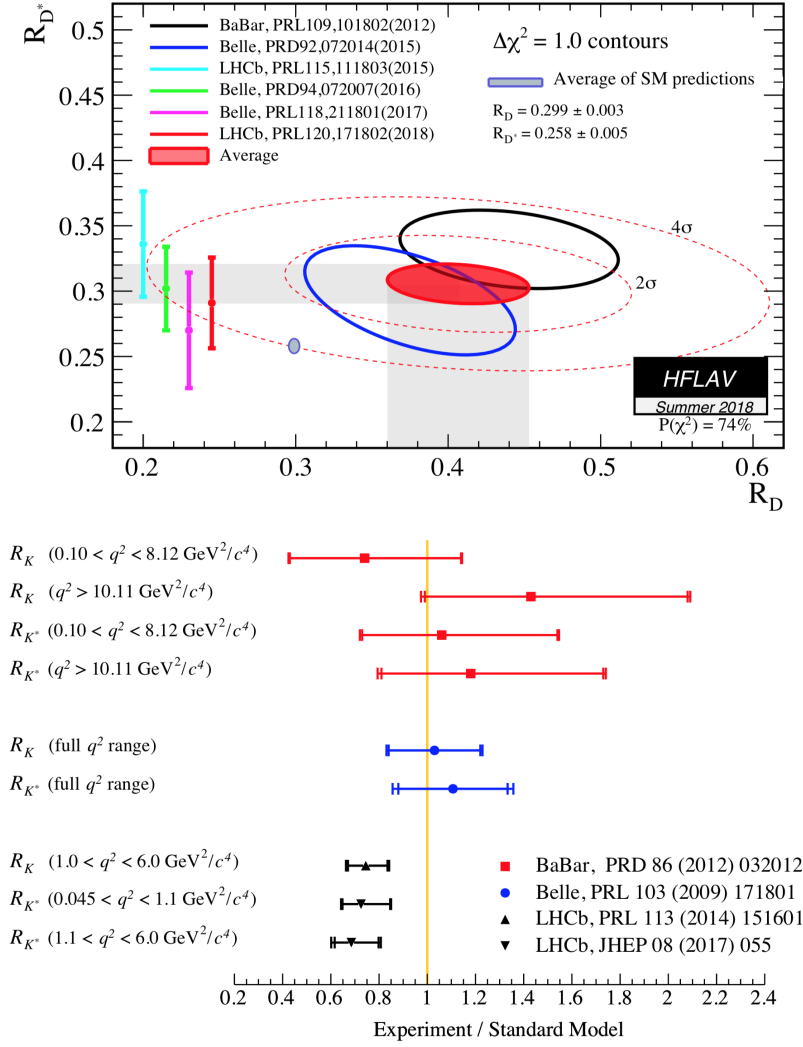
Figure 1.6 – Results of lepton flavour universality tests using $b \to cl^-\bar{\nu}_l$ transitions (top) and $b \to sl^+l^-$ transitions (bottom) as of summer 2018 [24].

effects: radiative b decays.

1.2 Radiative b decays as a probe for New Physics

Radiative b decays are flavour-changing neutral currents forbidden at tree level in the SM. Indeed, while flavour-changing charged transitions (with the exchange of a charged W boson such as $s \to uW^-$) are allowed in the SM and defined by the CKM matrix, no term in the SM Lagrangian allows the coupling of quarks of different flavours to a Z boson. Therefore, flavour-changing neutral transitions can occur only through loops such as the so-called *penguin diagram* and *box diagram* shown in Fig. 1.7.

14
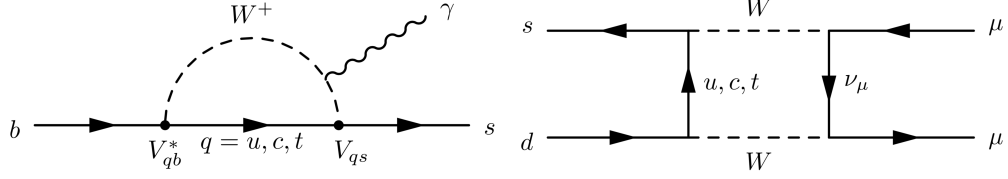
Figure 1.7 – Feynman representation of the penguin diagram of a $b \to s\gamma$ transition (left) and of the box diagram of a $K^0 \to \mu^+\mu^-$ decay (right) [25].

In the present work and in most of the radiative decays studied at LHCb, the main transition at stake is $b \to s\gamma$, which is very sensitive to NP effects due to two of its properties:

- It is **rare** in the SM. Because of the Glashow–Iliopoulos–Maiani (GIM) mechanism, the penguin loop shown in Fig. 1.7 is very suppressed. Inside the loop, an up-type quark (u,c or t) is exchanged, so the amplitude associated with this process is the sum of three contributions. Using the Feynman rules, each of these contributions is the product of the CKM matrix elements $V_{ib}^* V_{is}$ (where $i = u, c, t$) and of a term which depends on the mass of the exchanged quark $F(m_i)$. If the masses of the up-type quarks are degenerate ($m_u = m_c = m_t$), then the mass term factorizes and the amplitude of the $b \to s\gamma$ transition is proportional to $\sum_{i=u,c,t} V_{ib}^* V_{is}$, which is equal to 0 because of the unitarity of the CKM matrix. The fact that the quark masses are different (which is especially true in the up-quark sector) allows the process to exist despite this suppression, and also implies that the main contribution to $b \to s\gamma$ comes from the exchange of a t quark in the loop.

- As the top quark dominates in the loop, this transition is **sensitive to physics at high mass scales**. The exchange of a new heavy particle in the electroweak loop could change the phenomenology of this process with respect to the Standard Model prediction.

In the $b \to s\gamma$ transition, the W boson in the loop couples to an s quark of negative chirality. As a result, the emitted photon is predicted to be almost completely left-handed in the SM. In some NP models, new couplings with fields of positive chirality could be introduced and enhance the right-handed photon component. In the minimal supersymmetric model (MSSM) for example, left-right quark mixing causes a chirality flip along the gluino line in the electroweak penguin loop [26], while the right-handed neutrinos of some Grand Unification models could couple to right-handed quarks [27], causing the emission of right-handed photons. Left-right symmetry models would also allow a chirality flip of the top quark in the loop, resulting in mixings of right- and left-handed W bosons and changing the amount of right- and left-handed photons [28–30].

Because of strong confinement, the quarks involved in the $b \to s\gamma$ transition hadronize,

which makes theoretical predictions complicated, especially for the branching ratios of exclusive decays. From a theoretical point of view, the cleanest observable is the inclusive $B \to X_s \gamma$ branching fraction, where X_s refers to all the hadrons arising from the hadronization of the s quark. In this case, most of the contributions can be computed perturbatively [31], allowing for reliable comparisons with experimental results. The measurements of this branching fraction by BaBar and Belle [32, 33] result in strong constraints on NP scenarios in radiative decays [34], but still leave space for effects affecting the polarisation of the photon.

1.2.1 Effective hamiltonian for the $b \to s\gamma$ transition

The constraints on NP obtained through the measurements of various observables are very often expressed on *Wilson coefficients*, allowing for combinations of results across different decays and measured quantities.

These coefficients arise when a full theory is approximated (up to a given energy scale μ) as an effective field theory. The high energy degrees of freedom are integrated out in some coefficients called Wilson coefficients, and the operators encode only effects below the chosen energy scale. The effective hamiltonian of $b \to s\gamma$ transitions reads [34]

$$\mathcal{H}_{\text{eff}} = -\frac{4G_F}{\sqrt{2}} V_{tb} V_{ts}^* \left(\sum_{i=1}^{8} C_i(\mu) Q_i(\mu) + \sum_{i=7}^{8} C_i'(\mu) Q_i'(\mu) \right) , \tag{1.12}$$

where G_F is the Fermi constant linked to the strength of the weak decay process, Q_{1-6} are the SM four-quark operators, and $Q_7^{(\prime)}$ and $Q_8^{(\prime)}$ are the electromagnetic and chromomagnetic dipole operators respectively, expressed as

$$Q_7^{(\prime)} = \frac{e}{16\pi^2} m_b (\bar{s}_{L(R)} \sigma_{\mu\nu} b_{R(L)}) F^{\mu\nu} \tag{1.13}$$

and

$$Q_8^{(\prime)} = \frac{g_s}{16\pi^2} m_b (\bar{s}_{L(R)} \sigma_{\mu\nu} T^a b_{R(L)}) G^{a\mu\nu} . \tag{1.14}$$

The Wilson coefficients $C_i^{(\prime)}(\mu)$ indicate the relative importance of the local operators. In particular, the $C_7(\mu)$ and $C_7'(\mu)$ coefficients encode the couplings to left- and right-handed photons, respectively. In the SM, they are related by

$$\frac{C_7'}{C_7} = \frac{m_s}{m_b} \simeq 0.02 . \tag{1.15}$$

It is then usual to redefine a regularisation- and renormalisation-scheme independent

$C_7^{\text{eff}}(\mu)$ coefficient as

$$C_7^{\text{eff}}(\mu) = C_7(\mu) + \sum_{i=1}^{6} y_i C_i(\mu) \,, \qquad (1.16)$$

where $y = (0, 0, -\frac{1}{3}, -\frac{4}{9}, -\frac{20}{3}, -\frac{80}{9})$ [35]. In the Standard Model, the value of this coefficient, which encodes the couplings to left-handed photons, is $C_7^{\text{eff}}(\mu) = -0.2915$ at a scale $\mu = m_b = 4.8 \, \text{GeV}$ [36]. From now on C_7^{eff} will be referred to as C_7.

1.2.2 Different ways to measure C_7 and C_7'

The very first observation of a non-zero photon polarisation in a radiative $b \to s\gamma$ transition was obtained using $B^+ \to K^+ \pi^- \pi^+ \gamma$ decays recorded by the LHCb experiment in 2011 and 2012 [37]. It consisted in measuring an observable called the *up-down asymmetry* in several bins of the $K^+ \pi^- \pi^+$ invariant mass, and concluded that C_7 and C_7' were different from each other, but no other constraint could be set on these parameters. The method used in this measurement, described in detail in Sec. 1.4.1, is the base of the present work.

However, several other methods have provided constraints on the C_7 and C_7' coefficients:

- As pointed out previously, one of the strongest constraints on the Wilson coefficients comes from the measurement of the inclusive $B \to X_s\gamma$ branching fraction by Belle and BaBar [32,33]. This observable is proportional to $|C_7|^2 + |C_7'|^2$ and (along with additional branching fraction measurements of exclusive radiative decays) results in the constraints indicated in blue in Fig. 1.8.

- Another method consists in exploiting the time-dependent decay rates of $B_{(s)}^0 \to f_{CP}\gamma$ and $\bar{B}_{(s)}^0 \to f_{CP}\gamma$ where f_{CP} is a *CP* eigenstate. They are expressed as [38]

$$\Gamma_{B_{(s)}^0 \to f_{CP}\gamma}(t) \propto e^{-\Gamma_{(s)}t} \left[\cosh(\frac{\Delta\Gamma_{(s)}t}{2}) - \mathcal{A}_{f_{CP}}^{\Delta}\sinh(\frac{\Delta\Gamma_{(s)}t}{2}) \right.$$
$$\left. + \mathcal{C}_{f_{CP}} \cos(\Delta m_{(s)}t) - \mathcal{S}_{f_{CP}} \sin(\Delta m_{(s)}t) \right], \qquad (1.17)$$

$$\Gamma_{\bar{B}_{(s)}^0 \to f_{CP}\gamma}(t) \propto e^{-\Gamma_{(s)}t} \left[\cosh(\frac{\Delta\Gamma_s t}{2}) - \mathcal{A}_{f_{CP}}^{\Delta}\sinh(\frac{\Delta\Gamma_{(s)}t}{2}) \right.$$
$$\left. - \mathcal{C}_{f_{CP}} \cos(\Delta m_{(s)}t) + \mathcal{S}_{f_{CP}} \sin(\Delta m_{(s)}t) \right], \qquad (1.18)$$

where $\mathcal{C}_{f_{CP}}$ is the direct *CP* asymmetry, $\mathcal{S}_{f_{CP}}$ is the asymmetry associated with $B_{(s)}^0 - \bar{B}_{(s)}^0$ mixing, while $\Delta\Gamma_{(s)}$ and $\Delta m_{(s)}$ are the differences of decay widths and masses of the mass eigenstates of the $B_{(s)}^0 - \bar{B}_{(s)}^0$ system. The dependence on the Wilson coefficients arises in the $\mathcal{A}_{f_{CP}}^{\Delta}$ and $\mathcal{S}_{f_{CP}}$ coefficients which can be expressed

17

as

$$\mathcal{A}^{\Delta}_{f_{CP}} = \frac{2\,\mathcal{R}e\left[\frac{q}{p}(\bar{C}_7 C_7^* + \bar{C}_7' C_7'^*)\right]}{|C_7|^2 + |\bar{C}_7|^2 + |C_7'|^2 + |\bar{C}_7'|^2}\,, \tag{1.19}$$

$$\mathcal{S}_{f_{CP}} = \frac{2\,\mathcal{I}m\left[\frac{q}{p}(\bar{C}_7 C_7^* + \bar{C}_7' C_7'^*)\right]}{|C_7|^2 + |\bar{C}_7|^2 + |C_7'|^2 + |\bar{C}_7'|^2}\,, \tag{1.20}$$

where q and p are the mixing parameters of the $B^0_{(s)} - \bar{B}^0_{(s)}$ system. This technique has been used with several decays, in particular $B^0_s \to \phi\gamma$ decays at LHCb, and $B^0 \to \pi^0 K^0_{\rm S}\gamma$ decays at Belle and BaBar. As the separation of the B^0_s from the $\bar{B}^0_s$ mesons (referred to as *flavour-tagging*) is very challenging at LHCb, a first analysis was performed using an *untagged* technique [39] on Run 1 data: no difference is made between B^0_s and $\bar{B}^0_s$, so the two above decay rates are summed and the dependence in C_7 and C_7' comes only from $\mathcal{A}^{\Delta}_\phi$, resulting in the constraint shown in green in Fig. 1.8. The time-dependent tagged analysis has been performed later [40] using the same data set, and resulted in the first measurements of $\mathcal{S}_\phi$ and $\mathcal{C}_\phi$, both compatible with the Standard Model, and in a new measurement of $\mathcal{A}^{\Delta}_\phi$ which is compatible with both the value obtained in the untagged analysis and the SM value. Time-dependent analyses of $B^0 \to \pi^0 K^0_{\rm S}\gamma$ and $\bar{B}^0 \to \pi^0 K^0_{\rm S}\gamma$ have been performed by the Belle [41] and BaBar [42] collaborations, leading to the constraint shown in orange in Fig. 1.8.

- Useful constraints on C_7 and C_7' are also obtained by measuring angular distributions in $B^0 \to K^{*0}e^+e^-$ decays at low invariant dilepton mass squared q^2 [43]. The flavour changing transition in this decay is $b \to se^+e^-$, whose effective hamiltonian receives contributions from all above mentioned operators, but also from supplementary local operators $Q_9^{(\prime)}$ and $Q_{10}^{(\prime)}$ which encode the couplings to leptons,

$$Q_9^{(\prime)} = \frac{e^2}{16\pi^2} m_b (\bar{s}_{L/R}\gamma_\mu b_{L/R})(\bar{l}\gamma^\mu l) \tag{1.21}$$

and

$$Q_{10}^{(\prime)} = \frac{e^2}{16\pi^2} m_b (\bar{s}_{L/R}\gamma_\mu b_{L/R})(\bar{l}\gamma^\mu \gamma_5 l)\,. \tag{1.22}$$

However, in the region close to the photon pole (for very small values of q^2), the contributions from the $Q_7^{(\prime)}$ operators dominate and the angular distributions of the decay products (K^+, π^-, e^+ and e^-) are sensitive to C_7 and C_7'. The decay can be described in terms of the dilepton invariant mass squared and three angles, θ_l, θ_K and $\tilde{\phi}$ as defined in Ref. [43]. The differential decay rate for $B^0 \to K^{*0}e^+e^-$

and $\bar{B}^0 \to \bar{K}^{*0}e^+e^-$ reads

$$\frac{1}{d(\Gamma + \bar{\Gamma})/dq^2} \frac{d^4(\Gamma + \bar{\Gamma})}{dq^2 \, d\cos\theta_l \, d\cos\theta_K \, d\tilde{\phi}} =$$
$$\frac{9}{16\pi}[\frac{3}{4}(1 - F_{\mathrm{L}})\sin^2\theta_K + F_{\mathrm{L}}\cos^2\theta_K +$$
$$\left(\frac{1}{4}(1 - F_{\mathrm{L}})\sin^2\theta_K - F_{\mathrm{L}}\cos^2\theta_K\right)\cos2\theta_l +$$
$$\frac{1}{2}(1 - F_{\mathrm{L}})A_{\mathrm{T}}^{(2)}\sin^2\theta_K\sin^2\theta_l\cos2\tilde{\phi} +$$
$$(1 - F_{\mathrm{L}})A_{\mathrm{T}}^{\mathrm{Re}}\sin^2\theta_K\cos\theta_l +$$
$$\frac{1}{2}(1 - F_{\mathrm{L}})A_{\mathrm{T}}^{\mathrm{Im}}\sin^2\theta_K\sin^2\theta_l\sin2\tilde{\phi}] \, , \quad (1.23)$$

where F_{L} is the longitudinal asymmetry, $A_{\mathrm{T}}^{\mathrm{Re}}$ is proportional to the forward-backward asymmetry, while $A_{\mathrm{T}}^{\mathrm{Im}}$ and $A_{\mathrm{T}}^{(2)}$ are related to the Wilson coefficients C_7 and C_7' by

$$A_{\mathrm{T}}^{(2)}(q^2 \to 0) = \frac{2\,\mathcal{R}e(C_7 C_7'^*)}{|C_7|^2 + |C_7'|^2} \, , \quad (1.24)$$

$$A_{\mathrm{T}}^{\mathrm{Im}}(q^2 \to 0) = \frac{2\,\mathcal{I}m(C_7 C_7'^*)}{|C_7|^2 + |C_7'|^2} \, . \quad (1.25)$$

The four observables have been extracted from a fit of 124 events obtained in Run 1 data in the q^2 range $[0.002, 1.120]\,\mathrm{GeV}^2/c^4$. Despite the challenging poor resolution which affects the photon, this measurement resulted in the best individual constraint on C_7 and C_7', indicated in yellow (for $A_{\mathrm{T}}^{\mathrm{Im}}$) and purple (for $A_{\mathrm{T}}^{(2)}$, also denoted as P_1) in Fig. 1.8.
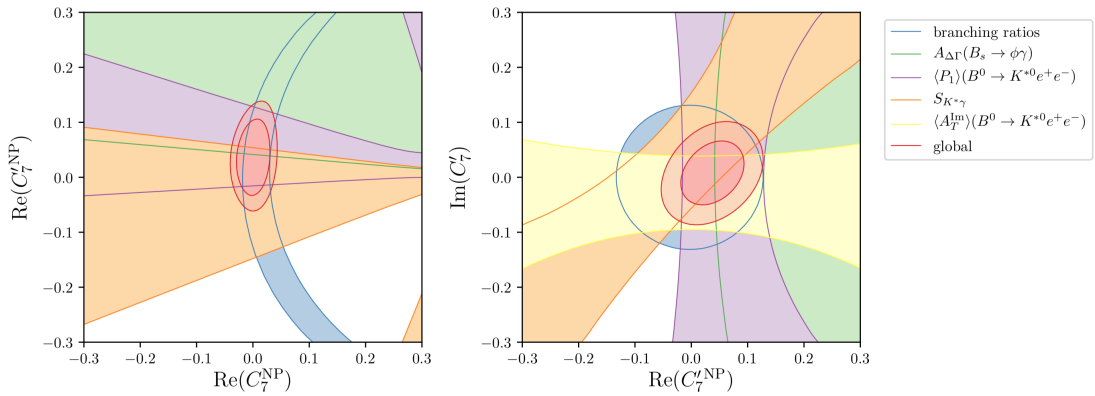
Figure 1.8 – Constraints on the Wilson coefficients C_7 and C_7' from various measurements (for which 1σ contours are shown), and from a global fit (where constraints at 1σ and 2σ level are drawn). C_7^{NP} and $C_7'^{\mathrm{NP}}$ refer to the NP contributions (as opposed to SM) to the C_7 and C_7' coefficients [34].

In addition to these measurements, other techniques have been proposed:

- Two ways of exploiting the $B^0 \to K_S^0 \pi^+ \pi^- \gamma$ decays (depending on the available number of events) have been proposed in Ref. [44]. The main idea is to exploit the CP asymmetry in one of the possible decay channels: $B^0 \to \rho^0 K_S^0 \gamma$, where $\rho^0 K_S^0$ is a CP eigenstate, which means that $\mathcal{S}_{\rho^0 K_S^0 \gamma}$ relates to the Wilson coefficients as in Eq. 1.20. The difficulty here is to isolate $B^0 \to \rho^0 K_S^0 \gamma$ from the plethora of possible decay chains in $B^0 \to K_S^0 \pi^+ \pi^- \gamma$ decays, so two ideas have been proposed to enable this measurement. The first option, better suited in case of low statistics, is to measure the time-dependent CP asymmetry of the entire system, $\mathcal{S}_{K_S^0 \pi^- \pi^+}$, by exploiting the time-dependent decay rates of $B^0 \to K_S^0 \pi^+ \pi^- \gamma$ decays, which can be written as in Eqs. 1.17 and 1.18. This asymmetry is expected to be proportional to $\mathcal{S}_{\rho^0 K_S^0 \gamma}$ with a proportionality coefficient $\mathcal{D} = \mathcal{S}_{K_S^0 \rho^0 g}/\mathcal{S}_{K_S^0 \pi^- \pi^+ \gamma}$, called *dilution factor*. This ratio can then be written as a function of the amplitudes of each of the decay channels involved in the $B^0 \to K_S^0 \pi^+ \pi^- \gamma$ decays, which allows the evaluation of this dilution factor separately using the amplitude parameters obtained from an amplitude analysis of $B^+ \to K^+ \pi^- \pi^+ \gamma$ decays, assuming isospin conservation.

  The other method, suitable for a larger number of events, consists in increasing the sensitivity of the measurement by performing it in various regions of the Dalitz plane $(m^2_{\pi^+ K_S^0}, m^2_{\pi^- K_S^0})$. A suggested partition includes two regions I and $\bar{I}$ characterized by $m^2_{\pi^+ K_S^0} < m^2_{\pi^- K_S^0}$ and $m^2_{\pi^+ K_S^0} < m^2_{\pi^- K_S^0}$ respectively. The corresponding CP asymmetries are $\mathcal{S}^I_{K_S^0 \pi^- \pi^+ \gamma}$ and $\mathcal{S}^{\bar{I}}_{K_S^0 \pi^- \pi^+ \gamma}$. Their sum gives the usual asymmetry $\mathcal{S}_{K_S^0 \pi^- \pi^+ \gamma}$, which yields very similar constraints as $\mathcal{S}_{\pi^0 K_S^0}$ in the $(\mathcal{R}e(C_7'^{\mathrm{NP}}), \mathcal{I}m(C_7'))$ plane (corresponding to the diagonal orange band from bottom left to up right in Fig. 1.8). A new observable, defined as $\mathcal{S}^-_{K_S^0 \pi^- \pi^+ \gamma} = \mathcal{S}^I_{K_S^0 \pi^- \pi^+ \gamma} - \mathcal{S}^{\bar{I}}_{K_S^0 \pi^- \pi^+ \gamma}$, has been shown to give complementary sensitivity to the Wilson coefficients, with a 1σ contour appearing as a diagonal band from up left to bottom right in the $(\mathcal{R}e(C_7'^{\mathrm{NP}}), \mathcal{I}m(C_7'))$ plane.

- The photon polarisation in $b \to s\gamma$ transition can also be accessed through the angular distributions in baryonic decays, as described in Ref. [45]. In the case of $\Lambda_b^0 \to \Lambda^0 \gamma$ decays, where Λ^0 subsequently decays to a proton p and a π^-, a unit vector $\hat{n}$ normal to the Λ_b^0 production plane is defined as

$$\hat{n} = \frac{\vec{p}_p \times \vec{p}_{\Lambda_b}}{|\vec{p}_p \times \vec{p}_{\Lambda_b}|}, \tag{1.26}$$

where $\vec{p}_p$ is the anticlockwise proton beam direction, and $\vec{p}_{\Lambda_b}$ is the Λ_b^0 momentum. Then, two angles are introduced: θ_Λ is the angle between the Λ^0 momentum and $\hat{n}$ in the Λ_b^0 rest frame, while θ_p is defined as the angle between the Λ flight direction and the momentum of the proton in the Λ rest frame. The differential decay rate

expressed as a function of these angles is

$$\frac{d\Gamma}{d\cos\theta_\Lambda d\cos\theta_p} \propto 1 - \alpha_\Lambda P_{\Lambda_b}\cos\theta_p\cos\theta_\Lambda - \alpha_\gamma^{\Lambda_b^0 \rightarrow \Lambda^0\gamma}(\alpha_\Lambda\cos\theta_p - P_{\Lambda_b}\cos\theta_\Lambda)\,, \quad (1.27)$$

where P_{Λ_b} is the initial Λ_b^0 polarisation, α_Λ is the Λ^0 weak decay parameter and $\alpha_\gamma^{\Lambda_b^0 \rightarrow \Lambda^0\gamma}$ is the photon polarisation in $\Lambda_b^0 \rightarrow \Lambda^0\gamma$ decays. For a generic $H_b \rightarrow H\gamma$ decay where H_b is a hadron containing a b quark and H is a hadronic system, the photon polarisation $\alpha_\gamma^{H_b \rightarrow H\gamma}$ is defined as

$$\alpha_\gamma^{H_b \rightarrow H\gamma} = \frac{\Gamma(H_b \rightarrow H\gamma_\mathrm{L}) - \Gamma(H_b \rightarrow H\gamma_\mathrm{R})}{\Gamma(H_b \rightarrow H\gamma_\mathrm{L}) + \Gamma(H_b \rightarrow H\gamma_\mathrm{R})}\,. \quad (1.28)$$

In the specific case of $\Lambda_b^0 \rightarrow \Lambda^0\gamma$ decays where Λ^0 is a well defined resonance, $\alpha_\gamma^{\Lambda_b^0 \rightarrow \Lambda^0\gamma}$ depends on the Wilson coefficients as

$$\alpha_\gamma^{\Lambda_b^0 \rightarrow \Lambda^0\gamma} = \frac{|C_7|^2 - |C_7'|^2}{|C_7|^2 + |C_7'|^2}\,. \quad (1.29)$$

Here, the knowledge of α_Λ, measured independently [46], would allow the extraction of P_{Λ_b} and $\alpha_\gamma^{\Lambda_b^0 \rightarrow \Lambda^0\gamma}$ through an angular analysis.

Another baryonic decay that can be exploited is $\Xi_b^- \rightarrow \Xi^-\gamma$, where $\Xi^- \rightarrow \Lambda^0\pi^-$ and $\Lambda^0 \rightarrow p\pi^-$. Due to the cascade of decays, the angular distributions for this decay are more complicated (details can be found in Ref. [45]), but it has been demonstrated that an angular analysis is sensitive to the initial Ξ_b^- polarisation P_{Ξ_b} and to the parameter $\alpha_\gamma^{\Xi_b^- \rightarrow \Xi^-\gamma}$, which also has the dependency in C_7 and C_7' indicated in Eq. 1.28 for a single Ξ^- resonance.

In the present work, a new method to measure the photon polarisation using an amplitude analysis of $B^+ \rightarrow K^+\pi^-\pi^+\gamma$ decays is presented and will be developed in the next section.

1.3 The photon polarisation in $B \rightarrow K\pi\pi\gamma$ decays

$B \rightarrow K\pi\pi\gamma$ decays give a handle on photon chirality thanks to the presence of three hadrons in the final state. This makes it possible to build a parity-odd triple product that changes sign when the photon chirality is flipped. Furthermore, and very importantly, the existence of interferences in the hadronic system allows this triple-product not to cancel in the differential decay rate.

Four types of $B \rightarrow K\pi\pi\gamma$ decays are discussed here:

- $B^+ \rightarrow K^+\pi^-\pi^+\gamma$

- $B^0 \to K^0 \pi^- \pi^+ \gamma$ (isospin partner of $B^+ \to K^+ \pi^- \pi^+ \gamma$)

- $B^0 \to K^+ \pi^- \pi^0 \gamma$

- $B^+ \to K^0 \pi^+ \pi^0 \gamma$ (isospin partner of $B^0 \to K^+ \pi^- \pi^0 \gamma$)

All these decays are assumed to proceed through two consecutive steps. First, the B meson decays weakly into a heavy kaonic resonance $K^i_{\rm res}$, followed by the strong decay $K^i_{\rm res} \to K \pi \pi$. The phenomenology of $B \to K \pi \pi \gamma$ decays is very complicated as many heavy kaonic resonances $K^i_{\rm res}$ are accessible and characterized by different values of spin J_i and parity P_i, which can interfere with each other. Some of the known heavy resonances include $K_1(1270)$ with spin-parity $J^P = 1^+$, $K_1^*(1410)$ with $J^P = 1^-$, and $K_2(1430)$ with $J^P = 2^+$.

All integer values of J are allowed except $J = 0$, which is forbidden because of the conservation of angular momentum. In the rest frame of the B with the z axis opposite to the photon direction, the two children particles have opposite momenta, $\vec{p}_\gamma = -\vec{p}_{K_{\rm res}}$. Therefore, the total angular momentum of the two particles $\vec{L} = \vec{r}_\gamma \times \vec{p}_\gamma + \vec{r}_{K_{\rm res}} \times \vec{p}_{K_{\rm res}}$ (where $\vec{r}_\gamma$ and $\vec{r}_{K_{\rm res}}$ are the position vectors) can be written $\vec{L} = (\vec{r}_\gamma - \vec{r}_{K_{\rm res}}) \times \vec{p}_\gamma$, which implies that $\vec{L}$ is orthogonal to $\vec{p}_\gamma$ and the projection of $\vec{L}$ on the z axis is zero. Using the fact that the B meson has spin 0, the conservation of angular momentum projected on the z axis then results in opposite spin projections for the photon and the kaonic resonance. As the spin projection of the photon can only take the values $+1$ or -1, that of the kaonic resonance is constrained to be -1 or $+1$, giving only two possibilities for the spin projections along the z axis, as shown in Fig. 1.9, which is possible only if J takes strictly positive integer values.

Furthermore, a wide variety of decay channels are observed in $K^i_{\rm res} \to K \pi \pi$ decays, offering many more possibilities for interference, which can be classified in three categories:

- Interferences between amplitudes with different intermediate states, for example $K_1(1270)^+ \to K^{*0} \pi^+ \to K^+ \pi^- \pi^+$ and $K_1(1270)^+ \to K^+ \rho^0 \to K^+ \pi^- \pi^+$.

- Interferences between different possible waves in the decay, for example the S and D waves in the decay $K_1(1270)^+ \to K^{*0} \pi^+$ where two values of the total orbital angular momentum, $L = 0$ and $L = 2$, are allowed.

- Interferences between $K^* \pi$ intermediate states characterized by different charges, for example $K_1(1270)^0 \to K^{*+} \pi^-$ and $K_1(1270)^0 \to K^{*0} \pi^0$. This kind of interference is only possible in $B^0 \to K^+ \pi^- \pi^0 \gamma$ and $B^+ \to K^0 \pi^+ \pi^0 \gamma$ decays, resulting in a richer interference set with respect to $B^+ \to K^+ \pi^- \pi^+ \gamma$ and $B^0 \to K^0 \pi^- \pi^+ \gamma$ decays.

$B \to K \pi \pi \gamma$ decays can be described in terms of five independent variables. The four-vectors associated with each of the four final state particles make up for 16 variables. All
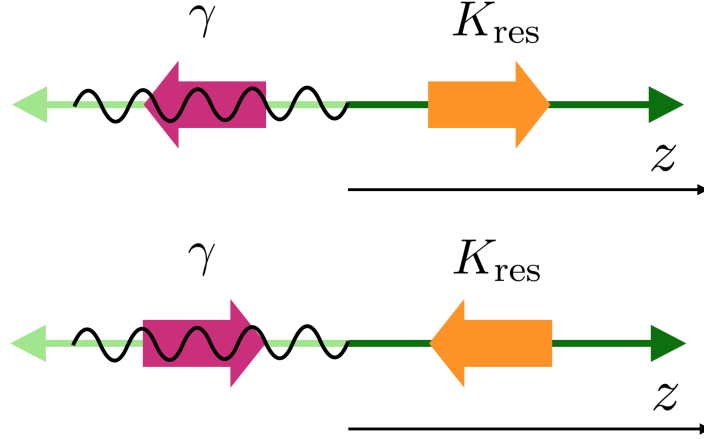
Figure 1.9 – Sketch of the projection of a $B \to K_{\mathrm{res}}\gamma$ decay on the z axis defined as opposite to the photon momentum in the rest frame of the B meson. The momenta of the photon and the kaonic resonance are shown in green, the spin of the photon in pink, and the z-component of the spin of the K_{res} in orange.

these particles are stable, giving rise to four mass constraints. As they all come from a common B meson, the energy-momentum conservation adds four more constraints. Finally, because the B meson has spin 0, the system is invariant under any rotation of space, which removes three variables, leaving only five independent kinematic variables: these can be chosen to be two angles ($\cos\theta$ and χ) describing the direction of the photon in the rest frame of the kaonic resonance K_{res} and three squared invariant masses (s_{123}, s_{12}, s_{23}). Here, following the conventions in Ref. [47], the indices 1, 2 and 3 refer respectively to the final-state π^+, π^- and K^+ for $B^+ \to K^+\pi^-\pi^+\gamma$, π^+, π^- and K^0 for $B^0 \to K^0\pi^-\pi^+\gamma$, π^-, π^0 and K^+ for $B^0 \to K^+\pi^-\pi^0\gamma$, and π^+, π^0 and K^0 for $B^+ \to K^0\pi^+\pi^0\gamma$ decays.

As illustrated in Fig. 1.10 for $B^+ \to K^+\pi^-\pi^+\gamma$ decays, in the rest frame of the kaonic resonance K_{res}, the normal to the hadronic decay plane is denoted by $\hat{n} = (\vec{p}_1 \times \vec{p}_2)/|\vec{p}_1 \times \vec{p}_2|$. The polar angle θ is the angle between $\hat{n}$ and the opposite of the photon momentum, so that $\cos\theta = -\hat{n} \cdot \vec{p}_\gamma/|\vec{p}_\gamma|$.[1] The angle χ is then defined from

$$\cos\chi = -\frac{(\hat{n} \times \vec{p}_1) \cdot (\hat{n} \times \vec{p}_\gamma)}{|\hat{n} \times \vec{p}_1| \, |\hat{n} \times \vec{p}_\gamma|}, \tag{1.30}$$

$$\sin\chi = -\frac{(\hat{n} \times \vec{p}_1) \times (\hat{n} \times \vec{p}_\gamma)}{|\hat{n} \times \vec{p}_1| \, |\hat{n} \times \vec{p}_\gamma|} \cdot \hat{n}. \tag{1.31}$$

---

[1]This definition of the polar angle corresponds to the one used in Ref. [47] and does not match the one in Ref. [37].

23
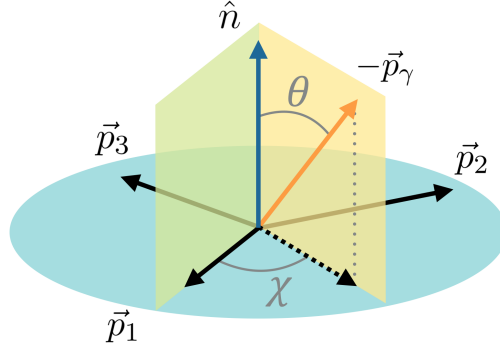
Figure 1.10 – Definitions of the angular variables used to describe the $K\pi\pi\gamma$ system in the $K\pi\pi$ center of mass. The indices 1, 2 and 3 refer respectively to the final-state hadrons π^+, π^- and K^+ for $B^+ \to K^+\pi^-\pi^+\gamma$, π^+, π^- and K^0 for $B^0 \to K^0\pi^-\pi^+\gamma$, π^-, π^0 and K^+ for $B^0 \to K^+\pi^-\pi^0\gamma$, and π^+, π^0 and K^0 for $B^+ \to K^0\pi^+\pi^0\gamma$ decays.

The differential decay rate for $\bar{B} \to \bar{K}\pi\pi\gamma$ decays (where by convention $\bar{B}$ stands for a meson of the type $b\bar{q}$ and $\bar{K}$ stands for a $s\bar{q}$ meson) that proceed through a set of resonances $\bar{K}^i_{\text{res}}$ can be written as [47]

$$\frac{\mathrm{d}\Gamma(\bar{B} \to \bar{K}\pi\pi\gamma)}{\mathrm{d}s_{123}} = \left|\sum_i c^i_{\text{R}}\mathcal{T}^i(s_{123})A^i_{\text{R}}\right|^2 + \left|\sum_i c^i_{\text{L}}\mathcal{T}^i(s_{123})A^i_{\text{L}}\right|^2, \tag{1.32}$$

where s_{123} is the invariant mass squared of the $K\pi\pi$ system, c^i_{R} and c^i_{L} are the right- and left-handed weak radiative decay amplitudes, $\mathcal{T}^i(s_{123})$ is the propagator associated with resonance $\bar{K}^i_{\text{res}}$, and A^i_{R} and A^i_{L} are the strong decay amplitudes for $\bar{K}^i_{\text{res, R/L}} \to \bar{K}\pi\pi$. The right- and left-handed amplitudes do not interfere since the photon polarisation is an observable quantity.

In the case of a single resonance $\bar{K}^i_{\text{res}}$, the decay rate simplifies as

$$\frac{\mathrm{d}\Gamma(\bar{B} \to \bar{K}^i_{\text{res}}(\to \bar{K}\pi\pi)\gamma)}{\mathrm{d}s_{123}} = |c^i_{\text{R}}\mathcal{T}^i(s_{123})A^i_{\text{R}}|^2 + |c^i_{\text{L}}\mathcal{T}^i(s_{123})A^i_{\text{L}}|^2, \tag{1.33}$$

For this resonance, a photon polarisation parameter λ^i_γ is defined in terms of the weak radiative decay amplitudes,

$$\lambda^i_\gamma \equiv \frac{|c^i_{\text{R}}|^2 - |c^i_{\text{L}}|^2}{|c^i_{\text{R}}|^2 + |c^i_{\text{L}}|^2}. \tag{1.34}$$

The generalized expression of the polarized weak decay amplitude associated with a

resonance $\bar{K}_{\mathrm{res}}^i$ in decays of a B^- or $\bar{B}^0$ meson can be written as [34]

$$\begin{pmatrix} c_{\mathrm{R}}^i \\ c_{\mathrm{L}}^i \end{pmatrix} = -\frac{4G_{\mathrm{F}}}{\sqrt{2}} V_{tb}V_{ts}^* \frac{e}{8\pi^2} \begin{pmatrix} \left(C_7'\, g^i(0) + h_{\mathrm{R}}^i\right) S_{\mathrm{R}}^i \\ \left(C_7\, g^i(0) + h_{\mathrm{L}}^i\right) S_{\mathrm{L}}^i \end{pmatrix}, \tag{1.35}$$

where G_{F} is the Fermi constant, V_{tb} and V_{ts} are CKM matrix elements, $g^i(0)$ is a common $\bar{B} \to \bar{K}_{\mathrm{res}}^i$ form-factor at $q^2 = 0$, C_7 and C_7' are the effective radiative Wilson coefficients (which include effective linear contributions from the other coefficients C_{1-6} in order to make them regularisation- and renormalisation-scheme independent as discussed in Sec. 1.2.1), and the quantities $h_{\mathrm{R/L}}^i$ encode remaining contributions from the Q_{1-6} and Q_8 hadronic operators (see Ref. [48] for more details). The factors S_{R}^i and S_{L}^i are called spin-factors and encode the angular distributions of the decay. Their expressions depend on the spin J_i and parity P_i of the kaonic resonance involved, and they can be related to each other by [47]

$$S_{\mathrm{L}}^i = P_i(-1)^{J_i-1}\, S_{\mathrm{R}}^i. \tag{1.36}$$

Assuming that the $h_{\mathrm{R/L}}^i$ terms are small enough to be neglected in the expressions of c_{R}^i and c_{L}^i, the photon polarisation parameter for a B^- or $\bar{B}^0$ meson reduces to

$$\lambda_\gamma^i = \frac{|C_7'|^2 - |C_7|^2}{|C_7'|^2 + |C_7|^2} \equiv -\lambda_\gamma, \tag{1.37}$$

i.e., the photon polarisation in the weak decay $\bar{B} \to \bar{K}_{\mathrm{res}}^i \gamma$ is the same for all kaonic resonances $\bar{K}_{\mathrm{res}}^i$ and it can be expressed only as a function of Wilson coefficients.[2] For decays of a B^+ or B^0 meson, the right- and left-handed weak radiative decay amplitudes $\bar{c}_{\mathrm{R}}^i$ and $\bar{c}_{\mathrm{L}}^i$ are given by

$$\begin{pmatrix} \bar{c}_{\mathrm{R}}^i \\ \bar{c}_{\mathrm{L}}^i \end{pmatrix} = -\frac{4G_{\mathrm{F}}}{\sqrt{2}} V_{tb}^* V_{ts} \frac{e}{8\pi^2} \begin{pmatrix} \left(C_7^*\, g^i(0) + h_{\mathrm{L}}^i\right) S_{\mathrm{R}}^i \\ \left(C_7'^*\, g^i(0) + h_{\mathrm{R}}^i\right) S_{\mathrm{L}}^i \end{pmatrix}. \tag{1.38}$$

Note that h_{R}^i and h_{L}^i are in general complex but enter in the above expressions without a conjugate because their phases are CP-even. Assuming once again that these terms can be neglected, the photon polarisation parameter for a B meson can be expressed as

$$\bar{\lambda}_\gamma^i \equiv \frac{|\bar{c}_{\mathrm{R}}^i|^2 - |\bar{c}_{\mathrm{L}}^i|^2}{|\bar{c}_{\mathrm{R}}^i|^2 + |\bar{c}_{\mathrm{L}}^i|^2} = \frac{|C_7|^2 - |C_7'|^2}{|C_7|^2 + |C_7'|^2} = \lambda_\gamma. \tag{1.39}$$

In the SM, the value of the photon polarisation parameter is expected to be $+1$ (up to corrections of the order of m_s^2/m_b^2) for decays of a B^+ or B^0 meson while it is expected

---

[2]It is sufficient to assume that the ratios $h_{\mathrm{R/L}}^i/g^i(0)$ are process independent to enable the definition of a photon polarisation parameter that does not depend on the kaonic resonance K_{res}^i. It is however far from clear that the differences in $g^i(0)$ and $h_{\mathrm{R/L}}^i$ for different kaonic resonances should be small. These corrections would need to be taken into account when translating the measurement of the photon polarisation to constraints on the Wilson coefficients.

to be -1 for decays of a B^- or $\bar{B}^0$ meson.

The differential decay rate for $\bar{B} \to \bar{K}\pi\pi\gamma$ decays can then be written explicitly as a function of λ_γ:

$$
\begin{aligned}
\frac{\mathrm{d}\Gamma(B \to K\pi\pi\gamma)}{\mathrm{d}s_{123}} \\
= \left| -\frac{4G_{\mathrm{F}}}{\sqrt{2}} V_{ts} V_{tb}^* \frac{e}{8\pi^2} \right|^2 \times \left(\frac{(1+\lambda_\gamma)}{2}|\mathcal{M}_{\mathrm{R}}|^2 + \frac{(1-\lambda_\gamma)}{2}|\mathcal{M}_{\mathrm{L}}|^2 \right) ,
\end{aligned}
\tag{1.40}
$$

where

$$
\mathcal{M}_{\mathrm{R/L}} = \sum_i g^i(0) S_{\mathrm{R/L}}^i \mathcal{T}^i(s_{123}) A_{\mathrm{R/L}}^i .
\tag{1.41}
$$

Here, it is useful to note that for $B \to K\pi\pi\gamma$ the photon polarisation parameter λ_γ is different from the usual definition of the photon polarisation in $B \to K\pi\pi\gamma$ decays $\alpha_\gamma^{B \to K\pi\pi\gamma}$ defined as[3]

$$
\alpha_\gamma^{B \to K\pi\pi\gamma} = \frac{\Gamma(B \to K\pi\pi\gamma_{\mathrm{R}}) - \Gamma(B \to K\pi\pi\gamma_{\mathrm{L}})}{\Gamma(B \to K\pi\pi\gamma_{\mathrm{R}}) + \Gamma(B \to K\pi\pi\gamma_{\mathrm{L}})} .
\tag{1.42}
$$

In Ref. [47], it is shown that the equality $\alpha_\gamma^{B \to K\pi\pi\gamma} = \lambda_\gamma$ is obtained only in the case of a single heavy kaonic resonance. As many kaonic resonances have been found to populate the $K\pi\pi$ system, these two parameters are different and λ_γ is the parameter that retains the most simple dependence on the Wilson coefficients.

1.4   Previous studies of $B^+ \to K^+\pi^-\pi^+\gamma$ decays

In LHCb, the easiest of the $B \to K\pi\pi\gamma$ decay modes from an experimental point of view is $B^+ \to K^+\pi^-\pi^+\gamma$, whose three charged tracks allow for a better reconstruction efficiency and a better resolution.

This decay mode has been previously studied by the Belle collaboration [51] as a normalization mode for their studies of $B^0 \to \rho^0 K_{\mathrm{S}}^0 \gamma$ decays and by the BaBar collaboration [52]. However, with only 1500 and 2500 signal candidates respectively, the limited size of the data sets prevented them to exploit all the degrees of freedom of the $K^+\pi^-\pi^+$ system. Belle performed a 2D fit on the invariant masses squared $m_{K^+\pi^-}^2$ and $m_{\pi^+\pi^-}^2$ while BaBar used only $m_{\pi^+\pi^-}^2$ to perform a fit.

---

[3]Note that the definition chosen here is the opposite of the definition given in Eq. 1.28. This is caused by different conventions adopted in the study of baryonic decays in Ref. [45] with respect to the studies of $B \to K\pi\pi\gamma$ decays in Refs. [47, 49, 50]. In the former, the photon polarisation is close to $+1$ for decays involving a b quark, while in the later the photon polarisation parameter is close to $+1$ when a $\bar{b}$ quark is involved. For the present study, we kept the latter.

With $14\,000$ $B^+ \to K^+\pi^-\pi^+\gamma$ signal decays available from the 2011 and 2012 data-taking years, LHCb could study these decays in more depth by measuring the up-down asymmetry and by performing a three dimensional fit of $m^2_{K^+\pi^-}$, $m^2_{\pi^+\pi^-}$ and $m^2_{\pi^+\pi^-}$ distributions [53], paving the way for the development of a full amplitude analysis using all five degrees of freedom of these decays.

1.4.1 Measurement of the up-down asymmetry

Due to the complexity of the $K\pi\pi$ system which was very poorly known at the time, the first study of photon polarisation in $B^+ \to K^+\pi^-\pi^+\gamma$ relied on a simplified approach: the measurement of the *up-down asymmetry* [37].

The main idea behind this simplification is that the $B \to K\pi\pi\gamma$ differential branching fraction has the following dependence on $\cos\theta$ [47]:

$$
\begin{aligned}
&\frac{\mathrm{d}\Gamma(B^+ \to K^+_{\mathrm{res}}\gamma \to K^+\pi^-\pi^+\gamma)}{\mathrm{d}s_{123}\,\mathrm{d}s_{12}\,\mathrm{d}s_{23}\,\mathrm{d}\chi\,\mathrm{d}\cos\theta} \\
&\qquad = \sum_{i=0,2,4} a_i(s_{123}, s_{12}, s_{23}, \chi)\cos^i\theta + \lambda_\gamma \sum_{j=1,3} a_j(s_{123}, s_{12}, s_{23}, \chi)\cos^j\theta.
\end{aligned}
\tag{1.43}
$$

After integration of Eq. 1.43 over the squared invariant masses and χ, the *up-down* asymmetry ($\mathcal{A}_{\mathrm{ud}}$) is defined as [47, 49]

$$
\mathcal{A}_{\mathrm{ud}} \equiv \frac{\int_0^1 \mathrm{d}\cos\theta \frac{\mathrm{d}\Gamma}{\mathrm{d}\cos\theta} - \int_{-1}^0 \mathrm{d}\cos\theta \frac{\mathrm{d}\Gamma}{\mathrm{d}\cos\theta}}{\int_{-1}^1 \mathrm{d}\cos\theta \frac{\mathrm{d}\Gamma}{\mathrm{d}\cos\theta}},
\tag{1.44}
$$

where the terms in even powers of $\cos\theta$ disappear, and the resulting asymmetry is directly proportional to λ_γ with a proportionality coefficient that depends on the resonance content of the $K\pi\pi$ system. Hence, if this up-down asymmetry is measured to be different from 0, the photon polarisation parameter must also be different from 0.

The measurement of the up-down asymmetry was conducted on a sample of $14\,000$ $B^+ \to K^+\pi^-\pi^+\gamma$ decays collected by the LHCb detector in 2011 and 2012. The background was removed using the sPlot technique [54] and the $K\pi\pi$ invariant mass distribution was obtained (see Fig. 1.11), showing a mixture of several $K\pi\pi$ resonances. As the value of the up-down asymmetry is expected to depend on the content of the system, its value has been measured separately in four different $K\pi\pi$ mass intervals. The first one, $[1.1, 1.3]\,\mathrm{GeV}/c^2$, is expected to be dominated by the $K_1(1270)^+$ resonance while the $[1.4, 1.6]\,\mathrm{GeV}/c^2$ interval has been chosen in order to receive its main contributions from

the $K_1(1400)^+$, $K_1^*(1410)^+$ and $K_2^*(1430)^+$ resonances. In the interval $[1.3, 1.4]\,\mathrm{GeV}/c^2$, all these resonances overlap, while the highest interval $[1.6, 1.9]\,\mathrm{GeV}/c^2$ receives also contributions of higher spin resonances.
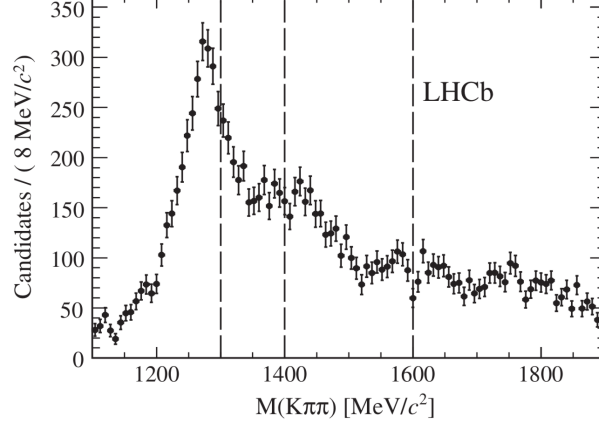
Figure 1.11 – Background-subtracted $K\pi\pi$ mass distribution of the $B^+ \to K^+\pi^-\pi^+\gamma$ signal [53]. The boundaries of the four intervals of interest are shown by dashed lines.

In the study, two different definitions of the angle θ have been considered: the default one is computed with $\hat{n}$ defined as the normalized $\vec{p}_{\pi,\mathrm{slow}} \times \vec{p}_{\pi,\mathrm{fast}}$ vector (where $\vec{p}_{\pi,\mathrm{slow}}$ and $\vec{p}_{\pi,\mathrm{fast}}$ are respectively the momenta of the lower and higher momentum pions), while the second one uses $\hat{n}$ defined as the normalized $\vec{p}_{\pi^-} \times \vec{p}_{\pi^+}$ vector[4]. Then, as the up-down asymmetry is expected to be opposite for B^+ and B^- candidates, a new angular variable is defined as $\cos\hat{\theta} = \mathrm{charge}(B)\cos\theta$.

In each of the mass intervals, the background-subtracted $\cos\hat{\theta}$ distribution is obtained, corrected for the selection acceptance, and is fitted with a normalized fourth-order Legendre polynomial function:

$$f(\cos\hat{\theta}; c_0 = 0.5, c_1, c_2, c_3, c_4) = \sum_{i=0}^{4} c_i L_i(\cos\hat{\theta})\,, \tag{1.45}$$

where $L_i(x)$ is the Legendre polynomial function of order i, and c_i is the corresponding coefficient. The up-down asymmetry is obtained as

$$\mathcal{A}_{\mathrm{ud}} = c_1 - \frac{c_3}{4}\,. \tag{1.46}$$

The fitted distributions of the default $\cos\hat{\theta}$ variable in the four $K\pi\pi$ mass intervals are shown in Fig. 1.12. Superimposed is a dashed red line showing the function $f(\cos\hat{\theta}; c_0 = 0.5, c_1 = 0, c_2, c_3 = 0, c_4)$ that would be obtained if λ_γ were 0. The resulting value of the up-down asymmetry in each bin is represented in Fig. 1.13 for the two angle definitions. These results allowed the rejection of the hypothesis $\lambda_\gamma = 0$ with a significance of 5.2σ

---

[4]Note that this definition is opposite to the one used in the present work.

using the default definition of $\cos\hat\theta$, and with a significance of 4.6σ using the alternative definition.
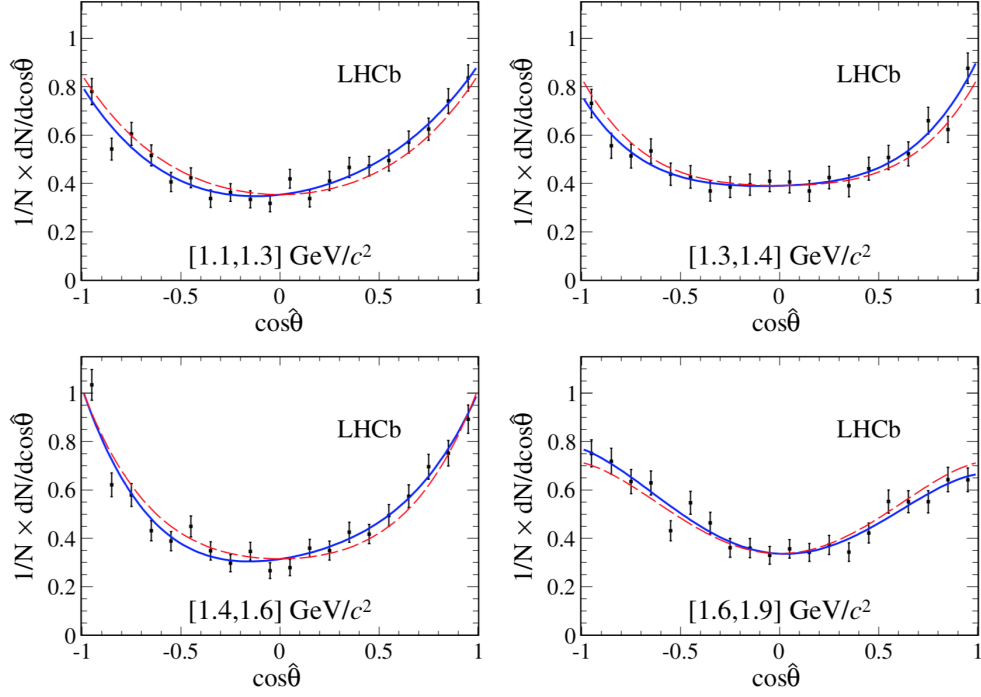
Figure 1.12 – Distributions of $\cos\hat\theta$ (using the default definition) for $B^+ \to K^+\pi^-\pi^+\gamma$ signal in four intervals of $K^+\pi^-\pi^+$ mass [53]. The solid blue (dashed red) curves show the results of the fits allowing all (only even) Legendre components up to the fourth order.

Unfortunately, this result could not be translated into a measurement of λ_γ because the knowledge of the $K\pi\pi$ system was not sufficient to determine the value of the proportionality coefficient between λ_γ and $\mathcal{A}_{\mathrm{ud}}$.

1.4.2 Knowledge of the $K\pi\pi$ system

In order to gain knowledge on the resonant structure of the $K\pi\pi$ mass system, a Dalitz analysis has been performed on the signal candidates obtained for the measurement of $\mathcal{A}_{\mathrm{ud}}$ [53]. The principle of this analysis is to use information from three of the five degrees of freedom of the system, namely the invariant mass squared $m^2_{K^+\pi^-\pi^+}$, $m^2_{K^+\pi^-}$ and $m^2_{\pi^+\pi^-}$, and to perform an unbinned maximum likelihood fit to separate the resonances and interferences that populate the $K^+\pi^-\pi^+$ mass range $[1.1, 1.9]\,\mathrm{GeV}/c^2$. For this fit, an integration is done on the angular variables of the photon (θ and ϕ), which simplifies the description of the various decay chains and allows for a first exploration of the system.
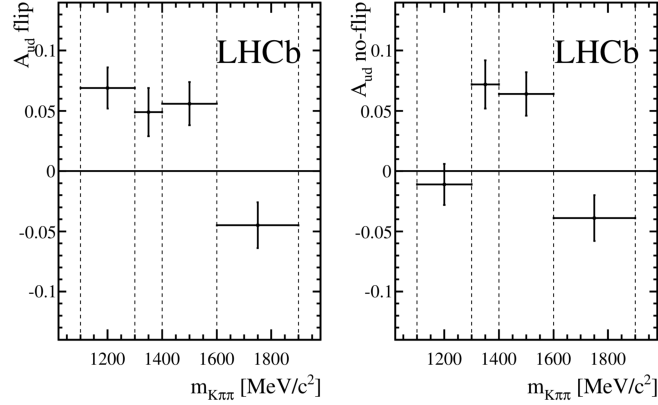
Figure 1.13 – Values of the up-down asymmetry $\mathcal{A}_{\text{ud}}$ obtained in four $K^+\pi^-\pi^+$ mass intervals, using the default definition ("flip" scenario, on the left) and the alternative definition ("no-flip", on the right) of $\cos\hat\theta$ [53].

The probability distribution function used to describe this system is defined as

$$\text{PDF}(\vec{m}|\Omega) = \frac{\xi(\vec{m})\mathcal{P}_{\text{S}}(\vec{m}|\Omega)\Phi_3(\vec{m})}{\int \xi(\vec{m})\mathcal{P}_{\text{S}}(\vec{m}|\Omega)\Phi_3(\vec{m})\text{d}\vec{m}} \,, \tag{1.47}$$

where $\vec{m}$ contains the three invariant masses of the hadronic system, ξ is the efficiency, $\Phi_3(\vec{m})$ is the three-body phase-space element, and Ω is the set of fit parameters $\{f_k, f_{\text{nr}}\}$ explained below. The signal function $\mathcal{P}_{\text{S}}(\vec{m}|\Omega)$ is computed as a sum of decay amplitudes $\mathcal{D}_k^J$, each of them corresponding to the $B^+ \to K_{\text{res}}^+\gamma \to K^+\pi^-\pi^+\gamma$ decay mode k with an intermediate kaonic resonance K_{res} of spin J. After integration on $\cos\theta$ and ϕ, the amplitudes with different values of J do not interfere, which gives the following expression for the signal function:

$$\mathcal{P}_{\text{S}}(\vec{m}|\Omega) = \sum_J \left| \sum_k f_k \mathcal{D}_k^J \right|^2 + |f_{\text{nr}}\mathcal{D}_{\text{nr}}| \,. \tag{1.48}$$

The complex coefficient f_k accounts for the magnitude and phase with respect to the reference amplitude of the category (defined by the spin J), for which f_{ref} is set to 1. The description of the amplitude for each decay mode, $\mathcal{D}_k^J$, is detailed in Ref. [53]. The amplitude $\mathcal{D}_{\text{nr}}$ accounts for a uniform non-resonant component that does not interfere with the other amplitudes. The three-dimensional efficiency function $\xi(\vec{m})$ is obtained by performing a 3D fit on simulated signal events, using a product of three polynomials (one for each of the dimensions) of order 3.

The result of the fit is shown in Fig. 1.14 with all the components superimposed. As they do not take into account different normalizations between the amplitudes, nor efficiency effects, the f_k coefficients cannot be used to describe the abundance of each decay mode.

(a) $m^2_{K^+\pi^-\pi^+}$

(b) $m^2_{K^+\pi^-}$

(c) $m^2_{\pi^+\pi^-}$

(d) Legend
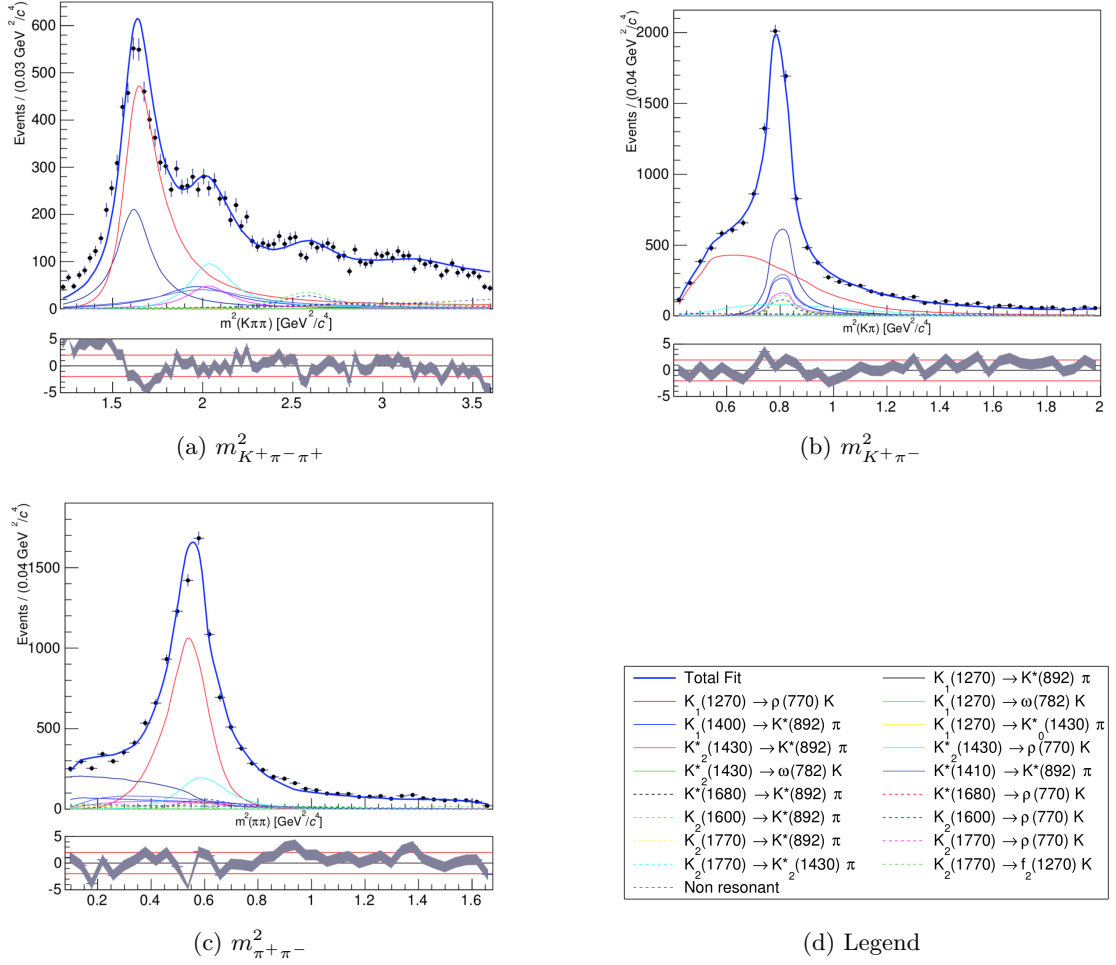
Figure 1.14 – Background-subtracted distributions of $m^2_{K^+\pi^-\pi^+}$, $m^2_{K^+\pi^-}$ and $m^2_{\pi^+\pi^-}$ for $B^+ \rightarrow K^+\pi^-\pi^+\gamma$ decays. The results of a simultaneous unbinned maximum likelihood fit is superimposed. Plots from Ref. [53].

Instead, a fit fraction is defined as

$$\mathrm{FF}_k = \frac{|f_k|^2 \int \mathcal{D}^J_k \mathcal{D}^{J*}_k \Phi_3(\vec{m}) \mathrm{d}\vec{m}}{\int \mathcal{P}_\mathrm{S}(\vec{m}|\Omega)\Phi_3(\vec{m})\mathrm{d}\vec{m}} . \tag{1.49}$$

A fit fraction is also introduced for the interference terms defined for interfering amplitudes and for $l > k$ as

$$\mathrm{FF}_{k,l} = \frac{2\mathcal{R}e\left[f_k f_l^* \int \mathcal{D}^J_k \mathcal{D}^{J*}_l \Phi_3(\vec{m}) \mathrm{d}\vec{m}\right]}{\int \mathcal{P}_\mathrm{S}(\vec{m}|\Omega)\Phi_3(\vec{m})\mathrm{d}\vec{m}} , \tag{1.50}$$

such that the sum of all fit fractions for individual amplitudes and interference systems is equal to 1.

31

Table 1.1 – Result of the Dalitz analysis of $B^+ \to K^+\pi^-\pi^+\gamma$ decays [53] with fit fraction uncertainties obtained from simulation.

J^P	Amplitude k	Fit fraction (%)
1^+	$K_1(1270)^+ \to K^*(892)^0\pi^+$	16.8 ± 0.9
	$K_1(1270)^+ \to K^+\rho(770)^0$	$39.9^{+0.6}_{-0.7}$
	$K_1(1270)^+ \to K^+\omega(782)^0$	$0.068^{+0.028}_{-0.180}$
	$K_1(1270)^+ \to K^*(1430)^0\pi^+$	$0.69^{+0.22}_{-0.20}$
	$K_1(1400)^+ \to K^*(892)^0\pi^+$	7.8 ± 0.8
1^-	$K^*(1410)^+ \to K^*(892)^0\pi^+$	$8.4^{+2.8}_{-3.3}$
	$K^*(1680)^+ \to K^*(892)^0\pi^+$	$3.5^{+1.7}_{-2.1}$
	$K^*(1680)^+ \to K^+\rho(770)^0$	2.4 ± 0.4
2^+	$K_2^*(1430)^+ \to K^*(892)^0\pi^+$	4.8 ± 1.0
	$K_2^*(1430)^+ \to K^+\rho(770)^0$	9.0 ± 0.8
	$K_2^*(1430)^+ \to K^+\omega(782)^0$	$0.30^{+0.13}_{-0.26}$
2^-	$K_2(1580)^+ \to K^*(892)^0\pi^+$	$4.4^{+0.9}_{-1.0}$
	$K_2(1580)^+ \to K^+\rho(770)^0$	$3.33^{+0.34}_{-0.50}$
	$K_2(1770)^+ \to K^*(892)^0\pi^+$	$3.0^{+0.6}_{-0.8}$
	$K_2(1770)^+ \to K^+\rho(770)^0$	$0.23^{+0.08}_{-0.32}$
	$K_2(1770)^+ \to K_2^*(1430)^0\pi^+$	$0.67^{+0.10}_{-0.09}$
	$K_2(1770)^+ \to K^+f_2(1270)^0$	$1.30^{+0.15}_{-0.16}$
Non resonant		4.1 ± 0.5

The fit fractions are detailed in Table 1.1. This study used the largest statistics available at the time, and its results give an idea of the content of the $K^+\pi^-\pi^+$ system. Two amplitudes are largely dominant, $K_1(1270)^+ \to K^+\rho(770)^0$ and $K_1(1270)^+ \to K^*(892)^0\pi^+$ with fit fractions of 40% and 17% respectively, accounting for more than half of the entire spectrum. This is compatible with a previous observation by the Belle collaboration [55] but contradicts previous theory estimates. In the rest of the spectrum, and especially at higher masses, many different amplitudes overlap with relatively similar fit fractions. As they are related to broad resonances, little discrimination is expected from using the mass distributions, and the use of angular information could help significantly in separating the resonances characterized by different spins. Moreover, this fit does not take into account any photon angular variables, which results mainly in a loss of sensitivity on the measurement of the complex phases between the amplitudes, which would be essential to determine the photon polarisation parameter λ_γ from a $\mathcal{A}_{\text{ud}}$ measurement as discussed in the following.
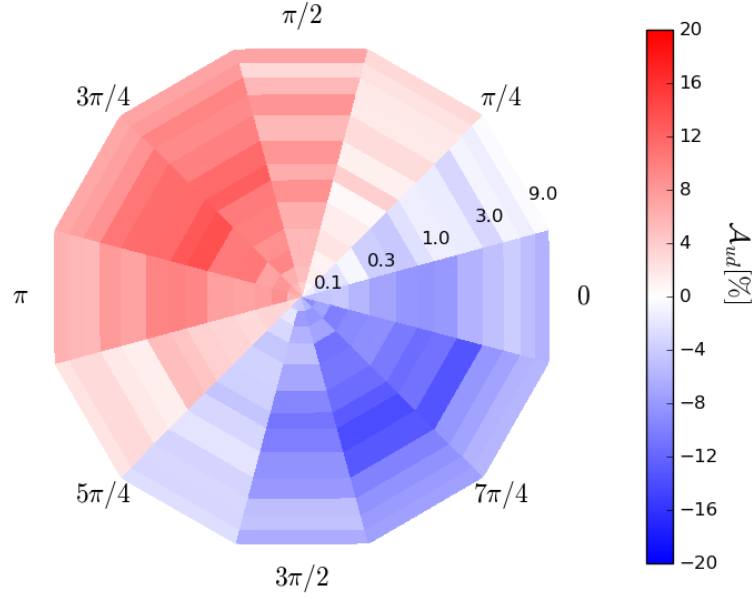
Figure 1.15 – Up-down asymmetry $\mathcal{A}_{ud}$ for simulated samples of $B^+ \to K_1(1270)^+\gamma$ decays governed by two amplitudes only, $K_1(1270)^+ \to K^+\rho(770)^0$ and $K_1(1270)^+ \to K^*(892)^0\pi^+$, shown as a function of the generated ratio of fractions (radial coordinate, from 0.1 to 9.0) and phase difference between the two amplitudes (polar coordinate).

1.4.3 Limits of the up-down asymmetry measurement

The effects of the resonant structure of the $K\pi\pi$ system on $\mathcal{A}_{ud}$ can be illustrated using a simplified $B^+ \to K_{\text{res}}^+\gamma$ model containing only two amplitudes corresponding to the two most abundant decays $K_1(1270)^+ \to K^+\rho(770)^0$ and $K_1(1270)^+ \to K^*(892)^0\pi^+$ with $\rho(770)^0 \to \pi^+\pi^-$ and $K^*(892)^0 \to K^+\pi^-$. Simulated samples of decays containing only right-handed photons are generated (using the formalism presented in the next chapter) with different relative fractions and phase differences between these amplitudes, and the up-down asymmetry is computed for each of them. The results in Fig. 1.15 show that the up-down asymmetry varies widely depending on the phase difference between the amplitudes, while it is less dependent on the relative fraction. This implies that, even in this simple model, the proportionality coefficient that relates the up-down asymmetry to the photon polarisation parameter depends strongly on the phase difference between the amplitudes, making the knowledge of this phase essential to measure the value of λ_γ; additionally, for some values of the relative phase, the proportionality coefficient vanishes, indicating that the measurement of the up-down asymmetry is not sensitive to λ_γ in such configurations.

To overcome these difficulties and measure the photon polarisation, all the information from the angular variables and from the squared invariant-mass distributions must be

combined in order to characterise the interferences between decay processes and their effect on λ_γ.

2 Proof-of-concept for the measurement of the photon polarisation using an amplitude analysis

In this chapter, a method to measure the photon polarisation parameter in $B^+ \to K^+\pi^-\pi^+\gamma$ decays is presented and the statistical uncertainty that can be obtained from this measurement is estimated.

2.1 Formalism

To develop our formalism, decays of B mesons to $K\pi\pi\gamma$ are assumed to proceed through a cascade of quasi-independent two-body decays, an approximation known as the *isobar model* [56, 57]. In this study, decay topologies of the form $B \to R_i\gamma$, $R_i \to R_jP_1$, and $R_j \to P_2P_3$ are considered, where R_i is a $K\pi\pi$ intermediate state, R_j is either a $K\pi$ or $\pi\pi$ resonant state and P_α is a final-state kaon or pion.

The expression of the differential decay rate in Eq. 1.40 can then be used to define a signal function for the $B \to K\pi\pi\gamma$ decays:

$$\mathcal{P}_s = \frac{(1+\lambda_\gamma)}{2}|\mathcal{M}_R|^2 + \frac{(1-\lambda_\gamma)}{2}|\mathcal{M}_L|^2, \tag{2.1}$$

where $\mathcal{M}_{R/L}$ are now expressed as

$$\mathcal{M}_{R/L} = \sum_k f_k \mathcal{A}_{k,R/L}(\boldsymbol{x}), \tag{2.2}$$

with $f_k = a_k e^{i\phi_k}$. The decay amplitude $\mathcal{A}_{k,R/L}(\boldsymbol{x})$ corresponds to a $B \to K\pi\pi\gamma$ process k involving resonances R_i and R_j and a right- or left-handed photon, and $\boldsymbol{x}$ is the set of four-vectors associated with the final-state particles in the rest frame of the B meson. The complex coefficient $f_k = a_k e^{i\phi_k}$ accounts for the magnitude a_k and phase ϕ_k of decay amplitude k and is assumed to be the same for decays with right- or left-handed photons.

The amplitude for a given decay mode k is the product of resonance propagators $\mathcal{T}$ for each intermediate two-body decay with relative angular momentum L, a normalised Blatt-Weisskopf coefficient B_{L_B} (given in Table 2.2) for the two-body decay of the B characterised by relative angular momentum L_B and breakup momentum q_B, and a spin factor $\mathcal{S}_{ij,\mathrm{R/L}}^k$ that encodes the dependence of the amplitude on angular momenta,

$$\mathcal{A}_{\mathrm{R/L}}^k(\boldsymbol{x}) = B_{L_B}(q_B(\boldsymbol{x}),0)\mathcal{T}_i^k(\boldsymbol{x})\mathcal{T}_j^k(\boldsymbol{x})\mathcal{S}_{ij,\mathrm{R/L}}^k(\boldsymbol{x}).$$

The coefficient $g^i(0)$ present in the expressions of in Eq. 1.41 is now included in the coefficient f_k, which also contains the respective strength and phase between the strong decay amplitudes, while the coefficient $S_{\mathrm{R/L}}^i$ is now included in the expression for $\mathcal{S}_{ij,\mathrm{R/L}}^k$ in a way that will be detailed in Section 2.1.2.

Before showing the details of the computations, a convention is adopted concerning the polarisation states of the photon. In order to define them, we chose to work in the reference frame of the B meson, with the z axis opposite to the photon direction. In this case, the polarisation vectors associated to a right- or left-handed photon correspond respectively to the spin projections $m_\gamma = -1$ and $+1$, and can be written

$$\epsilon^\mu(m_\gamma = \pm 1) = \frac{1}{\sqrt{2}}\begin{pmatrix} 0 \\ \mp 1 \\ -i \\ 0 \end{pmatrix}. \tag{2.3}$$

In the expressions that follow, we will consider equivalent the notations $\mathcal{S}_{ij,\mathrm{R}}^k = \mathcal{S}_{ij,m_\gamma=-1}^k$ and $\mathcal{S}_{ij,\mathrm{L}}^k = \mathcal{S}_{ij,m_\gamma=+1}^k$.

The spin factors $\mathcal{S}_{ij,\mathrm{R/L}}^k$ can now be computed using the covariant formalism developed in Refs. [58, 59]. In general, they can be expressed as

$$\mathcal{S}_{ij,m_\gamma}^k = \sum_{m_i,m_j} \langle P_2 P_3 | \mathcal{M} | R_j(m_j)\rangle \langle R_j(m_j) P_1 | \mathcal{M} | R_i(m_i)\rangle \langle R_i(m_i)\gamma(m_\gamma) | \mathcal{M} | B\rangle, \tag{2.4}$$

where m_i and m_j are the spin projections of resonance R_i and R_j, respectively, and $\mathcal{M}$ is the appropriate matrix element for each decay. Each of the terms $\langle AB | \mathcal{M} | R\rangle$ describe the two-body process $R \to AB$, and are computed as contractions of polarisation operators, projection tensors and angular momentum tensors as described in the two following sections. Here, the terms $\langle P_2 P_3 | \mathcal{M} | R_j(m_j)\rangle$ and $\langle R_j(m_j) P_1 | \mathcal{M} | R_i(m_i)\rangle$, which involve strong decays of massive particles, are to be treated separately from the term $\langle R_i(m_i)\gamma(m_\gamma) | \mathcal{M} | B\rangle$ which describes a specific weak decay with a massless particle. The rules to build the terms describing strong decays are explained in details in Ref. [60], and are summarized in Sec. 2.1.1. Section 2.1.2 shows how the weak decay term is computed for the sensitivity study shown in this chapter.

2.1.1 Description of the strong decay processes

In order to build the expression for a term $\langle AB|\mathcal{M}|R\rangle$ describing a strong decay, three types of tensors are needed: polarisation operators, projection tensors and angular momentum tensors.

Polarisation operators In the case of a particle of spin 0, which is invariant under space rotation, the polarisation tensor is of rank 0 and it is set to 1. For massive particles of mass M and spin projection m, three polarisation vectors associated with three different spin projections $m = -1, 0, 1$ can be defined in their rest frame as

$$\epsilon'^{\mu}(m = \pm 1) = \frac{1}{\sqrt{2}} \begin{pmatrix} 0 \\ \mp 1 \\ -i \\ 0 \end{pmatrix}, \quad \epsilon'^{\mu}(m = 0) = \begin{pmatrix} 0 \\ 0 \\ 0 \\ 1 \end{pmatrix}. \tag{2.5}$$

In the computation of the spin factors, these polarisation vectors are needed in an arbitrary frame (in which the massive particle of mass M has a four-momentum p and energy E). Their expression is obtained using a Lorentz transformation:

$$\epsilon'^{\mu}(p, m = \pm 1) = \frac{\mp 1}{\sqrt{2}M} \begin{pmatrix} p_x \pm ip_y \\ M + p_x(p_x \pm ip_y)/(E + M) \\ \pm iM + p_y(p_x \pm ip_y)/(E + M) \\ p_z(p_x \pm ip_y)/(E + M) \end{pmatrix}, \tag{2.6}$$

and

$$\epsilon'^{\mu}(p, m = 0) = \frac{1}{M} \begin{pmatrix} p_z \\ p_z p_x/(E + M) \\ p_z p_y/(E + M) \\ M + p_z^2/(E + M) \end{pmatrix}. \tag{2.7}$$

Generalized spin-2 polarisation tensors are then obtained by coupling spin-1 polarisation vectors,

$$\epsilon'^{\mu\nu}(p, m) = \sum_{m_1, m_2} \langle 1m_1, 1m_2|2m\rangle \epsilon'^{\mu}(p, m_1)\epsilon'^{\nu}(p, m_2), \tag{2.8}$$

where $\langle 1m_1, 1m_2|2m\rangle$ are Clebsch-Gordan coefficients. By construction, the polarisation tensors satisfy the Rarita-Schwinger conditions: they are traceless, symmetric and orthogonal to p.

Projection tensors   Spin projectors are used to project any tensor on the subspace spanned by a set of polarisation tensors. The spin-1 projection tensor associated with a massive particle is defined as

$$P_{(1)}^{\mu\nu}(p) = \sum_m \epsilon'^\mu(p, m)\epsilon'^{*\nu}(p, m) = -g^{\mu\nu} + \frac{p^\mu p^\nu}{M^2}, \tag{2.9}$$

where $g^{\mu\nu} = \text{diag}(+1, -1, -1, -1)$ is the Minkowski metric. The projection tensor $P_{(1)}^{\mu\nu}(p)$ satisfies the relation:

$$P_{(1)}^{\mu\nu}(p) = -P_{(1)\sigma}^{\mu}(p)P_{(1)}^{\sigma\nu}(p). \tag{2.10}$$

The spin-2 projection operator can then be obtained from the spin-1 projection operator as

$$\begin{aligned}
P_{(2)}^{\mu\nu\alpha\beta}(p) &= \sum_m \epsilon'^{\mu\nu}(p, m)\epsilon'^{*\alpha\beta}(p, m) \\
&= \frac{1}{2}\left(P_{(1)}^{\mu\alpha}(p)P_{(1)}^{\nu\beta}(p) + P_{(1)}^{\mu\beta}(p)P_{(1)}^{\nu\alpha}(p)\right) - \frac{1}{3}P_{(1)}^{\mu\nu}(p)P_{(1)}^{\alpha\beta}(p).
\end{aligned} \tag{2.11}$$

Angular-momentum tensors   The angular momentum tensor that describes a two-particle state of pure angular momentum L is obtained from the total four-momentum $p_R = p_1 + p_2$ and the relative four-momentum $q_R = p_1 - p_2$, where p_1 and p_2 are the final-state four-momenta. The angular momentum tensor is built by projecting the rank-L tensor of relative momenta $q_R^{\nu_1} q_R^{\nu_2}...q_R^{\nu_L}$ on the spin-L subspace

$$\begin{aligned}
&L_{(L)\mu_1\mu_2...\mu_L}(p_R, q_R) \\
&= (-1)^L P_{(L)\mu_1\mu_2...\mu_L\nu_1\nu_2...\nu_L}(p_R)q_R^{\nu_1} q_R^{\nu_2}...q_R^{\nu_L},
\end{aligned} \tag{2.12}$$

where the spin projection tensor reduces the number of degrees of freedom from 4^L to $2L + 1$.

Conservation laws in the strong interaction   In general, a decay process $\langle AB|\mathcal{M}|R\rangle$ where R, A and B are massive particles with spin S_R, S_A and S_B can be separated in different states characterized by the value of the angular momentum between the two daughters $\vec{L}_{AB}$ and total intrinsic spin $\vec{S}_{AB} = \vec{S}_A + \vec{S}_B$. As the total angular momentum is conserved, the values of $\vec{L}_{AB}$ must satisfy the condition

$$\vec{S}_R = \vec{L}_{AB} + \vec{S}_{AB}, \tag{2.13}$$

which reduces the possible number of spin-orbit combinations (L_{AB}, S_{AB}). In the case of strong interactions, the number of possible combinations is further reduced because of

the conservation of parity, which imposes

$$P_R = P_A P_B (-1)^{L_{AB}} , \tag{2.14}$$

where P_R, P_A and P_B are the intrinsic parities of R, A and B.

For example, in the decay of an axial vector (of spin parity $S^P = 1^+$) to a vector ($S^P = 1^-$) and a pseudo-scalar particle ($S^P = 0^-$), such as $K_1(1270)^+ \to K^*(892)^0 \pi^+$, we have

$$\vec{S}_{AB} = \vec{S}_A + \vec{S}_B = \vec{1} + \vec{0} = \vec{1} \quad \text{and} \quad \vec{S}_R = \vec{1} = \vec{L}_{AB} + \vec{S}_{AB} = \vec{L}_{AB} + \vec{1}, \tag{2.15}$$

which implies $\vec{L}_{AB} = \vec{0}$, $\vec{1}$ or $\vec{2}$. Parity conservation then limits L_{AB} to even values, so 0 or 2. This process allows for two different spin-orbit configurations ($L_{AB} = 0$, $S_{AB} = 1$) and ($L_{AB} = 2$, $S_{AB} = 1$) which are referred to as S and D-waves and will be described by different spin factors.

Rules to build spin factors For a two-body process $R \to AB$ with a spin-orbit configuration (L_{AB}, S_{AB}), the term $\langle AB, L_{AB}, S_{AB} | \mathcal{M} | R \rangle$ is computed as

$$\langle AB, L_{AB}, S_{AB} | \mathcal{M} | R \rangle = \epsilon_{(S_R)}(R) X(S_R, L_{AB}, S_{AB}) L_{(L_{AB})}(R) \Phi_{(S_{AB})} , \tag{2.16}$$

where

$$\Phi_{(S_{AB})} = P_{(S_{AB})}(R) X(S_{AB}, S_A, S_B) \epsilon^*_{(S_A)}(A) \epsilon^*_{(S_B)}(B) . \tag{2.17}$$

The term $\epsilon_{(S_R)}(R)$ is a polarisation tensor assigned to the decaying particle and $\epsilon^*_{(S_A)}(A)$ and $\epsilon^*_{(S_B)}(B)$ are conjugated polarisation tensors assigned to the children particles. The spin projector $P_{(S_{AB})}(R)$ and the angular momentum tensor $L_{(L_{AB})}(R)$ describe the spin and angular momentum coupling, respectively. All tensors must be contracted to give a scalar in Eq. 2.16, requiring in some cases the inclusion of the tensor $\epsilon_{\alpha\beta\gamma\delta} p_R^\delta$ through

$$X(j_a, j_b, j_c) = \begin{cases} 1 & \text{for } j_a + j_b + j_c \text{ even,} \\ \epsilon_{\alpha\beta\gamma\delta} p_R^\delta & \text{for } j_a + j_b + j_c \text{ odd,} \end{cases} \tag{2.18}$$

where p_R is the momentum of resonance R.

To obtain the spin factor associated with a given decay chain, the various two-body processes are combined and all the allowed spin projections that are not distinguishable are summed.

An example using only strong decays As an example, let us consider the decay chain $K_1(1270)^+ \to K^*(892)^0 (\to K^+ \pi^-) \pi^+$. As seen previously, the first two-body

decay $K_1(1270)^+ \to K^*(892)^0\pi^+$ has an S- and a D-wave. In an analogous way, it can be shown that the only possible spin-orbit configuration for the decay $K^*(892)^0 \to K^+\pi^-$ is a P-wave ($L_{AB} = 1$, $S_{AB} = 0$). In the following, the spin factor of the full decay chain including the S-wave of the $K_1(1270)^+ \to K^*(892)^0\pi^+$ is computed. For convenience, as the expressions of the spin factors depend only on the spin-parities of the particles involved, the particles $K_1(1270)^+$, $K^*(892)^0$, π^+, K^+ and π^- are referred to as A, V, P_1, P_2 and P_3 (where the letters A, V and P stand for axial-vector, vector and pseudo-scalar particles, respectively).

Following the rules described above, the term describing the S-wave of the $K_1(1270)^+ \to K^*(892)^0(\to K^+\pi^-)\pi^+$ decay can be expressed as

$$\langle VP_1, L_{AB} = 0, S_{AB} = 1| \, \mathcal{M} \, |A\rangle = \epsilon_\mu(A)P^{\mu\nu}_{(1)}(A)\epsilon^*_\nu(V) \,, \tag{2.19}$$

and similarly, the term for the decay $K^*(892)^0 \to K^+\pi^-$ is obtained:

$$\langle P_2P_3, L_{AB} = 1, S_{AB} = 0| \, \mathcal{M} \, |V\rangle = \epsilon_\sigma(V)L^\sigma_{(1)}(V) \,. \tag{2.20}$$

As the spin projections m_i of $K_1(1270)^+$ and m_j of $K^*(892)^0$ are not observable, the spin factor for the decay chain is computed as the following sum:

$$\mathcal{S}_{i,j} = \sum_{m_i, m_j} \langle P_2P_3, 1, 0| \, \mathcal{M} \, |V\rangle \langle VP_1, 0, 1| \, \mathcal{M} \, |A\rangle \tag{2.21}$$

$$= \sum_{m_i, m_j} \epsilon_\mu(A)P^{\mu\nu}_{(1)}(A)\epsilon^*_\nu(V)\epsilon_\sigma(V)L^\sigma_{(1)}(V) \,. \tag{2.22}$$

Using Eq. 2.9, the sum over the spin projections m_j is performed, so

$$\mathcal{S}_{i,j} = \sum_{m_i} \epsilon_\mu(A)P^{\mu\nu}_{(1)}(A)P_{\nu\sigma}(V)L^\sigma_{(1)}(V) \,. \tag{2.23}$$

Finally, the relation of Eq. 2.10 and the expression of the angular momentum tensor of Eq. 2.12 are used to simplify this expression:

$$\mathcal{S}_{i,j} = \sum_{m_i} \epsilon_\mu(A)P^{\mu\nu}_{(1)}(A)L_{(1)\nu}(V) \,. \tag{2.24}$$

2.1.2 Description of the weak decay process

Due to its specific $V - A$ structure and the fact that it involves a massless particle, the $B \to R_i\gamma$ transition is modelled separately from the strong decays. The term that describes the transition to a right-handed photon, $\langle R_i(m_i)\gamma(m_\gamma = -1)|\mathcal{M}|B\rangle$, corresponds to $S^i_{\rm R}$ of Eq. 1.41, and $\langle R_i(m_i)\gamma(m_\gamma = +1)|\mathcal{M}|B\rangle$ corresponds to $S^i_{\rm L}$, so these terms are related by Eq. 1.36.

As decays with a photon cannot be described in terms of spin-orbit couplings, the rules established in the previous section do not hold anymore. The terms $S^i_{\mathrm{R/L}}$ used to describe these decays must be built in a covariant way, and in such that they obey the relation of Eq. 1.36.

For the sensitivity study shown in the next sections, these terms were expressed as

$$J^{P_i}_i = 1^+ : S^i_{\mathrm{R/L}} = \epsilon^{*\mu}(\gamma)\epsilon^*_\mu(R_i)\,, \tag{2.25}$$

$$J^{P_i}_i = 1^- : S^i_{\mathrm{R/L}} = \pm\epsilon^{*\mu}(\gamma)\epsilon^*_\mu(R_i)\,, \tag{2.26}$$

$$J^{P_i}_i = 2^+ : S^i_{\mathrm{R/L}} = \pm L^\mu_{(1)}(B)\epsilon^*_{\mu\nu}(R_i)\epsilon^{*\nu}(\gamma)\,, \tag{2.27}$$

$$J^{P_i}_i = 2^- : S^i_{\mathrm{R/L}} = L^\mu_{(1)}(B)\epsilon^*_{\mu\nu}(R_i)\epsilon^{*\nu}(\gamma)\,, \tag{2.28}$$

such that they are covariant and the relation of Eq. 1.36 applies. In the computation of $S^i_{\mathrm{R/L}}$, the use of the spin projection $m_\gamma = \mp 1$ for the polarisation vector of the photon is implied.

2.1.3   Spin factors for the full decay chains

The spin factors for the entire decay chains are obtained using Eq. 2.4. Note that in this equation, the sum is performed on the spin projections m_i of the resonance R_i as explained above. However, the spin projections of the photon m_γ are not summed over because they are distinguishable. The resulting expressions for the spin factors used in this sensitivity study are shown in Table. 2.1.

Table 2.1 – Spin factors for different decay chains leading to $B \to P_1 P_2 P_3 \gamma$. The letters S, P, V, A refer to scalar, pseudoscalar, vector and axial-vector particles, respectively. T_+ and T_- are tensor particles with positive and negative parity, respectively. By default, the lowest total angular momentum L_{AB} accessible in each of the two-body decays is used. The symbol $[D]$ refers to decay chains where L_{AB} is set to 2. The $\pm$ sign is introduced for spin factors with a right-handed (resp. left-handed) photon.

Decay chain	Spin factor
$B \to A\gamma, A \to VP_1, V \to P_2P_3$	$\epsilon^*_\alpha(\gamma)P^{\alpha\beta}_{(1)}(A)L_{(1)\beta}(V)$
$B \to A\gamma, A[D] \to VP_1, V \to P_2P_3$	$\epsilon^*_\alpha(\gamma)L^{\alpha\beta}_{(2)}(A)L_{(1)\beta}(V)$
$B \to A\gamma, A \to SP_1, S \to P_2P_3$	$\epsilon^{*\alpha}(\gamma)L_{(1)\alpha}(A)$
$B \to V_1\gamma, V_1 \to V_2P_1, V_2 \to P_2P_3$	$\pm\epsilon^*_\alpha(\gamma)P^{\alpha\kappa}_{(1)}(V_1)\epsilon_{\kappa\lambda\mu\nu}L^\lambda_{(1)}(V_1)p^\mu_{V_1}P^{\nu\xi}_{(1)}(V_1)L_{(1)\xi}(V_2)$
$B \to T_-\gamma, T_- \to VP_1, V \to P_2P_3$	$L_{(1)\alpha}(B)\epsilon^*_\beta(\gamma)P^{\alpha\beta\lambda\mu}_{(2)}(T_-)L_{(1)\lambda}(T_-)P_{(1)\mu\nu}(T_-)L^\nu_{(1)}(V)$
$B \to T_-\gamma, T_- \to SP_1, S \to P_2P_3$	$L_{(1)\alpha}(B)\epsilon^*_\beta(\gamma)L^{\alpha\beta}_{(2)}(T_-)$
$B \to T_+\gamma, T_+ \to VP_1, V \to P_2P_3$	$\pm\epsilon_{\kappa\lambda\mu\nu}p^\kappa_{T_+}L_{(1)\alpha}(B)\epsilon^*_\beta(\gamma)P^{\alpha\beta\lambda\xi}_{(2)}(T_+)L^\mu_{(2)\xi}(T_+)P^{\nu\rho}_{(1)}(T_+)L_{(1)\rho}(V)$

Table 2.2 – Normalised Blatt-Weisskopf centrifugal barrier factors for angular momentum L. The meson radial parameter R is set to $1.5\,(\text{GeV}/c)^{-1}$ following a measurement by Belle [62].

L	$B_L(q, q_0)$
0	1
1	$\sqrt{\dfrac{1 + R^2 q_0^2}{1 + R^2 q^2}}$
2	$\sqrt{\dfrac{9 + 3R^2 q_0^2 + R^4 q_0^4}{9 + 3R^2 q^2 + R^4 q^4}}$

2.1.4 Lineshapes

For the needs of this sensitivity study, the lineshapes for the various resonances are assumed to be described by the product of a Blatt-Weisskopf normalised coefficient and a relativistic Breit-Wigner, which is mainly valid for narrow and non-overlapping resonances, so this assumption will be revisited for the amplitude analysis performed on data. The expression for the lineshapes used in this study is [61]

$$\mathcal{T}_{\text{BW}}(s, q, L) = \frac{\sqrt{c}\ B_L(q, 0)}{m_0^2 - s - im_0\Gamma(s, q, L)}, \tag{2.29}$$

where m_0 is the nominal mass of the resonance, s is the two-body invariant mass squared, L is the two-body relative angular momentum, q denotes the breakup momentum of the outgoing particle pair in the rest frame of the resonance and $\Gamma(s, q, L)$ is its energy-dependent width. The normalisation constant

$$c = \frac{m_0 \Gamma_0 \gamma_0}{\sqrt{m_0^2 + \gamma_0}}, \text{with } \gamma_0 = m_0\sqrt{m_0^2 + \Gamma_0^2}, \tag{2.30}$$

is meant to reduce the correlations between the coupling to the decay channel and the mass and width of the resonance. The width of the resonance for a decay into two particles is parametrised as

$$\Gamma(s, q, L) = \Gamma_0 \frac{m_0}{\sqrt{s}} \left(\frac{q}{q_0}\right)^{2L+1} B_L(q, q_0)^2, \tag{2.31}$$

where q_0 is the value of the breakup momentum at the resonance pole $s = m_0{}^2$, and $B_L(q, q_0)$ is the normalised Blatt-Weisskopf barrier factor, listed in Table 2.2.

2.2 Generator validation

The amplitude formalism described in Sect. 2.1 is implemented in a generator and fitter software framework called Mint, which was developed for the amplitude analysis of $D^0 \to K^+K^-\pi^+\pi^-$ decays at CLEO [63, 64]. In the context of the present work, several tests have been performed to validate the implementation of the lineshapes. A comparison between Mint and EvtGen [65] has been conducted by generating $B^+ \to K^+\pi^-\pi^+\gamma$ decays with a model in which only one single process was involved (for example $K_1(1270)^+ \to K^*(892)^0(\to K^+\pi^-)\pi^+$), resulting in very similar distributions in mass and angles. However, interferences between the different decay processes cannot be generated with EvtGen, so in order to check that the interferences between different decay processes were parametrized properly, up-down asymmetries were compared between theoretical predictions and simulated samples obtained with Mint. These samples were generated with a simple model involving two decay processes: $K_1(1400)^+ \to K^*(892)^0\pi^+$ S-wave, and D-wave. For this process, theoretical predictions of the up-down asymmetry (in the "flip" scenario) are available in Ref. [50] for different values of the relative phase ϕ_{DS} between these amplitudes, and a relative abundance (expressed as the ratio of fractions as defined in Eq. 2.35) of 4% between the D and the S waves. The theoretical computation also assume a null width for the $K_1(1400)^+$ resonance, and no barrier factors. Samples containing the same mixture of decay processes were generated with $\lambda_\gamma = +1$ using the formalism described above but with some modifications: no barrier factors were used, and the width of the $K_1(1400)$ Breit-Wigner was set to small but non-zero values (30 MeV and 10 MeV) because arbitrarily small values of the width can not be handled by the accept-reject method used in the generation process. The corresponding up-down asymmetries were computed from a fit using Legendre polynomials as in Eq. 1.45, and are reported in Table 2.3. The predicted and simulated values follow the same trend with maximal, minimal and zero values at the same points. However, the absolute value of the simulated up-down asymmetries are smaller than the predicted value, getting closer to the later as the width of the simulated resonance decreases. The remaining differences are attributed to the non-zero width, which could not be decreased further.

2.3 Method for an amplitude fit

The proposed method to determine the photon polarisation parameter λ_γ in $B \to K\pi\pi\gamma$ decays exploits all the degrees of freedom of the system to perform a maximum likelihood fit to the data using a probability density function (PDF) that depends explicitly on λ_γ. This amplitude fit allows the direct measurement of λ_γ, as well as of the relative magnitudes and phases of the different decay-chain amplitudes included in the model.

Table 2.3 – Up-down asymmetry in the "flip" scenario for $B \to K_1(1400)^+\gamma$ decays governed by two amplitudes only, $K_1(1400)^+ \to K^*(892)^0\pi^+$ S-wave and D-wave (where the ratio of fractions between the D and S waves is 4%), shown as a function of the phase difference ϕ_{DS} between these amplitudes. The predicted up-down asymmetries are from Ref. [50] and the fitted asymmetries correspond to different values of the generated width of the $K_1(1400)$ resonance.

ϕ_{DS} [degrees]	Predicted $\mathcal{A}_{\mathrm{ud}}$ [%] $\Gamma_{K_1(1400)} = 0\,\mathrm{MeV}/c^2$	Fitted $\mathcal{A}_{\mathrm{ud}}$[%] $\Gamma_{K_1(1400)} = 10\,\mathrm{MeV}/c^2$	Fitted $\mathcal{A}_{\mathrm{ud}}$[%] $\Gamma_{K_1(1400)} = 30\,\mathrm{MeV}/c^2$
0	0	-0.13 ± 0.29	0.27 ± 0.29
45	-7	-5.31 ± 0.29	-4.06 ± 0.29
90	-10	-7.25 ± 0.29	-5.62 ± 0.29
135	-7	-6.13 ± 0.29	-4.48 ± 0.29
180	0	-0.04 ± 0.29	-0.71 ± 0.29
225	7	5.62 ± 0.29	4.40 ± 0.29
270	10	7.44 ± 0.29	5.72 ± 0.29
315	7	5.64 ± 0.29	3.86 ± 0.29

2.3.1 Probability distribution function

The PDF is computed using the function $\mathcal{P}_\mathrm{s}$ given in Eq. 2.1 as

$$\mathcal{F}(\boldsymbol{x}|\Omega) = \frac{\xi(\boldsymbol{x})\mathcal{P}_\mathrm{s}(\boldsymbol{x}|\Omega)\Phi_4(\boldsymbol{x})}{\int \xi(\boldsymbol{x})\mathcal{P}_\mathrm{s}(\boldsymbol{x}|\Omega)\Phi_4(\boldsymbol{x})\,\mathrm{d}\boldsymbol{x}}, \tag{2.32}$$

where $\Omega = (\lambda_\gamma, \{a_k\}, \{\phi_k\})$ is the set of fit parameters, $\boldsymbol{x}$ is the set of four-vectors associated with the final-state particles in the rest frame of the B meson, $\Phi_4(\boldsymbol{x})$ is the four-body phase-space density, and $\xi(\boldsymbol{x})$ is the total signal efficiency, which accounts for detector acceptance, reconstruction, and event selection. The magnitude and phase of each amplitude k (a_k and ϕ_k) are measured with respect to those of amplitude 1, for which a_1 and ϕ_1 are fixed to 1 and 0, respectively.

A large sample of simulated events, generated according to an approximate model $\mathcal{P}_\mathrm{gen}$ is used to compute numerically the normalisation integral in the denominator of Eq. 2.32. The efficiency $\xi(\boldsymbol{x})$ is inherently taken into account by applying the event selection used in data to the simulated events. The normalisation integral can then be estimated as

$$\int \xi(\boldsymbol{x})\mathcal{P}_s(\boldsymbol{x}|\Omega)\Phi_4(\boldsymbol{x})\,\mathrm{d}\boldsymbol{x} = \frac{I_\mathrm{gen}}{N_\mathrm{sel}} \sum_j^{N_\mathrm{sel}} \frac{\mathcal{P}_s(\boldsymbol{x}_j|\Omega)}{\mathcal{P}_\mathrm{gen}(\boldsymbol{x}_j)} \tag{2.33}$$

with

$$I_{\text{gen}} = \int \xi(\boldsymbol{x}) \mathcal{P}_{\text{gen}}(\boldsymbol{x}) \Phi_4(\boldsymbol{x}) \, \mathrm{d}\boldsymbol{x}, \tag{2.34}$$

where N_{sel} is the total number of generated events that pass the selection criteria. The integral I_{gen} does not depend on the parameters of the fit, and therefore does not need to be evaluated to perform the maximisation.

For the studies presented in this chapter, the effect of the application of a selection is not considered, so $\xi(\boldsymbol{x}) = 1$.

The fraction of a decay mode k is defined as the ratio of the phase-space integral of the sum of right- and left-handed contributions over the phase-space integral of the function $\mathcal{P}_s$,

$$F_k = (1 + \lambda_\gamma) \frac{\int |f_k \mathcal{A}_{k,\text{R}}(\boldsymbol{x})|^2 \Phi_4(\boldsymbol{x}) \, \mathrm{d}\boldsymbol{x}}{2 \int \mathcal{P}_s(\boldsymbol{x}|\Omega) \Phi_4(\boldsymbol{x}) \, \mathrm{d}\boldsymbol{x}} + (1 - \lambda_\gamma) \frac{\int |f_k \mathcal{A}_{k,\text{L}}(\boldsymbol{x})|^2 \Phi_4(\boldsymbol{x}) \, \mathrm{d}\boldsymbol{x}}{2 \int \mathcal{P}_s(\boldsymbol{x}|\Omega) \Phi_4(\boldsymbol{x}) \, \mathrm{d}\boldsymbol{x}}. \tag{2.35}$$

Because of the interferences between the decay modes, the sum of these fractions may not be equal to unity. The interference term between the decay modes k and l, where $k > l$ is defined as

$$F_{kl} = (1 + \lambda_\gamma) \frac{\int \mathcal{R}e \left\{ f_k \mathcal{A}_{k,\text{R}}(\boldsymbol{x}) f_l^* \mathcal{A}_{l,\text{R}}^*(\boldsymbol{x}) \right\} \Phi_4(\boldsymbol{x}) \, \mathrm{d}\boldsymbol{x}}{\int \mathcal{P}_s(\boldsymbol{x}|\Omega) \Phi_4(\boldsymbol{x}) \, \mathrm{d}\boldsymbol{x}}$$
$$+ (1 - \lambda_\gamma) \frac{\int \mathcal{R}e \left\{ f_k \mathcal{A}_{k,\text{L}}(\boldsymbol{x}) f_l^* \mathcal{A}_{l,\text{L}}^*(\boldsymbol{x}) \right\} \Phi_4(\boldsymbol{x}) \, \mathrm{d}\boldsymbol{x}}{\int \mathcal{P}_s(\boldsymbol{x}|\Omega) \Phi_4(\boldsymbol{x}) \, \mathrm{d}\boldsymbol{x}}. \tag{2.36}$$

The sum of all the fractions and interference terms is equal to unity:

$$\sum_k F_k + \sum_{k>l} F_{kl} = 1. \tag{2.37}$$

2.3.2 Treatment of B^+ and B^- decays

In order to fit both the B^+ and B^- decays with the same PDF, we apply the CP transformation on the B^- candidates and then treat all candidates as B^+ decays. The PDF can then be interpreted as that of a "CP-averaged" model. In case of CP conservation, this model would describe both the B^+ decays and the CP-transformed B^- decays. In the $B^+ \to K^+\pi^-\pi^+\gamma$ decays, direct CP asymmetry is expected to be small and the value of the photon polarisation parameter is expected to be the same for both B^+ and CP-transformed B^- decays. In the data samples, CP is applied by

replacing the three-momenta of all the particles in the decay by their opposite value, and by conjugating the charge of all particles in the decay. A flag allows to keep track of the B^+ and B^- candidates.

2.3.3 Numerical integration

The number of simulated events needed to reach a sufficient precision for the numerical integration depends on the number of events in the fitted data set, on the model to be fitted and on the approximate model used to generate these events. The closer the approximate model to the fitted model, the less events need to be generated. For the studies presented in this chapter, the integration samples typically contained 25% of phase-space events in order to cover all available phase-space, and 75% of events generated according to an approximate model based on the decay chains present in the fit model. In order to estimate the number of events needed to perform the numerical integration for a given data-set size and fit model, 100 different integration samples containing N events each are generated with the same approximate model but a different random seed. The data-set is then fitted 100 times, using each time a different integration sample. The number N is chosen so that the standard deviation of the distribution of fitted values of λ_γ is less than a tenth of the average statistical uncertainty on this parameter from the fit. In this way, the bias on the measured value of λ_γ caused by the size of the integration sample can be neglected. For example, in the study involving a more realistic model of $B \to K\pi\pi\gamma$ decays shown in Sec. 2.4.2, the size of the integration sample was of 6.4 million events.

2.4 Sensitivity studies

The performance of the amplitude fitter is first studied by generating and subsequently fitting simulated data sets of $B \to K\pi\pi\gamma$ decays using models containing two or three decay processes. Once the methodology is validated, more realistic models of the $K\pi\pi$ system are used in order to obtain prospects for measurements of the photon polarisation parameter in B-physics experiments.

2.4.1 Proof of concept with simplified models

As illustrated in Fig. 1.15, the sensitivity to the photon polarisation parameter obtained from the up-down asymmetry depends primarily on the relative phase between amplitudes. The goal of this first study is mainly to explore the parameters that could influence the sensitivity of the measurement of λ_γ when it is performed with an amplitude analysis. The results presented in this section have been published in Ref. [66]. They have been obtained with an approximate parametrisation of the spin factor for the
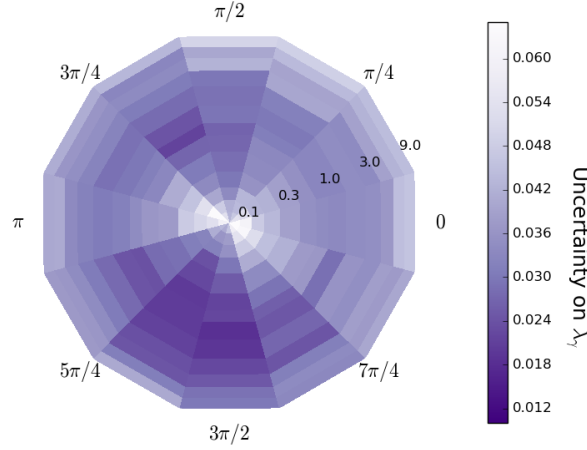
Figure 2.1 – Uncertainty on λ_γ obtained from amplitude fits of simulated samples of $B \to K_1(1270)^+\gamma$ decays governed by two amplitudes only, $K_1(1270)^+ \to K^+\rho(770)^0$ and $K_1(1270)^+ \to K^*(892)^0\pi^+$, shown as a function of the relative fraction (radial coordinate, from 0.1 to 9.0) and phase (polar coordinate) of the two amplitudes. Each bin contains the average uncertainty of 10 amplitude fits performed on samples generated with the same model.

$B \to R_i\gamma$ transition (which is detailed in the publication), and still apply for the exact parametrisation because the decay processes considered involve a single kaonic resonance: $K_1(1270)^+$. The two decay processes considered for this study, $K_1(1270)^+ \to K^+\rho(770)^0$ and $K_1(1270)^+ \to K^*(892)^0\pi^+$, are the same as the ones used for Fig. 1.15. This simplified model of the $K\pi\pi$ system is used to test the performance of the full amplitude fit, as well as its stability and the accuracy of the obtained uncertainties. The free parameters of the fit are the photon polarisation parameter λ_γ, and the magnitude and phase associated with the $K_1(1270)^+ \to K^+\rho(770)^0$ channel, the $K_1(1270)^+ \to K^*(892)^0\pi^+$ channel being chosen as a reference.

For each pair of relative fraction (as defined in Eq. 2.35) and phase considered, 10 simulated data sets of 8000 events are generated with $\lambda_\gamma = +1$ (close to the SM value) and fitted independently. The average uncertainty on λ_γ as a function of relative fraction and phase is shown in Fig. 2.1, where areas of higher colour saturation indicate regions with higher sensitivity to λ_γ: unlike $\mathcal{A}_{ud}$, the amplitude analysis is sensitive to λ_γ for all values of relative fractions and phases, with statistical uncertainties ranging from 0.01 to 0.05. A higher average uncertainty on λ_γ is seen for models in which the fraction of one amplitude is much larger than the other, and the maximum sensitivity is obtained for a phase difference of around $3\pi/2$ and a relative fraction of 1.5.

To evaluate the performance of the fit as a function of the photon polarisation parameter, the study is repeated for various generated values of λ_γ, and the results are shown
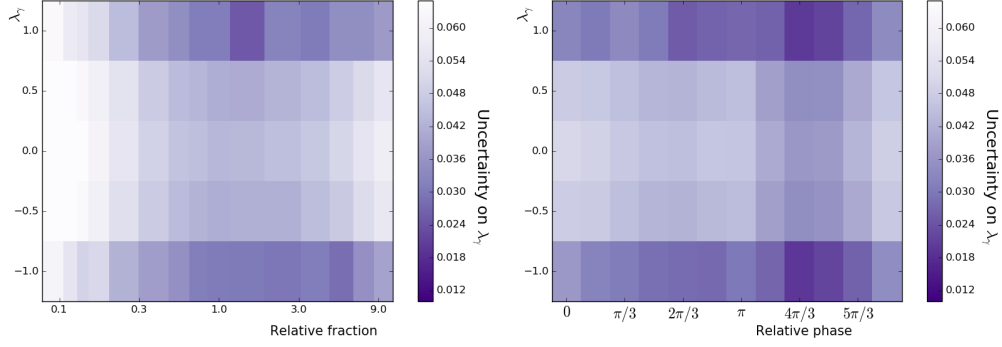
Figure 2.2 – Uncertainty on λ_γ obtained from amplitude fits of simulated samples of $B \to K_1(1270)^+\gamma$ decays governed by two amplitudes only, $K_1(1270)^+ \to K^+\rho(770)^0$ and $K_1(1270)^+ \to K^*(892)^0\pi^+$, shown as a function of the generated λ_γ value and the relative fraction (left) or phase difference (right) of the two amplitudes. Each bin contains the average uncertainty of 10 amplitude fits performed on samples generated with the same model.

in Fig. 2.2. The highest sensitivities to λ_γ are obtained for $\lambda_\gamma = \pm 1$, with increasing uncertainties observed as the generated absolute value of λ_γ decreases.

To study the fit accuracy and error estimation, 100 simulated data sets are generated and fitted for selected values of the model parameters (relative magnitude, relative phase and λ_γ). As asymmetric uncertainties are used in these fits, the quality of the parameter estimation is evaluated by checking that the distribution of the pull variable g is compatible with a standard normal distribution, where g is defined as [67]

$$g = \frac{\text{(true value)} - \text{(fit result)}}{|\text{positive uncertainty}|},\tag{2.38}$$

if (fit result) $\leq$ (true value), and

$$g = \frac{\text{(true value)} - \text{(fit result)}}{|\text{negative uncertainty}|},\tag{2.39}$$

otherwise.

The mean values and standard deviations of the fitted parameters and the associated pull parameters can be found in Table 2.4. For all models, each fit parameter has a Gaussian distribution centered on the generated value with a pull distribution of width consistent with unity, resulting in an unbiased measurement and correct error estimation.

As a final test, we study decays of B mesons to $K\pi\pi\gamma$ with a π^0 in the final state, which can have an additional source of interference from intermediate states that include a $K^*(892)$ resonance. It has been claimed that the presence of these additional interference terms results in a higher maximum possible up-down asymmetry [47], and

Table 2.4 – Results of unbinned maximum likelihood fits for 100 pseudo-experiments, for simplified two-amplitude models generated with various values of λ_γ, relative magnitudes and phases. The parameters a and ϕ stand respectively for the relative magnitude and phase between the decay with $K_1(1270)^+ \to K^+\rho(770)^0$ and the decay with $K_1(1270)^+ \to K^*(892)^0\pi^+$. The value $\phi = -0.91$ corresponds to a region of high up-down asymmetry while the values 0.82 and -2.32 correspond to a region of low up-down asymmetry. The magnitudes $a = 1.01$, 2.02 and 3.03 correspond to ratios of fractions between the two amplitudes of 0.62, 2.47 and 5.57, respectively.

| Parameter	True value	Mean value	Std deviation	μ_{pull}	σ_{pull}
a	2.02	2.017	0.03	0.10 ± 0.10	1.04 ± 0.07
ϕ	-0.91	-0.909	0.02	-0.09 ± 0.10	1.05 ± 0.07
λ_γ	1	1.002	0.04	-0.14 ± 0.10	1.09 ± 0.07
a	2.02	2.017	0.03	0.10 ± 0.10	1.03 ± 0.07
ϕ	-0.91	-0.911	0.03	0.03 ± 0.11	1.14 ± 0.08
λ_γ	0.875	0.873	0.04	0.03 ± 0.10	1.21 ± 0.08
a	2.02	2.019	0.03	0.06 ± 0.10	1.05 ± 0.07
ϕ	-0.91	-0.911	0.02	0.03 ± 0.10	0.99 ± 0.07
λ_γ	0.75	0.751	0.04	-0.05 ± 0.11	1.25 ± 0.08
a	2.02	2.020	0.04	0.01 ± 0.11	1.14 ± 0.07
ϕ	0.82	0.823	0.02	-0.09 ± 0.09	0.94 ± 0.07
λ_γ	1	1.001	0.04	-0.09 ± 0.12	1.17 ± 0.08
a	2.02	2.023	0.04	-0.06 ± 0.11	1.17 ± 0.07
ϕ	0.82	0.823	0.03	-0.13 ± 0.09	0.97 ± 0.06
λ_γ	0.875	0.870	0.04	0.11 ± 0.11	1.17 ± 0.08
a	2.02	2.022	0.04	-0.03 ± 0.09	1.03 ± 0.07
ϕ	0.82	0.822	0.03	-0.07 ± 0.09	0.92 ± 0.06
λ_γ	0.75	0.741	0.04	0.20 ± 0.09	1.03 ± 0.07
a	2.02	2.021	0.03	-0.03 ± 0.10	0.98 ± 0.07
ϕ	-2.32	-2.318	0.02	-0.11 ± 0.10	1.07 ± 0.07
λ_γ	1	1.001	0.02	-0.08 ± 0.11	1.11 ± 0.07
a	1.01	1.011	0.02	-0.06 ± 0.11	1.16 ± 0.08
ϕ	-0.91	-0.908	0.03	-0.09 ± 0.11	1.14 ± 0.07
λ_γ	1	1.002	0.04	-0.11 ± 0.11	1.12 ± 0.07
a	3.03	3.028	0.06	0.06 ± 0.10	1.03 ± 0.07
ϕ	-0.91	-0.907	0.03	-0.09 ± 0.10	1.02 ± 0.07
λ_γ	1	1.006	0.03	-0.36 ± 0.10	1.08 ± 0.07
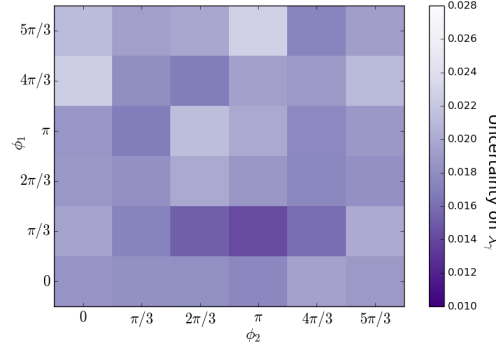
Figure 2.3 – Uncertainty on λ_γ obtained from amplitude fits of simulated samples of $B^0 \to K_1(1270)^0\gamma$ decays, shown as a function of the phase differences of the $K_1(1270)^0 \to K^+\rho(770)^-$ and $K_1(1270)^0 \to K^*(892)^0\pi^0$ decay modes relative to the $K_1(1270)^0 \to K^*(892)^+\pi^-$ decay mode, denoted as ϕ_1 and ϕ_2 respectively. Each bin contains the average uncertainty of 10 amplitude fits performed on samples generated with the same model.

thus that the analysis of $B^0 \to K^+\pi^-\pi^0\gamma$ decays could be potentially more sensitive to the photon polarisation than that of $B^+ \to K^+\pi^-\pi^+\gamma$ decays. The effect of an additional decay amplitude (and therefore additional interference terms) is studied using a $B^0 \to K_1(1270)^0\gamma$ model with three different $K_1(1270)^0$ decay channels, $K_1(1270)^0 \to K^+\rho(770)^-$, $K_1(1270)^0 \to K^*(892)^+\pi^-$, and $K_1(1270)^0 \to K^*(892)^0\pi^0$. Ten simulated data sets, each containing 8000 events, are generated for different values of the phase differences of the $K_1(1270)^0 \to K^+\rho(770)^-$ and $K_1(1270)^0 \to K^*(892)^0\pi^0$ amplitudes relative to the $K_1(1270)^0 \to K^*(892)^+\pi^-$ amplitude; all samples are generated with $\lambda_\gamma = +1$, with the decay rate for all amplitudes being equal. The uncertainty on the photon polarisation parameter for all models studied, shown in Fig. 2.3, is within the same range as seen in the two-amplitude $B^+ \to K^+\pi^-\pi^+\gamma$ model, showing that the amplitude analysis is not very sensitive to the number of interference terms in the $K\pi\pi$ system. We conclude that this amplitude analysis is sensitive to the photon polarisation parameter for all simplified models studied, for both charged and neutral decay modes.

2.4.2 Prospects using realistic models

$B^+ \to K^+\pi^-\pi^+\gamma$ decays

In light of the results of the proof-of-concept model, the most promising measurement of the photon polarisation parameter is expected to come from $B^+ \to K^+\pi^-\pi^+\gamma$ decays, which are the most abundantly reconstructed at LHCb and Belle II.

An estimate of the statistical sensitivity of a measurement of the photon polarisation from an amplitude analysis of $B^+ \to K^+\pi^-\pi^+\gamma$ decays is obtained using the model described

in Table 2.5, which provides a good approximation to the $K\pi$, $\pi\pi$ and $K\pi\pi$ invariant mass spectra observed in a data sample of 3 fb^{-1} collected by LHCb during Run 1 of the LHC [37, 53]. A total of 100 data sets of 14 000 events each, corresponding to the LHCb signal yield of Run 1 [37], are generated with $\lambda_\gamma = +1$. The fits of these samples yield a mean statistical uncertainty on λ_γ of 0.015. Figure 2.4 shows the distributions for the five variables for one of these simulated data sets along with the corresponding projections of the fit PDF. The pull means (μ_{pull}) and widths (σ_{pull}) of the complex coefficients a_k and ϕ_k, listed in Table 2.6, show that the uncertainties are mostly well estimated. The pull distribution associated with λ_γ has a mean of -0.38 ± 0.11 and a width of 1.18 ± 0.08, indicating that the obtained uncertainty on λ_γ is underestimated by about 20%, and that there is an evidence for a bias in the fitted value of λ_γ which amounts to around 40% of the statistical uncertainty. This bias cannot be linked to a specific fit parameter as the magnitude of the correlation coefficients between λ_γ and the other fit parameters typically lie below 20%. Taking into account a corrected uncertainty of 0.018, the comparison of this result with the simplified models discussed in the previous section suggests that the model complexity does not have a large effect on the statistical sensitivity to λ_γ.[1] This fact can be used to evaluate the gain in sensitivity that could be obtained by exploiting the additional 6 fb^{-1} of data that have been recorded by LHCb at a pp energy of 13 TeV in Run 2, where the B production cross-section is almost twice that at the Run 1 energy of $7-8$ TeV: assuming that a total of 50 000 signal decays are selected using the LHCb Run 1 and Run 2 data sets, the resulting corrected statistical uncertainty on the measurement of the photon polarisation parameter could reach 0.010. The bias in the value of λ_γ would have to be corrected for or accounted as a systematic uncertainty.

$B^0 \to K^+\pi^-\pi^0\gamma$ decays

$B^0 \to K^+\pi^-\pi^0\gamma$ decays can also be used to measure the photon polarisation parameter. The main difference with the $B^+ \to K^+\pi^-\pi^+\gamma$ decays used above is that the hadronic part of the decays is a priori more complex due to an additional source of interference involving $K^*(892)^0\pi^0$ and $K^*(892)^+\pi^-$ intermediate states in the decays of the heavy kaonic resonances $K_{\text{res}} \to K^+\pi^-\pi^0$.

Samples of 10 000 simulated signal events (corresponding to the number of expected $B^0 \to K^+\pi^-\pi^0\gamma$ decays to be reconstructed by Belle II with 5 ab^{-1} of integrated luminosity) are used to evaluate the sensitivity of a measurement of the photon polarisation parameter. As little is known about the hadronic system in such decays, a model of the $K\pi\pi$ system is obtained from the model used for the charged modes, assuming the relative magnitudes and phases of all allowed decay modes without a $K^*(892)\pi$ to be identical to those of the charged mode. In the case of modes with intermediate states that include a

---

[1]It is worth noting that more complex models typically entail larger systematic uncertainties, so this conclusion is valid only in what regards the statistical uncertainty obtained from the fit.

Figure 2.4 – Squared invariant-mass $(m^2_{K^+\pi^-\pi^+}, m^2_{K^+\pi^-}, m^2_{\pi^-\pi^+})$ and angular $(\cos\theta$ and $\chi)$ distributions for a single data set of $14\,000$ $B^+ \to K^+\pi^-\pi^+\gamma$ decays generated with the 14-amplitude model of Table 2.5. The red histograms represent the projections of the PDF obtained from the fit.

Table 2.5 – Model [53] used to describe the $K_{\rm res} \to K^+\pi^-\pi^+$ hadronic system in the $B^+ \to K^+\pi^-\pi^+\gamma$ sensitivity study. The table is divided in sections according to the spin-parity J^P of the $K_{\rm res}$ resonance. The mentions $[S]$ and $[D]$ refer to the wave of the heavy kaonic resonance decay. The amplitude with the S-wave decay $K_1(1270)^+ \to K^*(892)^0\pi^+$ is chosen as a reference for the magnitudes and phases.

J^P	Amplitude k	a_k	ϕ_k	Fraction (%)
1^+	$K_1(1270)^+ \to K^*(892)^0\pi^+$ [S]	1 (fixed)	0 (fixed)	15.3
	$K_1(1270)^+ \to K^*(892)^0\pi^+$ [D]	1.00	-1.74	0.6
	$K_1(1270)^+ \to K^+\rho(770)^0$	2.02	-0.91	37.9
	$K_1(1400)^+ \to K^*(892)^0\pi^+$	0.59	-0.76	7.4
1^-	$K^*(1410)^+ \to K^*(892)^0\pi^+$	0.11	0.00	7.9
	$K^*(1680)^+ \to K^*(892)^0\pi^+$	0.05	0.44	3.4
	$K^*(1680)^+ \to K^+\rho(770)^0$	0.04	1.40	2.3
2^+	$K_2^*(1430)^+ \to K^*(892)^0\pi^+$	0.28	0.00	4.5
	$K_2^*(1430)^+ \to K^+\rho(770)^0$	0.47	1.80	8.9
2^-	$K_2(1580)^+ \to K^*(892)^0\pi^+$	0.49	2.88	4.2
	$K_2(1580)^+ \to K^+\rho(770)^0$	0.38	2.44	3.2
	$K_2(1770)^+ \to K^*(892)^0\pi^+$	0.35	0.00	2.8
	$K_2(1770)^+ \to K^+\rho(770)^0$	0.08	2.53	0.2
	$K_2(1770)^+ \to K_2^*(1430)^0\pi^+$	0.07	-2.06	0.6

kaonic resonance and a pion, the branching fraction is divided equally between the $K_1(1270)^0 \to K^*(892)^0(\to K^+\pi^-)\pi^0$ and $K_1(1270)^0 \to K^*(892)^+(\to K^+\pi^0)\pi^-$ modes assuming isospin conservation. The unknown phase differences are set to the same values for both modes, which is satisfactory in the absence of a strong dependence of the sensitivity of the measurement on the phase difference. The resulting model, containing 23 amplitudes, is presented in Table 2.7 and distributions from a single simulated data set are shown in Fig. 2.5, along with the corresponding fit PDF projections.

Using the same procedure as for the charged mode, the pull means and widths of the complex coefficients a_k and ϕ_k are computed and shown in Table 2.8, and an uncertainty on the measurement of the photon polarisation of 0.016 is obtained from simulated signal samples. The pull mean of -0.64 ± 0.11 corresponds to the observation of a bias in the fitted value of λ_γ which amounts to around 60% of the statistical uncertainty obtained from the fit, where the magnitude of the correlation coefficients with the other fit parameters typically lies below 20%. This bias would have to be corrected for in the final result of the fit, or to be taken into account as a systematic uncertainty. The associated pull width of 1.19 ± 0.08 indicates that this uncertainty is also underestimated by around 20%; the corrected value of 0.019 is comparable to the one obtained with the charged mode, confirming that the additional interference patterns and the higher
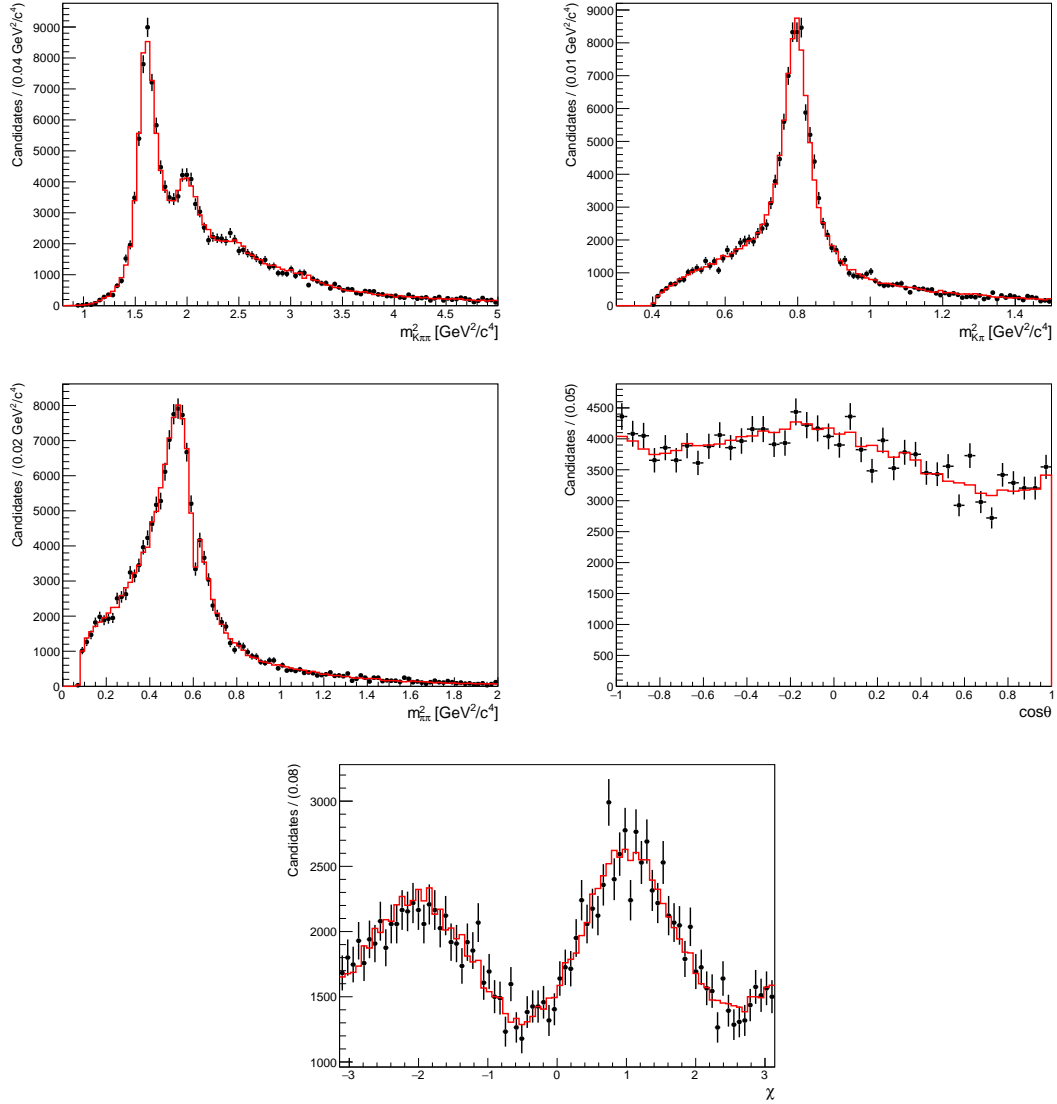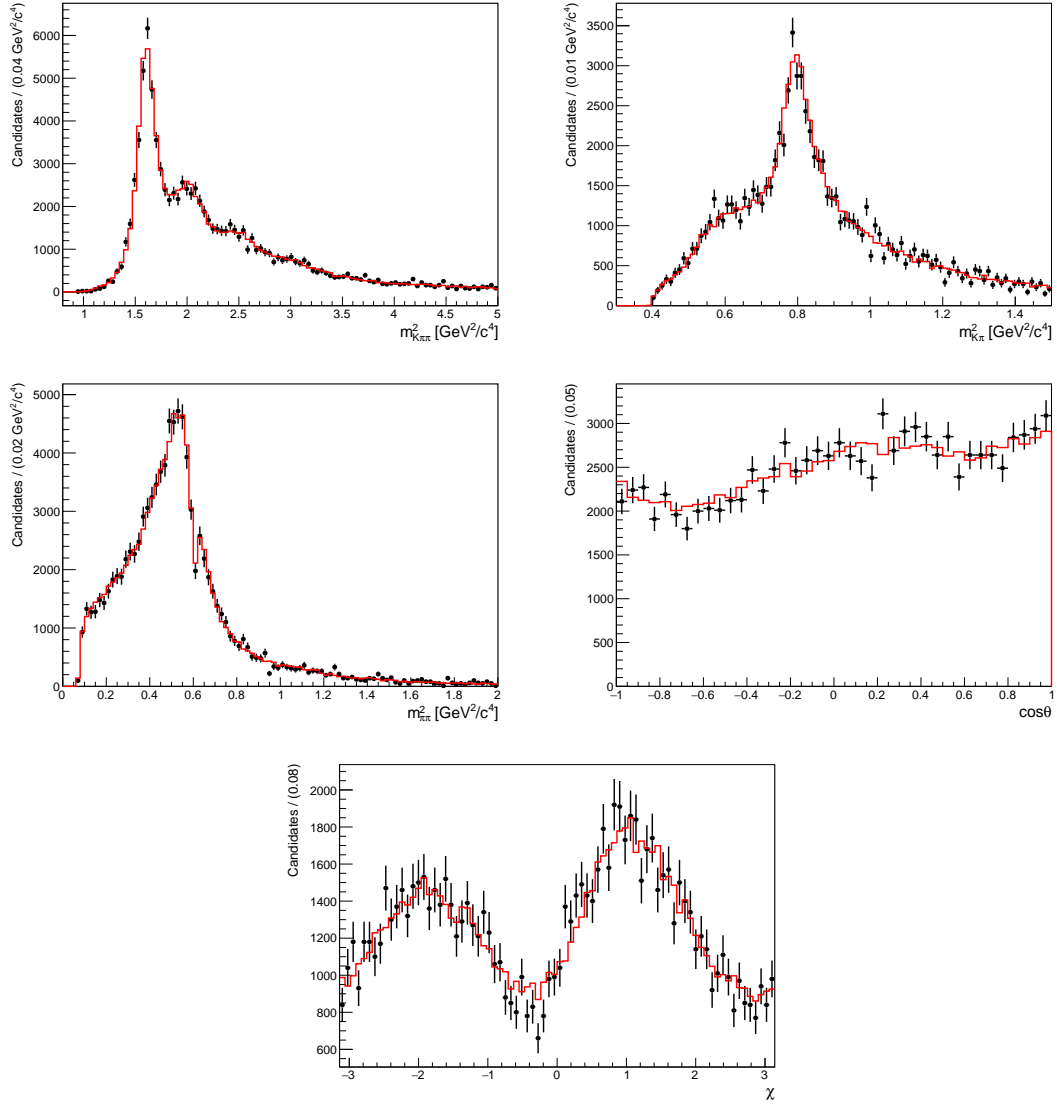
Figure 2.5 – Squared invariant-mass $(m^2_{K^+\pi^0\pi^-}, m^2_{K^+\pi^0}, m^2_{\pi^0\pi^-})$ and angular $(\cos\theta$ and $\chi)$ distributions for a single data set of $10\,000$ $B^0 \to K^+\pi^-\pi^0\gamma$ decays generated with the 23-amplitude model of Table 2.7. The red histograms represent the projections of the PDF obtained from the fit.

Table 2.6 – Pull parameters of the fit to $B^+ \to K^+\pi^-\pi^+\gamma$ samples for all magnitudes and phases relative to the amplitude with the S-wave decay $K_1(1270)^+ \to K^*(892)^0\pi^+$.

Amplitude k	Magnitude a_k		Phase ϕ_k	
	μ_{pull}	σ_{pull}	μ_{pull}	σ_{pull}
$K_1(1270)^+ \to K^*(892)^0\pi^+$ [D]	-0.04 ± 0.09	0.94 ± 0.06	0.13 ± 0.10	0.98 ± 0.06
$K_1(1270)^+ \to K^+\rho(770)^0$	0.04 ± 0.09	0.95 ± 0.06	0.40 ± 0.10	1.04 ± 0.07
$K_1(1400)^+ \to K^*(892)^0\pi^+$	-0.42 ± 0.10	1.06 ± 0.07	0.14 ± 0.09	0.90 ± 0.06
$K^*(1410)^+ \to K^*(892)^0\pi^+$	-0.44 ± 0.10	0.95 ± 0.06	0.21 ± 0.10	1.06 ± 0.07
$K^*(1680)^+ \to K^*(892)^0\pi^+$	0.20 ± 0.11	1.09 ± 0.08	0.07 ± 0.09	0.92 ± 0.06
$K^*(1680)^+ \to K^+\rho(770)^0$	0.00 ± 0.09	0.94 ± 0.06	0.07 ± 0.10	0.96 ± 0.06
$K_2^*(1430)^+ \to K^*(892)^0\pi^+$	0.52 ± 0.10	1.03 ± 0.06	0.03 ± 0.09	0.92 ± 0.06
$K_2^*(1430)^+ \to K^+\rho(770)^0$	0.14 ± 0.09	0.99 ± 0.07	0.07 ± 0.09	0.99 ± 0.07
$K_2(1580)^+ \to K^*(892)^0\pi^+$	-0.38 ± 0.10	0.98 ± 0.06	0.10 ± 0.10	1.01 ± 0.06
$K_2(1580)^+ \to K^+\rho(770)^0$	0.01 ± 0.10	0.99 ± 0.06	0.01 ± 0.10	1.03 ± 0.07
$K_2(1770)^+ \to K^*(892)^0\pi^+$	0.09 ± 0.09	0.95 ± 0.06	0.21 ± 0.11	1.01 ± 0.07
$K_2(1770)^+ \to K^+\rho(770)^0$	-0.09 ± 0.09	0.92 ± 0.06	0.16 ± 0.09	1.00 ± 0.06
$K_2(1770)^+ \to K_2^*(1430)^0\pi^+$	0.29 ± 0.10	0.88 ± 0.07	0.13 ± 0.09	0.93 ± 0.06

complexity of the $K\pi\pi$ system do not provide a significant improvement on the precision of the measurement. As a larger number of signal events is expected for the charged mode, our method would perform better using these decays, but the amplitude analysis of the neutral mode would provide a very interesting independent measurement of the λ_γ parameter.

2.4.3 Implications of a measurement of λ_γ

Using Eq. 1.37, the uncertainty on the measurement of the photon polarisation λ_γ can be translated in terms of constraints on the Wilson coefficients C_7 and C_7'. An expression in terms of C_7 and C_7' would also be possible if the corrections $h_{\mathrm{R/L}}^i$ were such that $h_{\mathrm{R/L}}^i/g^i(0)$ could be considered process independent, provided some theoretical input on these corrections is given. This potential presence of process-dependent corrections makes λ_γ less interesting to assess the size of NP effects with respect to other cleaner observables such as $\alpha_\gamma^{\Lambda_b^0 \to \Lambda^0\gamma}$ (which is discussed in Sec. 1.2.2), but its high statistical power, demonstrated in this study, compensates for that limitation, and the new constraints could compare to those already set by the $B^0 \to K^{*0}e^+e^-$ angular observables, or the inclusive $B \to X_s\gamma$ branching fraction shown in Fig. 1.8. Another interesting feature of λ_γ is that its dependence in C_7 and C_7' is complementary to previously cited measurements and it could provide crucial information to solve some ambiguities (such as the one on $\mathcal{Re}(C_7')$)

Table 2.7 – Model used to describe the $K_{\text{res}} \to K^+\pi^-\pi^0$ hadronic system in the $B^0 \to K^+\pi^-\pi^0\gamma$ sensitivity study. The table is divided in sections according to the spin-parity J^P of the K_{res} resonance. The mentions [S] and [D] refer to the wave of the heavy kaonic resonance decay. The amplitude with the S-wave decay $K_1(1270)^0 \to K^*(892)^0\pi^0$ is chosen as a reference for the magnitudes and phases.

J^P	Amplitude k	a_k	ϕ_k	Fraction (%)
	$K_1(1270)^0 \to K^*(892)^0\pi^0$ [S]	1(fixed)	0 (fixed)	8.0
	$K_1(1270)^0 \to K^*(892)^+\pi^-$ [S]	1.01	0.00	8.0
	$K_1(1270)^0 \to K^*(892)^+\pi^-$ [D]	0.98	-1.74	0.3
1^+	$K_1(1270)^0 \to K^*(892)^0\pi^0$ [D]	0.99	-1.74	0.3
	$K_1(1270)^0 \to K^+\rho(770)^-$	2.86	-0.91	39.7
	$K_1(1400)^0 \to K^*(892)^+\pi^-$	0.60	-0.76	3.8
	$K_1(1400)^0 \to K^*(892)^0\pi^0$	0.59	-0.76	3.8
	$K^*(1410)^0 \to K^*(892)^+\pi^-$	0.11	0.00	3.9
	$K^*(1410)^0 \to K^*(892)^0\pi^0$	0.11	0.00	3.9
1^-	$K^*(1680)^0 \to K^*(892)^+\pi^-$	0.05	0.44	1.7
	$K^*(1680)^0 \to K^*(892)^0\pi^0$	0.05	0.44	1.7
	$K^*(1680)^0 \to K^+\rho(770)^-$	0.06	1.40	2.4
	$K_2^*(1430)^0 \to K^*(892)^+\pi^-$	0.27	0.00	2.3
2^+	$K_2^*(1430)^0 \to K^*(892)^0\pi^0$	0.27	0.00	2.3
	$K_2^*(1430)^0 \to K^+\rho(770)^-$	0.63	1.80	8.9
	$K_2(1580)^0 \to K^*(892)^+\pi^-$	0.49	2.88	2.2
	$K_2(1580)^0 \to K^*(892)^0\pi^0$	0.49	2.88	2.2
	$K_2(1580)^0 \to K^+\rho(770)^-$	0.54	2.44	3.2
2^-	$K_2(1770)^0 \to K^*(892)^+\pi^-$	0.35	0.00	1.5
	$K_2(1770)^0 \to K^*(892)^0\pi^0$	0.35	0.00	1.5
	$K_2(1770)^0 \to K^+\rho(770)^-$	0.11	2.53	0.2
	$K_2(1770)^0 \to K_2^*(1430)^+\pi^-$	0.07	-2.06	0.3
	$K_2(1770)^0 \to K_2^*(1430)^0\pi^0$	0.07	-2.06	0.3

Table 2.8 – Pull parameters of the fit to $B^0 \to K^+\pi^-\pi^0\gamma$ samples for all magnitudes and phases relative to the amplitude with the S-wave decay $K_1(1270)^0 \to K^*(892)^0\pi^0$.

Amplitude k	Magnitude a_k		Phase ϕ_k	
	μ_{pull}	σ_{pull}	μ_{pull}	σ_{pull}
$K_1(1270)^0 \to K^*(892)^+\pi^-$ [S]	-0.02 ± 0.10	1.10 ± 0.10	-0.18 ± 0.09	0.95 ± 0.06
$K_1(1270)^0 \to K^*(892)^+\pi^-$ [D]	-0.13 ± 0.09	0.99 ± 0.06	-0.14 ± 0.09	0.97 ± 0.06
$K_1(1270)^0 \to K^*(892)^0\pi^0$ [D]	0.01 ± 0.11	1.12 ± 0.08	0.05 ± 0.11	1.14 ± 0.08
$K_1(1270)^0 \to K^+\rho(770)^0$	0.31 ± 0.10	1.07 ± 0.07	-0.16 ± 0.09	0.96 ± 0.06
$K_1(1400)^0 \to K^*(892)^+\pi^-$	0.27 ± 0.10	1.03 ± 0.07	-0.23 ± 0.10	1.04 ± 0.07
$K_1(1400)^0 \to K^*(892)^0\pi^0$	0.20 ± 0.09	0.96 ± 0.06	-0.31 ± 0.09	0.95 ± 0.06
$K^*(1410)^0 \to K^*(892)^+\pi^-$	0.01 ± 0.09	1.01 ± 0.07	-0.09 ± 0.09	0.95 ± 0.06
$K^*(1410)^0 \to K^*(892)^0\pi^0$	0.19 ± 0.10	1.03 ± 0.07	-0.09 ± 0.08	0.89 ± 0.06
$K^*(1680)^0 \to K^*(892)^+\pi^-$	0.32 ± 0.11	1.15 ± 0.08	-0.19 ± 0.10	1.06 ± 0.07
$K^*(1680)^0 \to K^*(892)^0\pi^0$	0.09 ± 0.11	1.10 ± 0.07	-0.21 ± 0.09	0.97 ± 0.06
$K^*(1680)^0 \to K^+\rho(770)^-$	0.15 ± 0.10	1.09 ± 0.07	-0.23 ± 0.09	1.01 ± 0.07
$K_2^*(1430)^0 \to K^*(892)^+\pi^-$	0.24 ± 0.10	1.05 ± 0.07	-0.33 ± 0.09	0.95 ± 0.06
$K_2^*(1430)^0 \to K^*(892)^0\pi^0$	0.08 ± 0.08	0.90 ± 0.06	-0.27 ± 0.09	0.89 ± 0.06
$K_2^*(1430)^0 \to K^+\rho(770)^-$	0.25 ± 0.11	1.09 ± 0.07	-0.24 ± 0.08	0.93 ± 0.06
$K_2(1580)^0 \to K^*(892)^+\pi^-$	0.05 ± 0.10	1.03 ± 0.07	-0.07 ± 0.08	0.91 ± 0.06
$K_2(1580)^0 \to K^*(892)^0\pi^0$	0.12 ± 0.09	0.98 ± 0.06	-0.25 ± 0.09	0.96 ± 0.06
$K_2(1580)^0 \to K^+\rho(770)^-$	0.05 ± 0.10	1.06 ± 0.07	0.09 ± 0.08	0.90 ± 0.06
$K_2(1770)^0 \to K^*(892)^+\pi^-$	0.07 ± 0.10	1.05 ± 0.07	0.04 ± 0.09	0.99 ± 0.07
$K_2(1770)^0 \to K^*(892)^0\pi^0$	0.18 ± 0.09	0.91 ± 0.06	-0.13 ± 0.09	0.92 ± 0.06
$K_2(1770)^0 \to K^+\rho(770)^-$	0.07 ± 0.09	0.97 ± 0.06	-0.03 ± 0.09	0.98 ± 0.06
$K_2(1770)^0 \to K_2^*(1430)^+\pi^-$	-0.10 ± 0.10	1.03 ± 0.07	-0.07 ± 0.10	0.98 ± 0.07
$K_2(1770)^0 \to K_2^*(1430)^0\pi^0$	0.10 ± 0.09	0.98 ± 0.06	-0.12 ± 0.10	1.03 ± 0.07

that result from the combination of all previous constraints. In all cases, the contributions from $h^i_{\mathrm{R/L}}$ will have to be studied theoretically in order to size these contributions and estimate how much they depend on the handedness of the photon, and on the process considered. In case these contributions were found to be small but not negligible, they would have to be taken into account as nuisance parameters.

A more precise measurement of C_7 could help understand the long-range contributions from $c\bar{c}$ loops. By identification, this would place better constraints on the long-range $c\bar{c}$ contributions adding up to the C_9 Wilson coefficient which is involved in the hamiltonian of $b \to sl^+l^-$ transitions, and help for example with the interpretation of R_{H_s} ratios.

2.4.4   Conclusions, limits and foreseen improvements

The performed studies demonstrate that, in the ideal case of a background-free sample without distortions due to experimental effects, and ignoring the differences between non-factorisable hadronic parameters between the resonances in the $K\pi\pi$ system, this amplitude analysis allows the measurement of the photon polarisation with a statistical uncertainty of around 0.010 on a sample of 50 000 $B^+ \to K^+\pi^-\pi^+\gamma$ decays corresponding to the signal statistics assumed for LHCb in Runs 1 and 2. Belle II is assumed to reconstruct about 10 000 $B^0 \to K^+\pi^-\pi^0\gamma$ decays with a data set corresponding to an integrated luminosity of $5\,\mathrm{ab}^{-1}$. The analysis of these data could also determine independently the photon polarisation with a statistical uncertainty of the order of 0.019, again ignoring background and experimental effects, as well as non factorisable hadronic uncertainties.

It has to be stressed that the presence of background and the resolution of the detector might degrade the measurement. These effects, which depend heavily on the detector and data-taking conditions, will have to be estimated carefully when applying the method on real data.

Additionally, in the fit to real events, the signal model will have to be improved in order to best describe the data, and the study presented in Sec. 2.4.2 will have to be repeated with the final model to check for intrinsic biases. For example, the changes will include using more realistic lineshapes to describe some of the decay processes, which are not well modeled by Breit-Wigner distributions. This will be developed in Chapter 5. The description of the spin factor for the weak decay $B \to R_i\gamma$ will also be improved by using the expressions given in Ref. [68], in which all the possible covariant terms have been properly taken into account. For a photon with a polarisation vector ϵ and a resonance

R_i with spin J_i, parity P_i and polarisation vector ϵ', these expressions read as:

$$J_i^{P_i} = 1^+ :$$
$$S_{\mathrm{R/L}}^i = \mp i \epsilon_{\mu\nu\rho\sigma} \epsilon^{*\mu} \epsilon'^{*\nu} P^\rho q^\sigma + ((\epsilon^* \cdot \epsilon'^*)(P \cdot q) - (\epsilon^* \cdot P)(\epsilon'^* \cdot q)), \tag{2.40}$$
$$J_i^{P_i} = 1^- :$$
$$S_{\mathrm{R/L}}^i = -i \epsilon_{\mu\nu\rho\sigma} \epsilon^{*\mu} \epsilon'^{*\nu} P^\rho q^\sigma \pm ((\epsilon^* \cdot \epsilon'^*)(P \cdot q) - (\epsilon^* \cdot P)(\epsilon'^* \cdot q)), \tag{2.41}$$
$$J_i^{P_i} = 2^+ :$$
$$S_{\mathrm{R/L}}^i = -i \epsilon_{\mu\nu\rho\sigma} \epsilon^{*\mu} \epsilon'^{*\nu\lambda} P_\lambda P^\rho q^\sigma \pm \epsilon^{*\mu}(\epsilon'^*_{\mathrm{R/L}\,\mu\sigma}(P \cdot q) - (P_\mu \epsilon'^*_{\sigma\nu} q^\nu))P^\sigma, \tag{2.42}$$

with $P = p_B + p'$ and $q = p_B - p'$, where p_B and p' refer to the four-momenta of the B meson and of the resonance R_i, respectively. Here, the "$\mp$" ("$\pm$") sign means "$-$" ("$+$") for index R and "$+$" ("$-$") for index L. The expression for a resonance of spin-parity 2^- is not given in this reference, but it can be obtained by taking the same covariant expressions as in Eq. 2.42 and imposing the relation of Eq. 1.36, which gives:

$$J_i^{P_i} = 2^- :$$
$$S_{\mathrm{R/L}}^i = \mp i \epsilon_{\mu\nu\rho\sigma} \epsilon^{*\mu} \epsilon'^{*\nu\lambda} P_\lambda P^\rho q^\sigma + \epsilon^{*\mu}(\epsilon'^*_{\mathrm{R/L}\,\mu\sigma}(P \cdot q) - (P_\mu \epsilon'^*_{\sigma\nu} q^\nu))P^\sigma, \tag{2.43}$$

These new expressions will change the interference pattern between different resonances, and will add a dependence in P and q that was not present in the study shown in this chapter. However, the angular and invariant mass squared distributions for single resonances are not strongly affected by these changes. The sensitivity, which appeared to depend loosely on the signal model, is not expected to change.

3 Experimental setup

The B^+ mesons studied in this thesis come from the hadronization of $b\bar{b}$ pairs produced in proton-proton (pp) collisions at the Large Hadron Collider, and their decays are recorded using a detector optimized for the study of b- and c-flavoured hadrons: the LHCb experiment.

3.1 The CERN LHC

Hosted at the European Laboratory for Particle Physics (CERN), the Large Hadron Collider (LHC) is a particle accelerator and collider consisting of two 27 km long rings in which bunches of protons or heavy ions circulate in opposite directions and collide in four interaction points.

The LHC has been designed to produce pp collisions at a centre-of-mass energy of 14 TeV with an instantaneous luminosity of 10^{34} cm^{-2} s^{-1}. Starting from 2010, the LHC actually delivered pp collisions at a lower centre-of-mass energy of 7 TeV up until the end of 2011, and then operated at 8 TeV in 2012. During this first data-taking period (Run 1), the consecutive proton bunch crossings were separated by 50 ns. At the end of 2012, the machine underwent a long technical stop before resuming in 2015 with proton bunches separated by 25 ns at a centre-of-mass energy of 13 TeV, which was kept constant during the entire Run 2 until the end of 2018. After a new long technical stop, the collider is expected to reach its design centre-of-mass energy of 14 TeV for the duration of Run 3, from 2021 to 2024.

The LHC is the last piece of an accelerator complex made of several machines in which the protons or heavy ions are accelerated at successively higher energies. The different steps of the proton cycle, shown in Fig. 3.1, are the following:

- Ionization of the hydrogen contained in a simple gas bottle by stripping away the electrons of hydrogen atoms thanks to an electric field.

- First acceleration in the Linear Accelerator 2 (LINAC 2) up to an energy of 50 MeV.
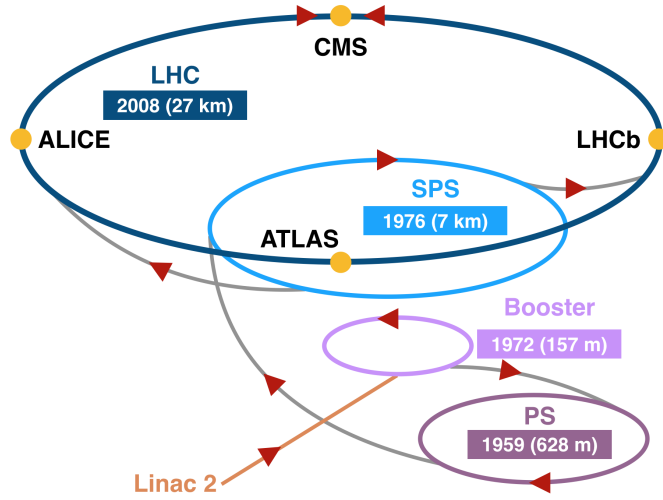
Figure 3.1 – Scheme of the LHC accelerator complex dedicated to the *pp* collisions in LHC Runs 1 and 2. The direction of travel of the protons is indicated by red arrows.

- Acceleration in the Booster, a small synchrotron which boosts the protons to 1 GeV.

- Acceleration in the Proton Synchrotron (PS) in which the protons reach 26 GeV.

- Acceleration in the Super Proton Synchrotron (SPS) up to an energy of 450 GeV, and separation into two beams that are injected separately in the LHC, in opposite directions.

- Acceleration in the LHC where the protons acquire their final energy and are collided in the interaction points.

Each of the four LHC interaction points hosts one of the large CERN experiments: ALICE, which exploits mainly heavy ion collisions, ATLAS and CMS, which are general purpose experiments, and LHCb, which is dedicated to the *indirect* searches of NP in heavy flavour physics phenomena, especially *CP* violation and measurements of observables in rare decays of hadrons with a *b* or a *c* quark.

3.2 The LHCb detector

The LHCb experiment is a single-arm forward spectrometer which has been designed to exploit the specific features of the *b*-hadron decays in the conditions of *pp* collisions [69].

At the LHC, the main production mechanism of $b\bar{b}$ pairs in *pp* collisions is gluon fusion. This production mode is characterized by a high momentum exchange between partons, resulting in the $b\bar{b}$ pairs to be emitted mainly in the direction of the higher momentum parton, at a small angle with respect to the beam. In order the exploit this particular

topology efficiently, the LHCb detector was built to cover the region of most likely emission of these pairs in a pseudorapidity (η) range between 2 and 5, where $\eta = -\ln[\tan(\theta/2)]$ and θ is the angle with respect to the direction of the beam. This corresponds to an angular coverage of 15 to 300 (250) mrad in the bending (non-bending) plane of the magnet. However, at the centre-of-mass energies delivered by the LHC, the fraction of inelastic pp collisions leading to the production of a b-hadron is only 1% or less, meaning that a strong discrimination must be achieved to separate the decays of interest from backgrounds coming from the pp collisions.

A specificity of the b and c hadrons is that they have relatively long lifetimes (of the order of 1.5 ps for the B^+, B^0, B^0_s and Λ^0_b hadrons, 1 ps for the D^+ meson, 0.5 ps for the D_s meson and 0.4 ps for the D^0 meson), so the point where they are produced (the primary vertex) is well separated from the point where they decay (the secondary vertex). In the LHC conditions, the B^+ mesons for example typically travel a distance of the order of one centimeter before decaying, whereas most of the other pp collision products are stable or decay promptly. The main feature of an experimental setup dedicated to the study of b-hadron decays is therefore an excellent vertex resolution which allows the separation of the secondary from the primary vertices.

In this context, operating directly at the luminosity delivered by the LHC to ATLAS and CMS would be very challenging because it would imply multiple pp collisions in the same event (pile-up), resulting in a large number of decay products in the detector which would make the separation of vertices very difficult. Additionally, this high multiplicity would create severe radiation damage in the detector and degrade the capabilities of its components. Therefore, a specific beam focusing method is used in order to operate at an instantaneous luminosity of $L = 4 \times 10^{32}$ cm^{-2} s^{-1} at the LHCb interaction point, so that the most probable number of pp interactions per bunch crossing is close to one [70]. At 13 TeV of centre-of-mass energy, the cross-section for $b\bar{b}$ pair production is around 600 μb [71], so the luminosity delivered to LHCb still allows the production of 10^{12} $b\bar{b}$ pairs per year at this energy.

Essential features for the study of b and c hadrons include:

- A high vertex resolution as explained above.

- A good particle identification to enable the precise characterization of the daughter particles.

- An excellent momentum resolution to measure masses accurately and reject backgrounds coming from wrong combinations of reconstructed objects (combinatorial background).

- A performant trigger system to reject background and select the decays of interest.
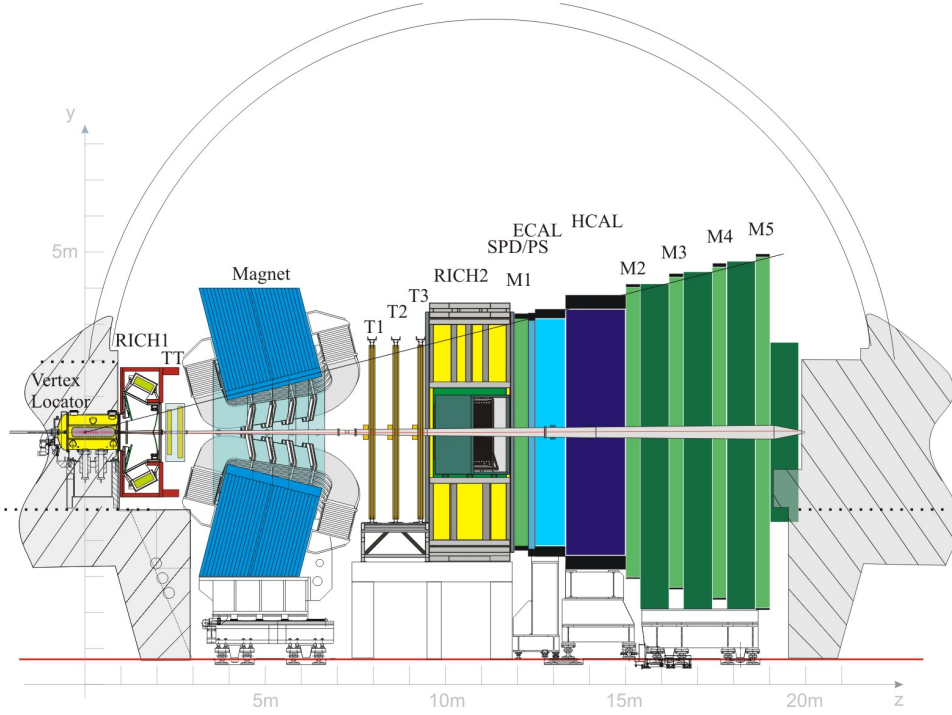
Figure 3.2 – Schematic layout of the LHCb detector and its system of coordinates [72].

The layout of the LHCb experiment, which is optimized to comply with these constraints, is shown in Fig. 3.2. The LHCb coordinate system has its origin at the nominal pp interaction point. The z axis is oriented in the direction of the detector, from the origin to the muon stations [72]. The vertical y axis points upwards and the horizontal x axis points outside of the LHC rings.

LHCb is made of two main subsystems:

- The **tracking system**, described in Sec. 3.3, provides precise information about the trajectory of the charged particles. It comprises the Vertex Locator (VELO), the magnet, the silicon tracker (ST) and the outer tracker (OT).

- The **particle identification system**, discussed in Sec. 3.4, is composed of the Ring Imaging Cherenkov detectors, the calorimeter systems and the muon systems.

3.3   The tracking system

The tracking system is dedicated to the reconstruction of charged particles and provides precise information about their charge and momentum. It allows a high momentum and vertex resolution for c and b hadrons. Charged particles are reconstructed as tracks from the hits in several sub-detectors before and after a dipole magnet that bends their

trajectory according to their momentum-to-charge ratio.

Upstream of this magnet, the tracking system is composed of the Vertex Locator (VELO) and the Tracker Turicensis (TT), both using silicon technology. The tracker placed downstream of the magnet consists of three tracking stations, each of them with an inner and an outer part. The Inner Tracker, situated at low angle with respect to the beam pipe, is in a zone of high occupancy for which a high resolution is needed. The Outer Tracker which surrounds the inner part is in a lower occupancy region, which makes a lower resolution acceptable.

During Run 1, the LHCb tracking system achieved a relative momentum resolution $\delta p/p$ of 0.4% for tracks of 5 GeV/c and of 0.6% for tracks of 100 GeV/c.

3.3.1   The Vertex Locator (VELO)

The main objective of the VELO (Fig. 3.3) is to separate the b- or c-hadron vertices (secondary vertices) from the pp collision vertex (primary vertex, PV), which are typically 0.01 to 1 cm away from each other. As the positions of the primary vertices are spread along the z axis, the VELO has been designed to cover the region $|z| < 10.6$ cm around the nominal interaction point. The information from the backward region $z < 0$ is also used to identify high multiplicity events due to pile-up.

The VELO is made of two sets of 21 half-circular silicon stations which provide radial r and azimuthal ϕ coordinates of the hits. These stations are assembled in order to be as close as possible to the beam, inside a vacuum vessel in which they are mounted on two movable supports. In this way, the VELO can be opened during LHC injection and dumping phases such that the detector is 4 cm away from the beam, and it can be closed for data-taking with sensors only 8 mm away from the beam. When the VELO is closed, there is a small overlap between the stations on each side of the beam which is useful for alignment.

Each 300 μm thick silicon sensor measures either the radial or azimuthal coordinate. The r and ϕ coordinates, as well as the z coordinate of the station, give the 3D localisation of a hit with a resolution that ranges from 5 to 25 μm, depending on the track angle and the width of the silicon strips (which are finer towards the central region) at the hit position.

This results in an offline-reconstructed PV resolution of the order of 40 μm in the transverse (x, y) plane.
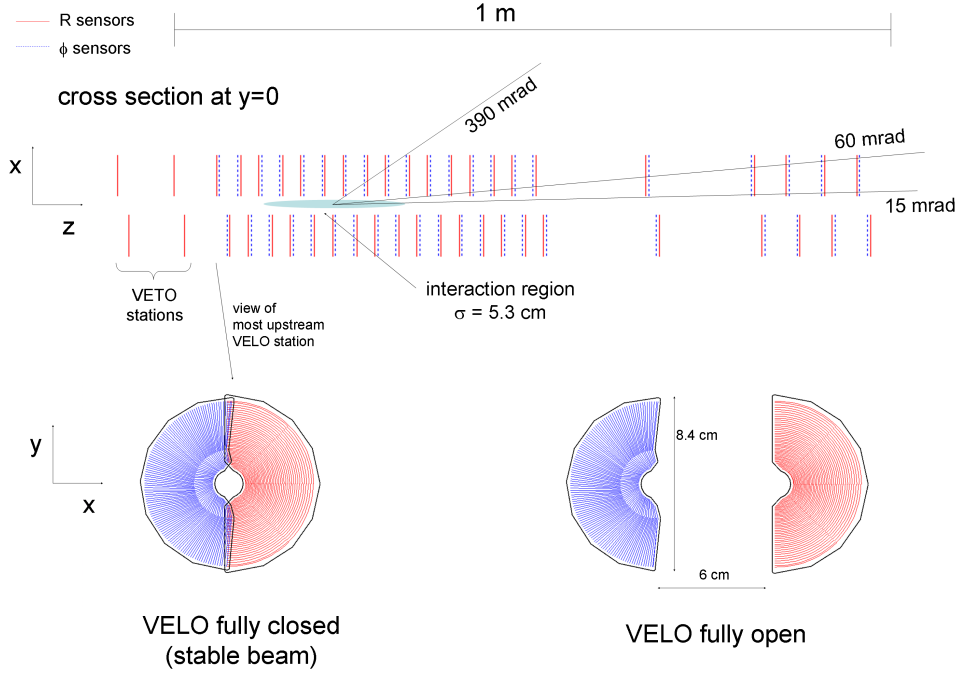
Figure 3.3 – Sketch of individual r and ϕ stations, and of their arrangement inside the vertex locator (VELO).

3.3.2 The dipole magnet

The role of the magnet is to produce the magnetic field allowing a precise determination of the momentum of the charged particles. The polarity of the dipole magnet can be inverted during data taking in order to cancel detection asymmetry in tracking which could affect the CP asymmetry measurements.

The magnet is made of two conical shaped non super-conducting coils of 27 tons each, mounted on a 1450-ton iron frame.

The integrated magnetic field of $4\,\mathrm{Tm}$ in the region $0 < z < 10\,\mathrm{m}$ has been chosen in order to allow a good momentum resolution of the tracking system. To ensure a good tracking performance, this field has to be known precisely and has therefore been measured by an array of Hall probes and parametrized in the whole volume of the detector.

3.3.3 The silicon tracker

The silicon tracker is dedicated to the detection of hits of charged particles in the regions of high occupancy after the vertex locator. It is composed of two parts situated

respectively upstream and downstream of the magnet: the Tracker Turicensis (TT) and the Inner Tracker (IT). These two sub-detectors make use of silicon microstrip sensors which fulfill three critical requirements:

- An excellent spatial resolution (of the order of $50\,\mu$m for sensors with a pitch of $200\,\mu$m).

- A good signal-to-noise ratio, which reduces the probability of reconstructing *ghost* tracks (tracks that are not originating from a true particle).

- A high radiation tolerance, which is essential in the regions covered by the TT (where the occupancy in minimum bias events is of 5×10^{-2}) and the IT (where this occupancy is 1.5×10^{-2}).

In order to avoid the superposition of consecutive events, a fast shaping time of $25\,$ns has been chosen for both silicon trackers.

The tracker turicensis   The TT is placed before the magnet and has been optimized for the detection of low momentum tracks deflected outside of acceptance by the magnet. It is made of two pairs of two $150 \times 130\,$cm^2 layers in the plane transverse to the beam axis with parallel silicon microstrips. In order to allow a 2D measurement of the hit position, the two outside planes have vertical microstrips while the strips in the two middle planes are inclined by a stereo angle of $+5°$ and $-5°$ with respect to the vertical axis, as shown in Fig. 3.4. It covers a total active area of $8.4\,$m^2.

The inner tracker   Situated at the centre of the outer tracker, the IT covers only 2% of the surface of the tracking system after the magnet, but it detects 20% of the tracks because of the larger density close to the beam pipe. This area corresponds to regions in which the cheaper straw-tube technology used for the outer tracker cannot cope with the high occupancy. The IT is made of three stations along the beam direction, each of them being a replica of a structure of 4 detector boxes placed in a cross shape around the beam pipe, as illustrated in Fig. 3.5. Each of these detector boxes has four detection layers (two vertical and two tilted as for the TT) with 7 detector modules each.

To avoid secondary interactions which increase the number of tracks and hence reduce the performance of the tracking system, the material budget in the inner region is reduced to a minimum. Hence, $320\,\mu$m-thick silicon sensors are used in the top and bottom layers while $410\,\mu$m-thick sensors are placed in the side boxes.
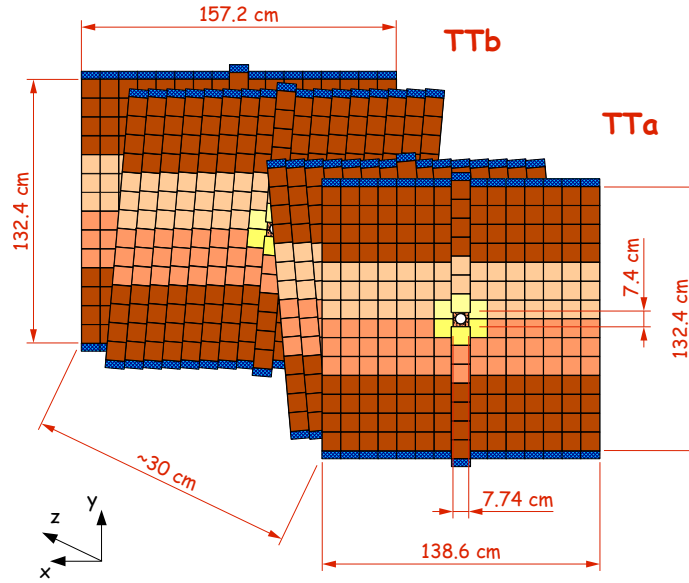
Figure 3.4 – Layout of the Tracker Turicensis [73].
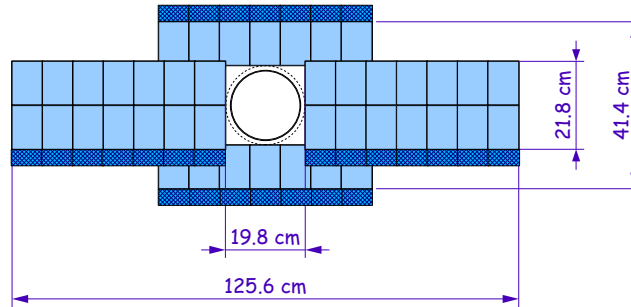
Figure 3.5 – Layout of an Inner Tracker station [73].

3.3.4 The outer tracker

The OT is a gaseous straw-tube detector which measures the hits outside of the IT. The position of the hit is obtained from the drift time of the ions which are freed when a charged particle goes through the tube.

The OT is also made of three stations which consist of $6 \times 5\,\mathrm{m}^2$ pannels surrounding the IT stations. Each of the OT stations has 72 modules composed of two layers of $4.9\,\mathrm{mm}$ diameter tubes as indicated on Fig. 3.6. All these tubes (around $55\,000$ in total) have an inner gold-plated tungsten wire which acts as a cathode to collect the positively charged ions, while the outer region allows fast signal transmission and provides shielding. The tubes are filled with a mixture of argon (70%) and CO_2 (30%) in order to ensure a
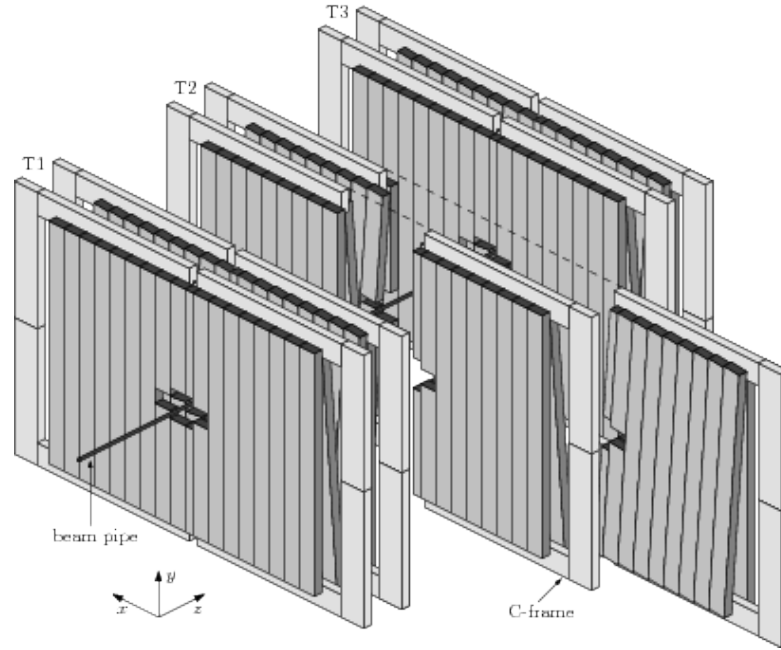
Figure 3.6 – Layout of the Outer Tracker [73]. The cross-shape around the beam pipe leaves space for the Inner Tracker.

drift-time below 50 ns, a spatial resolution of 200 µm and resistance against ageing. This lower resolution with respect to that of the IT is compensated by the fact that straw tubes are cheaper and easier to handle, and provides sufficient tracking performance in the region of low occupancy.

3.3.5 Track reconstruction

Several types of tracks (illustrated in Fig. 3.7) can be distinguished depending on the sub-detectors in which they are reconstructed:

- The **VELO tracks** are seen only in the VELO by both r and ϕ sensors. These tracks can have a large polar angle and are used mainly for the reconstruction of primary vertices.

- The **T tracks** are only in T stations (each of them made of an OT station and its inner IT station) and correspond mostly to the decays of very long-lived particles or to secondary interactions in the detector.

- The **upstream tracks**, reconstructed in the VELO and TT only, have a low momentum and fly out of acceptance. They are rarely used because of poor momentum resolution.
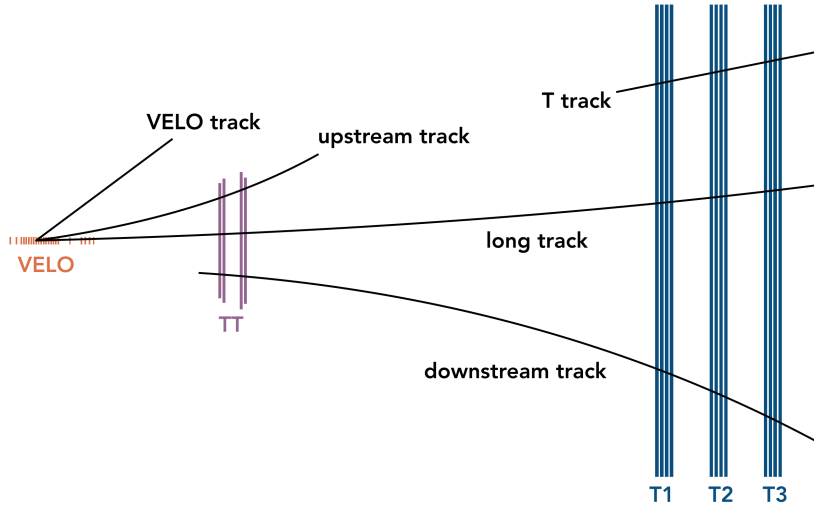
Figure 3.7 – Sketch showing the different categories of tracks reconstructed in the LHCb detector [74].

- The **downstream tracks**, in TT and T stations, correspond mostly to decay products of long-lived particles such as K_S^0 or Λ.

- The **long tracks** are seen in all the sub-detectors of the tracking system and are the most commonly used in data analyses.

The track reconstruction algorithm depends on the type of tracks [75]. In Run 1, the reconstruction of long tracks in LHCb was done in three steps:

- First, a search for VELO hits that are compatible with a straight line is performed and VELO tracks are formed.

- These tracks are associated with hits from the T stations (IT or OT) and then from the TT using an extrapolation approach. This matching is time consuming but avoids the use of tracking stations inside the magnet, which would be difficult to operate due to a high occupancy caused by the low-momentum particles from secondary interactions trapped in the magnetic field. Limiting the number of tracking stations also keeps the material budget low.

- The VELO tracks and selected hits in the T stations are fitted together with compatible TT hits and their parameters are estimated with a χ^2 minimization.

In Run 2, the timing of the track reconstruction has been improved significantly by reconstructing track segments using both the VELO and TT information, and then by extrapolating these tracks (whose direction is better defined) to the T stations for the hit search.

3.4 The particle identification system

Several crucial measurements in flavour physics rely on the precise knowledge of the identity of particles. For example, in certain signal decays involving charged kaons, protons or muons, charged pions constitute a major background. In radiative B decays, it is also of foremost importance to separate photons from electrons and π^0 in order to avoid contaminations by charmless decays or decays with a converted photon (to an e^+e^- pair). Assigning an identity to the measured particles is the main goal of the particle identification system, which consists of three parts: the Ring Imaging Cherenkov detectors (RICH) which identify the different charged hadrons species, the calorimeters which differentiate the hadrons from photons and electrons, and the muon system which detects the muons.

3.4.1 The Ring Imaging Cherenkov detectors

Two RICH detectors are used in LHCb in order to identify the charged particles. Their main objective is to discriminate between pions, kaons and protons in a large momentum range, using a technology based on the Cherenkov effect. When a charged particle traverses a medium characterized by a refraction index n with a speed $v > c/n$, where c is the speed of light in vacuum, it emits electromagnetic radiation at an angle θ with respect to its flight direction:

$$\cos\theta = \frac{c}{n\,v}\,.$$

(3.1)

These Cherenkov photons are reflected by a combination of flat and spherical mirrors out of LHCb acceptance where they are captured by Hybrid Photon Detectors (HPDs), which are protected from the residual magnetic field by iron screens. The information from the HPDs is then used to reconstruct the Cherenkov light emission angles, which are given as an input to the particle identification algorithms.

The momentum spectrum is softer at large angles with respect to the beam, and harder at small angles. In order to cover the full momentum range, two RICH detectors are used with radiators characterized by different refraction indices.

The RICH1 detector, upstream of the magnet, covers the full LHCb acceptance, in the low momentum range $(1 - 60\,\mathrm{GeV}/c)$. It uses $\mathrm{C_4F_{10}}$ as radiator. In Run 1, aerogel was also used in RICH1 to improve the very low momentum identification, but it was removed in Run 2 because its contribution was worse than expected and it was difficult to integrate in the Run 2 trigger scheme due to the large rings produced and the large

number of Cherenkov photons which were consuming too much CPU time [76].

The RICH2 detector is placed downstream of the magnet, between the tracking stations and the calorimeters. Its coverage is limited to the inner regions, with an acceptance going from ± 15 mrad to ± 200 mrad in the bending plane, and to ± 100 mrad in the non-bending plane. Its design has been optimized for particles with higher momenta, between 15 and 100 GeV/c. The CF_4 radiator has a tunable refraction index.
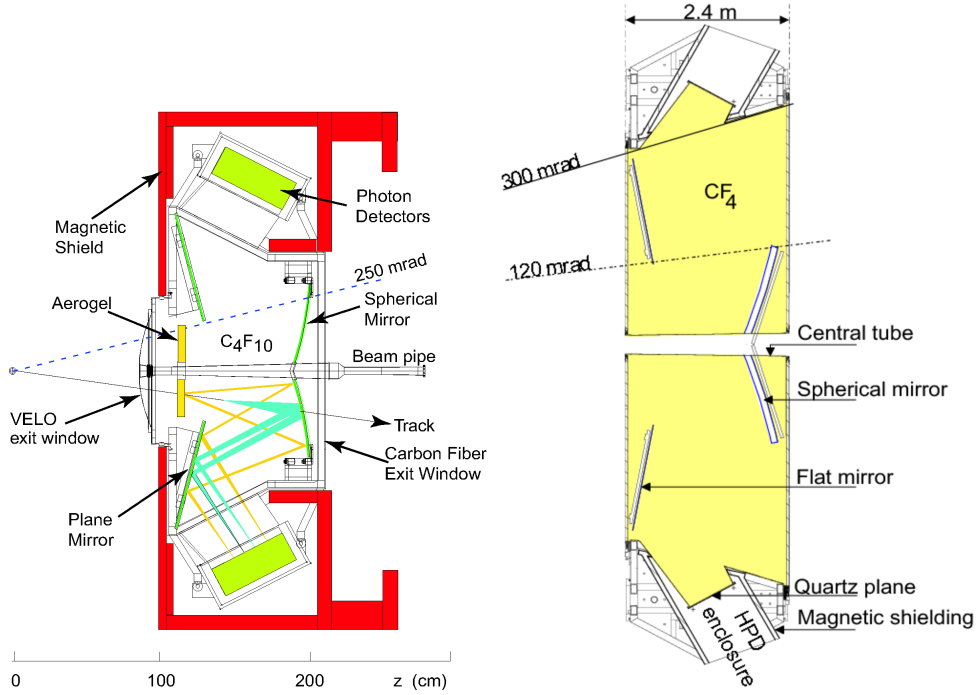
Figure 3.8 – Layout of the RICH1 (left) and RICH2 (right) subdetectors [73].

3.4.2 The calorimeter system

The identification of electrons, photons and hadrons is performed by the calorimeter system which provides energy and position measurements, as well as information for the trigger. The calorimeter system is composed of four subdetectors following the layout in Fig. 3.9:

- The electromagnetic and hadronic calorimeters (ECAL and HCAL) are used to get the energy and position of the electromagnetic and hadronic showers.

- A preshower detector (PS) in front of the ECAL after a lead converter allows the separation of electromagnetic from hadronic showers using the longitudinal profile of electromagnetic showers.

- A scintillating pad detector (SPD) in front of the lead converter and PS is used to

separate charged from neutral particles and to estimate the number of tracks for the first trigger stage.

As the hit density in the subdetectors varies by two orders of magnitudes in the plane orthogonal to the beam, the SPD, PS, ECAL and HCAL have a variable segmentation. The ECAL, PS and SPD are divided in three sections with different cell sizes, while the HCAL has two sections and bigger cell size because of the larger lateral extension of hadronic showers. In order to get a fast evaluation of the energy and position of the trigger candidates, the segmentation of the various subdetectors is approximately projective in the direction of the interaction point.

All the elements of the calorimeter are based on a similar technology: scintillation light is brought by wavelength shifting fibres to photo-multiplier tubes (PMTs). The single fibres in SPD and PS cells are read by multi-anode PMTs while the fibre bundles in the ECAL and HCAL are read by individual photo-tubes.

The calorimeter system achieves a 95% photon detection efficiency while rejecting 45% of the π^0 background.

The pad and preshower detectors   The SPD/PS system is composed of a 15 mm lead converter (which amounts to 2.5 radiation lengths) between two identical planes of rectangular scintillator pads with high granularity. The SPD is situated before the converter and the PS after. Each subdetector is divided into inner, middle and outer cells with sizes 4×4, 6×6 and $12 \times 12\,\mathrm{cm}^2$. The SPD cells are smaller by 0.45%. The SPD is used to separate photons from electrons in the first trigger stage. It gives binary information which allows a very fast response. The charged particles deposit energy in it while the neutrals don't. Potential misidentification comes from photon conversion in the upstream material and backwards moving charged particles generated in the lead converter.

The electromagnetic calorimeter   In order to fully contain the electromagnetic showers and to ensure an optimal energy resolution, the thickness of the ECAL has been chosen to be 25 radiation lengths. The design is based on the Shashlik calorimeter technology: scintillator planes interleaved with lead plates are read out by wavelength shifting fibres perpendicular to the scintillators. This allows a good compromise between cost and energy resolution, fast response, good radiation resistance and reliability. The design energy resolution is

$$\frac{\sigma_E}{E} = \frac{10\%}{\sqrt{E}} \oplus 1\% \quad (E \text{ in GeV})\,, \tag{3.2}$$

73

where the first term is due to the statistical fluctuation of the shower and the second term is the systematic uncertainty of the calibration. The maximum transverse energy is limited by the maximum possible gain of the PMTs. For the LHCb calorimeter, the threshold has been optimized for b physics, $0 < E_\text{T} < 10\,\text{GeV}$. Beyond this limit, the detector saturates. As the effect of ageing and the performance vary from cell to cell, a calibration has to be performed regularly to obtain calibration coefficients per cell.
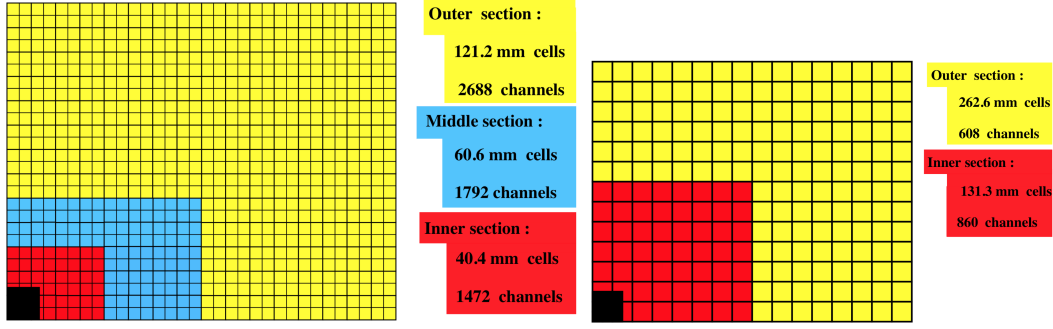
Figure 3.9 – Layout of the PS/SPD/ECAL systems (left) and the HCAL system (right) [77].

The hadronic calorimeter   The hadronic calorimeter is used for the trigger and the particle identification. It uses tiles of scintillating material alternating with iron absorber plates for a total weight of about 500 tons. The structure is a bit special as the scintillating tiles are placed parallel to the beam axis and alternate with 1 cm thick plates of iron. The length of the tiles in the longitudinal direction is chosen to match the hadron interaction length in steel. Due to the limited space in the cavern, the HCAL is only 5.6 radiation lengths thick. This introduces a leakage for the most energetic particles, but the measured energy using the HCAL alone has been shown to be wrong by less than 3% for 80 GeV pions [78]. The design resolution is

$$\frac{\sigma_E}{E} = \frac{80\%}{\sqrt{E}} \oplus 10\% \quad (E \text{ in } \text{GeV}) . \tag{3.3}$$

The HCAL is also divided in two different sections (instead of three for the rest of the calorimeter system): the inner one has square cells of 131.3 mm, and the outer one has cells of 262.6 mm.

3.4.3   The muon system

The muon system is specialized in the detection and identification of muons, and is used to provide information for the high-momentum muon trigger. As muons have a long lifetime, $\tau_\mu = 2.2\,\mu\text{s}$, so $c\tau_\mu = 659\,\text{m}$, and a very low interaction probability, they traverse the
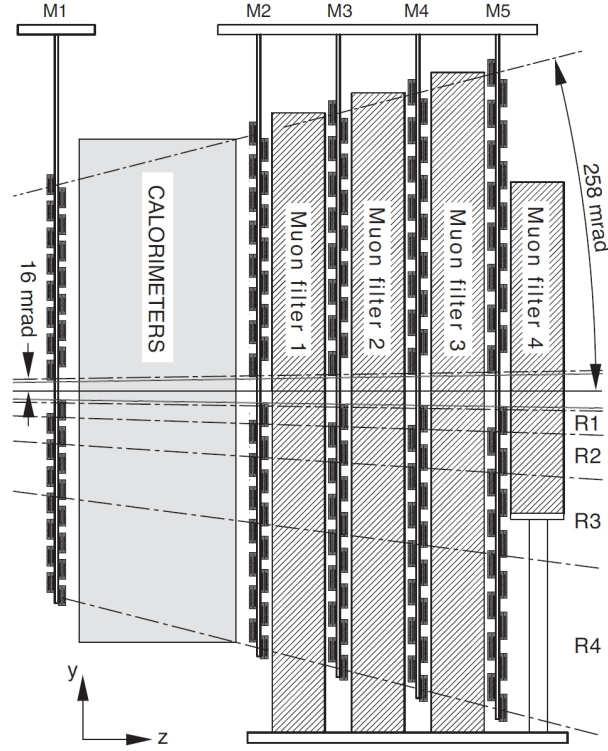
Figure 3.10 – Layout of the muon systems [79].

entire detector while the other charged particles are filtered out. Consequently, the muon systems are placed at the very end of the detector. They consist of five stations $M_1 - M_5$ of rectangular shape which cover an acceptance from 20 to 306 mrad in the bending plane, and from 16 to 258 mrad in the non-bending plane, as indicated in Fig. 3.10. An efficiency of around 20% is reached for muons from inclusive semileptonic b decays. The five stations are made of multi-wire proportional chambers (MWPC) orthogonal to the beam axis. M_1 is placed in front of the calorimeters and is used to improve the transverse momentum measurement in the trigger. Downstream of the calorimeter, $M_2 - M_5$ are interleaved with 80 cm thick iron absorbers to select the penetrating muons.

3.4.4 Particle identification

Each type of particle is characterized by a different signature (Fig. 3.11). The charged particles (electrons, muons, pions, protons and kaons) are identified using input from the RICH, the muon system and the calorimeters, while the identification of neutral objects (*e.g.* photons and π^0) use only information from the calorimeters.
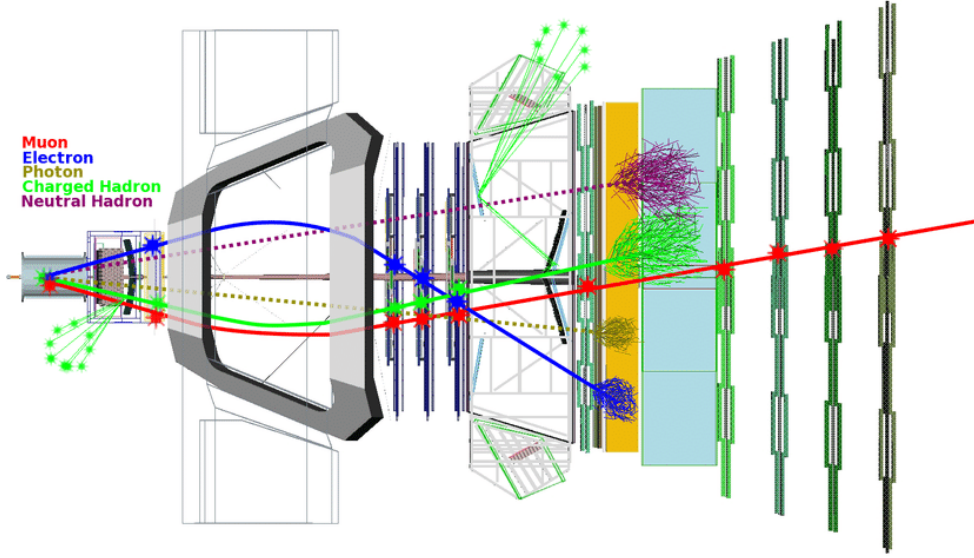
Figure 3.11 – Schematic representation of the signatures of the muons, electrons, photons, charged and neutral hadrons in the LHCb detector. The hits in the various sub-detectors, calorimeter showers and RICH rings are shown for each type of particle [25].

Identification of charged particles   A pattern recognition algorithm matches the observed patterns of Cherenkov rings in the RICH detector with the ones that would be produced by the reconstructed tracks under a certain set of mass hypotheses. As a first step, all tracks are assumed to be pions (the most probable type of charged particle in LHCb) and a global likelihood that compares the observed and expected patterns under that hypothesis is computed. Then, for each track successively, other identification hypotheses (electron, muon, proton or kaon) are tested and a new global likelihood is computed. In the end, the set of mass hypotheses assigned to the tracks is the one that maximizes the global likelihood [80].

The values of the likelihood for various identification hypotheses are also combined with information from the other sub-detectors and used by neural networks in order to predict the probability $ProbNN_X$ of a given track to be of a certain type X.

Muon identification   The muon identification takes information from the RICH, the calorimeter and the muon systems [81]. First, a loose selection of potential muons is performed using hits found in the muon chambers within a field of interest around the extrapolation of a given track from the tracking system. Then, a likelihood comparing the muon and non-muon hypotheses is computed using the distance between the hits in the muon stations and the extrapolated track. This likelihood is then combined with information from the RICH and the calorimeters to assign a muon identification probability.

Electron identification   The electron identification is mainly built from calorimeter and RICH information. Electrons are seen as ECAL clusters (groups of 3×3 adjacent cells around a local maximum of energy) associated with tracks. In order to match clusters with tracks, a χ^2_γ variable is defined based on the distance between the clusters and the extrapolated tracks. Small values of χ^2_γ are typical of clusters from charged particles while high values identify neutral clusters. Additionally, electrons are separated from hadrons using the fact that they radiate more photons through Bremsstrahlung and they deposit most of their energy inside the PS and ECAL while they do not reach the HCAL.

Identification of neutral particles   As it uses only input from the calorimeter systems, the identification of neutral particles is far more challenging than that of the charged particles, which typically reaches 90% of efficiency and below 5% of mis-identification probability. The photon candidates are reconstructed as neutral clusters in the ECAL, so clusters associated with high values of χ^2_γ. A separation is made between the *converted* photons (which created an electron-positron pair before the lead absorber) and the *unconverted* ones by using the number of hits in the SPD. Neutral pions decay into two photons, which are well separated when the π^0 transverse momentum lies below $2.5\,\text{GeV}/c$. These *resolved* π^0 are reconstructed by finding pairs of calorimeter clusters with a total invariant mass compatible with the π^0 mass hypothesis. However, for transverse momenta over $2.5\,\text{GeV}/c$, the angle between the two emitted photons can be so small that they are seen as a single cluster in the calorimeter. To reconstruct these *merged* π^0, each cluster is split into two superimposed subclusters and their respective energy is iteratively recomputed using the expected energy distribution from photon showers. The cluster is then identified as a merged π^0 if the distance between the two photons is kinematically allowed and if their invariant mass is compatible with that of a π^0. The reconstruction and identification efficiency has been evaluated on a sample of π^0 coming from $B \to \pi^-\pi^+\pi^0$ decays and is shown in Fig. 3.12.

3.5   The LHCb trigger

At the interaction point, the bunch crossing rate delivered by the LHC is close to $40\,\text{MHz}$, which is impossible to record with present resources. The role of the trigger is to reduce the rate of recorded events down to a few kHz by operating a first data selection in two stages: the hardware-based stage (called L0) which uses raw information from the detector to operate a very fast selection, and a software based stage divided in two steps (HLT1 and HLT2) in which the events are fully reconstructed and further selected. The trigger schemes used during Run 1 and Run 2 are described in Fig. 3.13 and explained in the following paragraphs.
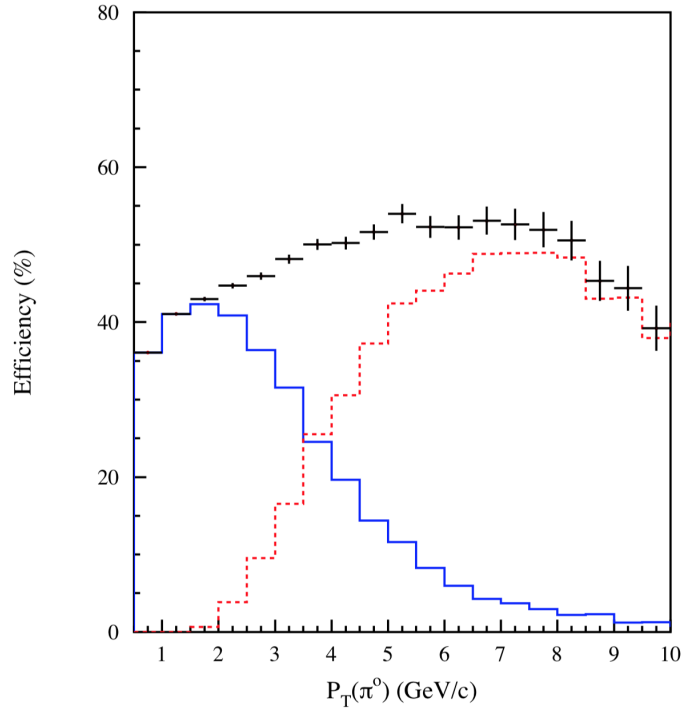
Figure 3.12 – Reconstruction and identification efficiencies of resolved (plain blue histogram) and merged (dashed red histogram) π^0 together with their sum (black points) as a function of the transverse momentum of the π^0, estimated on a sample of $B \to \pi^- \pi^+ \pi^0$ decays [82].

3.5.1 Run 1 trigger

Hardware-based level The main objective of L0 is to reduce the event rate in order to allow a readout of 1 MHz, currently limited by the front-end electronics [83]. To perform this task at a high rate, only the information from the fast systems can be used. Input from the muon systems is used to trigger on one or two high-momentum muons, while the electrons, photons and hadrons are triggered by the calorimeters. The number of hits in the SPD also gives information used to veto events with high occupancy. The total 1 MHz bandwidth is shared between different specific selections (trigger lines) according to their physics reach. The main categories of trigger lines are the following:

- In the muon trigger (400 kHz), muon track segments are reconstructed only in the muon systems by searching for hits aligned in straight lines pointing to the interaction point. One or two muon candidates are required at this stage.

- In the hadron trigger (450 kHz), a cluster with high transverse energy is looked for in the hadronic calorimeter and is required to match with a cluster in the electromagnetic calorimeter.

- The photon trigger uses the cluster of highest transverse energy in the electromag-

LHCb 2012 Trigger Diagram

40 MHz bunch crossing rate

L0 Hardware Trigger : 1 MHz readout, high E_T/P_T signatures

450 kHz h±	400 kHz μ/μμ	150 kHz e/γ

Software High Level Trigger

Introduce tracking/PID information, find displaced tracks/vertices

Offline reconstruction tuned to trigger time constraints

Mixture of exclusive and inclusive selection algorithms

5 kHz (0.3 GB/s) to storage

2 kHz Inclusive Topological	2 kHz Inclusive/ Exclusive Charm	1 kHz Muon and DiMuon

LHCb 2015 Trigger Diagram

40 MHz bunch crossing rate

L0 Hardware Trigger : 1 MHz readout, high E_T/P_T signatures

450 kHz h±	400 kHz μ/μμ	150 kHz e/γ

Software High Level Trigger

Partial event reconstruction, select displaced tracks/vertices and dimuons

Buffer events to disk, perform online detector calibration and alignment

Full offline-like event selection, mixture of inclusive and exclusive triggers

12.5 kHz (0.6 GB/s) to storage

Figure 3.13 – Trigger schemes used in Run 1 (left) and Run 2 (right) [83, 84].

netic calorimeter, which is required to match with hits in the PS but not in the SPD.

- The electron trigger uses the same ECAL cluster but requires matching hits in the SPD. The photon and electron trigger lines share a bandwidth of 150 kHz.

Around 10% of the events are selected by several trigger lines.

Software-based level The software-based level runs on about 29 000 CPU cores and performs a further selection using reconstructed tracks and vertices and particle identification. In HLT1, the rate is reduced from 1 MHz to 70 kHz by performing a first reconstruction using the full detector information and by operating inclusive selections (not specific to a given decay channel). Typical requirements include high transverse-momentum tracks, high transverse energy ECAL clusters, tracks with large impact parameters with respect to the primary vertex or muon pairs with high invariant mass. In HLT2, all the tracks with a transverse momentum above 300 MeV/c are reconstructed and the rate is brought down to 5 kHz using both inclusive and exclusive selections. The main inclusive lines, the *topo* lines, are based on the selection of systems with 2, 3 or 4 tracks forming a vertex displaced from the primary vertex thanks to multivariate

classifiers.

3.5.2 Run 2 trigger

In Run 2, the trigger has been modified for a better optimization and data quality [84]. The L0 bandwidth division has been optimized but the structure remained the same. The main changes concern the software-based trigger. During Run 1, the time-consuming HLT2 stage was applied directly after HLT1, and events were stored only after the two operations, making the process inefficient. In Run 2, the data flow has been changed so that the events are buffered to disk after HLT1 and are processed later on by HLT2. This intermediate buffer also allows the online alignment and calibration to be performed, hence improving the quality of the data obtained as an output of the trigger. These improvements also lead to the creation of a dedicated trigger stream (the *Turbo stream*) in which only the information from the signal candidates is stored, and whose goal is to allow for certain physics analyses directly on the data coming out of the trigger [85]. All these improvements led to a rate of recorded events of $12.5\,\mathrm{kHz}$.

3.6 The LHCb software

The LHCb software is based on the assumption that events can be treated nearly independently of each other. This idea is encoded in the GAUDI framework [86] which relies on loops over events, each of them containing information on which GAUDI tools and algorithms can be run. This framework is flexible enough to be able to treat simulated events and real data alike. Several software packages allow to handle different parts of the data flow:

- **GAUSS** allows the simulation of the particles and their interactions with the detector [87, 88]. It is divided in several applications dedicated to specific tasks. PYTHIA [89] is used to simulate the *pp* collisions while the decays of particles are in general handled by EVTGEN [65]. The final state radiations are generated using PHOTOS [90], and the interactions between the generated particles and the detectors are simulated using the GEANT4 package [91, 92].

- **BOOLE** performs the digitization. The electronic response as well as the hardware stage of the trigger are simulated in this package which gives an output in the same format as the real data.

- **MOORE** runs the software trigger on both real data and simulated events.

- **BRUNEL** performs the full track reconstruction and particle identification on real and simulated data.
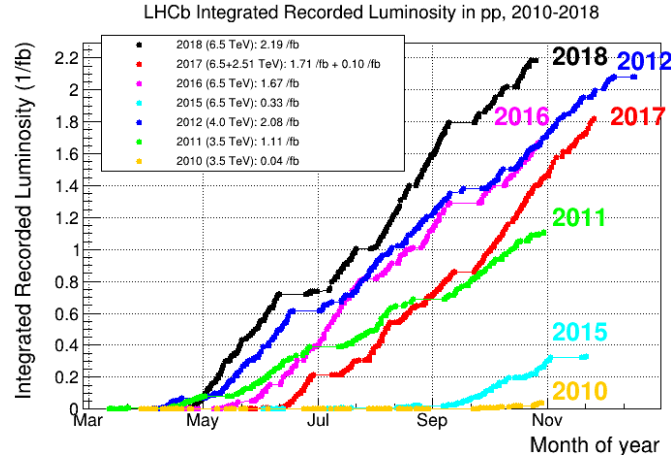
Figure 3.14 – Integrated luminosity recorded by the LHCb experiment in *pp* collisions from 2010 to 2018 [93].

- **DAVINCI** is an offline analysis tool which allows the construction and selection of signal decays using combinations of objects and requirements on kinematics, topology and particle identification.

3.7 Data samples

The good performance of LHCb in Run 1 and Run 2 has allowed the recording of large *pp* collision data sets at various centre-of-mass energies. During Run 1, the LHC delivered collisions at $\sqrt{s} = 7\,\text{TeV}$, and an integrated luminosity of $0.04\,\text{fb}^{-1}$ has been recorded in 2010 and $1.1\,\text{fb}^{-1}$ in 2011. In 2012, the centre-of-mass energy has been increased to $\sqrt{s} = 8\,\text{TeV}$ and $2.1\,\text{fb}^{-1}$ of data were recorded, as shown in Fig. 3.14. In Run 2, at $\sqrt{s} = 13\,\text{TeV}$, the integrated luminosity was $0.3\,\text{fb}^{-1}$ in 2015, $1.7\,\text{fb}^{-1}$ in 2016, $1.7\,\text{fb}^{-1}$ in 2017 and $2.2\,\text{fb}^{-1}$ in 2018.

3.8 The detector upgrade

The upgrade of the LHCb detector [94], in 2019–2020, will extend the physics reach of the experiment by allowing it to run at higher luminosity in order to take maximal advantage from the next two runs of the LHC, currently scheduled in 2021–2024 (Run 3) and 2028–2030 (Run 4). First, the recent developments in hardware and software will allow to multiply by five the instantaneous luminosity and operate the detector at $\mathcal{L} = 2 \times 10^{33}\,\text{cm}^2\,\text{s}^{-1}$, which will result in a collected integrated luminosity of around $50\,\text{fb}^{-1}$ at the end of Run 4. This implies five times more collisions per bunch-crossing (pile-up) in the LHCb detector, and hence much higher radiation damage. In addition, the current limitations of the LHCb trigger scheme will be overcome by removing the

hardware stage and operating a full event reconstruction at the inelastic *pp* collision rate ($\sim 30\,\mathrm{MHz}$). To summarize, the design of the upgraded experiment is driven by three main constraints:

1. Higher occupancy (five times more pile-up than in Run 2),

2. Higher fluence (so higher radiation damage),

3. 30 MHz event reconstruction.

In order to cope with these new conditions, the LHCb detector will be nearly totally renewed.

In the upgraded trigger scheme, the main differences with respect to Run 2 trigger is that the L0 hardware-based level will be removed, which implies that all the front-end electronics need to be changed to run at 40 MHz. A full event reconstruction will be performed and the events will be streamed in different inclusive and exclusive selections. The events will then be buffered to disk in order to calibrate and align the detector online. In a second stage, high precision particle identification information as well as track quality information will be added to the events. A further selection will be performed and the events will be saved to disk at a rate of 2–$5\,\mathrm{GB\,s^{-1}}$. Following the ideas behind the *Turbo stream*, disk space will be optimized by storing only the triggered signal candidates of the inclusive selections, while the exclusive selections will save full event information.

The RICH will be kept with some modifications, as well as the ECAL and HCAL. The SPD/PS system will be removed as it is no longer needed in the trigger [95]. The M1 station will be removed and a shield will be installed between the calorimeters and the muon system in order to reduce the occupancy in the other muon stations.

The tracking system will undergo major changes as all tracking stations will be replaced, in order to maintain the performance of the detector in terms of tracking efficiency and vertex resolution in a much more difficult environment [96]. The VELO is replaced with a pixel-based vertex locator (the VELOpix) which has a finer granularity (the pixels area is only $55 \times 55\,\mathrm{\mu m^2}$) and is placed closer to the beam (the closest pixels are only $5.1\,\mathrm{mm}$ from the beam, to be compared with $7.8\,\mathrm{mm}$ in the VELO [97]). Upstream of the magnet, the TT is replaced with the Upstream Tracker (UT) which is based on the same technology but with a finer granularity and closer to the beam. Downstream of the magnet, a scintillating fibre tracker (SciFi), submitted to a lower fluence than the UT, will replace the IT and OT which cannot cope with the upgrade luminosity. Scintillating fibres have been chosen as the base technology for this tracker because they offer a good compromise between price and radiation hardness. The $11\,000\,\mathrm{km}$ of $250\,\mathrm{\mu m}$ diameter fibres organised in $2.5\,\mathrm{m}$ long mats convert the energy deposited by charged particles into light, which is then transported along the fibres and detected by silicon photomultiplier (SiPM) arrays.

The implementation of the digitization process in the SciFi tracker was an important part of the work performed during this PhD thesis. I contributed mainly to the effective simulation of the photon production and propagation in the fibres, to the optimization of the digitization step in terms of timing, and to the code that allowed comparisons between simulated SciFi module response and real module response coming from test beam campaigns. This work is documented in an LHCb internal note [98] and the corresponding code has been added to the BOOLE package in the official LHCb software.

4 Signal selection and mass fit

The $B^+ \to K^+\pi^-\pi^+\gamma$ decays are selected in data sets collected by the LHCb detector in 2011 and 2012 (Run 1), and 2016 and 2017 (partial Run 2). They correspond to integrated luminosities of 1.1, 2.1, 1.7 and $1.7\,\text{fb}^{-1}$ at centre-of-mass energies of 7, 8, 13 and 13 TeV, respectively. The data collected in 2015 are discarded due to the lack of calorimeter calibration for this year.

This chapter describes the selection of signal candidates. The data samples and the simulated data sets used in this analysis are listed. The trigger selection is presented, followed by the stripping selection and the offline selection. Then, the various components of the mass fit to the $B^+ \to K^+\pi^-\pi^+\gamma$ candidates are described and several sources of background are studied. Finally, the results of the mass fit are presented, as well as the background subtraction procedure used to obtain the distribution of the variables on which the amplitude analysis is to be performed.

4.1 Data and simulation samples

Two different selections are devised following the same strategy : one selection for Run 1 data and one for 2016–2017 data. Due to the low statistics of the 2011 data set, the selection of Run 1 data is optimized using only 2012 data and Monte Carlo (MC) simulation and is applied to both the 2011 and 2012 data sets. As the data-taking conditions are very similar for the data sets collected in 2016 and 2017, the same selection is applied on both data sets and is optimized using the Run 2 MC simulation samples available at the time of this work, which are generally simulated in the 2016 data-taking conditions.

The MC simulated data sets used to study the signal and background contributions are generated with the 2012 (MC12), 2016 (MC16) and 2017 (MC17) data-taking conditions. In all these samples, the pp collisions are simulated using the GAUSS application described in Sec.3.6. The interactions of the simulated particles with the detector are implemented in the GEANT4 toolkit [91,92]. The set of samples used in the analysis of Run 1 are simulated in the 2012 data-taking conditions while the samples used in the analysis of Run 2 are

Table 4.1 – List of samples of fully simulated B decay events used for the analysis of 2011 and 2012 data.

	MC production	Number of events
$B^+ \to K_1(1270)^+\gamma$	sim06b MC12	2.034×10^6
$B^+ \to K_1(1400)^+\gamma$	sim06b MC12	2.005×10^6
$B^+ \to K^*(1410)^+\gamma$	sim06b MC12	2.027×10^6
$B^0 \to K^{*0}\gamma$	sim08d MC12	6.053×10^6
$B^+ \to K^{*0}\pi^+\gamma$	sim08c MC12	1.523×10^6
$B^+ \to \bar{D}^0(\to K^+\pi^-\pi^0)\pi^+$	sim08f MC12	2.091×10^6
$B^+ \to \bar{D}^0(\to K^+\pi^-\pi^0)\rho^+(\to \pi^+\pi^0)$	sim08e MC12	2.119×10^6
$B^+ \to \bar{D}^{*0}(\to \bar{D}^0(\to K^+\pi^-)\gamma)\pi^+$	sim08e MC12	1.032×10^6
$B^+ \to \bar{D}^{*0}(\to \bar{D}^0(\to K^+\pi^-)\pi^0)\pi^+$	sim08e MC12	1.008×10^6
$B^+ \to K^{*+}(\to K^+\pi^0)\pi^+\pi^-$	sim08e MC12	2.012×10^6
$B^0 \to K_1(1270)^0\gamma$	sim06b MC12	1.843×10^6
$B^+ \to K_1(1270)^+\eta$	sim08c MC12	1.522×10^6
$B^+ \to a_1^+(\to \pi^+\pi^-\pi^+)\gamma$	sim06b MC12	2.027×10^6

generally simulated in the 2016 data-taking conditions. For $B^+ \to \bar{D}^0(\to K^+\pi^-\pi^0)\pi^+$ decays in Run 2, the sample generated in the 2016 data-taking conditions is not large enough, so a sample with the 2017 data-taking conditions is used instead. These samples are shown in Tables 4.1 and 4.2. The large simulated data samples intended for the amplitude analysis and referred to as "cocktail" contain an incoherent mixture of $B^+ \to K^+\pi^-\pi^+\gamma$ decays simulated using the EVTGEN generator and involving several resonances and decay chains without interferences, as listed in Table 4.3. The motivation for this specific composition is explained in Sec. 5.4.

4.2 General strategy of the event selection

The selection of signal candidates is performed in three steps:

- The trigger filters events at data-taking time and decides which events are recorded. The others are definitively lost.

- In the stripping step, the fully reconstructed events undergo a first loose selection of B candidates decaying to three charged tracks and a neutral object in the calorimeter.

- The $B^+ \to K^+\pi^-\pi^+\gamma$ candidates are further selected in two steps: a cut-based selection followed by a multivariate selection.

Table 4.2 – List of samples of fully simulated B decay events used for the analysis of 2016 and 2017 data. The composition of the "cocktail" samples is given in Table 4.3.

	MC production	Number of events
$B^+ \to K_1(1270)^+\gamma$	sim09b MC16	3.007×10^6
$B^+ \to K_{\mathrm{res}}^+\gamma$ (cocktail)	sim09f MC16	5.745×10^6
$B^+ \to K_{\mathrm{res}}^+\gamma$ (cocktail)	sim09f MC17	8.061×10^6
$B^+ \to K^+\pi^-\pi^+\gamma$ (phase-space)	sim09f MC16	1.252×10^6
$B^+ \to K^+\pi^-\pi^+\gamma$ (phase-space)	sim09f MC17	0.568×10^6
$B^0 \to K^{*0}\gamma$	sim09c MC16	4.068×10^6
$B^+ \to K^{*0}\pi^+\gamma$	sim09b MC16	2.012×10^6
$B^+ \to \bar{D}^0(\to K^+\pi^-\pi^0)\pi^+$	sim09b MC16	0.208×10^6
$B^+ \to \bar{D}^0(\to K^+\pi^-\pi^0)\pi^+$	sim09h MC17	1.016×10^6
$B^+ \to \bar{D}^0(\to K^+\pi^-\pi^0)\rho^+(\to \pi^+\pi^0)$	sim09d MC16	1.007×10^6
$B^+ \to \bar{D}^{*0}(\to \bar{D}^0(\to K^+\pi^-)\gamma)\pi^+$	sim09c MC16	1.317×10^6
$B^+ \to \bar{D}^{*0}(\to \bar{D}^0(\to K^+\pi^-)\pi^0)\pi^+$	sim09c MC16	2.603×10^6
$B^+ \to K^{*+}(\to K^+\pi^0)\pi^+\pi^-$	sim09d MC16	1.034×10^6
$B^0 \to K_1(1270)^0\gamma$	sim09b MC16	0.518×10^6
$B^+ \to K_1(1270)^+\eta$	sim09b MC16	0.514×10^6
$B^+ \to K_1(1270)^+\pi^0$	sim09h MC16	2.529×10^6
$B^+ \to a_1^+(\to \pi^+\pi^-\pi^+)\gamma$	sim09d MC16	0.511×10^6

4.3 Trigger selection

The trigger filters the events at data-taking time in order to reduce their rate from 40 MHz down to 5 kHz. The first level of trigger (`L0`) uses the information coming from the calorimeters and the muon systems in order to take a fast decision on whether or not to keep the event. It is meant to reduce the event rate to 1 MHz, at which the detector can be read out. The second level is based on software and is divided into two stages (`Hlt1` and `Hlt2`) in order to optimize the computing resources. `Hlt1` performs a partial reconstruction of the event and a selection. In `Hlt2`, the events are fully reconstructed and selected further. The requirements on each signal candidate are the following:

- At `L0`: As the decay products of the B meson are expected to have a high transverse energy or momentum, the event is selected if one of the objects used to build the signal candidate leaves a high energy deposit in the electromagnetic. This corresponds to requiring the signal candidate to pass either the `L0Photon` or `L0Electron` decision line.

- At `Hlt`:

    - In Run 1: A single detached track with high momentum is searched for, depending on the `L0` line that has been triggered. Therefore, the events are

Table 4.3 – Composition of the "cocktail" samples of fully simulated $B^+ \to K_{\mathrm{res}}^+ \gamma \to K^+ \pi^- \pi^+ \gamma$ signal events. The table is divided in sections according to the spin-parity J^P of the K_{res} resonance.

J^P	K_{res} decay	Fraction (%)
	$K_1(1270)^+ \to K^*(892)^0\pi^+$	16.62
	$K_1(1270)^+ \to K^+\rho(770)^0$	39.61
1^+	$K_1(1270)^+ \to K^+\omega(782)^0$	0.09
	$K_1(1270)^+ \to K_0^*(1430)^0\pi^+$	0.68
	$K_1(1400)^+ \to K^*(892)^0\pi^+$	8.00
	$K^*(1410)^+ \to K^*(892)^0\pi^+$	8.50
1^-	$K^*(1680)^+ \to K^*(892)^0\pi^+$	7.08
	$K^*(1680)^+ \to K^+\rho(770)^0$	4.92
	$K_2^*(1430)^+ \to K^*(892)^0\pi^+$	5.07
2^+	$K_2^*(1430)^+ \to K^+\rho(770)^0$	9.14
	$K_2^*(1430)^+ \to K^+\omega(782)^0$	0.29

required to pass one of the following lines in `Hlt1`: `B_Hlt1TrackAllL0` or `B_Hlt1TrackPhoton`. At `Hlt2`, the events are required to pass one of the following sets of trigger lines:

* the radiative topological `Hlt2` lines (`B_Hlt2RadiativeTopoTrackTOS` and `B_Hlt2RadiativeTopoPhotonL0` in 2011, `B_Hlt2RadiativeTopo-Track` and `B_Hlt2RadiativeTopoPhoton` in 2012) which select inclusively the B candidates with at least two tracks and a high transverse energy photon;

* the general topological line selecting B decays to three tracks (`B_Hlt2-Topo3BodyBBDT`).

– In Run 2: At `Hlt1`, a single detached track or a combination of two tracks is looked for by requiring the signal candidate to pass either the `B_Hlt1TrackMVA` or the `B_Hlt1TwoTrackMVA` line. At `Hlt2`, a combination of three tracks is performed and selected by the `B_Hlt2RadiativeIncHHHGamma` line.

At each level, the event is required to be triggered on signal (`TOS`), which means that the particles of the signal candidate are sufficient to fire the trigger line.

4.4   Stripping selection

The stripping configurations used for the data obtained in 2011, 2012, 2016 and 2017 are `S21r1`, `S21`, `S28r1p1` and `S29r2`, respectively. In all cases, the stripping line used

to select the event is the `Beauty2XGamma3pi` line, in which three tracks without particle identification requirements are combined to form the vertex of a heavy kaonic resonance, which is then combined with a high-energy photon to form the B meson candidate. The cuts applied at this stage, listed in Table 4.4, are slightly different for the two data-taking periods to adapt to the evolving data-taking conditions. The main requirements applied at this step are the following:

- Requirements on track p and p_{T} are aimed at removing the soft tracks contributing mainly to combinatorial background.

- The tracks accidentally reconstructed from random hits in the tracking systems are removed based on their probability to be fake tracks ("ghost probability").

- The three-track system is required to form a good quality vertex with a small enough χ^2_{vtx} value.

- Soft photons from radiation are removed by requiring a minimum transverse energy.

- The photon identification confidence level is used to remove calorimeter clusters caused by hadrons. This variable is the output of a Neural Network classifier using information from the calorimeter system such as the energy deposits and the shower shapes in the PS and ECAL, the ratio of energies deposited in the ECAL and the HCAL in the region of the cluster, the multiplicity of hits in the SPD in front of the cluster, and a variable that quantifies the compatibility of the cluster with the closest reconstructed track [99].

- The DIRA is the cosine of the angle between the momentum of the reconstructed B meson and the direction from the best primary vertex (PV) and the decay vertex. As the B meson comes from the PV, the value of the DIRA should be 1 for the signal. A cut on this variable is used to remove random combinations of tracks.

- Another variable that measures the compatibility of the reconstructed B candidate with the PV is χ^2_{IP}, which is computed as the difference of the fit χ^2 of the PV with and without the B candidate. If the B actually comes from the PV, this difference is expected to be small.

- The decay vertex of the B is required to be of good quality, with a small enough $\chi^2_{\mathrm{vtx}}/\mathrm{ndf}$ value.

In the Run 2 data sets, additional variables related to the isolation of tracks have been saved in the stripping stage, in contrast to Run 1 data sets in which these variables are not available.

Table 4.4 – Requirements applied for the stripping selection.

Variable	2011–2012	2016–2017	Unit
Track p_{T}	> 300	> 300	MeV/c
Track p	> 1000	> 1000	MeV/c
Track χ^2/ndf	< 3	< 3	
Track χ^2_{IP}	> 16	> 20	
Track ghost probability	< 0.4	< 0.4	
Three-track p_{T}	> 1500	> 1000	MeV/c
Three-track χ^2_{vtx}	< 10	< 9	
Three-track invariant mass	$\in [0, 7900]$	$\in [0, 7900]$	MeV/c^2
Photon E_{T}	> 2000	> 2000	MeV
γ confidence level	> 0	> 0	
Photon and tracks $\sum p_{\mathrm{T}}$	> 5000	> 3000	MeV/c
B meson DIRA	> 0	> 0	
B meson χ^2_{vtx}	< 9	< 9	
B meson χ^2_{IP}	< 9	< 9	
B meson invariant mass	$\in [2900, 9000]$	$\in [2400, 6500]$	MeV/c^2

4.5 Offline selection

The first step of the offline selection is cut-based and aims at removing mainly combinatorial background. In a second step, the data are further filtered by applying a multivariate selection.

4.5.1 Cut-based pre-selection

Before applying the offline selection, the energy of the photon is calibrated again in data and MC samples with more precise calibration constants. In order to get rid of potential border effects due to this so-called post-calibration, a tighter cut on the photon transverse energy is introduced.

In order to clean up the samples before the multivariate selection, requirements are imposed on the following set of variables:

- A harder cut is imposed on the γ confidence level.

- The γ/π^0 separation variable is a multivariate discriminator built from the ECAL and PS information and meant at separating the photons from the so-called merged π^0. At $p_{\mathrm{T}} > 4\,\mathrm{GeV}/c$, a photon pair coming from the π^0 decay is merged: it forms a single calorimeter cluster that can fake a photon. The algorithm takes advantage

- of the more elliptical shape of the clusters from merged π^0, and of their energy distribution focused on two points instead of one, in order to discriminate between γ and π^0.

- Particle identification variables (ProbNN) using information from the RICH are combined together in order to better discriminate between the tracks associated with a pion and those associated with a kaon.

- A b-hadron isolation $\Delta\chi^2$ is meant at discriminating signal from partially reconstructed backgrounds for which one charged track is not reconstructed. In order to compute it, a track of the event is combined with the decay vertex of the B meson candidate and the latter is refitted to obtain its new χ^2 value. The isolation $\Delta\chi^2$ is obtained as the opposite of the difference between the χ^2 of the original vertex and the minimum of the χ^2 values obtained when testing each track in the rest of the event.

- The $K\pi\pi$ mass is chosen to be between 1100 and 1900 MeV/c^2 in order to improve the signal-to-background ratio and avoid the peak corresponding to the decay $D_s^+ \to K^+\pi^+\pi^-$, as can be seen in Fig. 4.1.

Due to the large branching fraction of the decay $B^+ \to \bar{D}^0\rho^+$, a potentially dangerous background arises from $B^+ \to \bar{D}^0(\to K^+\pi^-\pi^0)\rho^+(\to \pi^+\pi^0)$ decays where one of the π^0 mesons is reconstructed as a γ and the other one escapes selection.

In case the π^0 that escapes the selection is the one coming from the $\bar{D}^0$, then the γ in the $B^+ \to K^+\pi^-\pi^+\gamma$ candidate is actually a π^0 coming from a ρ^+. So the combination of the π^+ with the neutral particle for which the π^0 mass is now assumed should peak at the ρ mass. As shown in Fig. 4.2, this background can be removed by requiring the $\pi^+\pi^0$ mass to be larger than 1100 MeV/c^2, without effect on the signal.

Another possibility is that the π^0 from the ρ^+ resonance escapes selection, and the one from the $\bar{D}^0$ is mis-identified as a γ. In this case it is expected that the mass of the $K^+\pi^-\gamma$ system where the γ mass hypothesis is replaced by that of a π^0 peaks at the $\bar{D}^0$ mass. Hence, requiring that the $K^+\pi^-\pi^0$ mass is above 2200 MeV/c^2 efficiently gets rid of this background, as shown in Fig. 4.3.

All the preselection requirements are summarized in Table 4.5.

4.5.2 Multivariate selection against combinatorial background

A further reduction of the amount of background coming from random combinations of tracks is performed using a multivariate classifier which takes as input a set of variables and predicts the probability of the candidate to be either signal or background. The

(a) Data 2016

(b) Data 2012

Figure 4.1 – 2D joint distribution of the $K^+\pi^-\pi^+\gamma$ and $K^+\pi^-\pi^+$ masses in 2016 and 2012 data. The peak corresponding to the D_s^+ mass is visible in the $K\pi\pi$ mass spectrum around $1968\,\text{MeV}/c^2$. Credits to Ref. [100].

(a) Data 2016

(b) MC 2016

Figure 4.2 – 2D joint distribution of the $K^+\pi^-\pi^+\gamma$ and $\pi^+\pi^0$ masses in 2016 data and signal MC. The peak corresponding to the ρ^+ mass is visible in the $\pi^+\pi^0$ mass spectrum around $770\,\mathrm{MeV}/c^2$. Credits to Ref. [100].
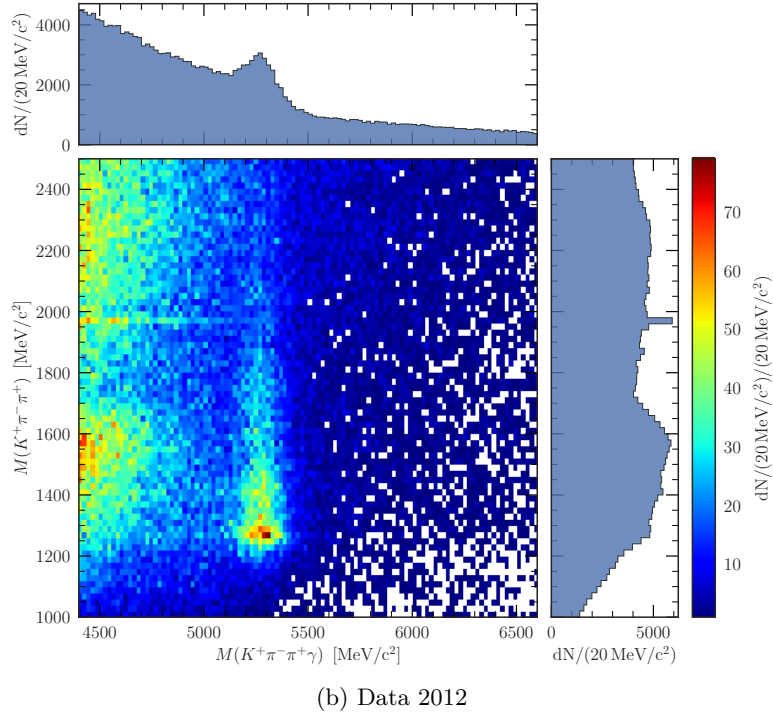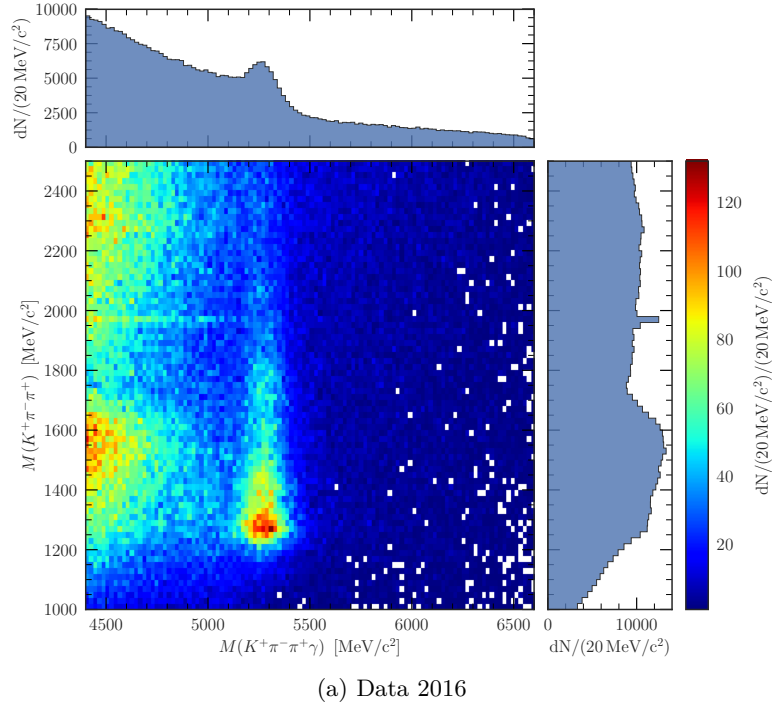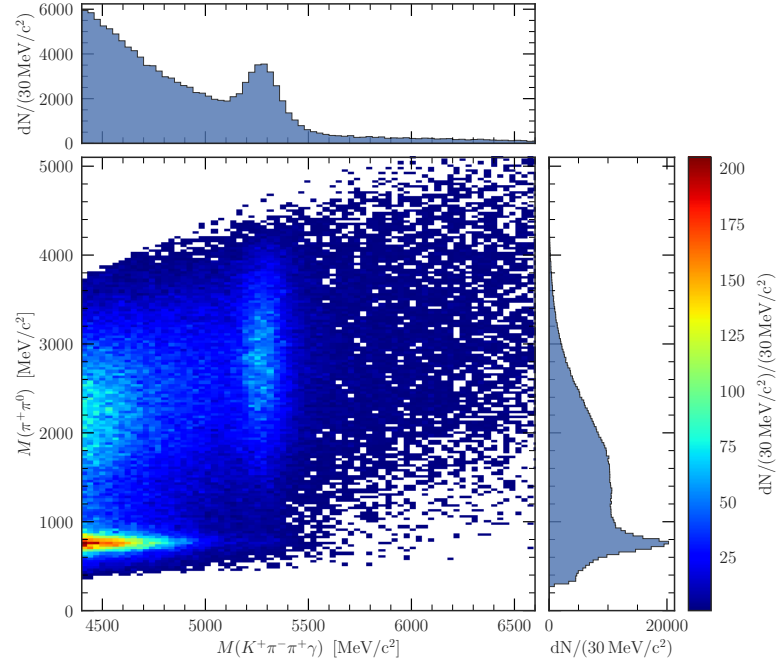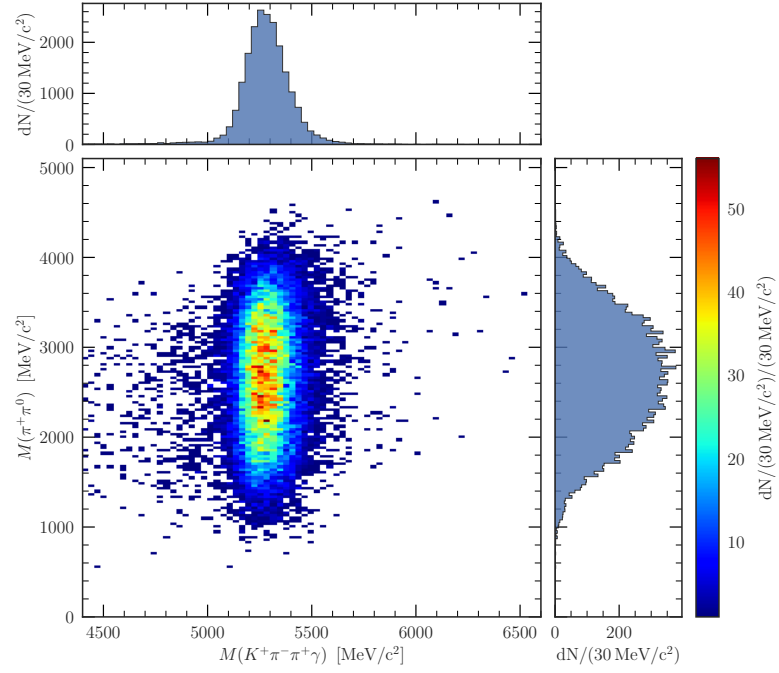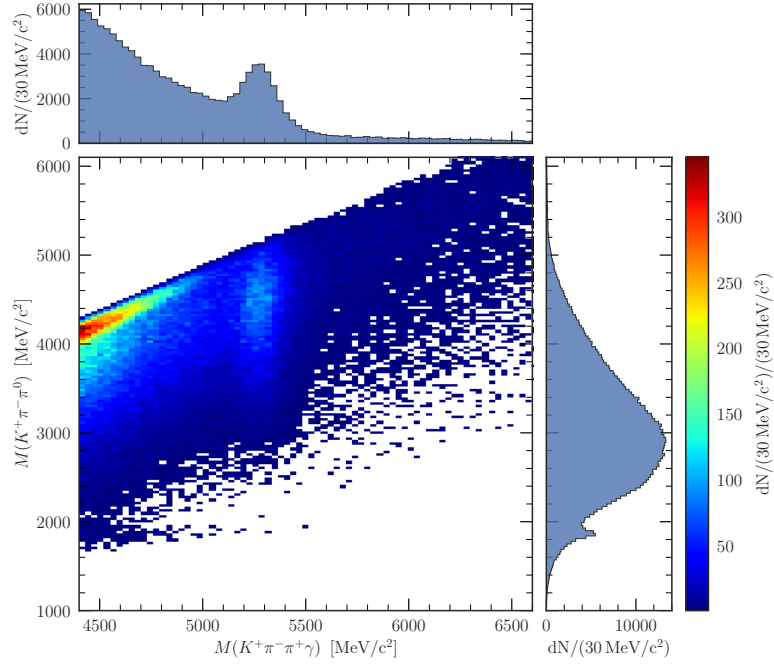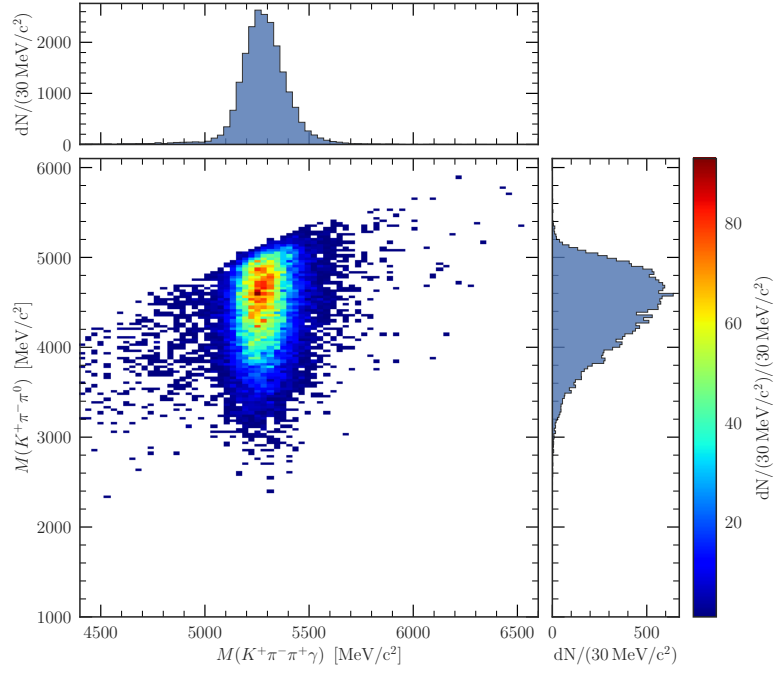
(a) Data 2016

(b) MC 2016

Figure 4.3 – 2D joint distribution of the $K^+\pi^-\pi^+\gamma$ and $K^+\pi^-\pi^0$ masses in 2016 data and signal MC. The peak corresponding to the $\bar{D}^0$ mass is visible in the $K^+\pi^-\pi^0$ mass spectrum around $1865\,\mathrm{MeV}/c^2$. Credits to Ref. [100].

Table 4.5 – Requirements applied for the offline preselection.

Variable	2011–2012	2016–2017	Unit
Photon E_{T}	> 3000	> 3000	MeV
B meson p_{T}	> 5000	> 4000	MeV/c
B meson isolation $\Delta\chi^2$	> 5	> 5	
γ/π^0 separation	> 0.7	> 0.7	
γ confidence level	> 0.2	> 0.2	
$\mathrm{ProbNN}_K(K^+) \times (1 - \mathrm{ProbNN}_\pi(K^+))$	> 0.2	> 0.2	
$\mathrm{ProbNN}_\pi(\pi^+) \times (1 - \mathrm{ProbNN}_K(\pi^+))$	> 0.2	> 0.2	
$\mathrm{ProbNN}_\pi(\pi^-) \times (1 - \mathrm{ProbNN}_K(\pi^-))$	> 0.2	> 0.2	
$K\pi\pi$ mass	$\in [1100, 1900]$	$\in [1100, 1900]$	MeV/c^2
$K^+\pi^-\pi^0$ mass	> 2200	> 2200	MeV/c^2
$\pi^+\pi^0$ mass	> 1100	> 1100	MeV/c^2

classifier chosen for this task is described in details in Ref. [100], and is based on a set of decision trees (simple and weak predictive models) subject to gradient boosting: the trees are weighted and combined together to form a more accurate predictive model by iterations in which a loss function is minimized. The *XGBoost* [101] library offers an optimized implementation of such gradient boosting algorithms, which are known to be fast and accurate with two main drawbacks: sensitivity to noise and over-fitting. The latter effect happens when the model is so complex that it predicts perfectly the classification of the data set on which it is trained, but fails to generalize to a new data set. In order to reduce this dangerous over-fitting, some hyper-parameters of the classifier can be tuned:

- The learning rate η, ranging from 0 to 1, is a shrinkage parameter applied on the weight given to a new tree in order to reduce its influence on the updated model. A low value of η makes the algorithm more conservative.

- The L^1 regularisation parameter α penalizes model complexity by adding to the loss function a term proportional to α times the sum of absolute values of the weights.

- The subsample fraction indicates the proportion of the data picked at random on which trees will be built at each boosting iteration.

In order to limit the training time, the number of trees at each iteration is fixed to 1000, and the depth of each tree, which is the longest path from the root to a leaf, is set to 2.

For the purpose of separating signal events from combinatorial background, two gradient boosting algorithms are trained for the selection of candidates in 2011–2012 (2016–2017) data sets. Offline selected $B^+ \to K_1(1270)^+\gamma$ MC events generated in the 2012 (2016)

running conditions are used as a proxy for the signal, while the proxy for background consists of events in the upper mass sideband of the signal peak, defined as $m_{K\pi\pi\gamma} > 5620\,\mathrm{MeV}/c^2$, in the offline-selected data sets collected in 2011 and 2012 (2016 and 2017).

Feature selection   The features given as input to the classification algorithm are chosen to be independent of the reconstructed B mass and well reproduced in MC (so the PID variables are excluded):

- the vertex χ^2 of the three charged tracks;

- the χ^2_{IP} (defined in Sec. 4.4) of the B meson;

- the minimum χ^2_{IP} for the three charged tracks, which reflects the displacement of these tracks with respect to the PV;

- the flight distance χ^2, which is the χ^2 of a fit where the B candidate and the PV are fitted as a single vertex; if the B meson is far from the PV, this value is expected to be large;

- the DIRA variable which is the cosine of the angle between the B momentum and the direction from the PV to the decay vertex of the B meson (see Sec. 4.4);

- the B meson isolation $\Delta\chi^2$ defined in Sec. 4.5.1.

In addition, the following features, which were not available in Run 1, are used for Run 2:

- a B meson isolation variable built with two tracks added to the B vertex instead of a single one;

- a χ^2_{IP} of the B computed using the next best primary vertex instead of the best one;

- cone isolation variables for the B meson, the photon and the kaonic resonance K_{res}. These variables give information about the charged tracks contained in cones drawn around the trajectory of a particle of interest X. In this study, three values of the cone radius R are used, $R = 1$, 1.35 or 1.7, which means that all the charged tracks entering the computation of the isolation variables are such that their difference in pseudo-rapidity $\delta\eta$ and azimuthal angle $\delta\phi$ with respect to the trajectory of the particle of interest obey the relation $\sqrt{(\delta\eta)^2 + (\delta\phi)^2} < R$. Within this cone, the track multiplicity (not including any track forming the particle of interest) is computed, as well as the sum of p and sum of p_{T} over this set of tracks. Two

additional variables defined within this cone are the p asymmetry

$$\text{Cone } p \text{ asymmetry} = \frac{p(X) - \sum\limits_{\text{track} \in \text{cone}} p(\text{track})}{p(X) + \sum\limits_{\text{track} \in \text{cone}} p(\text{track})} \tag{4.1}$$

and the analogous p_T asymmetry. The two asymmetries are expected to be close to 1 for well isolated particles.

Considering the large number of variables available in Run 2 for the training of the classifier, a selection of the most interesting ones is performed. A first classifier with a reasonable set of hyper-parameters is hence trained on one third of the 2016–2017 data set and associated MC. A test data sample which amounts to one sixth of the data is used to assess the quality of the training and the absence of over-fitting. Using this classifier, it is possible to evaluate the relative importance of each variable in the final prediction, and the 15 most discriminant ones are selected for the classifier optimization described below.

Classifier training and optimization The following sequence is used to train and optimize the classifier:

- In order to avoid applying the classification to events that have been used to train the classifier, the full sample consisting of the signal MC events and data events from the upper B^+ mass sideband is randomly divided into two data sets of equal size $A0$ and $A1$.

- Each of these two subsamples is then divided into a training and a testing data set that amount to 2/3 and 1/3 of the subsample, respectively.

- Two separate classifiers sharing the same set of hyper-parameters are trained on the training subsamples of $A0$ and $A1$. Their individual performance is evaluated by computing the area under the ROC curve. The over-fitting is estimated by plotting for each classifier the distributions of the classifier output for the signal and background in the training and testing data sets, as shown in Fig. 4.4 in the case of $A0$. A Kolmogorov-Smirnov test is performed to check the compatibility of the distributions for the background events in the training and testing data sets, and the same is done for the signal events. If the p-value of these two tests is above 0.1, the distributions are compatible and there is no over-fitting.

- This procedure is repeated several times for different sets of hyper-parameters, and the optimal configuration is chosen as the one where the largest value of the minimum performance of the two classifiers is obtained with no over-fitting.
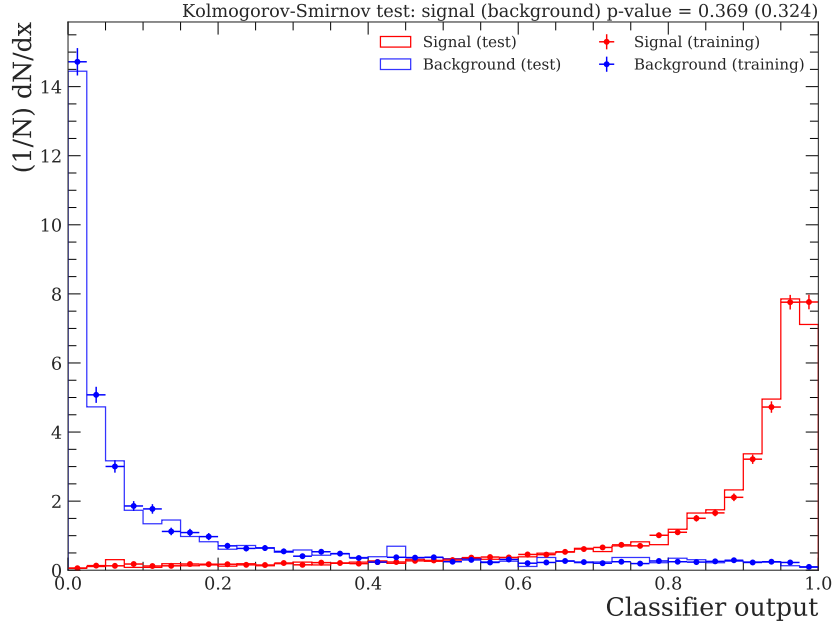
Figure 4.4 – Distribution of the output variable of the optimized classifier $A0$ for the background and signal of the testing and training data sets. The p-value of the Kolmogorov-Smirnov tests performed in order to assess the compatibility between the distributions obtained for the testing and training data sets are shown at the top for the signal and background events. Credits to Cyrille Praz for the figure.

- Once the two classifiers are chosen and trained, a cut is performed on each of the two output variables in order to maximize the sensitivity defined as $S/\sqrt{S+B}$ where S and B are respectively the number of expected signal and background events in a signal region of $\pm 200 \, \text{MeV}/c^2$ around the B^+ mass: $[5080, 5480] \, \text{MeV}/c^2$. For the classifier trained on $A0$, the cut is optimized using the associated testing sample in $A0$, and the same goes for the $A1$ sample.

- Finally, the classifier trained and tested on $A0$ is applied on $A1$, as well as the corresponding cut on the output variable, and vice-versa. For each of the other events in the samples, one of the classifiers is chosen randomly, its output is computed and the associated cut is applied.

Results For the two classifiers aimed at selecting signal candidates in the 2011–2012 data sets, the optimized set of hyper-parameters is shown in Table 4.6 and results in areas under the ROC curve of 0.93 and 0.94. The optimal selection for each of these two classifiers is to require the output variable to be above 0.15.

For the selection of the candidates in the 2016–2017 data sets, the 15 most important features are found to be the χ^2_{IP} of the B^+ candidate and of the three charged tracks of

Table 4.6 – Optimized set of hyper-parameters found for the classifiers used for the selection of signal candidates in the 2011–2012 and the 2016–2017 data sets.

Variable	2011–2012	2016–2017
Learning rate	0.05	0.05
Regularization parameter	5	5
Subsample fraction	0.1	0.1

the daughter particles, the vertex χ^2 of the three charged tracks, the DIRA variable and the one-track vertex isolation of the B^+, the χ^2_{IP} of the B^+ with respect to the second best primary vertex, the p_{T} asymmetry in a cone around the B^+ direction with $R = 1$, 1.35 and 1.7, the p_{T} asymmetry in a cone of $R = 1$ around the γ direction, the sum of p in a cone of $R = 1$ around the B^+ and around the γ, and finally the B vertex χ^2. Using these variables, the hyper-parameters are optimized following the procedure described above and the resulting parameters are listed in Table 4.6. The area under the ROC curve for the best configuration is 0.95 for both classifiers. The optimal cut is also found to be the same (0.15) for both classifiers.

Additionally to this study, other classifiers have been trained in order to reduce the amount of partially reconstructed background, using data events from the lower mass sideband $(m_{K\pi\pi\gamma} < 5080\,\mathrm{MeV}/c^2)$ as a proxy for background. The same input variables were provided to these classifiers, but none of them resulted in a satisfactory discrimination, so only the multivariate classifiers trained against combinatorial background are kept for this study.

4.6   Signal and background studies

4.6.1   Signal model

The $K^+\pi^-\pi^+\gamma$ mass distributions are studied using the $B^+ \to K^+\pi^-\pi^+\gamma$ signal MC samples listed in Tables 4.1 and 4.2. As the data-taking conditions were similar throughout each of the runs, 2012 (2016) MC is used to describe the signal events in the 2011–2012 (2016–2017) data sets. The 2016 MC samples used for this study contain only $K_1(1270)$ decays, while the 2012 MC samples contain $K_1(1270)$, $K_1(1400)$ and $K^*(1410)$ decays.

After applying the selection, the $K^+\pi^-\pi^+\gamma$ mass distribution is fitted using a double-tail Crystal Ball PDF,

$$f_{\mathrm{CB}}(x; \mu_B, \sigma, \alpha_L, \alpha_R, n_L, n_R) = N \times \begin{cases} A_L(B_L - \frac{x-\mu_B}{\sigma})^{-n_L} & \text{for } \frac{x-\mu_B}{\sigma} \leq -|\alpha_L| \\ A_R(B_R - \frac{x-\mu_B}{\sigma})^{-n_R} & \text{for } \frac{x-\mu_B}{\sigma} \geq |\alpha_R| \\ \exp(-\frac{(x-\mu_B)^2}{2\sigma^2}) & \text{for } -|\alpha_L| < \frac{x-\mu_B}{\sigma} < |\alpha_R| \end{cases},$$
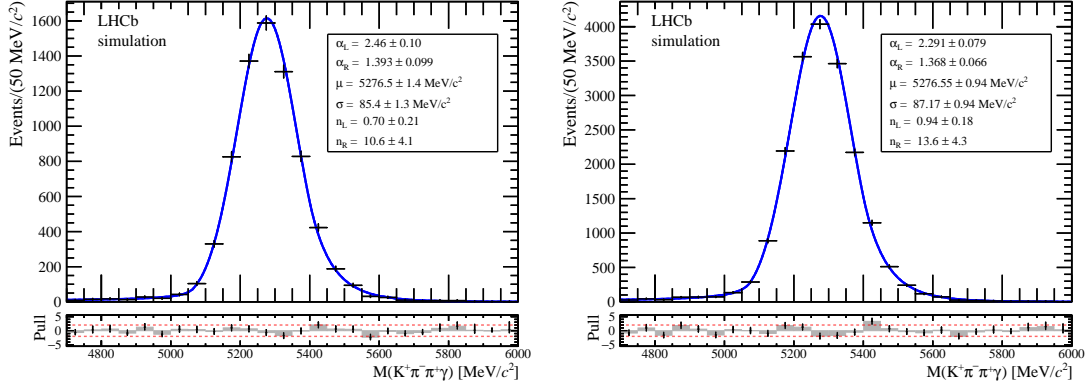
Figure 4.5 – Mass distribution of $B^+ \to K^+\pi^-\pi^+\gamma$ candidates selected in 2012 (left) and 2016 (right) $B^+ \to K_1(1270)^+\gamma$ MC samples. The result of a fit to a double-tail Crystal Ball PDF is superimposed.

Table 4.7 – Fitted values of the double-tail Crystal Ball function parameters in 2012 and 2016 signal MC.

Parameter	2012 $K_1(1270)\gamma$	2012 $K_1(1400)\gamma$	2012 $K^*(1410)\gamma$	2016 $K_1(1270)\gamma$	Unit
μ_B	5276.5 ± 1.4	5278.2 ± 1.3	5278.1 ± 1.2	5276.6 ± 0.9	MeV/c^2
σ	85.4 ± 1.3	89.4 ± 1.2	87.0 ± 1.1	87.2 ± 0.9	MeV/c^2
α_L	2.46 ± 0.10	2.42 ± 0.15	2.45 ± 0.10	2.29 ± 0.08	
α_R	1.39 ± 0.10	1.73 ± 0.10	1.79 ± 0.12	1.37 ± 0.07	
n_L	0.70 ± 0.21	0.70 ± 0.30	0.76 ± 0.23	0.94 ± 0.18	
n_R	10.6 ± 4.1	4.6 ± 1.1	4.2 ± 1.1	13.6 ± 4.3	

$$(4.2)$$

where N is a normalisation factor and

$$A_L = \left(\frac{n_L}{|\alpha_L|}\right)^{n_L} \exp\left(-\frac{\alpha_L^2}{2}\right), \quad B_L = \frac{n_L}{|\alpha_L|} - |\alpha_L|,$$

$$A_R = \left(-\frac{n_R}{|\alpha_R|}\right)^{n_R} \exp\left(-\frac{\alpha_R^2}{2}\right), \quad B_R = -\frac{n_R}{|\alpha_R|} + |\alpha_R|.$$

All parameters are left free in the fits to simulated signal events shown in Figs. 4.5 and 4.6, and their fitted values are shown in Table 4.7. These values show a reasonable agreement between the various resonances, with the largest deviations seen in the parameters describing the right tail, α_R and n_R. As the $K_1(1270)$ resonance is the most abundant in data [53], the shape parameters from $B^+ \to K_1(1270)^+\gamma$ MC will be used to describe the signal in the mass fit to data.
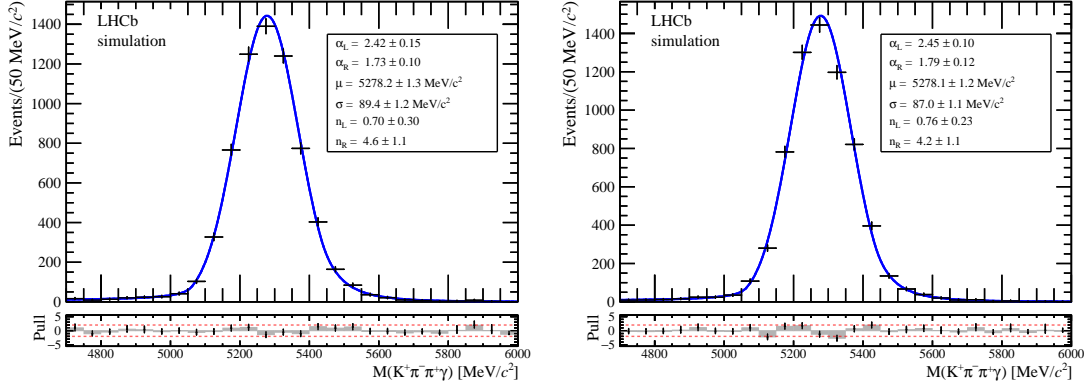
Figure 4.6 – Mass distribution of $B^+ \to K^+\pi^-\pi^+\gamma$ candidates selected in 2012 $B^+ \to K_1(1400)^+\gamma$ (left) and $B^+ \to K^*(1410)^+\gamma$ (right) MC samples. The result of a fit to a double-tail Crystal Ball PDF is superimposed.

4.6.2 Double mis-identification of same-sign K and π

In the stripping, all three tracks of the signal decay are assumed to be pions, so a $B^+ \to \pi^+\pi^-\pi^+\gamma$ candidate is formed. In a subsequent step, two $B^+ \to K^+\pi^-\pi^+\gamma$ candidates are derived by replacing in turn the mass hypothesis of one of the two positively charged pions by that of a kaon. Then, the offline selection is applied and, in most of the cases, the particle identification requirement eliminates one of these two candidates. The fraction of events for which two candidates are kept after offline selection is 0.3%, 0.4%, 0.8% and 0.7% in 2011, 2012, 2016 and 2017, respectively. Considering their low abundance, these multiple candidates are kept in order to avoid introducing biases in the selection.

4.6.3 Specific background studies

Several exclusive B decays with very similar final states can contaminate the $B^+ \to K^+\pi^-\pi^+\gamma$ mass spectrum:

- $B^+ \to a_1^+(\to \pi^+\pi^-\pi^+)\gamma$ decays where a pion is mis-identified as a kaon;

- B-hadron decays to a $K^+\pi^-\pi^+\pi^0$ final state, where the π^0 is either resolved (and one of the daughter photons escapes selection) or merged (and is seen as a single calorimeter cluster), such as $B^+ \to \bar{D}^0(\to K^+\pi^-\pi^0)\pi^+$ and $B^+ \to K^{*+}(\to K^+\pi^0)\pi^+\pi^-$;

- $B^+ \to \bar{D}^0(\to K^+\pi^-\pi^0)\rho^+(\to \pi^+\pi^0)$ decays, which have been discussed in Sec. 4.5.1;

- B decays involving a D^* with a neutral object in its decay products, such as $B^+ \to \bar{D}^{*0}(\to \bar{D}^0(\to K^+\pi^-)\gamma)\pi^+$ or $B^+ \to \bar{D}^{*0}(\to \bar{D}^0(\to K^+\pi^-)\pi^0)\pi^+$;

101

- $B^0 \to K_1(1270)^0\gamma$ decays where the π^0 from $K_1(1270)^0 \to K^+\pi^-\pi^0$ is ignored and a π^- from the rest of the event is wrongly associated with the decay;

- $B^+ \to K^+\pi^-\pi^+\eta(\to \gamma\gamma)$ or $B^+ \to K^+\pi^-\pi^+\pi^0(\to \gamma\gamma)$ decays, where one γ is not used to form the candidate.

The contamination associated with each of the exclusive decays mentioned above is computed from simulation using the formula

$$C_{\mathrm{bkg}} = \frac{N_{\mathrm{bkg}}}{N_{\mathrm{sig}}} = \frac{2\,\mathcal{L}\,\sigma(pp \to b\bar{b})\,f_{\mathrm{bkg}}\,\mathcal{B}_{\mathrm{bkg}}\,\epsilon_{\mathrm{bkg}}}{2\,\mathcal{L}\,\sigma(pp \to b\bar{b})\,f_{\mathrm{sig}}\,\mathcal{B}_{\mathrm{sig}}\,\epsilon_{\mathrm{sig}}} = \frac{f_{\mathrm{bkg}}\,\mathcal{B}_{\mathrm{bkg}}\,\epsilon_{\mathrm{bkg}}}{f_{\mathrm{sig}}\,\mathcal{B}_{\mathrm{sig}}\,\epsilon_{\mathrm{sig}}}\,, \tag{4.3}$$

where N is the number of events expected in the full fitting mass range, $\mathcal{L}$ is the total integrated luminosity, $\sigma(pp \to b\bar{b})$ is the $b\bar{b}$ production cross-section in pp collisions, f is the fragmentation fraction, $\mathcal{B}$ is the branching fraction product of the full decay chain given in Table 4.8, and ϵ is the total reconstruction and selection efficiency given in Table 4.9. The mass interval considered for the efficiencies is also the full fitting mass range 4300–6500 MeV/c^2.

The estimation of the unknown branching fractions of $B^+ \to K^+\pi^-\pi^+\eta$ and $B^+ \to K^+\pi^-\pi^+\pi^0$ decays is explained in the paragraphs dedicated to these backgrounds. The branching ratio of $B^+ \to a_1^+(\to \pi^+\pi^-\pi^+)\gamma$ decays can be estimated by noting that they involve a $b \to d$ transition while $B^+ \to K^+\pi^-\pi^+\gamma$ decays imply a $b \to s$ transition. This allows to write the ratio of branching fractions as a function of the *CKM* matrix elements V_{td} and V_{ts} as

$$\frac{\mathcal{B}(B^+ \to \pi^+\pi^-\pi^+\gamma)}{\mathcal{B}(B^+ \to K^+\pi^-\pi^+\gamma)} \simeq \left|\frac{V_{td}}{V_{ts}}\right|^2 \simeq 0.04\,. \tag{4.4}$$

These decays are hence very suppressed with respect to $B^+ \to K^+\pi^-\pi^+\gamma$ decays.

Table 4.8 – List of potential peaking backgrounds and their branching fraction products obtained from PDG [19] or estimated (when no uncertainty is quoted). The branching fraction of the $B^+ \to K^+\pi^-\pi^+\gamma$ signal is taken as $\mathcal{B}_{\mathrm{sig}} = (2.58 \pm 0.15) \times 10^{-5}$ [19].

Decay chain	$\mathcal{B}_{\mathrm{bkg}}$
$B^+ \to a_1^+(\to \pi^+\pi^-\pi^+)\gamma$	1.03×10^{-6}
$B^+ \to \bar{D}^0(\to K^+\pi^-\pi^0)\pi^+$	$(6.6 \pm 0.3) \times 10^{-4}$
$B^+ \to K^{*+}(\to K^+\pi^0)\pi^+\pi^-$	$(2.5 \pm 0.3) \times 10^{-5}$
$B^+ \to \bar{D}^0(\to K^+\pi^-\pi^0)\rho^+(\to \pi^+\pi^0)$	$(1.9 \pm 0.3) \times 10^{-3}$
$B^+ \to \bar{D}^{*0}(\to \bar{D}^0(\to K^+\pi^-)\gamma)\pi^+$	$(6.7 \pm 0.3) \times 10^{-5}$
$B^+ \to \bar{D}^{*0}(\to \bar{D}^0(\to K^+\pi^-)\pi^0)\pi^+$	$(1.23 \pm 0.05) \times 10^{-4}$
$B^0 \to K^+\pi^-\pi^0\gamma$	$(4.1 \pm 0.4) \times 10^{-5}$
$B^+ \to K^+\pi^-\pi^+\eta(\to \gamma\gamma)$	5.0×10^{-6}
$B^+ \to K^+\pi^-\pi^+\pi^0$	4.5×10^{-6}

Table 4.9 – List of potential peaking backgrounds, together with their efficiency and contamination in the full B^+ mass range in 2012 and 2016 MC. When less than 10 candidates pass the selection, a 90% confidence level upper limit is quoted. The efficiencies of the $B^+ \to K_1(1270)^+\gamma$ signal are $\epsilon_{\mathrm{sig}}^{2012} = (3.61 \pm 0.04) \times 10^{-3}$ and $\epsilon_{\mathrm{sig}}^{2016} = (6.44 \pm 0.05) \times 10^{-3}$.

Decay chain	Year	ϵ_{bkg}	C_{bkg}
$B^+ \to a_1^+(\to \pi^+\pi^-\pi^+)\gamma$	2012	$(1.13 \pm 0.08) \times 10^{-4}$	$(0.13 \pm 0.01)\%$
	2016	$(3.13 \pm 0.27) \times 10^{-4}$	$(0.19 \pm 0.02)\%$
$B^+ \to \bar{D}^0(\to K^+\pi^-\pi^0)\pi^+$	2012	$< 3.7 \times 10^{-6}$	$< 2.6\%$
	2017	$< 2.9 \times 10^{-6}$	$< 1.2\%$
$B^+ \to K^{*+}(\to K^+\pi^0)\pi^+\pi^-$	2012	$< 1.5 \times 10^{-6}$	$< 0.04\%$
	2016	$< 6.1 \times 10^{-6}$	$< 0.09\%$
$B^+ \to \bar{D}^0(\to K^+\pi^-\pi^0)\rho^+(\to \pi^+\pi^0)$	2012	$(8.5 \pm 3.9) \times 10^{-6}$	$(17.4 \pm 8.3)\%$
	2016	$(1.19 \pm 0.45) \times 10^{-5}$	$(13.6 \pm 5.6)\%$
$B^+ \to \bar{D}^{*0}(\to \bar{D}^0(\to K^+\pi^-)\pi^0)\pi^+$	2012	$< 3.0 \times 10^{-6}$	$< 0.39\%$
	2016	$< 1.8 \times 10^{-6}$	$< 0.14\%$
$B^+ \to \bar{D}^{*0}(\to \bar{D}^0(\to K^+\pi^-)\gamma)\pi^+$	2012	$< 4.6 \times 10^{-6}$	$< 0.33\%$
	2016	$< 2.3 \times 10^{-6}$	$< 0.09\%$
$B^0 \to K^+\pi^-\pi^0\gamma$	2012	$< 3.1 \times 10^{-6}$	$< 0.14\%$
	2016	$< 2.3 \times 10^{-5}$	$< 0.56\%$
$B^+ \to K^+\pi^-\pi^+\eta(\to \gamma\gamma)$	2012	$(1.58 \pm 0.03) \times 10^{-3}$	$(8.5 \pm 1.1)\%$
	2016	$(2.62 \pm 0.07) \times 10^{-3}$	$(7.9 \pm 1.0)\%$
$B^+ \to K^+\pi^-\pi^+\pi^0$	2016	$(3.05 \pm 0.04) \times 10^{-3}$	$(8.2 \pm 1.4)\%$

As seen from Table 4.9, the only potentially significant contaminations are those from $B^+ \to K^+\pi^-\pi^+\eta$, $B^+ \to K^+\pi^-\pi^+\pi^0$ and $B^+ \to \bar{D}^0(\to K^+\pi^-\pi^0)\rho^+(\to \pi^+\pi^0)$ decays. These decays are accounted for in the mass fit with dedicated background components. We describe below studies to determine the shapes of these components.

$B^+ \to K^+\pi^-\pi^+\eta \, (\to \gamma\gamma)$ decays

The $B^+ \to K^+\pi^-\pi^+\eta$ decays, where η decays into $\gamma\gamma$ and one γ is not used to form the candidate, is a potentially dangerous background because it lies very close to the signal peak.

A simple calculation assuming perfect resolution shows that for $B^+ \to K^+\pi^-\pi^+\eta$ decays proceeding through the intermediate resonance $K_1(1270)$ and reconstructed as $B^+ \to K^+\pi^-\pi^+\gamma$, the $K^+\pi^-\pi^+\gamma$ invariant mass distribution has its upper end-point at the mass of the B^+ minus $30\,\mathrm{MeV}/c^2$. For heavier resonances, this distance tends to increase. When including the mass resolution, this distribution enters largely the signal region.

The contamination from this background is estimated with simulated events, assuming that the ratio between the branching fractions for $B^+ \to K^+\pi^-\pi^+\eta$ and $B^+ \to K^+\pi^-\pi^+\gamma$ decays is the same as for $B^+ \to K^{*+}\eta$ and $B^+ \to K^{*+}\gamma$ decays. From the latest
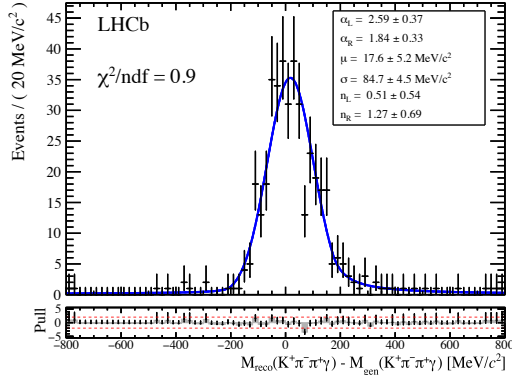
Figure 4.7 – Distribution of the reconstructed minus generated mass (without the missing photon) for truth-matched $B^+ \to K^+\pi^-\pi^+\eta$ events reconstructed as $B^+ \to K^+\pi^-\pi^+\gamma$ in 2016 MC. The result of a fit to a double-tail Crystal Ball PDF is superimposed.
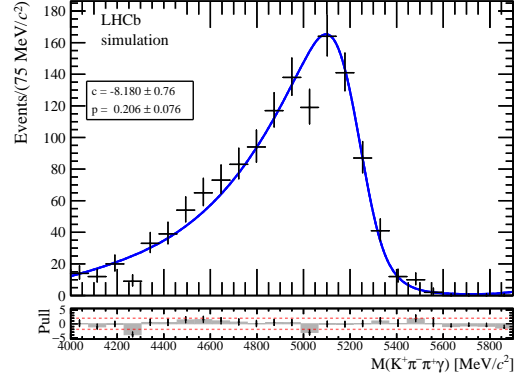
Figure 4.8 – Mass distribution of $B^+ \to K^+\pi^-\pi^+\eta$ decays reconstructed as $B^+ \to K^+\pi^-\pi^+\gamma$ in 2016 MC. The result of a fit to an Argus of fixed end-point $30\,\mathrm{MeV}/c^2$ below the B^+ mass and convolved with a double-tail Crystal Ball PDF fixed from the 2016 signal MC is superimposed.

measurements [19], the value of this ratio is 0.49 ± 0.05. Using the ratio of efficiencies between this background and the signal, the contamination in the full fitting range is estimated to be 8.5% in Run 1 and 7.9% in Run 2.

This background is modelled with a shape describing the true mass distribution of $B^+ \to K^+\pi^-\pi^+\eta$ decays reconstructed as $B^+ \to K^+\pi^-\pi^+\gamma$, convolved with a function accounting for the resolution of the detector. The shape of the true mass distribution is studied with simulated events and is modelled by an Argus PDF,

$$f_{\mathrm{Argus}}(x; m_0, c, p) = Nx\left(1 - \frac{x^2}{m_0^2}\right)^p \exp\left\{c\left(1 - \frac{x^2}{m_0^2}\right)\right\} \quad \text{for } 0 \leq x \leq m_0,$$

where N is a normalization factor and the parameters m_0, c and p are called the end-point, curvature and power, respectively.

For the $B^+ \to K^+\pi^-\pi^+\gamma$ candidates coming from $B^+ \to K^+\pi^-\pi^+\eta$ decays, the resolution function is studied by plotting the difference between the reconstructed $K^+\pi^-\pi^+\gamma$ mass and the invariant mass computed using the true momenta of the reconstructed K^+, π^-, π^+ and γ. This distribution is shown in Fig. 4.7 in truth-matched 2016 MC and is fitted with a double-tail Crystal Ball PDF whose parameters (except μ_B) are found to be reasonably compatible with those of the signal.

Finally, the $K^+\pi^-\pi^+\gamma$ invariant mass distribution in $B^+ \to K^+\pi^-\pi^+\eta$ decays reconstructed as $B^+ \to K^+\pi^-\pi^+\gamma$ is modelled by an Argus PDF with its end-point fixed $30\,\mathrm{MeV}/c^2$ below the B^+ mass, and convolved with a double-tail Crystal Ball PDF whose parameters are fixed from the fit to $B^+ \to K_1(1270)^+\gamma$ signal MC reported in Table 4.7.

Only the c and p parameters of the Argus PDF are left free. The resulting fit is shown in Fig. 4.8.

$B^+ \to K^+\pi^-\pi^+\pi^0 (\to \gamma\gamma)$ decays

Other potentially dangerous backgrounds are $B^+ \to K^+\pi^-\pi^+\pi^0$ decays, where the π^0 decays into two photons. Contrary to the photons coming from an η meson, which are always well separated in the calorimeter, those coming from a π^0 (which is much lighter than the η) are in general very close to each other or even merged, as explained in Sec. 4.5.1. For this reason, the neutral object in the reconstructed $B^+ \to K^+\pi^-\pi^+\gamma$ candidate carries all or part of the energy of the two photons coming from the B^+ meson, which means that the distribution of the $K^+\pi^-\pi^+\gamma$ mass is much more peaked around the B^+ mass.

The contamination from this background is estimated with a sample of simulated $B^+ \to K_1(1270)^+\pi^0$ decays, assuming that the ratio between the branching fractions of $B^+ \to K^+\pi^-\pi^+\pi^0$ and $B^+ \to K^+\pi^-\pi^+\gamma$ decays is the same as for $B^+ \to K^{*+}\pi^0$ and $B^+ \to K^{*+}\gamma$ decays. Using the measurements reported in Ref. [19], the value of this ratio is 0.17 ± 0.02. This results in a contamination in the full fitting range of 8.2% in Run 2. As no simulated sample with $B^+ \to K_1(1270)^+\pi^0$ decays is available for Run 1, the same contamination of 8.2% is assumed in Run 1.

As the two photons coming from the π^0 tend to merge in a single cluster, the reconstructed γ candidate carries all or part of the energy of the photon pair, so the PDF for this background component cannot be described by the signal resolution function convolved with an Argus function. Instead, this background is modeled by a double-tail Crystal Ball with parameters obtained from a fit to $B^+ \to K_1(1270)^+\pi^0$ simulated events as shown in Fig. 4.9.

In the fit to data, all the parameters of the double-tail Crystal Ball for this background are fixed to their value in 2016 MC, except for the mean of the distribution, which is set to $\mu_B - \Delta(\mu_B^{\mathrm{MC}}, \mu_{\pi^0}^{\mathrm{MC}})$, where μ_B is the mean of the signal distribution in data, and $\Delta(\mu_B^{\mathrm{MC}}, \mu_{\pi^0}^{\mathrm{MC}})$ is the difference between the means of the mass distributions in $B^+ \to K_1(1270)^+\gamma$ and $B^+ \to K_1(1270)^+\pi^0$ 2016 MC. This allows to take into account possible calibration effects that would shift the mean of the signal mass peak between the different years.

Partially reconstructed background with one missing pion

The invariant mass spectrum in the full fit range also receives contributions from partially reconstructed B decays where one more pion is emitted but not used in the detector. One example are the $B^+ \to \bar{D}^0(\to K^+\pi^-\pi^0)\rho^+(\to \pi^+\pi^0)$ decays discussed above, but
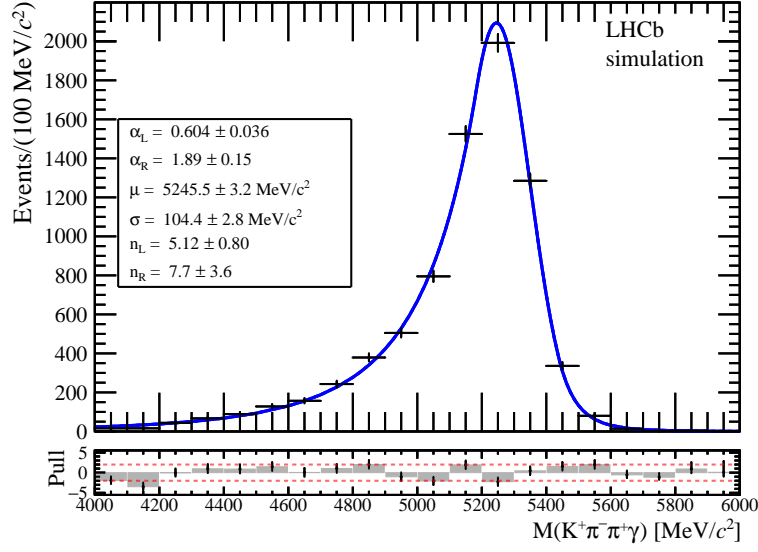
Figure 4.9 – Mass distribution of $B^+ \to K_1(1270)^+\pi^0$ decays reconstructed as $B^+ \to K^+\pi^-\pi^+\gamma$ in 2016 MC. The result of a fit to a double-tail Crystal Ball PDF is superimposed.

there may be many others.

This background is modeled with an Argus function convolved with a double-tail Crystal Ball function that encodes the resolution of the detector. Due to the lack of a sizable MC sample for $B^+ \to K^+\pi^-\pi^+\gamma$ decays, a MC sample of $B^0 \to K^{*0}\gamma$ decays is used as a proxy for the signal and a MC sample of $B^+ \to K^{*0}\pi^+\gamma$ decays reconstructed as $B^0 \to K^{*0}\gamma$ is used as a proxy for the partially reconstructed background with one missing pion. In order to study the resolution function to be used for this background, the distribution of the reconstructed minus generated $K^+\pi^-\gamma$ mass for truth-matched $B^+ \to K^{*0}\pi^+\gamma$ candidates has been obtained (as shown in Fig. 4.10) and compared with the resolution in the signal proxy $B^0 \to K^{*0}\gamma$ (as shown in Fig. 4.11). The parameters of the double-tail Crystal Ball functions used to describe these two distributions are found to be compatible except for the width, which is significantly smaller in the case of the partially reconstructed background. The ratio between the widths of the former and the latter distributions is found to be $r = 0.88 \pm 0.03$ in 2012 and $r = 0.91 \pm 0.02$ in 2016.

Several checks have been performed concerning these resolution functions. As shown in Fig. 4.12, the width of the resolution function is comparable between the several heavy kaonic resonances involved in the $B^+ \to K^{*0}\pi^+\gamma$ decay. Additionnally, it can be noted in the same figure that when the decays are fully reconstructed, the width of the resolution function is always wider than the width of the resolution of partially reconstructed decays, indicating that the photon, even if it dominates the resolution function, cannot be assumed to be the only contributor.
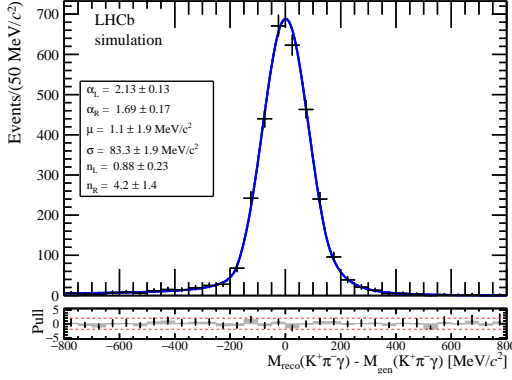
Figure 4.10 – Distribution of the reconstructed minus generated $K^+\pi^-\gamma$ mass for truth-matched $B^+ \to K^{*0}\pi^+\gamma$ candidates in 2016 MC simulation. The result of a fit to a double-tail Crystal Ball PDF is superimposed.

Figure 4.11 – Distribution of the $K^+\pi^-\gamma$ invariant mass for selected $B^0 \to K^{*0}\gamma$ candidates in 2016 MC simulation. The result of a fit to a double-tail Crystal Ball PDF is superimposed.

Finally, the parameters of the mass shape used to describe the background where one pion is missing are obtained as follows: the parameters of the double-tail Crystal Ball function are fixed to be the same as for the signal, except for the width which is set to r times the width of the signal function, and the end-point of the Argus is constrained to be equal to the mass of the B meson minus one neutral pion mass. The c and p parameters of the Argus are obtained from a fit to simulated $B^+ \to K^{*0}\pi^+\gamma$ events reconstructed as $B^0 \to K^{*0}\gamma$, where the resolution function is that of simulated $B^0 \to K^{*0}\gamma$ decays with the width multiplied by r, and the end-point is fixed to the mass of the B meson minus that of a charged pion (as a charged pion is missing in this case). The result of this fit is shown in Fig. 4.13.

4.6.4 Generic background models

Partially reconstructed background with two or more missing pions

In the remaining partially reconstructed decays considered as a background component in the mass fit, two or more pions are not used to form the candidates. This background component encompasses many types of decays and is hence modeled with a generic shape for partially reconstructed backgrounds called *RooPhysBkg* [102], the expression of which is

$$f_{\text{phys}}(x, m_p, \sigma_p, c_p) = N \int_{-\infty}^{+\infty} x' \left(1 - \frac{x'^2}{m_p^2}\right) \Theta(m_p - x') e^{-c_p x'} \frac{1}{\sqrt{2\pi}\sigma_p} e^{-\frac{1}{2}\left(\frac{x-x'}{\sigma_p}\right)^2} dx' ,$$

where m_p, c_p and σ_p are the end-point, the curvature and the width of the distribution, N is a normalisation factor and Θ is the step function. In the fit to data, the end-point
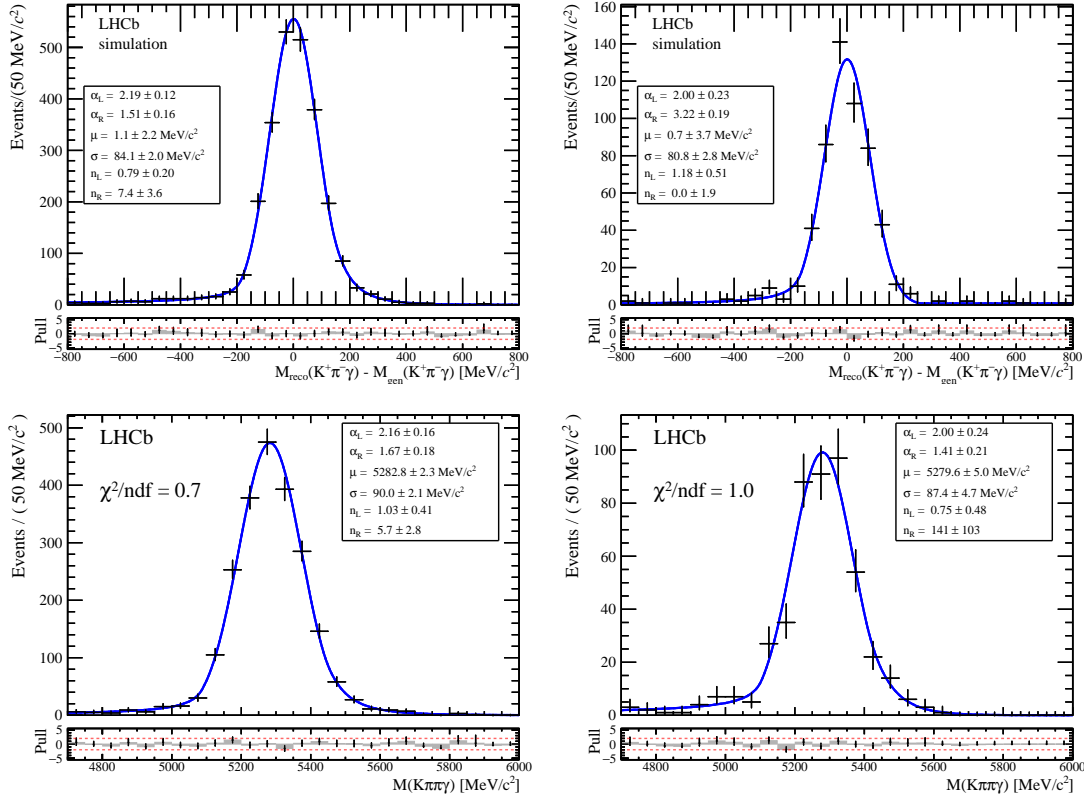
Figure 4.12 – Top: Distributions of the reconstructed minus generated $K^+\pi^-\gamma$ mass for truth-matched 2016 $B^+ \to K_{\rm res}^+(\to K^{*0}\pi^+)\gamma$ MC where the $K_{\rm res}$ is required to be a $K_1(1400)^+$ (left) or a $K_1(1680)^+$ (right). The result of a fit to a double-tail Crystal Ball PDF is superimposed and shows a good agreement between the two cases. Bottom: Distributions of the reconstructed $K^+\pi^-\pi^+\gamma$ mass in truth-matched 2016 $B^+ \to K_{\rm res}^+(\to K^{*0}\pi^+)\gamma$ MC where the $K_{\rm res}$ is required to be a $K_1(1400)^+$ (left) or a $K^*(1680)^+$ (right). The superimposed result of a fit to a double-tail Crystal Ball PDF also shows a good agreement between the two cases.

of this function is fixed to the B meson mass minus two times the neutral pion mass. All the other parameters are left free.

Combinatorial background

As many tracks and calorimeter clusters are produced in each proton-proton collision, it is likely that objects unrelated to the signal decay are combined to form a candidate, the invariant mass of which lies within the fitting range. In the nominal fit, this combinatorial background is described with an exponential function.
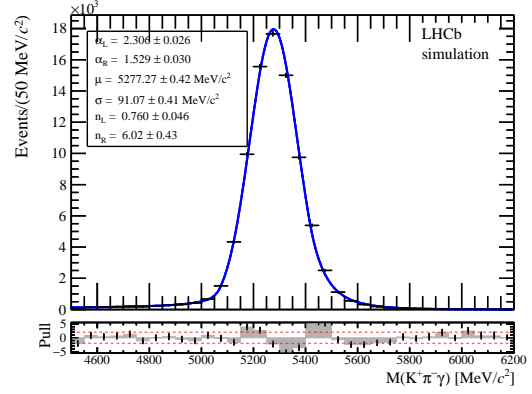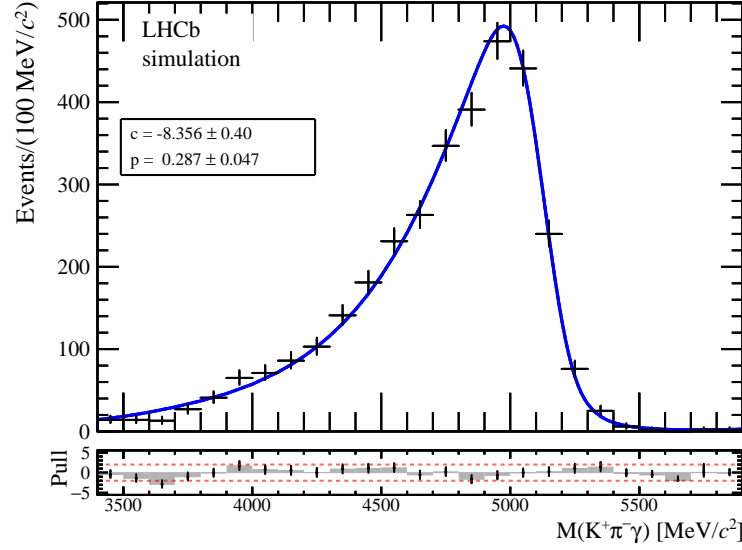
Figure 4.13 – Distribution of the $K^+\pi^-\gamma$ invariant mass for selected $B^+ \to K^{*0}\pi^+\gamma$ candidates in 2016 MC simulation. The result of a fit to an Argus function convolved with the double-tail Crystal Ball PDF fixed from the 2016 $B^0 \to K^{*0}\gamma$ MC, but with a width fixed to that of the distribution in Fig. 4.10, is superimposed.

4.7 Mass fit

4.7.1 Description of the fit

The PDF used to fit the data is a sum of all the relevant components listed above.

The signal function is modeled with a double-tail Crystal Ball PDF whose tail parameters $\alpha_{\mathrm{R/L}}$ and $n_{\mathrm{R/L}}$ are obtained from $B^+ \to K_1(1270)^+\gamma$ MC:

$$f_{\mathrm{sig}}(x; \mu_B, \sigma) = f_{\mathrm{CB}}(x; \mu_B, \sigma, \alpha_L = \alpha_L^{\mathrm{MC}}, \alpha_R = \alpha_R^{\mathrm{MC}}, n_L = n_L^{\mathrm{MC}}, n_R = n_R^{\mathrm{MC}}). \quad (4.5)$$

The background model features five components:

- The $B^+ \to K^+\pi^-\pi^+\pi^0$ background is modelled with a double-tail Crystal Ball PDF whose parameters are obtained from MC, except the mean of the distribution μ that is set to $\mu_B - \Delta(\mu_B^{\mathrm{MC}}, \mu_{\pi^0}^{\mathrm{MC}})$ as explained in Sec. 4.6.3:

$$\begin{aligned} f_{\pi^0}(x; \mu_B) = &f_{\mathrm{CB}}(x; \mu = \mu_B - \Delta(\mu_B^{\mathrm{MC}}, \mu_{\pi^0}^{\mathrm{MC}}), \sigma = \sigma^{\pi^0}, \alpha_L = \alpha_L^{\pi^0}, \alpha_R = \alpha_R^{\pi^0}, \\ &n_L = n_L^{\pi^0}, n_R = n_R^{\pi^0}). \end{aligned} \quad (4.6)$$

- The $B^+ \to K^+\pi^-\pi^+\eta$ background is modelled with an Argus PDF convolved with

109

a resolution function fixed to be the same as for the signal,

$$f_\eta(x; \mu_B, \sigma) = f_{\text{Argus}}(x; m_0 = \mu_B - m_{0,\eta}, c = c_\eta, p = p_\eta) \otimes f_{\text{sig}}(x; \mu = 0, \sigma), \quad (4.7)$$

where $m_{0,\eta}$ is set to $30\,\text{MeV}/c^2$ as explained in Sec. 4.6.3. The parameters c_η and p_η of the Argus PDF are obtained from the $B^+ \to K^+\pi^-\pi^+\eta$ MC by fitting the distribution of $B^+ \to K^+\pi^-\pi^+\eta$ decays reconstructed as $B^+ \to K^+\pi^-\pi^+\gamma$ using an Argus of free c and p convolved with a double-tail Crystal Ball function whose tail and width parameters are set from $B^+ \to K_1(1270)^+\gamma$ MC, and whose mean parameter is set to 0.

- The background with one missing pion is also modelled with an Argus PDF convolved with the signal resolution:

$$\begin{aligned} f_{1\,\text{miss}\,\pi}(x; \mu_B, \sigma) = & f_{\text{Argus}}(x; m_0 = \mu_B - m_{\pi^0}, c = c_{1\,\text{miss}\,\pi}, p = p_{1\,\text{miss}\,\pi}) \\ & \otimes f_{\text{sig}}(x; \mu = 0, r\,\sigma), \end{aligned} \quad (4.8)$$

where the end-point m_0 is set to $\mu_B - m_{\pi^0}$. The resolution function is also fixed to be that of the signal except for the width, which is multiplied by r. The parameters r, $c_{1\,\text{miss}\,\pi}$ and $p_{1\,\text{miss}\,\pi}$ are fixed as explained in Sec. 4.6.3.

- The background with two or more missing pions is modelled with a *RooPhysBkg* PDF, where the end-point m_p is set to $\mu_B - 2\,m_{\pi^0}$:

$$f_{2\,\text{miss}\,\pi}(x; \mu_B, \sigma, c_p) = f_{\text{phys}}(x; m_p = \mu_B - 2\,m_{\pi^0}, \sigma_p = \sigma, c_p). \quad (4.9)$$

The parameter c_p is left free in the fit.

- The combinatorial background is modelled with a decaying exponential PDF,

$$f_{\text{comb}}(x; \tau) = N \exp(\tau\,x), \quad (4.10)$$

where N is a normalization factor and τ is left free in the fit.

The total fit function is the sum of all these components,

$$\begin{aligned} f_{\text{tot}}(x; N_{\text{sig}}, N_{1\,\text{miss}\,\pi}, N_{2\,\text{miss}\,\pi}, N_{\text{comb}}, \mu_B, \sigma, c_p, \tau) = & N_{\text{sig}}\,f_{\text{sig}}(x; \mu_B, \sigma) \\ & + N_{\text{sig}}\,C_{\pi^0}\,f_{\pi^0}(x; \mu_B) \\ & + N_{\text{sig}}\,C_\eta f_\eta(x; \mu_B, \sigma) \\ & + N_{1\,\text{miss}\,\pi}\,f_{1\,\text{miss}\,\pi}(x; \mu_B, \sigma) \\ & + N_{2\,\text{miss}\,\pi}\,f_{2\,\text{miss}\,\pi}(x; \mu_B, \sigma, c_p) \\ & + N_{\text{comb}}\,f_{\text{comb}}(x; \tau), \end{aligned}$$

where the yields N_{sig}, $N_{1\,\text{miss}\,\pi}$, $N_{2\,\text{miss}\,\pi}$ and N_{comb} are left free, while the yield of the $B^+ \to K^+\pi^-\pi^+\pi^0$ and $B^+ \to K^+\pi^-\pi^+\eta$ backgrounds are set to $N_{\text{sig}}\,C_{\pi^0}$ and $N_{\text{sig}}\,C_\eta$, respectively. The contamination in the full fit range C_{π^0} is estimated to 8.2% in 2016 MC and is considered constant throughout all the years. The contamination C_η is considered constant throughout Run 1 (Run 2), and is fixed to its value of 8.5% (7.9%) reported in Table 4.9.

In an ideal case, the yields of the $B^+ \to K^+\pi^-\pi^+\pi^0$ and $B^+ \to K^+\pi^-\pi^+\eta$ backgrounds should have been left free in the fit, but the large number of degrees of freedom and the high correlation between their shapes and that of the signal does not allow for a good convergence.

Due to different data-taking conditions, the fractions of the various backgrounds is expected to be slightly different from year to year. The calorimeter calibration, which has a direct effect on the parameters μ_B and σ, also varies from a year to another. For these reasons, the fit is performed separately for the 2011, 2012, 2016 and 2017 data sets.

4.7.2   Results

The results of the fit are shown for the each of the data-taking years in Figs. 4.14 (linear scale) and 4.15 (log scale). The fitted parameters are reported in Table 4.10. The combinatorial background seems to behave differently for various data-taking years, with a smaller absolute value of τ in 2011. The resolution of the signal remains constant throughout 2012, 2016 and 2017, but it is worse in 2011, because of a different calorimeter calibration and trigger configuration. A total of $47\,449 \pm 321$ signal decays are observed combining all data-taking years. The number of events observed in Run 1, $12\,437 \pm 157$, is smaller than the one reported in the previous analysis of $B^+ \to K^+\pi^-\pi^+\gamma$ [53]. This difference can be explained by the fact that the $B^+ \to K^+\pi^-\pi^+\pi^0$ and $B^+ \to K^+\pi^-\pi^+\eta$ backgrounds were neglected in the previous analysis while they are now accounted for, and by changes in selection efficiency.

4.8   Background subtraction

4.8.1   sPlot technique

In order to perform the amplitude analysis of $B^+ \to K^+\pi^-\pi^+\gamma$ decays, two options can be considered. The first one consists in modeling the background and the signal distributions in all degrees of freedom of the system, and subsequently perform the amplitude analysis with a PDF for each of these components. However, as the backgrounds contaminating the $B^+ \to K^+\pi^-\pi^+\gamma$ mass spectrum are poorly known, their distributions cannot be modeled via simulations. These distributions cannot be extrapolated from the $K^+\pi^-\pi^+\gamma$
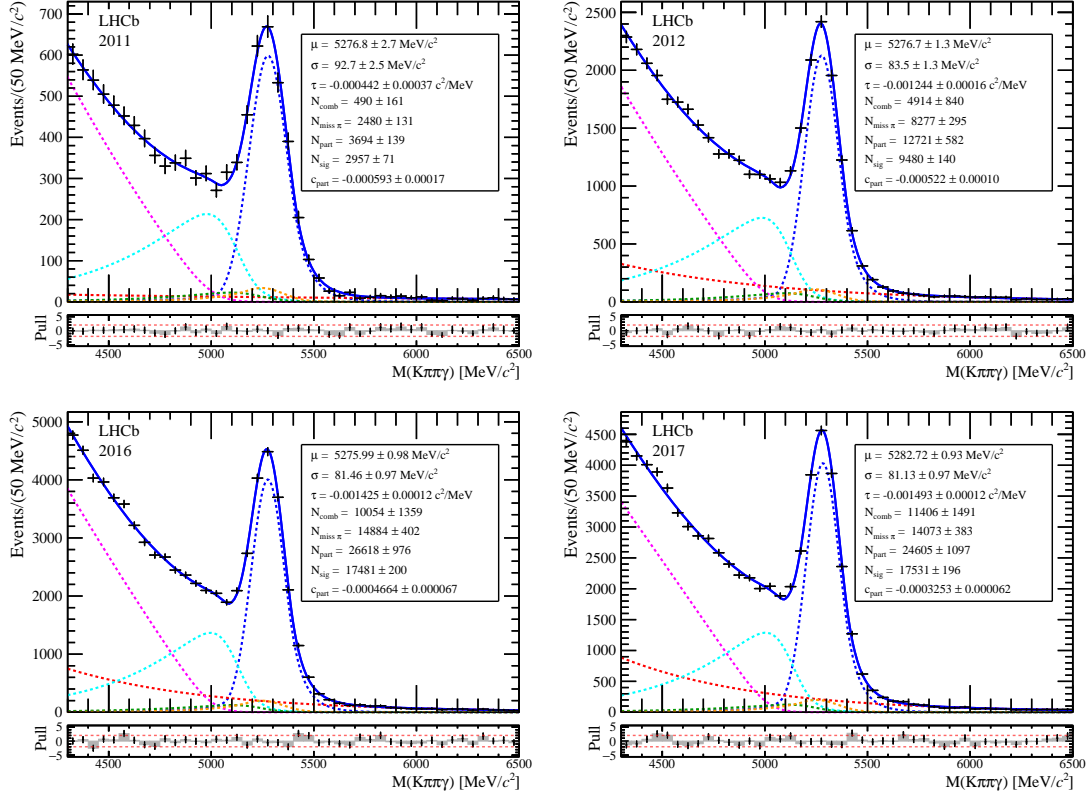
Figure 4.14 – Invariant mass distribution of the $B^+ \to K^+\pi^-\pi^+\gamma$ candidates selected in the 2011 (upper left), 2012 (upper right), 2016 (lower left) and 2017 (lower right) data sets. The total fit function is shown as the solid blue curve. It is the sum of the following components shown as dashed curves: $B^+ \to K^+\pi^-\pi^+\gamma$ signal (blue), $B^+ \to K^+\pi^-\pi^+\eta$ background (green), $B^+ \to K^+\pi^-\pi^+\pi^0$ background (orange), background with one missing pion (cyan), background with at least two missing pions (magenta) and combinatorial background (red).

mass sidebands either because of the multiple overlapping background components. In the end, the second method is used, which consists in statistically subtracting the background distributions from the data set. This background subtraction procedure, usually referred to as the *sPlot* technique [54], consists in using the information from a discriminating variable x, here the $K^+\pi^-\pi + \gamma$ invariant mass, to assign to each event a set of weights (called sWeights) that allow the distribution of any other variable y (which has to be uncorrelated to x) to be obtained for each of the species present in the data set. This is done by means of an extended maximum likelihood fit to the discriminant variable distribution x (in our case, the $K^+\pi^-\pi^+\gamma$ invariant mass), in which for each fit component (or species) i, the shape of the associated PDF f_i is fixed, and the yield N_i is left free to vary.
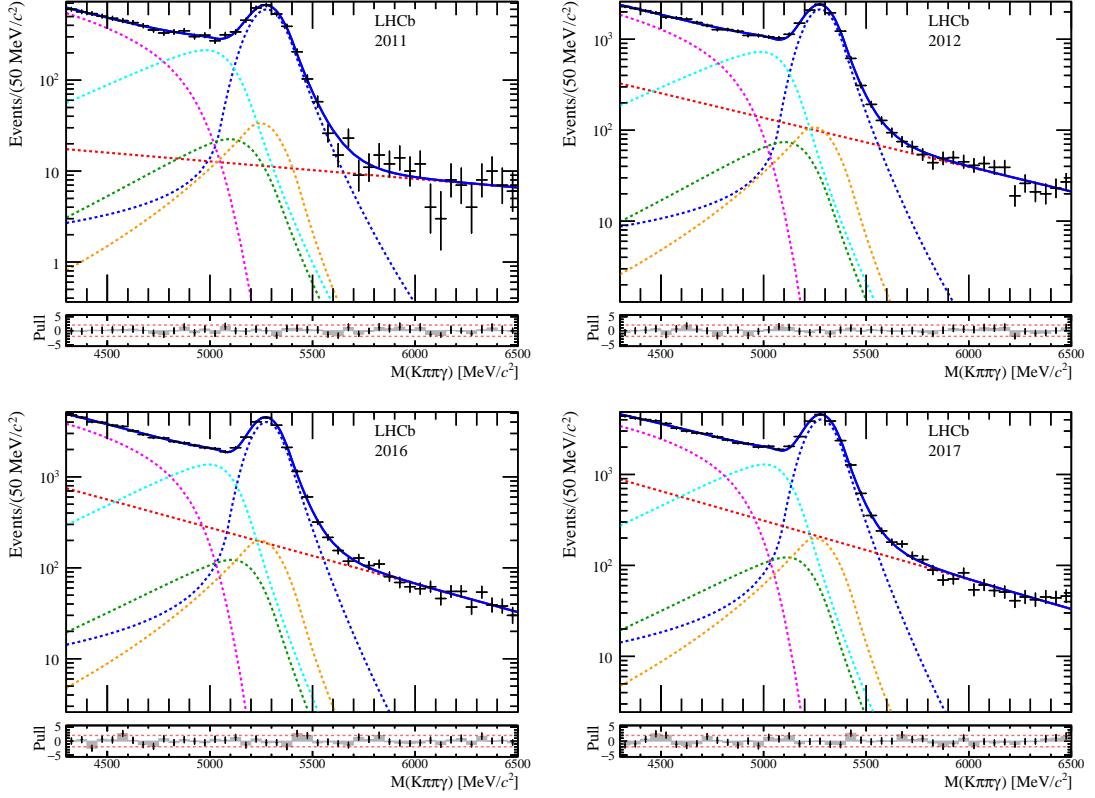
Figure 4.15 – Invariant mass distribution of the $B^+ \to K^+\pi^-\pi^+\gamma$ candidates selected in the 2011 (upper left), 2012 (upper right), 2016 (lower left) and 2017 (lower right) data sets, in logarithmic scale. The total fit function is shown as the solid blue curve. It is the sum of the following components shown as dashed curves: $B^+ \to K^+\pi^-\pi^+\gamma$ signal (blue), $B^+ \to K^+\pi^-\pi^+\eta$ background (green), $B^+ \to K^+\pi^-\pi^+\pi^0$ background (orange), background with one missing pion (cyan), background with at least two missing pions (magenta) and combinatorial background (red).

In this case, the log likelihood reads:

$$\mathcal{L}(N_1, .., N_{n_c}) = \sum_{e=1}^{N} \ln \left\{ \sum_{i=1}^{n_c} N_i f_i(x_e) \right\} - \sum_{i=1}^{n_c} N_i \,, \tag{4.11}$$

where $f_i(x_e)$ is the value of the PDF component f_i evaluated for event e, N is the total number of events in the data sample and n_c is the number of components in the mass fit.

The sWeight s_i that allows to recover the distribution of the y variable for the species i is then

$$s_i(x_e) = \frac{\sum_{j=1}^{n_c} \mathbf{V}_{ij} f_j(x_e)}{\sum_{k=1}^{n_c} N_k f_k(x_e)}, \tag{4.12}$$

Table 4.10 – Fit parameters obtained from the mass fit of the $B \to K\pi\pi\gamma$ candidates selected in the 2011, 2012, 2016 and 2017 data sets.

Fit parameter	2011	2012	2016	2017
N_{sig}	2957 ± 71	9480 ± 140	$17\,481 \pm 200$	$17\,531 \pm 196$
$N_{1\,\text{miss}\,\pi}$	2480 ± 131	8297 ± 295	$14\,884 \pm 402$	$14\,073 \pm 383$
$N_{2\,\text{miss}\,\pi}$	3694 ± 139	$12\,721 \pm 582$	$26\,618 \pm 976$	$24\,605 \pm 1097$
N_{comb}	490 ± 161	4914 ± 840	$10\,054 \pm 1359$	$11\,406 \pm 1491$
$\mu_B\,[\,\text{MeV}/c^2]$	5276.8 ± 2.7	5276.7 ± 1.3	5276.0 ± 1.0	5282.7 ± 0.9
$\sigma\,[\,\text{MeV}/c^2]$	92.7 ± 2.5	83.5 ± 1.3	81.5 ± 1.0	81.1 ± 1.0
$c_p\,[10^{-4}\,c^2/\,\text{MeV}]$	-5.9 ± 1.7	-5.2 ± 1.0	-4.7 ± 0.7	-3.2 ± 0.6
$\tau\,[10^{-4}\,c^2/\,\text{MeV}]$	-4.4 ± 3.7	-12.4 ± 1.6	-14.2 ± 1.2	-14.9 ± 1.2

where $\mathbf{V}_{ij}$ is the covariance matrix defined as

$$\mathbf{V}_{ij}^{-1} = \frac{\partial^2(-\mathcal{L})}{\partial N_i \partial N_j} = \sum_{e=1}^{N} \frac{f_i(x_e)f_j(x_e)}{\left(\sum_{k=1}^{n_c} N_k f_k(x_e)\right)^2} \,. \tag{4.13}$$

4.8.2 Description of the fit

In principle, the background subtraction is applied by allowing the yields of each independent component (or species) to vary in the fit. In the present case, even with the shape parameters μ_B, σ, c_p and τ fixed, it is not possible to free both the yields for the $B^+ \to K^+\pi^-\pi^+\eta$ and the $B^+ \to K^+\pi^-\pi^+\pi^0$ backgrounds because the fit does not converge. In order to be able to perform the background subtraction, these two components are combined as a single contribution, which is valid only if they have similar distributions in the variables y of interest (which are the ones used in the amplitude fit). As both η and π^0 mesons have a spin-parity 0^-, the angular distributions of $B^+ \to K^+\pi^-\pi^+\eta$ and $B^+ \to K^+\pi^-\pi^+\pi^0$ decays are expected to be sufficiently similar to justify the merging of the two components. Their common PDF is defined as:

$$f_{\eta\pi^0}(x) = \frac{C_\eta}{(C_\eta + C_{\pi^0})} f_\eta(x) + \frac{C_{\pi^0}}{(C_\eta + C_{\pi^0})} f_{\pi^0}(x)\,, \tag{4.14}$$

where C_η and C_{π^0} are the fixed contamination values used in the previous fit.

Table 4.11 – Fit parameters obtained in the background subtraction method from a fit of the $B^+ \to K^+\pi^-\pi^+\gamma$ candidates selected in the 2011, 2012, 2016 and 2017 data sets.

Fit parameter	2011	2012	2016	2017
N_{sig}	2893 ± 157	9284 ± 262	$17\,485 \pm 379$	$17\,310 \pm 378$
$N_{\eta\pi^0}$	643 ± 339	2054 ± 569	2806 ± 838	3353 ± 837
$N_{1\,\mathrm{miss}\,\pi}$	2374 ± 260	7927 ± 457	$14\,891 \pm 633$	$13\,703 \pm 634$
$N_{2\,\mathrm{miss}\,\pi}$	3715 ± 99	$12\,792 \pm 203$	$26\,617 \pm 285$	$24\,664 \pm 296$
N_{comb}	492 ± 43	4919 ± 185	$10\,054 \pm 287$	$11\,407 \pm 318$

The total fit function used at this stage is then

$$
\begin{aligned}
f_{\mathrm{tot}}(x; N_{\mathrm{sig}}, N_{\eta\pi^0}, N_{1\,\mathrm{miss}\,\pi}, N_{2\,\mathrm{miss}\,\pi}, N_{\mathrm{comb}}) = {} & N_{\mathrm{sig}}\, f_{\mathrm{sig}}(x) \\
& + N_{\eta\pi^0}\, f_{\eta\pi^0}(x) \\
& + N_{1\,\mathrm{miss}\,\pi}\, f_{1\,\mathrm{miss}\,\pi}(x) \\
& + N_{2\,\mathrm{miss}\,\pi}\, f_{2\,\mathrm{miss}\,\pi}(x) \\
& + N_{\mathrm{comb}}\, f_{\mathrm{comb}}(x)\,.
\end{aligned}
$$

4.8.3 Results

The results of the likelihood maximization are shown in Fig. 4.16 and the fitted yields are listed in Table 4.11. A good agreement is found between these yields and those reported in Table 4.10, but the uncertainties from the fit are different. For example, the parameter N_{comb} has now lower uncertainties because the τ parameter, to which it is correlated, is now fixed. However, the uncertainty on the signal yields from the background-subtraction fit is now higher, mainly because of the similarity between the signal mass shape and the PDF $f_{\eta\pi^0}(x)$ which induces a correlation between N_{sig} and $N_{\eta\pi^0}$. This uncertainty impacts directly the sensitivity of the measurement of the photon polarisation parameter, as shown in next chapter. A way to reduce it would be to add the $B^+ \to K^+\pi^-\pi^+\eta$ and the $B^+ \to K^+\pi^-\pi^+\pi^0$ PDF to another contribution, for example the background with one missing pion, in order to obtain a single PDF for these three species. Inside this PDF, the relative fraction of each of these three components would be fixed to the value found in the previous mass fit. In this case, the yield of this new background component would be less correlated with the signal yield, and the uncertainty on the signal yield would be significantly reduced. But it would introduce a new source of systematic uncertainty, potentially difficult to estimate: because the $m^2_{K^+\pi^-\pi^+}$, $m^2_{K^+\pi^-}$, $m^2_{\pi^-\pi^+}$, $\cos\theta$ and χ distributions of the background with one missing pion are a priori different from those of the backgrounds with $B^+ \to K^+\pi^-\pi^+\eta$ and $B^+ \to K^+\pi^-\pi^+\pi^0$ decays, the background subtraction could alter these distributions and introduce biases on the subsequent measurement of the photon polarisation.
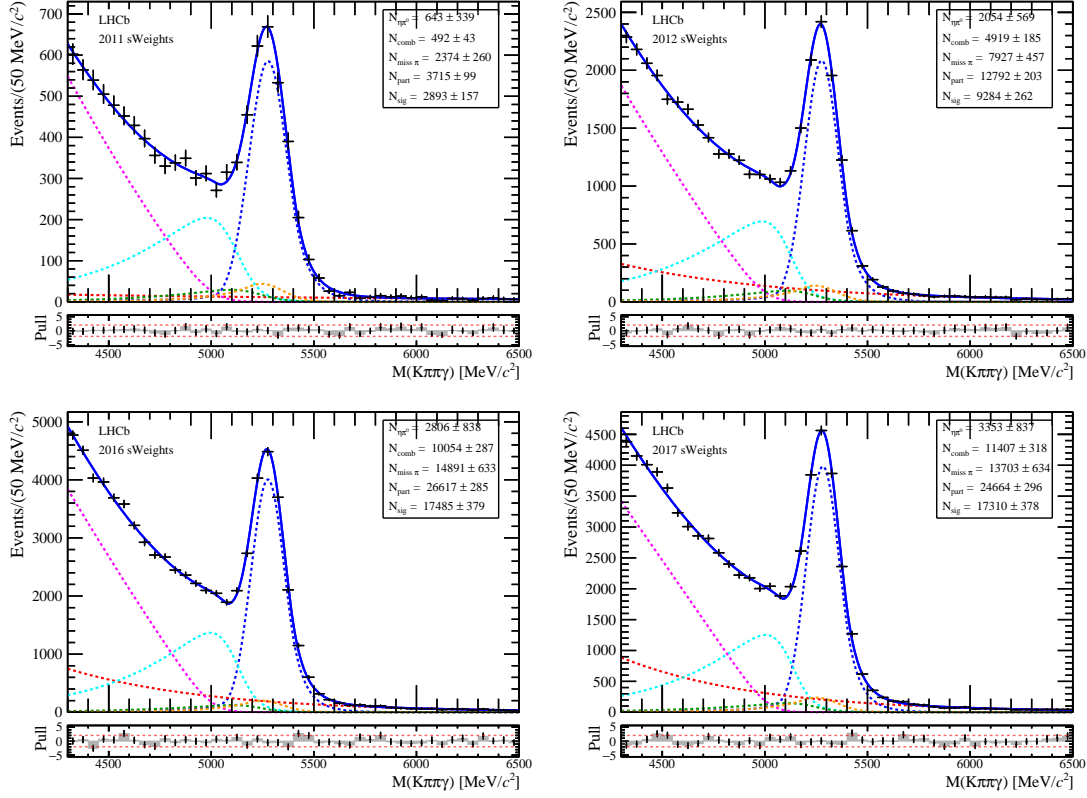
Figure 4.16 – Invariant mass distribution of the $B^+ \to K^+\pi^-\pi^+\gamma$ candidates selected in the 2011 (upper left), 2012 (upper right), 2016 (lower left) and 2017 (lower right) data sets. The total fit function used to compute sWeights is shown as the solid blue curve. It is the sum of the following components shown as dashed curves: $B^+ \to K^+\pi^-\pi^+\gamma$ signal (blue), $B^+ \to K^+\pi^-\pi^+\eta$ background (green), $B^+ \to K^+\pi^-\pi^+\pi^0$ background (orange), background with one missing pion (cyan), background with at least two missing pions (magenta) and combinatorial background (red).

Using the expression of Eq. 4.12, sWeights are computed and background subtracted distributions are obtained. For illustration purposes, the background-subtracted distributions of all data-taking years are added together and CP-conjugated as explained in Sec. 2.3.2. The weighted signal distributions of the variables $m^2_{K^+\pi^-\pi^+}$, $m^2_{K^+\pi^-}$, $m^2_{\pi^-\pi^+}$, $\cos\theta$ and χ are shown in Fig. 4.17. Figure 4.18 shows the background-subtracted $K^+\pi^-\pi^+$ mass spectrum as well as the definition of the four $K^+\pi^-\pi^+$ mass bins used in Ref. [53]. Figure 4.19 shows the background-subtracted $\cos\theta$ distribution obtained in these four bins, and asymmetries indicating a non-zero polarisation for the photon are already visible. These figures do not account for the effects of acceptance, which is not expected to introduce asymmetries.
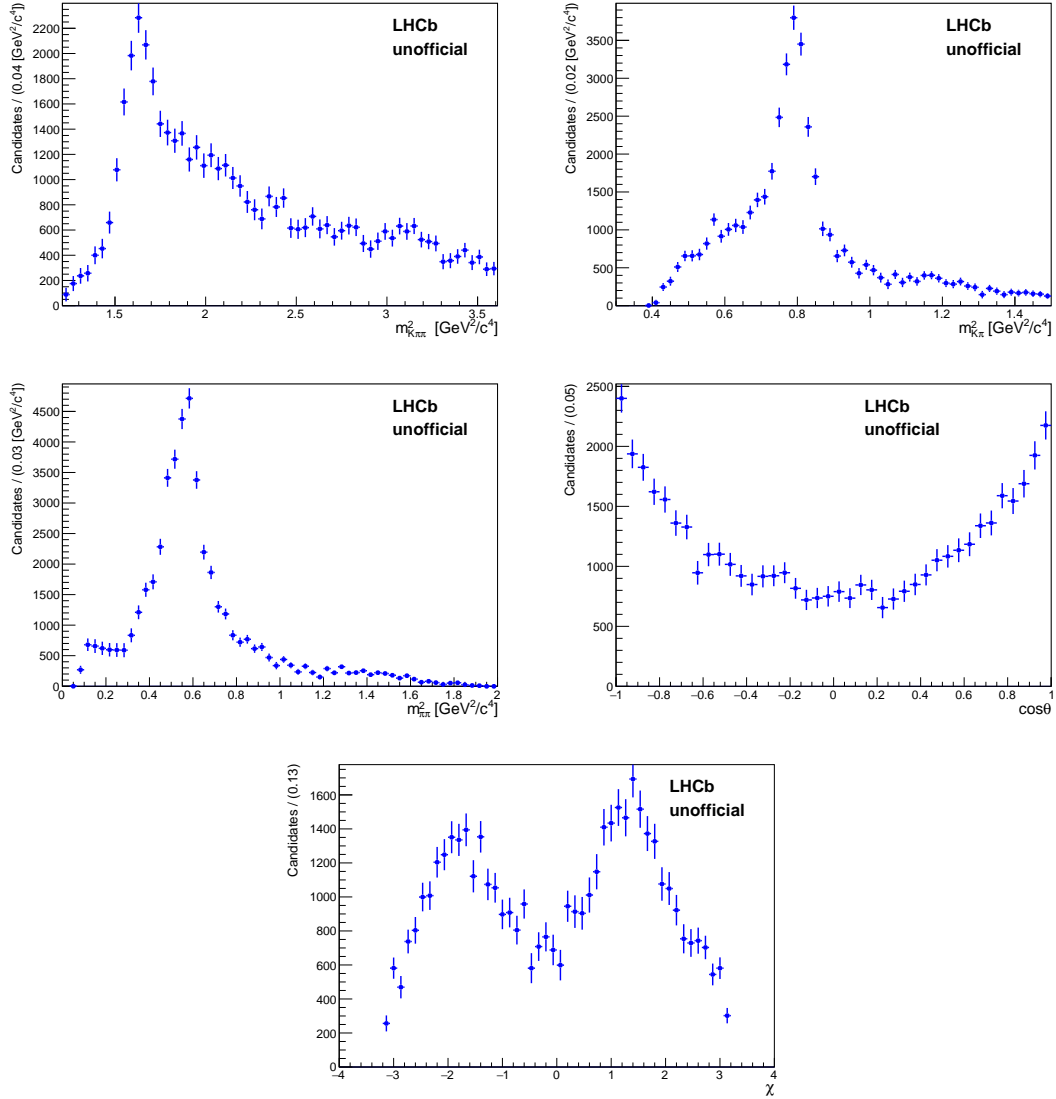
Figure 4.17 – Squared invariant-mass $(m^2_{K^+\pi^-\pi^+}, m^2_{K^+\pi^-}, m^2_{\pi^-\pi^+})$ and angular $(\cos\theta$ and $\chi)$ distributions for background subtracted data samples corresponding to the 2011, 2012, 2016 and 2017 data-taking years added together.
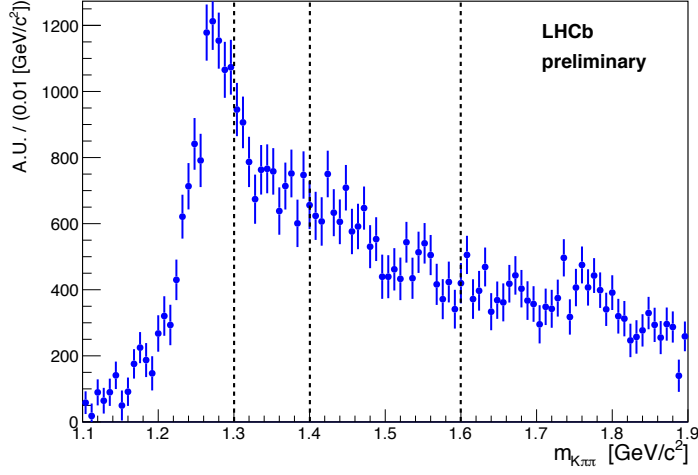
Figure 4.18 – Distribution of $m_{K^+\pi^-\pi^+}$ for background subtracted data samples corresponding to the 2011, 2012, 2016 and 2017 data-taking years added together, with the separation between the bins used in Ref. [53] in dashed black lines.
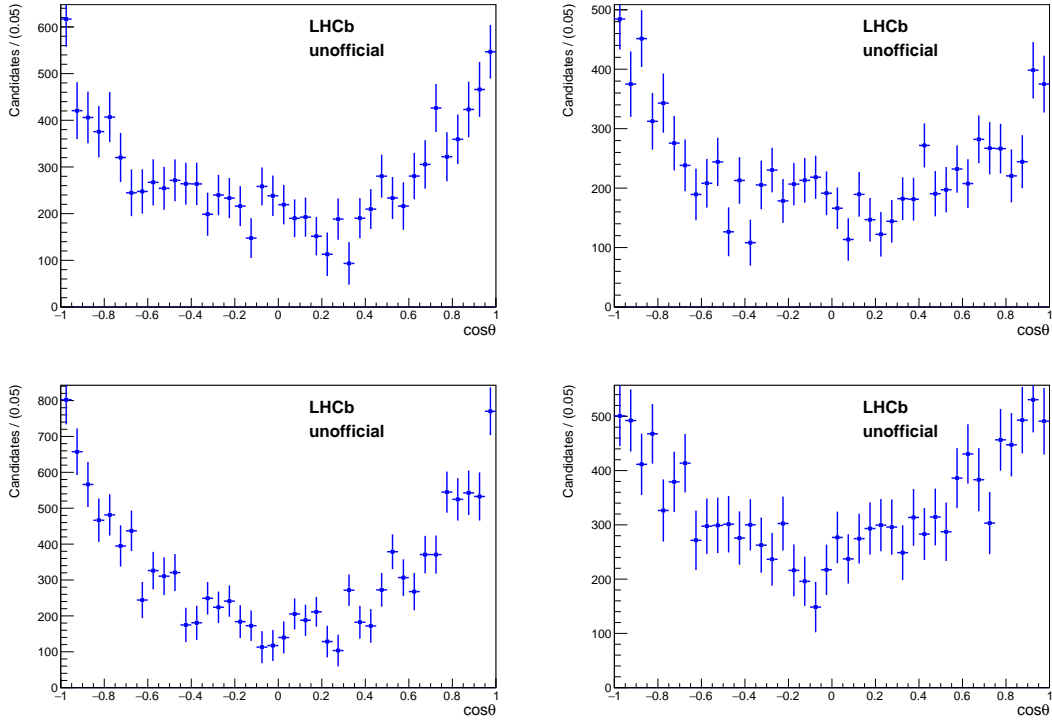
Figure 4.19 – Distribution of the angular variable $\cos\theta$ for background subtracted data samples corresponding to the 2011, 2012, 2016 and 2017 data-taking years added together, shown in four different bins of $m_{K^+\pi^-\pi^+}$: $[1.1, 1.3]\,\mathrm{GeV}/c^2$ (top left), $[1.3, 1.4]\,\mathrm{GeV}/c^2$ (top right), $[1.4, 1.6]\,\mathrm{GeV}/c^2$ (center left) and $[1.6, 1.9]\,\mathrm{GeV}/c^2$ (center right).

5 Towards an amplitude analysis of $B^+ \to K^+\pi^-\pi^+\gamma$ decays

In this chapter, several aspects of the $B^+ \to K^+\pi^-\pi^+\gamma$ amplitude analysis are explored in order to prepare for the measurement of the photon polarisation parameter using the data recorded in 2011, 2012, 2016 and 2017. The strategy of the proposed measurement is shown first, while the following sections concentrate on identifying the aspects that need to be taken into account in the method proposed in Chapter 2 in order to deal with real data.

5.1 A roadmap for the measurement of the photon polarisation in $B^+ \to K^+\pi^-\pi^+\gamma$ decays

The measurement of the polarisation of the photon using an amplitude analysis of $B^+ \to K^+\pi^-\pi^+\gamma$ decays can be separated in four main stages:

- The selection of $B^+ \to K^+\pi^-\pi^+\gamma$ candidates in the LHCb data sets is performed in three steps: the trigger, stripping and offline selections that have been explained in Secs. 4.3, 4.4 and 4.5.

- The mass fits allow the separation of the $B^+ \to K^+\pi^-\pi^+\gamma$ decays from the backgrounds that populate the mass range 4300–6500 MeV/c^2, as described in Secs. 4.7 and 4.8. A first fit is used to fix the shape parameters, while a subsequent one provides the basis for the background subtraction. In these fits, it appears that two sources of background are particularly dangerous because they have a reconstructed $K^+\pi^-\pi^+\gamma$ mass distribution similar to that of the signal: the backgrounds coming from $B^+ \to K^+\pi^-\pi^+\eta$ and $B^+ \to K^+\pi^-\pi^+\pi^0$ decays.

- The amplitude analysis step consists in performing a maximum likelihood fit using a likelihood based on the probability distribution function determined in Eq. 2.32

of Chapter 2,

$$\mathcal{F}(\boldsymbol{x}|\Omega) = \frac{\xi(\boldsymbol{x})\mathcal{P}_{\mathrm{s}}(\boldsymbol{x}|\Omega)\Phi_4(\boldsymbol{x})}{\int \xi(\boldsymbol{x})\mathcal{P}_{\mathrm{s}}(\boldsymbol{x}|\Omega)\Phi_4(\boldsymbol{x})\,\mathrm{d}\boldsymbol{x}} \, , \tag{5.1}$$

where the integral at the denominator is computed numerically. However, as data are now used instead of noise-free simulations, several modifications are introduced. First, the input $\boldsymbol{x}$, the set of four-vectors associated with the final-state particles, is now affected by the resolution of the detector. This effect is discussed in Sec. 5.2. Then, the weights from the background subtraction method have to be taken into account in the likelihood, as explained in Sec. 5.3. Section 5.4 describes the samples to be used for the numerical integration. To take maximal advantage of the statistical power of the available data set, the fit is performed simultaneously in all data-taking years: the likelihoods are computed for each year with their own integration samples but a shared set of fit parameters Ω, and are multiplied before the maximization.

The amplitude analysis itself will be performed in two steps:

  ◇ The **model building** consists in determining which decay processes contribute to the $K^+\pi^-\pi^+\gamma$ final state and how they can be best described. First, the lineshapes for some of these decay processes are improved with respect to those shown in the sensitivity study of Chapter 2, as described in Sec. 5.5. The contributing decay processes are chosen using an iterative procedure explained in Sec. 5.6, in which the value of the photon polarisation parameter is hidden.

  ◇ The **measurement of the photon polarisation parameter** will be performed once the nominal model for the $K^+\pi^-\pi^+\gamma$ system is determined. The statistical sensitivity of this measurement using the background-subtracted data sets for 2011, 2012, 2016 and 2017 is estimated in Sec. 5.7.

• Finally, a plan to evaluate the main systematic uncertainties is presented in Sec. 5.8, and several cross-checks proposed in order to test the hypotheses made in the measurement are described in Sec. 5.9.

5.2 Momentum resolution

An effect that was neglected in the toy studies shown in Chapter 2 is the detector resolution, which affects the measurement of the components of the four-momenta of the children particles and modifies their values with respect to the true values. This effect is stronger for the photons, which are reconstructed only as clusters in the calorimeter, while the charged hadrons are measured more precisely in the tracking system thanks to the reconstruction of their trajectories and their good identification. The values of each of the components of the four-momenta of the children particles are obtained from the measured quantities via a fit that uses a "bottom-up" approach: at each decay vertex,

Table 5.1 – Resolution on the five variables describing the $K\pi\pi\gamma$ system estimated as the standard deviation of the distribution of the difference between the reconstructed and the generated values in truth-matched simulated signal events from the 2016 "cocktail" MC samples.

Variable	Resolution	Resolution after B-mass constraint
χ	0.4022 ± 0.0007	0.3561 ± 0.0006
$\cos\theta$	0.0577 ± 0.0001	0.0549 ± 0.0001
$m^2_{K\pi\pi}\,[\,\mathrm{MeV}^2/c^4]$	$168\,627 \pm 299$	$167\,757 \pm 297$
$m^2_{K\pi}\,[\,\mathrm{MeV}^2/c^4]$	$66\,453 \pm 118$	$66\,425 \pm 118$
$m^2_{\pi\pi}\,[\,\mathrm{MeV}^2/c^4]$	$68\,948 \pm 122$	$68\,957 \pm 122$

the parameters of a parent particle are determined with a least-squares fit to its children particles, adding the constraint that those originate from a common point. As a result, the constraints upstream of a decay vertex do not contribute to the knowledge of the parameters of this decay, which means in particular that the accuracy of the measurement of the photon momentum is dominated by the resolution of the calorimeter. As they are expressed as a function of the momenta of the children particles, the five degrees of freedom of the $K\pi\pi\gamma$ system, and in particular those related to the photon momentum, $\cos\theta$ and χ, are also expected to be affected by this resolution effect.

In order to improve the momentum resolution of all children particles in the signal candidates, it is actually possible to re-fit all momenta using an approach in which all the parameters in a decay chain are obtained simultaneously, under the constraints that the children come from a common vertex and that the mass of the common parent particle is $m_{B^+} = 5279.33\,\mathrm{MeV}/c^2$. In our case, this approach called "decay tree fit" [103] is expected to result primarily in a better measurement of the momentum of the photon. The momenta of the children particles obtained from this fit are called "B-mass constrained" and can be used to recompute the variables $m^2_{K\pi\pi}$, $m^2_{K\pi}$, $m^2_{\pi\pi}$, $\cos\theta$ and χ.

The 2016 "cocktail" signal MC is used to estimate the resolution of the detector on these five variables. For this purpose, each variable is computed from the reconstructed, B-mass-constrained or generated children-particle momenta, and the resolution is then approximated as the standard deviation of the distribution of the difference between these two values. Table 5.1 shows that the B-mass constraint helps mainly in improving the measurement of $\cos\theta$ and χ while the resolutions on the purely hadronic variables $m^2_{K\pi\pi}$, $m^2_{K\pi}$ and $m^2_{\pi\pi}$ remain mostly unimproved.

In the signal PDF, the numerator of $\mathcal{F}(\boldsymbol{x}|\Omega)$ of Eq. 2.32 is evaluated using the B-mass-constrained variables $\boldsymbol{x}$, while in the normalisation integral of Eq. 2.33,

$$\int \xi(\boldsymbol{x})\mathcal{P}_s(\boldsymbol{x}|\Omega)\Phi_4(\boldsymbol{x})\,\mathrm{d}\boldsymbol{x} = \frac{I_{\mathrm{gen}}}{N_{\mathrm{sel}}} \sum_j^{N_{\mathrm{sel}}} \frac{\mathcal{P}_s(\boldsymbol{x}_j|\Omega)}{\mathcal{P}_{\mathrm{gen}}(\boldsymbol{x}_j)}\,, \tag{5.2}$$

the numerator $\mathcal{P}_s(\boldsymbol{x}_j|\Omega)$ is evaluated using the B-mass-constrained values of $\boldsymbol{x}_j$, and the denominator $\mathcal{P}_{\text{gen}}(\boldsymbol{x}_j)$ is computed using the generated values of the variables.

Although the effects of resolution are mitigated by the use of the B-mass constraint, the values of the input momenta are changed with respect to their true values, which also modifies the value of the PDF estimated in $\boldsymbol{x}$. This could introduce a bias in the measurement, which will have to be estimated and taken into account as a systematic uncertainty as described in Sec. 5.8.4.

5.3   Background subtraction in the fit function

The background subtraction in the amplitude fit is performed by introducing the s-weights in the function to be minimized, $\Psi(\Omega)$, which now depends on the signal function described in Eq. 2.32 as

$$\Psi(\Omega) = -2\,\mathcal{S}\sum_{i=1}^{N_{\text{data}}} s_{\text{sig}}(\boldsymbol{x_i})\ln(\mathcal{F}(\boldsymbol{x_i}|\Omega))\,, \tag{5.3}$$

where N_{data} is the number of candidates in the data sample and $\mathcal{S}$ is a normalisation constant given by

$$\mathcal{S} = \frac{\sum_{i=1}^{N_{\text{data}}} s_{\text{sig}}(\boldsymbol{x_i})}{\sum_{i=1}^{N_{\text{data}}} (s_{\text{sig}}(\boldsymbol{x_i}))^2}\,. \tag{5.4}$$

which accounts for the statistical uncertainties coming from the s-weight procedure [104]. The fit is performed simultaneously in all data-taking years by adding the functions $\Psi(\Omega)$ computed for each year with their own integration samples but a shared set of fit parameters Ω, before the minimization.

In order for the background subtraction not to bias the amplitude fit, the correlations between the invariant mass of the $B^+ \to K^+\pi^-\pi^+\gamma$ candidates (from which the s-weights are obtained) and the variables that describe the system, $m^2_{K^+\pi^-\pi^+}$, $m^2_{K^+\pi^-}$, $m^2_{\pi^-\pi^+}$, $\cos\theta$ and χ, must be small. These correlations have been studied on the signal "cocktail" MC, as seen in Figs. 5.1 and 5.2 for the B-mass constrained variables. The correlations are already low for the variables before the B-mass constraint as they range between 0.1% and 0.5%, the highest value being reached for $m^2_{K^+\pi^-\pi^+}$. After the B-mass constraint, these correlations are all at the 0.1% or lower, and are hence considered negligible.
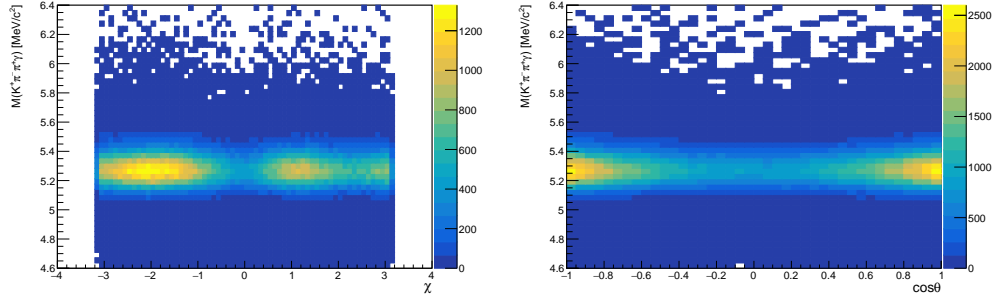
Figure 5.1 – Correlations between the $K^+\pi^-\pi^+\gamma$ invariant mass and the angular variables of the photon, χ (left) and $\cos\theta$ (right) after B-mass constraint in 2016 "cocktail" MC.

5.4 Monte Carlo integration samples

As stated earlier, simulated MC events are used in order to perform the numerical integration of the signal PDF $\mathcal{F}(\boldsymbol{x_i}|\Omega)$ and to take into account the efficiency of the data selection. The model used to generate this integration sample needs to cover all phase-space and to be as close as possible to the signal model so that the numerical integration needs less simulated events. For the needs of this analysis, different MC integration samples have been generated using the EvtGen generator in the conditions of each data-taking year. For each year, one sample is generated with a phase-space distribution, and another one, the "cocktail" MC, with an incoherent mixture of decay chains adapted from the model obtained in the Dalitz analysis of $B^+ \rightarrow K^+\pi^-\pi^+\gamma$ decays shown in Table 1.1, but without interferences and simplified due to the absence of some resonances in this generator. In particular, the proportions of decays with a $K^*(1680)^+$ resonance have been enhanced to compensate for the absence of $K_2(1580)^+$ and $K_2(1770)^+$. The resulting composition is shown in Table 4.3. In order to save CPU time, a fast simulation technique called ReDecay [105] is used. It consists in reusing several times (100 by default) the same signal B meson and the same underlying event, and decay this B meson differently for each simulated event, which allows the computing time to be divided by two orders of magnitude.

5.5 Improvements to the signal model

Before fitting the value of the photon polarisation parameter in data, a nominal signal model $\mathcal{P}_s(\boldsymbol{x}|\Omega)$ has to be determined. The first point to note is that some of the decay processes involved in the $B^+ \rightarrow K^+\pi^-\pi^+\gamma$ decays are not well described by the Breit-Wigner lineshapes used in Sec. 2.1.4. The main improvements to the lineshapes in the signal model used to fit data include the following changes:

⋄ The decay of the $\rho(770)^0$ broad resonance to $\pi^-\pi^+$ will be described by a Gounaris-
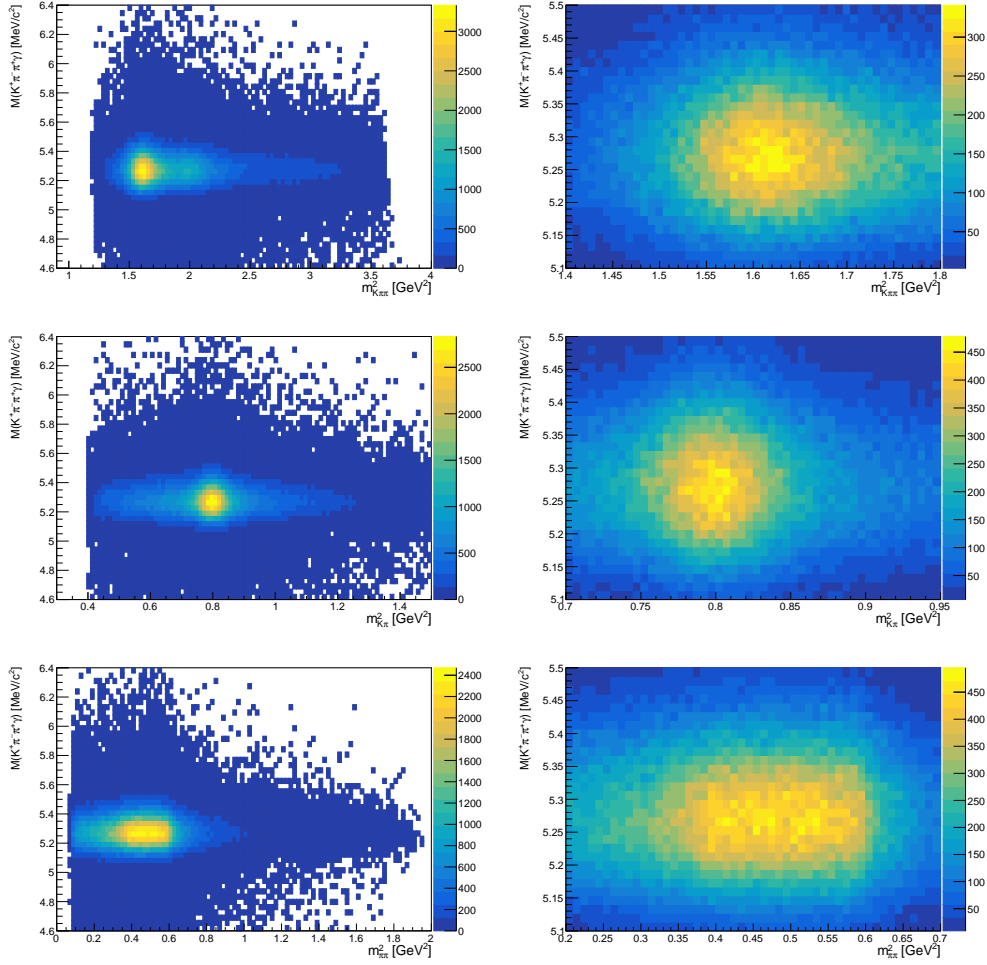
Figure 5.2 – Correlations between the $K^+\pi^-\pi^+\gamma$ invariant mass and the three variables $m^2_{K^+\pi^-\pi^+}$, $m^2_{K^+\pi^-}$ and $m^2_{\pi^-\pi^+}$ after B-mass constraint in 2016 "cocktail" MC. Sub-figures on the right-hand side show zooms in the most densely populated regions.

Sakurai distribution [106].

◇ A common lineshape will be used to describe the $\rho(770)^0$ and $\omega(782)$ resonances, which lie very close to each other and hence overlap significantly [107],

$$\mathcal{T}_{\rho-\omega}(s,q,L) = \mathcal{T}_{\rho}(s,q,L) \left[\frac{1 + \Delta B \mathcal{T}_{\omega}(s,q,L)}{1 - \Delta^2 \mathcal{T}_{\rho}(s,q,L)\mathcal{T}_{\omega}(s,q,L)} \right], \tag{5.5}$$

where $\mathcal{T}_{\rho}(s,q,L)$ is the Gounaris-Sakurai lineshape used to describe the $\rho(770)^0$, $\mathcal{T}_{\omega}(s,q,L)$ is a Breit-Wigner lineshape describing the $\omega(782)$ resonance, B is a complex parameter which is left free in the fit, and $\Delta = 0.002\,\text{MeV}$ is a fixed parameter describing the amplitude of the isospin breaking effect that allows the $\omega(782)$ state to decay into two pions.

Additionally, alternative lineshapes will be considered where appropriate, *i.e.* if the fit can be sensitive to their free parameters. In particular, the $K\pi$ S-wave, which contains the pole $K^*(1430)^0$, can be described using the K-matrix formalism [108]. This formalism, which has been originally designed to describe scattering processes, can be modified to model production processes and it is particularly well suited to describe broad overlapping resonances.

5.6 Nominal model construction

As many decay modes can be involved a priori in the $K^+\pi^-\pi^+\gamma$ system, and as very little is known about them, the first step of the amplitude fit will consist in selecting the most relevant contributions independently of the value of the photon polarisation. To this end, the value of the photon polarisation is hidden (or "blinded") in the fit so as not to introduce a bias at this stage. In all the minimizer outputs and logs, an unknown "blinding offset" is added to the value of the photon polarisation parameter, while its error is left unchanged. It is only once the signal model is chosen that the value of the photon polarisation is unblinded by uncovering the blinding offset. The selection of the contributing decay modes is done by means of an iterative procedure described in the following, which requires a way to assess the quality of the amplitude fit.

5.6.1 Fit quality assessment

The quality of the fit is assessed by means of a χ^2 estimator, which is defined using an adaptative binning scheme. This scheme consists in recursively dividing each input variable range into two ranges containing approximately the same number of data candidates. The procedure stops when each bin contains between 5 and 9 events. The χ^2 estimator makes use of the observed event yield in a given bin j defined as

$$N_{\text{obs},j} = \sum_{i=1}^{N_{\text{data},j}} s_{\text{sig}}^i, \qquad \sigma_{\text{obs},j} = \sqrt{\sum_{i=1}^{N_{\text{data},j}} (s_{\text{sig}}^i)^2}, \tag{5.6}$$

and of the expected number of events in this bin, computed from the MC integration events using the signal function,

$$N_{\text{exp},j} = A \sum_{i=1}^{N_{\text{MC},j}} W_{\text{MC}}^i, \qquad \sigma_{\text{exp},j} = A\sqrt{\sum_{i=1}^{N_{\text{MC},j}} (W_{\text{MC}}^i)^2}. \tag{5.7}$$

where $N_{\mathrm{data},j}$ and $N_{\mathrm{MC},j}$ are the number of data and MC events falling in bin j. The weights W^i_{MC} and normalisation A are defined respectively as

$$W^i_{\mathrm{MC}} = w^i_{\mathrm{MC}} \frac{\mathcal{P}_s(\boldsymbol{x}_i)}{\mathcal{P}_{\mathrm{gen}}(\boldsymbol{x}_i)} \quad \text{and} \quad A = \frac{\sum_{k=1}^{N_{\mathrm{data}}} s^k_{\mathrm{sig}}}{\sum_{k=1}^{N_{\mathrm{MC}}} w^k_{\mathrm{MC}} \frac{\mathcal{P}_s(\boldsymbol{x}_k)}{\mathcal{P}_{\mathrm{gen}}(\boldsymbol{x}_k)}} \,, \tag{5.8}$$

where the MC weights w_{MC} account for possible reweighting of the MC sample (for calibration of PID variables for example), while $\mathcal{P}_s$ and $\mathcal{P}_{\mathrm{gen}}$ are the probability distribution functions associated to the signal candidates and the simulated MC events, respectively. The χ^2 estimator associated with the fit of a sample from a single data-taking year is then computed as

$$\chi^2 = \sum_j^{N_{\mathrm{bins}}} \frac{(N_{\mathrm{obs},j} - N_{\mathrm{exp},j})^2}{\sigma^2_{\mathrm{obs},j} + \sigma^2_{\mathrm{exp},j}} \,. \tag{5.9}$$

The quality of the simultaneous fit is assessed by summing the values of the χ^2 estimators for each year, and by dividing the result by the number of degrees of freedom, which is equal to the sum of the $N_{\mathrm{bins}} - 1$ in each data samples, minus the number of fit parameters in Ω.

5.6.2   Model building

An accurate model of the $K^+\pi^-\pi^+\gamma$ system will be essential to describe properly the complicated interference patterns in the $B^+ \to K^+\pi^-\pi^+\gamma$ decays. The signal model is built recursively, starting from a base model containing the 11 dominant decay modes found in the Dalitz analysis, and shown in Table 5.2. The data samples are first fitted using the base model, and the value of the χ^2 per degree of freedom is computed. Then each of the decay processes from the list in Table 5.3 is added in turns to the model, a new fit is performed and a new value of the fit quality is obtained. The decay process that brings the best improvement to the fit χ^2 per degrees of freedom is kept. The process is repeated up until the χ^2 per degree of freedom does not improve significantly anymore, under the condition that the fit converges and that errors on the fitted parameters remain reasonable.

Alternative lineshapes, in particular the use of K-matrices in order to better describe the S-wave amplitudes, will be tried once the model is built, and they will be kept if the fit is sensitive to their internal parameters. It is only after the signal model is fixed that the value of the photon polarisation parameter will be unblinded.

Table 5.2 – Decay processes used in the base model for the amplitude analysis of $B^+ \to K^+\pi^-\pi^+\gamma$ decays. When the wave number is not specified, the lowest accessible wave is implied.

J^P	Amplitude k
1^+	$K_1(1270)^+ \to K^*(892)^0\pi^+$ $K_1(1270)^+ \to K^+\rho(770)^0 - \omega(782)^0$ $K_1(1400)^+ \to K^*(892)^0\pi^+$
1^-	$K^*(1410)^+ \to K^*(892)^0\pi^+$ $K^*(1680)^+ \to K^*(892)^0\pi^+$
2^+	$K_2^*(1430)^+ \to K^*(892)^0\pi^+$ $K_2^*(1430)^+ \to K^+\rho(770)^0 - \omega(782)^0$
2^-	$K_2(1580)^+ \to K^*(892)^0\pi^+$ $K_2(1580)^+ \to K^+\rho(770)^0 - \omega(782)^0$ $K_2(1770)^+ \to K^*(892)^0\pi^+$
Non resonant	$K\pi\pi$

5.7 Sensitivity including the background subtraction

The effects from the detector resolution and choice of a signal model could result in a bias on the value of the photon polarisation parameter. These biases will have to be estimated and their size assigned as a systematic uncertainty. However, the effect from the presence of backgrounds can already be taken into account in order to estimate a more realistic number for the statistical sensitivity that can be reached by a measurement using the 2011, 2012, 2016 and 2017 LHCb data sets.

In Sec. 2.4.2, the statistical uncertainty on a measurement of λ_γ has been shown to be $\sigma_\gamma = 0.018$ when using 14 000 signal events without backgrounds.

For S pure signal events, one can then extrapolate the formula:

$$\sigma_\gamma = 0.018 \, \frac{\sqrt{14\,000}}{\sqrt{S}} \, . \tag{5.10}$$

In the presence of backgrounds, we actually obtain a sample of N_{obs} signal events determined with an uncertainty $\sigma_{N_{\mathrm{obs}}}$ (which, if backgrounds are present, should be larger than $\sqrt{N_{\mathrm{obs}}}$). In order for a sample of S pure signal events to have an equivalent

Table 5.3 – Additional decay processes used in the model building for the amplitude analysis of $B^+ \to K^+\pi^-\pi^+\gamma$ decays. When the wave number is not specified, the lowest accessible wave is implied.

J^P	Amplitude k
1^+	$K_1(1270)^+ \to K^*(892)^0\pi^+$ [D]
	$K_1(1270)^+ \to K^+\rho(770)^0 - \omega(782)^0$ [D]
	$K_1(1400)^+ \to K^*(892)^0\pi^+$ [D]
	$K_1(1270)^+ \to K^*(1430)^0\pi^+$
	$K_1(1400)^+ \to K^+\rho(770)^0 - \omega(782)^0$ [S,D]
	$K_1(1400)^+ \to K^*(1430)^0\pi^+$
1^-	$K^*(1410)^+ \to K^+\rho(770)^0 - \omega(782)^0$
	$K^*(1680)^+ \to K^+\rho(770)^0 - \omega(782)^0$
2^+	$K_2^*(1430)^+ \to K^+ f_2(1270)^0$
2^-	$K_2(1580)^+ \to K^*(892)^0\pi^+$ [F]
	$K_2(1580)^+ \to K^+\rho(770)^0 - \omega(782)^0$ [F]
	$K_2(1770)^+ \to K^*(892)^0\pi^+$ [F]
	$K_2(1580)^+ \to K^+\rho(770)^0 - \omega(782)^0$ [P,F]
	$K_2(1580)^+ \to K_2^*(1430)^0\pi^+$
	$K_2(1580)^+ \to K^+ f_2(1270)^0$ [S,D]
	$K_2(1770)^+ \to K^+\rho(770)^0 - \omega(782)^0$ [P,F]
	$K_2(1770)^+ \to K_2^*(1430)^0\pi^+$
	$K_2(1770)^+ \to K^+ f_2(1270)^0$ [S,D]

"statistical power", it needs to have the same signal significance, i.e.

$$\frac{N_{\text{obs}}}{\sigma_{N_{\text{obs}}}} = \frac{S}{\sqrt{S}} = \sqrt{S}. \tag{5.11}$$

So the uncertainty on λ_γ can be approximated as

$$\sigma_\gamma = 0.018\sqrt{14\,000}\,\frac{\sigma_{N_{\text{obs}}}}{N_{\text{obs}}}. \tag{5.12}$$

In the fits used to obtain the background subtracted distributions in the previous chapter, the total signal yield is $46\,972 \pm 616$, which leads to an uncertainty $\sigma_\gamma = 0.028$. This uncertainty is larger than the one obtained using $14\,000$ events in an ideal situation, showing that the presence of backgrounds impacts significantly the quality of the measurement of λ_γ. However, as explained in Sec. 4.8.3, the high uncertainty on the signal yield is dominated by the correlations between the signal shape and the shape that models $B^+ \to K^+\pi^-\pi^+\eta$ and $B^+ \to K^+\pi^-\pi^+\pi^0$ backgrounds. It is likely, in this case, that our formula overestimates the degradation of the measurement caused by the

presence of backgrounds.

A lower bound on the uncertainty in the presence of backgrounds can be obtained by using the resulting signal yield of the fit used to obtain the shape parameters : $47\,449 \pm 321$. In this case, the uncertainty on λ_γ is $\sigma_\gamma = 0.014$, which represents a small loss of sensitivity with respect to the case of a sample of pure signal, but does not take into account the uncertainties coming from the background-subtraction procedure.

The numbers estimated above show that in spite of the presence of backgrounds, the measurement of λ_γ would remain very precise with an uncertainty between 0.014 and 0.028. For a proper evaluation of the uncertainty coming from the background subtraction procedure, dedicated studies based on toy simulations or boot-strapping will be necessary, as highlighted in Ref. [109].

5.8 Systematic uncertainties

Four main categories of uncertainties affecting the fitted value of the photon polarisation parameters have been identified: the uncertainties coming from the B mass fit, those coming from the signal model in the amplitude fit, from the size of the MC integration sample and from the resolution on the momenta. The following sections give a non-exhaustive list of the identified uncertainties and the proposed methods to estimate them.

5.8.1 Uncertainties from the B mass fit

Several sources of uncertainties arise from the B mass fit. They can generally be estimated by changing the values of the fixed parameters in this B mass fit and repeating the measurement of λ_γ:

- The uncertainty from the contaminations of $B^+ \to K^+\pi^-\pi^+\eta$ and $B^+ \to K^+\pi^-\pi^+\pi^0$ decays is obtained by varying the value of the contamination from each of these backgrounds by $\pm 1\sigma$, where σ is the uncertainty on the estimated contamination.

- The uncertainty coming from the assumption that the ratio of branching fractions for $B^+ \to K^+\pi^-\pi^+\pi^0$ and $B^+ \to K^+\pi^-\pi^+\gamma$ decays is the same as for $B^+ \to K^{*+}\pi^0$ and $B^+ \to K^{*+}\gamma$ decays is evaluated by using instead the ratio of branching fractions for $B^0 \to K^{*0}\pi^0$ and $B^0 \to K^{*0}\gamma$ decays in order to compute the contaminations.

- The uncertainty from each of the fixed shape parameters for these backgrounds are also obtained by varying their values by $\pm 1\sigma$, where σ is the uncertainty on the considered shape parameter from the fit on simulated data.

- The uncertainty from the width of the resolution function used in the partially reconstructed background with one missing pion is computed by varying the ratio r by $\pm 1\sigma$, where σ is the uncertainty on r obtained from the fit on simulated events.

- The uncertainty from the choice of a fitting range is obtained by changing the upper mass limit or the lower mass limit of this range by around $100\,\mathrm{MeV}/c^2$ (in order to keep a good handle on all the background components).

5.8.2 Uncertainties from the amplitude model

The uncertainties on λ_γ coming from the amplitude model will be estimated as follows:

- The uncertainty from the choice of the parametrization of the ρ-ω mixing is evaluated by parametrizing the ρ and ω decay chains independently, the first with a Gounaris-Sakurai distribution and the second with a relativistic Breit-Wigner distribution.

- The uncertainty from the fixed parameters in the fit (resonance widths, masses and radii) is obtained by varying each of these parameters by $\pm 1\sigma$ around its nominal value and repeating the fit.

- The uncertainty from the choice of decay processes used in the fit model is obtained by adding the decay chain with the highest significance amongst those which have been excluded in the model building method, and by repeating the fit. The same procedure is repeated by removing the last amplitude that has been added to the signal model.

- The uncertainty from the intrinsic bias of the fit model is estimated very similarly to what has been done is Sec. 2.4.2. A hundred pseudo-experiments are generated using the final signal model and are subsequently fitted with the same model. The difference between the mean of the fitted values and the generated value is assigned as the uncertainty.

5.8.3 Uncertainties from the size of the MC integration sample

If the MC integration sample is too small and does not cover properly all the regions populated by the signal model, the value of λ_γ could be biased.

The uncertainty resulting from this limited sample size is estimated by generating a sample of fully simulated signal candidates using the final signal model and with the number of pure signal events that corresponds to the statistical power of the data set. Then, 100 different MC integration samples are generated with EVTGEN with the same

model and the same number of events than the candidates surviving the selection in the integration sample used in the fit to the LHCb data. The sample of simulated signal candidates is fitted using each time a different MC integration sample, and the standard deviation of the distribution of the fitted λ_γ value in these fits is assigned as the systematic uncertainty.

5.8.4 Uncertainties from the resolution on the momenta

In the signal PDF used in the amplitude analysis, the reconstructed momenta of the daughter particles are used as input in two places: in the numerator of the signal PDF, and in the numerator of the normalisation integral. In order to estimate how the resolution of the detector affects the measurement of λ_γ, 100 samples of simulated events are generated using the signal model, with a number of events corresponding to the statistical power of the fitted data set. These samples will include a full simulation of the LHCb detector and each of them will be fitted twice (always using the set of normalization events used in the fit to data). In the first fit, the generated (true) values of the momenta will be used in the numerators of the PDF and of the normalization integral, while in the second fit, the B-mass constrained values of the momenta will be used instead. The mean difference between the central values obtained in these fits will be assigned as a systematic uncertainty.

5.9 Cross-checks

Several cross-checks will be performed in order to validate the use of the background subtraction method and to confirm hypotheses adopted in the fit procedure.

5.9.1 Comparing background subtraction and upper side of the signal peak

The background subtraction method will be cross-checked by performing a new amplitude fit without sWeights using only the upper part of the signal B mass peak, in the range $[\mu_B, \mu_B + 2\sigma]\,\mathrm{MeV}/c^2$ (where σ is the width of the B peak corresponding to this data-taking year), after implementing a tight cut on the BDT variable so as to drastically reduce the amount of combinatorial background. In this case, the only background that contaminates the signal comes from $B^+ \to K^+\pi^-\pi^+\pi^0$ decays and accounts for less than 5% of the total yield. As the five variables that describe the $B^+ \to K^+\pi^-\pi^+\gamma$ system are expected to be nearly uncorrelated to the reconstructed B mass, the fit obtained using the upper mass of the signal peak and the one using s-weighted distributions are expected to give compatible λ_γ values.

5.9.2   Fit separately B^+ and B^-

The assumption of negligible amount of direct CP asymmetry is cross-checked by separating the fitted sample in two sub-samples, one containing only B^+ decays, and the other one containing only CP-conjugated B^- decays as explained in Sec. 2.3.2. The two data sets are fitted independently using the final signal model and are expected to give the same value of λ_γ.

5.9.3   Fit separately the data-taking years and magnet polarities

The data sets for different years and magnet polarities are fitted separately and are expected to give the same value of λ_γ.

5.9.4   Fit in bins of the $K\pi\pi$ mass

Another central assumption made when constructing the signal function is that the λ_γ parameter does not depend on the kaonic resonance considered. If possible, this assumption will be checked by performing the fit separately in several bins of the $K\pi\pi$ invariant mass, which contain different mixtures of the aforementioned kaonic resonances. Depending on the chosen bins, these fits can be made very difficult due to the fact that some of the resonances will appear only as tails and might end-up being very loosely constraint. However, the presence of differences, if observed, would have very interesting implications for the phenomenology of $B \to K\pi\pi\gamma$ decays because they would suggest that the hadronic contributions $h^i_{\mathrm{R/L}}$ of Eq. 1.35 can not be neglected in the expression of the weak radiative amplitudes, and would need to be evaluated.

6 Conclusion

In the Standard Model, the photons produced in $b \to s\gamma$ transitions are expected to be mostly left-handed, but several new physics scenarios could introduce additional couplings allowing for a right-handed component. Thanks to the rich interference patterns between resonant modes in the $K^+\pi^-\pi^+$ hadronic final state, $B^+ \to K^+\pi^-\pi^+\gamma$ decays are sensitive to the photon polarisation. If hadronic uncertainties can be controlled, a measurement of the photon polarisation parameter λ_γ in these decays would allow to set new constraints on the Wilson coefficients C_7 and C_7' which parametrize the SM and new physics contributions to the radiative penguin operator involved in $b \to s\gamma$ transitions.

A previous study based on the measurement of up-down asymmetries using $14\,000$ $B^+ \to K^+\pi^-\pi^+\gamma$ decays selected in the data collected by the LHCb experiment in 2011 and 2012 has shown that the photon polarisation parameter λ_γ is significantly different from zero [37, 53]. However, the actual value of λ_γ cannot be determined from this measurement due to the lack of knowledge of the $K^+\pi^-\pi^+$ system.

Two main goals were pursued in this thesis. The first one consisted in showing how the limitations of the up-down asymmetry measurement could be overcome by means of an amplitude analysis using simultaneously all 5 degrees of freedom of the $K^+\pi^-\pi^+\gamma$ system. A complete method for this amplitude analysis has been proposed, implemented with all technical details and tested. Simulations of signal samples generated according to a simplified model have demonstrated that the sensitivity achieved with this method does not depend strongly on the signal model. Using a more realistic model of $B^+ \to K^+\pi^-\pi^+\gamma$ decays derived from Ref. [53], it has been shown that a measurement of λ_γ with a sample of $14\,000$ signal events can reach a promising statistical uncertainty as small as 0.018, which means that the method itself offers a high statistical sensitivity to this parameter in the absence of backgrounds and detector effects. A similar study performed with $B^0 \to K^+\pi^-\pi^0\gamma$ decays has also shown that a good sensitivity could be achieved using 5 ab^{-1} of data collected at Belle II.

The second goal of this thesis was to prepare for a measurement of λ_γ in $B^+ \to K^+\pi^-\pi^+\gamma$ decays using a total of $6.6\,\mathrm{fb}^{-1}$ of data collected by the LHCb experiment in 2011, 2012, 2016 and 2017 at centre-of-mass energies of 7, 8 and 13 TeV. A selection of $B^+ \to K^+\pi^-\pi^+\gamma$ decay candidates has been developed and the contaminations from

several sources of background have been estimated. Backgrounds from $B^+ \to K^+\pi^-\pi^+\eta$ and $B^+ \to K^+\pi^-\pi^+\pi^0$ decays, which are not well constrained by current measurements and were neglected in the previous analysis, have been shown to contaminate significantly the signal region and need to be accounted for in the mass fit. A background subtraction method has been applied in order to obtain the data sets to be used in the amplitude analysis. A sample containing about $47\,000$ $B^+ \to K^+\pi^-\pi^+\gamma$ decay candidates has been obtained. Finally, a road-map for the amplitude analysis of $B^+ \to K^+\pi^-\pi^+\gamma$ decays has been proposed, and a list of potential sources of systematic uncertainties identified. An estimation of the sensitivity on λ_γ taking into account the background contaminations indicates that the uncertainty on this parameter could reach a value of 0.028.

To conclude, this work paves the way for a measurement of the photon polarisation parameter λ_γ, which is an important test of the Standard Model. It demonstrates the feasibility of an amplitude analysis of $B^+ \to K^+\pi^-\pi^+\gamma$ decays, and identifies the main sources of potential biases that could affect the measurement. The high sensitivity of the measurement of λ_γ, even in the presence of background, establishes the excellent potential of an amplitude analysis using LHCb data, making it one of the best avenues to test the handedness of the photon in radiative B decays.

One of the main limitations of this analysis comes from the unknown contaminations of $B^+ \to K^+\pi^-\pi^+\eta$ and $B^+ \to K^+\pi^-\pi^+\pi^0$ decays in the signal region. A measurement of the branching ratios of these decays, currently limited by the size of the collected data set, could improve significantly the sensitivity of the amplitude analysis. In this respect, the data collected by the upgraded LHCb detector in Run 3 (2021–2024), where the instantaneous luminosity is expected to be multiplied by 5, should allow to study these decays and evaluate their branching ratios, opening new prospects for this amplitude analysis.

Bibliography

[1] ATLAS collaboration, G. Aad *et al.*, *Observation of a new particle in the search for the Standard Model Higgs boson with the ATLAS detector at the LHC*, Phys. Lett. **B716** (2012) 1, `arXiv:1207.7214`.

[2] CMS collaboration, S. Chatrchyan *et al.*, *Observation of a new boson at a mass of 125 GeV with the CMS experiment at the LHC*, Phys. Lett. **B716** (2012) 30, `arXiv:1207.7235`.

[3] CMS collaboration, A. M. Sirunyan *et al.*, *Combined measurements of Higgs boson couplings in proton-proton collisions at $\sqrt{s} =$ 13 TeV*, Eur. Phys. J. C **79** (2018) 421, Submitted to Eur.Phys.J.

[4] ATLAS collaboration, G. Aad *et al.*, *Combined measurements of Higgs boson production and decay using up to 80 fb^{-1} of proton-proton collision data at $\sqrt{s} =$ 13 TeV collected with the ATLAS experiment*, Phys. Rev. **D101** (2020) 012002, `arXiv:1909.02845`.

[5] S. Rossel and R. Wehner, *Polarization vision in bees*, Nature **323** (1986) 128.

[6] P. Kraft, C. Evangelista, M. Dacke, T. Labhart, and M. V. Srinivasan, *Honeybee navigation: following routes using polarized-light cues*, Philos. Trans. R. Soc. Lond. B, Biol. Sci. **366** (2011) 703.

[7] Adapted from Wikipedia, *Spin angular momentum of light*, https://en.wikipedia.org/wiki/Spin_angular_momentum_of_light.

[8] B. Pontecorvo, *Neutrino experiments and the problem of conservation of leptonic charge*, Sov. Phys. JETP **26** (1968) 984, [Zh. Eksp. Teor. Fiz. 53 (1967) 1717].

[9] Super-Kamiokande collaboration, Y. Ashie *et al.*, *Evidence for an oscillatory signature in atmospheric neutrino oscillations*, Phys. Rev. Lett. **93** (2004) 101801.

[10] D. J. Gross and F. Wilczek, *Ultraviolet behavior of non-abelian gauge theories*, Phys. Rev. Lett. **30** (1973) 1343.

[11] H. D. Politzer, *Reliable perturbative results for strong interactions?*, Phys. Rev. Lett. **30** (1973) 1346.

[12] J. H. Christenson, J. W. Cronin, V. L. Fitch, and R. Turlay, *Evidence for the 2π decay of the K_2^0 meson*, Phys. Rev. Lett. **13** (1964) 138.

[13] Belle collaboration, K. Abe, K. Abe, R. Abe, I. Adachi, B. S. Ahn, H. Aihara, M. Akatsu, G. Alimonti, and K. Asai, *Observation of large CP violation in the neutral B meson system*, Phys. Rev. Lett. **87** (2001) 091802.

[14] BaBar collaboration, B. Aubert, D. Boutigny, J.-M. Gaillard, A. Hicheur, Y. Karyotakis, J. P. Lees, P. Robbe, and V. Tisserand, *Observation of CP violation in the B^0 meson system*, Phys. Rev. Lett. **87** (2001) 091801.

[15] LHCb collaboration, R. Aaij, C. Abellán Beteta, B. Adeva, M. Adinolfi, C. A. Aidala, Z. Ajaltouni, and S. Akar, *Observation of CP violation in charm decays*, Phys. Rev. Lett. **122** (2019) 211803.

[16] L.-L. Chau and W.-Y. Keung, *Comments on the parametrization of the kobayashi-maskawa matrix*, Phys. Rev. Lett. **53** (1984) 1802.

[17] L. Wolfenstein, *Parametrization of the kobayashi-maskawa matrix*, Phys. Rev. Lett. **51** (1983) 1945.

[18] S. Stone, *New physics from flavour*, PoS **ICHEP2012** (2013) 033, arXiv:1212.6374.

[19] Particle Data Group, M. Tanabashi *et al.*, *Review of particle physics*, Phys. Rev. **D98** (2018) 030001.

[20] CKMfitter group, J. Charles *et al.*, *Current status of the standard model CKM fit and constraints on $\Delta F = 2$ new physics*, Phys. Rev. **D91** (2015) 073007, arXiv:1501.05013, updated results and plots available at http://ckmfitter.in2p3.fr/.

[21] R. Foot, H. Lew, and R. R. Volkas, *Electric-charge quantization*, J. Phys. **G 19** (1993) 361.

[22] A. Hook, *TASI Lectures on the strong CP problem and axions*, PoS **TASI2018** (2019) 004, arXiv:1812.02669.

[23] L. Canetti, M. Drewes, and M. Shaposhnikov, *Matter and antimatter in the universe*, New J. Phys. **14** (2012) 095012.

[24] S. Bifani, S. Descotes-Genon, A. Vidal, and M.-H. Schune, *Review of Lepton Universality tests in B decays*, J. Phys. G **46** (2018) .

[25] A. Puig Navarro, *First measurements of radiative B decays in LHCb*, PhD thesis, Barcelona University, 2012, CERN-THESIS-2012-025.

[26] L. Everett, G. Kane, S. Rigolin, L.-T. Wang, and T. Wang, *Alternative approach to b → sγ in the uMSSM*, JHEP **01** (2002) 022, `arXiv:hep-ph/0112126`.

[27] A. Tayduganov, E. Kou, and A. Le Yaouanc, *The strong decays of K_1 resonances*, Phys. Rev. **D85** (2012) 074011, `arXiv:1111.6307`.

[28] J. C. Pati and A. Salam, *Lepton number as the fourth color*, Phys. Rev. **D10** (1974) 275, Erratum ibid. **D11** (1975) 703.

[29] R. N. Mohapatra and J. C. Pati, *A natural left-right symmetry*, Phys. Rev. **D11** (1975) 2558.

[30] R. N. Mohapatra and J. C. Pati, *Left-right gauge symmetry and an isoconjugate model of CP violation*, Phys. Rev. **D11** (1975) 566.

[31] M. Misiak *et al.*, *Estimate of $\mathcal{B}(\bar{B} \to X_s\gamma)$ at $O(\alpha_s^2)$*, Phys. Rev. Lett. **98** (2007) 022002, `arXiv:hep-ph/0609232`.

[32] BaBar collaboration, J. P. Lees *et al.*, *Precision measurement of the $B \to X_s\gamma$ photon energy spectrum, branching fraction, and direct CP asymmetry $A_{CP}(B \to X_{s+d}\gamma)$*, Phys. Rev. Lett. **109** (2012) 191801, `arXiv:1207.2690`.

[33] Belle collaboration, T. Saito *et al.*, *Measurement of the $\bar{B} \to X_s\gamma$ branching fraction with a sum of exclusive decays*, Phys. Rev. **D91** (2015) 052004, `arXiv:1411.7198`.

[34] A. Paul and D. M. Straub, *Constraints on new physics from radiative b decays*, JHEP **2017** (2017) 27.

[35] K. G. Chetyrkin, M. Misiak, and M. Munz, *Weak radiative B meson decay beyond leading logarithms*, Phys. Lett. **B400** (1997) 206, `arXiv:hep-ph/9612313`, Erratum: Phys. Lett. **B425** (1998) 414.

[36] T. Blake, G. Lanfranchi, and D. M. Straub, *Rare B decays as tests of the Standard Model*, Prog. Part. Nucl. Phys. **92** (2017) 50, `arXiv:1606.00916`.

[37] LHCb collaboration, R. Aaij *et al.*, *Observation of photon polarization in the b → sγ transition*, Phys. Rev. Lett. **112** (2014) 161801, `arXiv:1402.6852`.

[38] F. Muheim, Y. Xie, and R. Zwicky, *Exploiting the width difference in $B_s \to \phi\gamma$*, Phys. Lett. **B664** (2008) 174, `arXiv:0802.0876`.

[39] LHCb collaboration, R. Aaij *et al.*, *First measurement of the photon polarization in radiative B_s^0 decays*, Phys. Rev. Lett. **118** (2017) 021801, `arXiv:1609.02032`.

[40] LHCb collaboration, R. Aaij *et al.*, *Measurement of CP-violating and mixing-induced observables in $B_s^0 \to \phi\gamma$ decays*, Phys. Rev. Lett. **123** (2019) 081802, `arXiv:1905.06284`.

[41] Belle collaboration, Y. Ushiroda *et al.*, *New measurement of time-dependent CP-violating asymmetry in $B^0 \to K_s^0 \pi^0 \gamma$ decay*, Phys. Rev. Lett. **94** (2005) 231601, `arXiv:hep-ex/0503008`.

[42] BaBar collaboration, B. Aubert *et al.*, *Measurement of time-dependent CP asymmetry in $B^0 \to K_S^0 \pi^0 \gamma$ decays*, Phys. Rev. **D 78** (2008) 071102.

[43] LHCb collaboration, R. Aaij *et al.*, *Angular analysis of the $B^0 \to K^* e^+ e^-$ decay in the low-q^2 region*, JHEP **04** (2015) 064, `arXiv:1501.03038`.

[44] S. Akar, E. Ben-Haim, J. Hebinger, E. Kou, and F.-S. Yu, *The time-dependent CP asymmetry in $B^0 \to K_{res} \gamma \to \pi^+ \pi^- K_S^0 \gamma$ decays*, JHEP **09** (2019) 034, `arXiv:1802.09433`.

[45] L. M. García Martín, B. Jashal, F. Martínez Vidal, A. Oyanguren, S. Roy, R. Sain, and R. Sinha, *Radiative b-baryon decays to measure the photon and b-baryon polarization*, Eur. Phys. J. **C79** (2019) 634, `arXiv:1902.04870`.

[46] BESIII collaboration, M. Ablikim *et al.*, *Polarization and entanglement in baryon-antibaryon pair production in electron-positron annihilation*, Nature Phys. **15** (2019) 631, `arXiv:1808.08917`.

[47] M. Gronau and D. Pirjol, *Photon polarization in radiative B decays*, Phys. Rev. **D66** (2002) 054008, `arXiv:hep-ph/0205065`.

[48] A. Paul and D. M. Straub, *Constraints on new physics from radiative B decays*, JHEP **04** (2017) 027, `arXiv:1608.02556`.

[49] M. Gronau, Y. Grossman, D. Pirjol, and A. Ryd, *Measuring the photon polarization in $B \to K \pi \pi \gamma$*, Phys. Rev. Lett. **88** (2002) 051802, `arXiv:hep-ph/0107254`.

[50] M. Gronau and D. Pirjol, *Reexamining the photon polarization in $B \to K \pi \pi \gamma$*, Phys. Rev. **D 96** (2017) 013002.

[51] Belle collaboration, J. Li *et al.*, *Measurement of the time-dependent CP asymmetries in $B^0 \to K_S^0 \rho^0 \gamma$ decays*, Phys. Rev. Lett. **101** (2008) 251601.

[52] S. Akar, *Study of $B \to K \pi \pi \gamma$ dacays with the BaBar experiment: the photon helicity and the resonant structure of the $K^+ \pi^- \pi^+$ system*, PhD thesis, Université Pierre et Marie Curie - Paris VI, 2013.

[53] G. Veneziano, *Towards the measurement of photon polarisation in the decay $B^+ \to K^+ \pi^- \pi^+ \gamma$*, PhD thesis no. 6896, EPFL, 2016.

[54] M. Pivk and F. R. Le Diberder, *sPlot: A statistical tool to unfold data distributions*, Nucl. Instrum. Meth. **A555** (2005) 356, `arXiv:physics/0402083`.

[55] Belle collaboration, H. Yang *et al.*, *Observation of $B^+ \to K_1(1270)^+\gamma$*, Phys. Rev. Lett. **94** (2005) 111802, arXiv:hep-ex/0412039.

[56] R. M. Sternheimer and S. J. Lindenbaum, *Extension of the isobaric nucleon model for pion production in pion-nucleon, nucleon-nucleon, and antinucleon-nucleon interactions*, Phys. Rev. **123** (1961) 333.

[57] D. J. Herndon, P. Söding, and R. J. Cashmore, *Generalized isobar model formalism*, Phys. Rev. **D11** (1975) 3165.

[58] C. Zemach, *Use of angular-momentum tensors*, Phys. Rev. **140** (1965) B97.

[59] S. U. Chung, *General formulation of covariant helicity-coupling amplitudes*, Phys. Rev. **D57** (1998) 431.

[60] P. d'Argent, *Amplitude analysis of $B^+ \to J/\psi\, K\pi\pi$ decays at the LHCb experiment*, Master's thesis, Physikalisches Institut Heidelberg, 2014.

[61] G. Breit and E. Wigner, *Capture of slow neutrons*, Phys. Rev. **49** (1936) 519.

[62] Belle collaboration, H. Guler *et al.*, *Study of the $K^+\pi^-\pi^+$ final state in $B^+ \to J/\psi\, K^+\pi^+\pi^-$ and $B^+ \to \psi' K^+\pi^+\pi^-$*, Phys. Rev. **D83** (2011) 032005.

[63] CLEO collaboration, M. Artuso *et al.*, *Amplitude analysis of $D^0 \to K^+K^-\pi^+\pi^-$*, Phys. Rev. **D85** (2012) 122002, arXiv:1201.5716.

[64] P. d'Argent, N. Skidmore, J. Benton, J. Dalseno, E. Gersabeck, S. Harnew, P. Naik, C. Prouve, and J. Rademacker, *Amplitude analyses of $D^0 \to \pi^+\pi^-\pi^+\pi^-$ and $D^0 \to K^+K^-\pi^+\pi^-$ decays*, JHEP **05** (2017) 143, arXiv:1703.08505.

[65] D. J. Lange, *The EvtGen particle decay simulation package*, Nucl. Instrum. Meth. **A462** (2001) 152.

[66] V. Bellée, P. Pais, A. Puig Navarro, F. Blanc, O. Schneider, K. Trabelsi, and G. Veneziano, *Using an amplitude analysis to measure the photon polarisation in $B \to K\pi\pi\gamma$ decays*, Eur. Phys. J. **C79** (2019) 622, arXiv:1902.09201.

[67] L. Demortier and L. Lyons, *Everything you always wanted to know about pulls*, Tech. rep. CDF/ANAL/PUBLIC/5776, 2002.

[68] J. Hebinger, *B mesons phenomenology to the search of a signal beyond the Standard Model*, PhD thesis, Université Paris-Saclay, 2017.

[69] LHCb collaboration, A. A. Alves Jr. *et al.*, *The LHCb detector at the LHC*, JINST **3** (2008) S08005.

[70] LHCb collaboration, *LHCb Technical Proposal*, https://cds.cern.ch/record/622031, 1998.

[71] LHCb collaboration, R. Aaij *et al.*, *Measurement of the b-quark production cross-section in 7 and 13* TeV*pp collisions*, Phys. Rev. Lett. **118** (2017) 052002, Erratum ibid. **119** (2017) 169901, `arXiv:1612.05140`.

[72] LHCb collaboration, R. Aaij *et al.*, *LHCb detector performance*, Int. J. Mod. Phys. **A30** (2015) 1530022, `arXiv:1412.6352`.

[73] LHCb collaboration, *LHCb detector public page*, `http://lhcb-public.web.cern.ch/LHCb-public/en/detector/Detector-en.html`.

[74] LHCb collaboration, R. Aaij *et al.*, *Measurement of the track reconstruction efficiency at LHCb*, JINST **10** (2015) P02007, `arXiv:1408.1251`.

[75] B. Storaci, *Optimization of the LHCb track reconstruction*, J. Phys. Conf. Ser. **664** (2015) 072047.

[76] A. Papanestis and C. D'Ambrosio, *Performance of the LHCb RICH detectors during the LHC Run II*, Nucl. Instrum. Meth. **A876** (2017) 221, `arXiv:1703.08152`.

[77] LHCb collaboration, *LHCb calorimeters: Technical Design Report*, CERN-LHCC-2000-036, 2000.

[78] LHCb collaboration, A. Martens, *The large hadron collider beauty experiment calorimeters*, Proc. INIS-UA **175** (2010) 655.

[79] A. A. Alves Jr. *et al.*, *Performance of the LHCb muon system*, JINST **8** (2013) P02022, `arXiv:1211.1346`.

[80] M. Adinolfi *et al.*, *Performance of the LHCb RICH detector at the LHC*, Eur. Phys. J. **C73** (2013) 2431, `arXiv:1211.6759`.

[81] F. Archilli *et al.*, *Performance of the muon identification at LHCb*, JINST **8** (2013) P10020, `arXiv:1306.0249`.

[82] O. Deschamps, F. P. Machefert, M. H. Schune, G. Pakhlova, and I. Belyaev, *Photon and neutral pion reconstruction*, CERN-LHCb-2003-091, 2003.

[83] R. Aaij *et al.*, *The LHCb trigger and its performance in 2011*, JINST **8** (2013) P04022, `arXiv:1211.3055`.

[84] R. Aaij *et al.*, *Performance of the LHCb trigger and full real-time reconstruction in Run 2 of the LHC*, JINST **14** (2019) P04013, `arXiv:1812.10790`.

[85] S. Benson, V. Gligorov, M. A. Vesterinen, and J. M. Williams, *The LHCb turbo stream*, J. Phys. Conf. Ser. **664** (2015) 082004.

[86] G. Barrand *et al.*, *GAUDI: A software architecture and framework for building HEP data processing applications*, Comp. Phys. Commun. **140** (2001) 45.

[87] M. Clemencic *et al.*, *The LHCb simulation application, Gauss: Design, evolution and experience*, J. Phys. Conf. Ser. **331** (2011) 032023.

[88] I. Belyaev *et al.*, *Handling of the generation of primary events in Gauss, the LHCb simulation framework*, J. Phys. Conf. Ser. **331** (2011) 032047.

[89] T. Sjöstrand, S. Mrenna, and P. Skands, *A brief introduction to PYTHIA 8.1*, Comput. Phys. Commun. **178** (2008) 852, `arXiv:0710.3820`.

[90] P. Golonka and Z. Was, *PHOTOS Monte Carlo: A precision tool for QED corrections in Z and W decays*, Eur. Phys. J. **C45** (2006) 97, `arXiv:hep-ph/0506026`.

[91] Geant4 collaboration, S. Agostinelli *et al.*, *Geant4: A simulation toolkit*, Nucl. Instrum. Meth. **A506** (2003) 250.

[92] Geant4 collaboration, J. Allison, K. Amako, J. Apostolakis, H. Araujo, P. A. Dubois *et al.*, *Geant4 developments and applications*, IEEE Trans. Nucl. Sci. **53** (2006) 270.

[93] LHCb collaboration, *LHCb integrated luminosity*, `http://lhcb-public.web.cern.ch/lhcb-public/Images2018/IntRecLumiR12.png`.

[94] LHCb collaboration, *Framework TDR for the LHCb Upgrade: Technical Design Report*, CERN-LHCC-2012-007, 2012.

[95] LHCb collaboration, *LHCb PID Upgrade Technical Design Report*, CERN-LHCC-2013-022, 2013.

[96] LHCb collaboration, *LHCb Tracker Upgrade Technical Design Report*, CERN-LHCC-2014-001, 2014.

[97] LHCb collaboration, *LHCb VELO Upgrade Technical Design Report*, CERN-LHCC-2013-021, 2013.

[98] V. Bellée, M. S. Bieker, J. A. De Vries, S. Esen, L. Pescatore, J. Van Tilburg, and J. T. Wishahi, *Simulation of the SciFi detector*, CERN-LHCb-INT-2018-023, 2018.

[99] M. Hoballah, *Measurement of the photon polarization using $B_s^0 \rightarrow \phi\gamma$ at LHCb*, PhD thesis, Université Blaise Pascal - Clermont-Ferrand II, 2015.

[100] C. Praz, *Optimisation of the $B^+ \rightarrow K^+\pi^-\pi^+\gamma$ selection at LHCb*, Master's thesis, EPFL, 2018.

[101] T. Chen and C. Guestrin, *XGBoost: A scalable tree boosting system*, `arXiv:1603.02754`.

[102] B. Adeva *et al.*, *Roadmap for selected key measurements of LHCb*, LHCb-PUB-2009-029, 2010.

[103] W. D. Hulsbergen, *Decay chain fitting with a Kalman filter*, Nucl. Instrum. Meth. **A552** (2005) 566, `arXiv:physics/0503191`.

[104] Y. Xie, *sFit: a method for background subtraction in maximum likelihood fit*, `arXiv:0905.0724`.

[105] D. Müller, M. Clemencic, G. Corti, and M. Gersabeck, *ReDecay: A novel approach to speed up the simulation at LHCb*, Eur. Phys. J. **C78** (2018) 1009, `arXiv:1810.10362`.

[106] G. J. Gounaris and J. J. Sakurai, *Finite-width corrections to the vector-meson-dominance prediction for $\rho \to e^+e^-$*, Phys. Rev. Lett. **21** (1968) 244.

[107] CMD-2 collaboration, R. R. Akhmetshin *et al.*, *Measurement of $e^+e^- \to \pi^+\pi^-$ cross-section with CMD-2 around ρ-meson*, Phys. Lett. **B527** (2002) 161.

[108] S. Chung, J. Brose, R. Hackmann, E. Klempt, S. Spanier, and C. Strassburger, *Partial wave analysis in k-matrix formalism*, Annalen der Physik **507** (1995) 404 .

[109] C. Langenbruch, *Parameter uncertainties in weighted unbinned maximum likelihood fits*, `arXiv:1911.01303`.

Violaine BELLÉE

@ **violaine.bellee@protonmail.com**

☎ **(+41)78 724 92 22**

⊠ **Avenue de Morges, 33, 1004 Lausanne, Switzerland**

Education

2020 **Ph.D. in Particle Physics**, *EPFL, Switzerland*,
Title of the thesis: "Amplitude analysis for the measurement of the photon polarisation in $B \to K\pi\pi\gamma$ decays", supervised by O. Schneider.

2015 **Master Degree in Physics**, *EPFL, Switzerland*,
Title of the thesis: "Search for $B_s^0 \to \phi\phi\gamma$ at LHCb", supervised by K. Trabelsi.

2015 **Master Degree in Engineering**, *École Centrale Paris, France*,
First year project: "Retrieving the heat from the gas released by an oxygen steel furnace for ERAMET Research"
Second year project: "Calibration and data analysis for the BiPo3 detector" (SuperNEMO collaboration).

Research experience

2015–2020 **Ph.D. student**, *EPFL, Lausanne*.
○ Data analysis of $B \to K\pi\pi\gamma$ decays: Developed a new method to measure the photon polarisation in these decays (leading to publication), contributed to the implementation of tools to use this method on data from LHCb, performed the selection of events and the mass fit
○ Simulation of the SciFi tracker: Contributed to the improvements and optimization of the code that simulates the electronic response of the scintillating fibre tracker in LHCb
Roles and responsibilities.
○ Responsible for the maintenance and modernization of the code that performs the first step of data selection after trigger (stripping) for the "radiative decays" sub-working group at LHCb
○ Working group liaison in charge of the stripping lines of the "rare decays" working group at LHCb

Software tutorials

9–11 May 2018 **Co-organized the LHCb Impactkit software tutorial**, *CERN, Switzerland*, with C. Burr.
○ *Main objective*: Teach researchers advanced data analysis software knowledge through hands-on sessions and a short hackathon
○ *Number of participants*: 26 students and over 15 teachers and helpers

30 Oct – 3 Nov 2017	**Co-organized the first LHCb and Alice Starterkit software tutorial**, *CERN, Switzerland*, with C. Burr, D. Berzano and R. A. Bertens.

- *Main objectives*: Teach newcomers good coding practices, software literacy, and the basics of data analysis software, favour integration and networking of young researchers
- *Main challenge*: Initiate the coordination between two large-size international collaborations to organize a common tutorial event with hands-on sessions and excellent support
- *Number of participants*: 75 students and over 30 teachers and helpers

Publications

V. Bellée, P. Pais, A. Puig Navarro, F. Blanc, O. Schneider, K. Trabelsi, *"Using an amplitude analysis to measure the photon polarisation in $B \to K\pi\pi\gamma$ decays"*, Eur. Phys. J. C (2019) 79: 622, arXiv:1902.09201

V. Bellée, on behalf of the LHCb Collaboration, *"Radiative B Decays at LHCb"*, Proceedings of the XIIth International Conference on Beauty, Charm, and Hyperons in Hadronic Interactions (2016)

D. Berzano, C. Burr, H. Beck, V. Bellée, R. A. Bertens and A. Puig Navarro, on behalf of the ALICE and LHCb Collaborations, *"Software training for the next generation of physicists: joint experience of LHCb and ALICE"*, EPJ Web of Conferences 214, 05044 (2019)

Also in the author list of 223 publications as part of the LHCb Collaboration

Internal LHCb documentation

V. Bellée, M. Bieker, J. De Vries, S. Esen, L. Pescatore, J. Van Tilburg, J. Wishahi, *"Simulation of the SciFi detector"*, CERN-LHCb-INT-2018-023 (2018)

G. Andreassi, V. Bellée, V. Franco Lima, C. Marin Benito, A. Puig, P. Stefko, *"Introducing the HOP mass in the LHCb software"*, CERN-LHCb-INT-2017-012 (2017)

Talks in conferences and workshops

23 May 2019	**7th Edition of the Large Hadron Collider Physics Conference** (Puebla, Mexico) *"LHCb Upgrade I"* and *"Recent results using rare decays with LHCb"*
10 Apr 2019	**Photon polarisation in $B \to K\pi\pi\gamma$ decays Workshop** (Strasbourg, France) *"Amplitude fit of $B \to K\pi\pi\gamma$: Formalism and limitations"*
29 Aug 2018	**Annual Meeting of the Swiss Physical Society** (Lausanne, Switzerland) *"Photon polarisation in radiative b-hadron decays at LHCb"*
27 Mar 2018	**Joint WLCG and HSF Workshop 2018** (Naples, Italy) *"The LHCb Starterkit"*
23 Feb 2018	**Lake Louise Winter Institute 2018** (Lake Louise, Canada) *"B physics anomalies and lepton flavour universality in $b \to sll$ transitions"*

144

05 Oct 2017	**Photon polarisation in $B \to K\pi\pi\gamma$ decays Workshop** (Lausanne, Switzerland) *"Measurement of the photon polarisation in $B \to K\pi\pi\gamma$ decays: formalism, method and validation studies"*
25 Aug 2017	**Joint Annual Meeting of the Swiss Physical Society and the Austrian Physical Society** (Geneva, Switzerland) *"Investigation for photon polarisation in $B \to K\pi\pi\gamma$ decays at LHCb"*
14 Jun 2016	**XIIth International Conference on Beauty, Charm, and Hyperons in Hadronic Interactions** (Fairfax, USA) *"Radiative B Decays at LHCb"*

Teaching activities

Nov 2018 & Nov 2019	**Teacher in hands-on lessons at Starterkit software tutorials:** *"LHCb data flow"*, *"Introduction to LHCb software"*, *"Interactively exploring data sets"* and *"Decay tree fitters"*
May 2018	**Teacher in hands-on lessons at the LHCb Impactkit software tutorial:** *"Advanced LHCb software"* and *"Version control with Gitlab"*
Sep 2015 – May 2018	**Teaching assistant at EPFL:** *"Nuclear and particle physics"* for 3rd year students (2 semesters) *"Laboratory of nuclear physics"* for 3rd year students (3 semesters) *"General Physics"* for 1st year students (5 semesters)
Sep 2012 – Apr 2013	**Examiner in weekly oral examination in Physics** at Lycée Lakanal (Sceaux, France) for 2nd year students in Classe préparatoire (intensive 2-year preparation for the national examination for the French "Grandes Écoles")

Outreach activities

Feb 2020 Feb 2019 & Feb 2018	**Gave presentations in schools for the International Day of Girls and Women in Science** (organized by CERN) Presented my work at LHCb to 3 classes in 2018, 3 in 2019 and 4 in 2020 with students aged 6 to 17
12 Mar 2018	**Contributed to the LHCb International Masterclasses** at CERN Aimed at showing the real life of particle physicists to high-school students through virtual visits of CERN and real measurements exercises
Jun–Aug 2010	**Animated and organised scientific activities** with the GAHQ (Groupe Astronomique Hague Querqueville) in France for groups of children and teenagers Activities: Astronomy observations, solar-powered car races and sending water rockets to the stars! Also participated in **CERN Open Days** (showing experiments with liquid nitrogen and supra-conductivity) and **EPFL Open Days** (informing visitors about the activities of the Laboratory of High Energy Physics)

Physics and machine-learning schools

20 Jun – 3 Jul 2018	**European School of High-Energy Physics** (Maratea, Italy) Trained for science communication in the media (especially for live interviews) Outreach project on the first measurement of the W boson mass at the LHC

12–17 Feb 2017	**CHIPP Winter School of Particle Physics** (Sorenberg, Switzerland) Main subjects covered: Neutrinos and future facilities, detectors, flavour physics, cosmic rays, dark matter
20–26 Jun 2016	**Second Machine Learning in High Energy Physics Summer School** (Lund, Sweden) Participated in a Kaggle competition of machine-learning involving an optimization of trigger decisions

Summer internships

Jul–Aug 2014	**Summer internship at LPHE** (Lausanne, Switzerland) Project: *"Resolution studies for the Cosmic Ray Telescope"* Studies of the effect of misalignment on the spatial resolution of a cosmic ray telescope made of scintillating fibres
Jul–Aug 2013	**Summer internship at CERN** (Geneva, Switzerland) Project: *"Establish a signature for the production of two Higgs bosons decaying to a di-photon pair and a pair of b-jets at CMS"* Studies performed on simulated data
Jun–Aug 2009	**Summer internship at GANIL** (Grand Accélérateur National d'Ions Lourds) in Caen, France Financed via the JANUS program of IN2P3 *"Measurement of the lifetime of a rare isotope of oxygen"* Set up the electronics and calibrated the plastic detector used for the measurement, and analyzed the data

Languages and computer skills

Languages: French (native), English (fluent), Spanish (independent)

OS: Linux, MacOS, Windows

Programming languages: Python, C++

Version control: Github, Gitlab

Agile project management: Jira

Interactive computing: Jupyter

Machine learning: Theano, Keras, Lasagne, Scikit-learn

Extracurricular activities and hobbies

Sports	○ Running: half-marathons and trail ○ Rowing: qualified for the French University Rowing Championship in 2012 and 2013 ○ Horse riding: 10-year practice, eventing competitions (combining dressage, cross-country and show jumping)
Theater	○ Organized the one-week student theatre festival *Arrache-Cœur* in 2012 ○ In charge of the Theatre section in the student association dedicated to art-related events at Centrale Paris in 2012, managed the partnership with *La Comédie Française* and other theaters in Paris to provide students with low-price tickets ○ Acted in the student theatre play *Carnage* by Yasmina Reza in 2013
Other arts	○ Strong interest in graphic novels and comics (reading them and drawing them) ○ Heavy reader, occasional painter